

Towards 3D Printed Osteoimmunomodulatory Surface Patterns

Nouri Goushki, M.

DOI

[10.4233/uuid:4b8ed184-757b-48e6-bc0b-10d71428af81](https://doi.org/10.4233/uuid:4b8ed184-757b-48e6-bc0b-10d71428af81)

Publication date

2022

Document Version

Final published version

Citation (APA)

Nouri Goushki, M. (2022). *Towards 3D Printed Osteoimmunomodulatory Surface Patterns*. [Dissertation (TU Delft), Delft University of Technology]. <https://doi.org/10.4233/uuid:4b8ed184-757b-48e6-bc0b-10d71428af81>

Important note

To cite this publication, please use the final published version (if applicable).
Please check the document version above.

Copyright

Other than for strictly personal use, it is not permitted to download, forward or distribute the text or part of it, without the consent of the author(s) and/or copyright holder(s), unless the work is under an open content license such as Creative Commons.

Takedown policy

Please contact us and provide details if you believe this document breaches copyrights.
We will remove access to the work immediately and investigate your claim.

TOWARDS
**3D Printed
Osteoimmunomodulatory
Surface Patterns**

TOWARDS

3D Printed Osteoimmunomodulatory Surface Patterns

Dissertation

for the purpose of obtaining the degree of doctor
at Delft University of Technology
by the authority of the Rector Magnificus, Prof.dr.ir. T.H.J.J. van der Hagen,
Chair of the Board for Doctorates
to be defended publicly on
Wednesday 13 April 2022 at 12:30 o'clock

by

Mahdiyeh NOURI GOUSHKI

Master of Science in Chemical Engineering - Polymer Engineering,
Sharif University of Technology, Tehran, Iran,
Born in Baft, Iran

This dissertation has been approved by the promotors.

Composition of the doctoral committee:

Rector Magnificus,	Chairman
Prof.dr. A.A. Zadpoor,	Delft University of Technology, promotor
Dr.ir. E.L. Fratila-Apachitei,	Delft University of Technology, copromotor

Independent members:

Prof.dr. M.J. Dalby,	University of Glasgow, UK
Prof.dr. L.J.W. van der Laan,	Erasmus University Medical Center (MC)
Prof.dr.ir. H.H. Weinans,	Utrecht University
Prof.dr. P.G. Steeneken,	Delft University of Technology

Keywords: osteoimmunomodulatory topography, bone regeneration, 3D printing, biomaterials

Printed by: Gildeprint

Cover design: Arrays of submicron pillars that polarize immune cells (macrophages) from an inflammatory (pink) towards a prohealing response (yellow). At the later stage, the pillars accelerate the formation of bone.

Designed by Ella Maru Studio. The cover of this book has been featured in Nanoscale journal.

Copyright ©2022 by M. Nouri Goushki

ISBN 978-94-6384-327-0

An electronic version of this dissertation is available at

<http://repository.tudelft.nl>



Summary

Osteoimmunomodulation (OIM) is a mechanism through which orthopedic biomaterials may modulate the function of immune cells to promote osteogenesis. OIM is considered a potentially effective way for improving osseointegration. The surface characteristics of orthopedic implants (*e.g.*, topography, wettability, surface chemistry, and charge) can significantly influence their potential OIM behavior. Modifying these properties can, therefore, be considered a powerful method for achieving the described OIM response.

In recent years, the study of the interactions between cells and surface topographies has attracted much attention. The stiffness of the substrate and the design of nanotopographical features have been known to determine stem cell fate. Furthermore, the scale of topographies plays a significant role in modulating cellular responses in the bone microenvironment due to the micro/ nanostructure of the bone. Among the different possible length scales of topographies, the role of submicron topographies on OIM functions has been less frequently studied. That is partially because it is quite challenging to fabricate surface topographies with controlled shapes and dimensions. Moreover, the currently available technologies for the fabrication of submicron features usually involve multiple fabrication techniques and steps.

In this thesis, uniform submicron patterns are, for the first time, 3D printed with controlled dimensions using a single-step nanoprinting technique called two-photon polymerization (2PP). In addition, the effects of the dimensions of the 3D printed submicron pillars on the response of two types of cells involved in the OIM process (*i.e.*, preosteoblast and immune cells) are extensively studied, both separately using monocultures and in interaction with each other using a direct co-culture model performed in the presence of submicron pillars. The topic and objectives are further introduced in **Chapter 1**.

In **Chapter 2** and **Chapter 3**, the 3D printing methods required for fabricating submicron pillars are improved to optimize the uniformity of the printed pillars, strengthen the adhesion of the submicron features to the substrate, and reduce the printing time. We further investigate the effects of the printing parameters (*i.e.*, laser power and laser scanning speed) on the dimensions of the pillars at the submicron scale and the mechanical properties of the printed material. As a proof of concept, the submicron patterns are integrated into 3D structures that are fabricated using a single-step process, thereby creating scaffolds whose surfaces are decorated with surface ornaments. The submicron patterns are also integrated into microfluidic chips to enable studies under dynamic cell culture conditions. Since the conventional print configurations are more efficient in fabricating homogeneous and reproducible pillars, we select this configuration to produce the arrays of submicron pillars that are used for all the subsequent *in vitro* studies.

The material used is compatible with all the three different cell types used in this thesis, namely murine preosteoblasts, human mesenchymal stem cells, and murine macrophages.

Once the conditions for pattern fabrication are established, we investigate the effects of the dimension of the submicron pillar, particularly the height and interspacing of the pillars, on the response of preosteoblasts (**Chapter 4**) and macrophages (**Chapter 5**).

In **Chapter 4**, the early and late responses of murine preosteoblast cells (MC3T3-E1) to submicron patterns are analyzed. The early investigations (*i.e.*, up to 24 hours of culture) include: **(i)** the quantification of the cell adhesion characteristics through single-cell force spectroscopy; **(ii)** a study of the cytoskeletal organization and focal adhesions; **(iii)** a study of the settling states of the cells on the different patterns; **(iv)** an investigation of the mechanical characteristics of the cells residing on the patterned surfaces using atomic force microscopy. The study of the late cellular response primarily focuses on the extracellular matrix produced by the cells after 21 days of culture. The cells interacting with taller and denser pillars are characterized by numerous thick actin stress fibers and greater values of the elastic modulus. Interestingly, the same pillars significantly upregulate the expression of osteopontin by the cells under both osteogenic and non-osteogenic conditions. Our findings paint, with an unprecedented level of mechanistic detail, a picture of at least one possible cascade of events from initial cell adhesion to eventual matrix mineralization. In addition, submicron scale pillars with a specific height and interspace could induce the osteogenic differentiation of preosteoblasts without osteogenic supplements. These results strongly support the role of submicron physical cues as modulators of cell behavior with beneficial effects on osteogenesis.

In **Chapter 5**, we study the effects of the same series of patterns on murine macrophages (J774.A.1). The aim is to investigate if the patterns induce macrophage polarization. Together with the findings of **Chapter 4**, these results enable us to identify the range of pillar dimensions within which both osteogenic and immune responses could be positively regulated. Therefore, we investigate the effects of the patterns on macrophages under two different testing conditions: **(i)** in the presence of soluble inflammatory factors, and **(ii)** when using proinflammatory M1-activated macrophages. The findings indicate that the taller and denser pillars could regulate the polarization of macrophages towards an anti-inflammatory phenotype, which is a desirable transition for subsequent osteogenesis. Interestingly, the same patterns enhanced the matrix mineralization of preosteoblast cells in a non-osteogenic culture medium. Therefore, our results reveal submicron scale patterns are able to generate both osteogenic and immunomodulatory *in vitro* cellular responses. This novel concept of multifunctional topographies opens up a new approach for enhancing the OIM behavior of orthopedic biomaterials.

Having learned about the osteogenic and immune behaviors of cells in interaction with the submicron pillar, the study presented in **Chapter 6** embarks on another challenge, namely to study the cell-cell and cell-pattern interactions by establishing a direct co-culture model involving the macrophages and preosteoblasts. Firstly, we study the interactions between the M1-stimulated macrophages and

preosteoblasts (OBs) at various cell ratios and over different culturing times. Subsequently, we investigate the impacts of the submicron pillars on the two types of cells in the established direct co-culture model. M1 and OBs remain alive and proliferate actively in a mixture of DMEM and α -MEM (1:1), regardless of the cell ratio in the co-cultures. On day 7, the expression of PGE2 and TNF- α are upregulated in the co-cultures relative to the monocultures of OBs and M1s, respectively. Interestingly, the incorporation of 3D printed submicron pillars in the co-culture model enhances the differentiation of OBs, as revealed by the relatively higher RUNX2 expression. Our findings highlight the importance of direct co-culture models and the role of submicron patterns in the osteoimmunomodulation process.

In **Chapter 7**, we conclude with an overall discussion about the main findings of this dissertation as well as some recommendations for future research.

Samenvatting

Osteoimmunomodulatie (OIM) is een eigenschap van bot-biomaterialen en verwijst naar hun vermogen om de functies van immuuncellen te moduleren tot het bevorderen van osteogenese. OIM wordt beschouwd als een krachtige methode om bot integratie van het implantaat te verbeteren. De fysiochemische eigenschappen, van met name het oppervlak (*bijv.* topografie, hydrofiliciteit, oppervlaktechemie en lading), kan de OIM van een biomateriaal significant beïnvloeden. Hierom wordt het moduleren van deze eigenschappen gezien als een krachtig hulpmiddel voor het behalen van een juiste OIM reactie.

De afgelopen jaren trok de studie van de interacties tussen cellen en topografieën veel aandacht. Het is inmiddels bekend dat zowel de stijfheid van het substraat, als het ontwerp van topografische kenmerken op nanoschaal het lot van stamcellen kunnen bepalen. Bovendien speelt de schaal van topografieën een belangrijke rol in het moduleren van cellulaire reacties in het botmicromilieu als gevolg van de micro/ nanostructuur van het bot. De rol van submicron topografieën op OIM-functies is het minst bestudeerd in vergelijking tot andere lengte schalen. De reden hiervoor is voornamelijk dat het nog steeds een grote uitdaging is om topografieën met gecontroleerde vormen en dimensies (*d.w.z.* fysieke patronen) te vervaardigen. Bovendien zijn er gewoonlijk meerdere fabricagetechnieken/stappen nodig om submicron-structuren te creëren.

In dit onderzoek gebruikten we een geavanceerde productietechniek, namelijk direct laser writing (DLW), om submicron-patronen te ontwikkelen in één stap. Vervolgens hebben we uitgebreid de rol onderzocht van de dimensies van de submicron-pilaren op de ruimtelijke organisatie van de cellen die betrokken zijn bij de OIM-functie, *d.w.z.* preosteoblasten en immuuncellen. We hebben het onderwerp en de doelstellingen in **Hoofdstuk 1** geïntroduceerd.

In **Hoofdstuk 2** en **3** hebben we verschillende printconfiguraties bestudeerd om de uniformiteit van de geprinte pilaren te verbeteren, de adhesie van de submicron-structuren aan het substraat te verbeteren en de printtijd te verkorten. We hebben verder de effecten onderzocht van printparameters (*d.w.z.* snelheid en laserkracht) op de afmetingen van de submicron-pilaren en de mechanische eigenschappen van het geprinte (bulk)materiaal. Om het concept te bewijzen hebben we de patronen geïntegreerd **(i)** in 3D-structuren, die in dezelfde stap werden vervaardigd, wat resulteerde in scaffolds met oppervlakte ornamenten en **(ii)** in microfluidische chips om studies onder dynamische celcultuuromstandigheden mogelijk te maken. Omdat de conventionele printconfiguratie sneller was bij het vervaardigen van homogene en reproduceerbare pilaren, hebben we deze configuratie geselecteerd om de arrays van submicron-pilaren te produceren voor alle daaropvolgende *in vitro* studies. Het gebruikte materiaal was niet cytotoxisch voor de drie verschillende celtypen die in dit proefschrift werden onderzocht: muis pre-

osteoblasten, menselijke mesenchymale stamcellen (hMSCs) en muis macrofagen.

Nadat de juiste printinstellingen vastgesteld waren, hebben we in de volgende twee hoofdstukken de effecten onderzocht van specifieke pilaareigenschappen, namelijk verschillende hoogten (300 nm, 500 nm, 1000 nm) en tussenruimtes (700 nm, 1000 nm), op de preosteoblasten (**Hoofdstuk 4**) en macrofagen (**Hoofdstuk 5**).

In **Hoofdstuk 4** we hebben onderzocht de vroege en late respons van preosteoblastcellen op de verschillende patronen. Specifiek gaat het/ons onderzoek naar de vroege respons over: **(i)** het kwantificeren van de krachten tussen de cellen en het substraat op korte tijdschaal (na 2 s en 60 s); **(ii)** de cytoskeletale organisatie (actinevezels), de vorming, en de kenmerken van focale adhesies en de verspreidingspatroon van de cellen op de verschillende patronen na één dag op kweek te hebben gestaan; **(iii)** het mechanisch in kaart brengen van levende cellen op verschillende patronen ook na 24 uur groei; **(iv)** een onderzoek naar de mechanische eigenschappen van cellen gehecht aan patroonoppervlakken, met behulp van atoomkrachtmicroscopie. Voor de late cellulaire respons hebben we ons geconcentreerd op de extracellulaire matrix die door de cellen na 21 dagen groei wordt geproduceerd. De cellen die interacteren met langere en dichtere pilaren werden gekenmerkt door talrijke dikke actine stressvezels en een hoge elastische modulus. Interessant genoeg hebben dezelfde pilaren de expressie van osteopontine door de cellen onder zowel osteogene als niet-osteogene omstandigheden aanzienlijk verbeterd. Onze bevindingen schetsen een beeld van minstens één mogelijke cascade van gebeurtenissen die met aanvankelijke celadhesie begint en uiteindelijke matrixmineralisering voortzet, veroorzaakt door een initiële verandering in cellulaire functies (*bijv.*, de organisatie van celcytoskeleton en cel elastische modulus). Bovendien tonen ze aan dat submicron-pilaren met een specifieke hoogte en tussenruimte osteogene differentiatie van preosteoblasten kunnen veroorzaken bij afwezigheid van osteogene supplementen.

In **Hoofdstuk 5** hebben we het effect van dezelfde serie patronen op macrofagen bestudeerd. Het doel was eerst te onderzoeken of de patronen macro-polarisatie veroorzaken. Ten tweede, door te relateren aan de bevindingen van **hoofdstuk 4**, om te analyseren of er een reeks pilaar-dimensies bestaat die zowel een osteogene als positieve immuunrespons zou kunnen aansturen. Daarom hebben we de effecten van de patronen op macrofagen onder twee verschillende omstandigheden onderzocht: **(i)** in de aanwezigheid van oplosbare ontstekingsfactoren en **(ii)** bij het gebruik van pro-inflammatoire M1 geactiveerde macrofagen. Onze data liet zien dat de langere en dichtere pilaren de polarisatie van macrofagen konden moduleren naar een anti-inflammatoire fenotype, wat een wenselijke overgang is voor latere osteogenese. Interessant genoeg veroorzaakte dezelfde patronen osteogene differentiatie van preosteoblastcellen bij afwezigheid van osteogene supplementen. Ons onderzoek wijst dus uit dat er patronen bestaan die zowel osteogene als immunomodulatoire cellulaire reacties *in vitro* kunnen veroorzaken. Dit nieuwe concept van multifunctionele topografieën demonstreert een nieuwe aanpak voor het verbeteren van de OIM-eigenschap van botbiomaterialen in cocultuur-modellen (**Hoofdstuk 6**).

Na geleerd te hebben over het osteogene en immuun gedrag van cellen tijdens

de interactie met de submicron-pilaar, onderzoeken we in **Hoofdstuk 6** een andere uitdaging, namelijk het bestuderen van de cel-cel- en cel-patroon-interacties door het opzetten van een direct co-cultuurmodel bestaande uit macrofagen en preosteoblasten. Als eerste hebben we de interacties onderzocht tussen murine M1-macrofagen (J774A.1) en murine-preosteoblasten (MC3T3-E1) bij verschillende celverhoudingen en over verschillende kweektijden met behulp van een direct co-cultuurmodel. Vervolgens hebben we het effect van submicron-pilaren op de twee soorten cellen in het ontwikkelde directe co-cultuurmodel bestudeerd. Zowel M1 als OBS bleven in leven en verspreidden zich actief in het mengsel van DMEM en α -MEM (1:1), ongeacht de celverhouding in de co-culturen. Op dag 7 nam de expressie van PGE2 en TNF- α in de co-cultuur toe in verhouding tot, respectievelijk, de mono-gekweekte osteoblasten en M1s. Interessant genoeg heeft de integratie van 3D-geprinte submicron-pilaren in het co-cultuurmodel de differentiatie van preosteoblasten versterkt, zoals blijkt uit de relatief hogere RUNX2-expressie, en de ontsteking gemoduleerd. Onze bevindingen benadrukken het belang van directe co-cultuurmodellen en de rol van submicron-patronen in het osteoimmunomodulatieproces.

In **Hoofdstuk 7** sluiten we af met een algemene discussie en aanbevelingen. Het werk dat we presenteren in dit proefschrift werpt licht op 3D prints van submicron-patroon die relevant zijn voor de regeneratie van botweefsel. We onthulden het potentieel van submicron-pilaren met een specifieke hoogte en tussenruimte om osteoimmunomodulatoire eigenschappen te bereiken. Deze kennis baant de weg naar het ontwerpen van osteoimmunomodulatoire topografieën voor *in vivo* testen.

Contents

Summary	V
Samenvatting	IX
Nomenclature	XVI
1 Introduction	1
1.1 Regenerative biomaterials for bone implants	2
1.2 Osteoimmunomodulatory biomaterials	3
1.3 Aim, objectives, and outline of the thesis	5
2 Submicron Patterns-On-a-Chip: Fabrication of a Microfluidic Device Incorporating 3D Printed Surface Ornaments	11
2.1 Introduction	12
2.2 Materials and methods	13
2.2.1 Nanopatterning using 2PP	13
2.2.2 Upscaling of nanopatterns and fabrication of a multiscale 3D scaffold	15
2.2.3 Characterization of the nanopatterns	15
2.2.4 Image processing and quantification	15
2.2.5 Fabrication of the microfluidic device	15
2.2.6 Delamination test	16
2.2.7 Dynamic cell culture	16
2.2.8 Cell viability	17
2.3 Results and discussion	17
2.3.1 Fabrication of reproducible uniform nanopatterns	17
2.3.2 Characterization of nanopatterns	20
2.3.3 Fabrication of multiscale structures	24
2.3.4 Cytocompatibility	26
2.4 Conclusions	27
2.5 Supplementary information	27
2.5.1 Effects of substrate type and print configurations on the nanopatterns uniformity	27
2.5.2 Effect of tilt correction on the nanopatterns uniformity	29

2.5.3	Effect of 2PP parameters on the dimensions and uniformity of nanopatterns	29
3	3D Printing of Large Areas of Highly Ordered Submicron Patterns for Modulating Cell Behavior	33
3.1	Introduction	34
3.2	Materials and methods	35
3.2.1	Fabrication of the patterns	35
3.2.2	Microscopic characterization of the patterns	36
3.2.3	Contact angle measurement	36
3.2.4	Mechanical characterization	36
3.2.5	Cell experiments	38
3.2.6	Computational models	39
3.3	Results and discussion	40
3.3.1	Pattern fabrication	40
3.3.2	Mechanical properties	43
3.3.3	Water contact angle	43
3.3.4	Response of MC3T3-E1 cells to the 2PP patterns	44
3.4	Conclusions	48
4	3D Printed Submicron Patterns Reveal the Interrelation between Cell Adhesion, Cell Mechanics, and Osteogenesis	51
4.1	Introduction	52
4.2	Materials and methods	53
4.2.1	Fabrication of the patterns	53
4.2.2	Characterization of the patterns	54
4.2.3	Cell experiments	55
4.2.4	Computational models	58
4.3	Results and discussion	58
4.3.1	Characterization of the patterns	59
4.3.2	Differential effects of the patterns on cell adhesion, morphology, and elastic modulus	62
4.3.3	Summary of the early cellular responses on submicron pillars	71
4.3.4	Effects of the patterns on the ECM	72
4.4	Conclusions	74
5	3D Printed Submicron Patterns Orchestrate the Response of Macrophages	77
5.1	Introduction	78
5.2	Materials and methods	79
5.2.1	Fabrication of the patterns	79
5.2.2	Characterization of the patterns	79
5.2.3	Cell culture conditions	80
5.2.4	Cell viability	80
5.2.5	Seeding cells on the patterns with inflammatory cytokines .	81
5.2.6	M1/M2 macrophages controls	81

5.2.7	Immunoassay of IL-10	81
5.2.8	Griess assay of NO	81
5.2.9	Culturing of M1 stimulated macrophages on the patterns	82
5.2.10	Immunofluorescence imaging	82
5.2.11	Image analysis	82
5.2.12	Statistical analysis	82
5.3	Results	83
5.3.1	Characterization of the patterns	83
5.3.2	Macrophages morphology on submicron pillars with(out) inflammatory cytokines	84
5.3.3	Macrophage polarization on submicron pillars	86
5.3.4	Morphology and polarization of M1 macrophages on submicron pillars	88
5.4	Discussion	89
5.5	Conclusions	91
6	Osteoimmunomodulatory Potential of 3D Printed Submicron Patterns Assessed in a Direct Co-culture Model	93
6.1	Introduction	94
6.2	Materials and methods	95
6.2.1	Cell preculture	95
6.2.2	Direct co-culture of macrophages and OBs	96
6.2.3	Direct co-culture of M1s and OBs on the patterned surfaces	96
6.2.4	Cytokines profile	97
6.2.5	Cells viability	97
6.2.6	Osteogenic and mineralization markers	97
6.2.7	Image analysis	98
6.2.8	Statistical analysis	99
6.3	Results and discussion	99
6.3.1	Macrophage activation	99
6.3.2	Direct co-culture of M1 macrophages and MC3T3-E1 cells	99
6.3.3	Modulation of OIM response via submicron pillars	104
6.4	Conclusions	106
7	Concluding Remarks	109
7.1	General discussion	110
7.1.1	3D printing of submicron patterns	110
7.1.2	Modulating the response of multiple cell types by submicron patterns	112
7.1.3	Co-culture of osteogenic and inflammatory cells on submicron pillars	115
7.2	Main findings of this thesis	116
7.3	Future research directions	118
	References	121
	Acknowledgements	147

List of Publications	152
Curriculum Vitae	156

Nomenclature

α -MEM	Alpha minimal essential medium
β -GL	Beta-glycerol phosphate
2PP	Two-photon polymerization
AA	Acrylic acid
AC	Allylamine
AFM	Atomic force microscope
Akt	Serine/threonine protein kinase B
ALP	Alkaline phosphatase
AM	Additive manufacturing
ARG	Arginase
ARS	Alizarin Red S
ATR	Attenuated total reflection
BMP	Bone morphogenetic protein
BMSC	Bone marrow-derived mesenchymal stem cells
BSA	Bovine serum albumin
BSP	Bone sialoprotein
CAD	Computer aided design
CalceinAM	Calcein acetoxymethyl ester
CCR7	C-C chemokine receptor type 7
CD206	The mannose receptor
CM	Conditioned medium
COX2	Cyclooxygenase 2

<i>CVD</i>	Chemical vapor deposition
<i>DAPI</i>	4,6-diamidino-2-phenylindole
<i>Dexa</i>	Dexamethasone
<i>DiLL</i>	Dip-in laser lithography
<i>DLW</i>	Direct laser writing
<i>DMEM</i>	Dulbecco's modified eagle's medium
<i>DNA</i>	Deoxyribonucleic acid
<i>EBID</i>	Electron beam induced deposition
<i>EBL</i>	Electron beam lithography
<i>ECM</i>	Extracellular matrix
<i>ELISA</i>	Enzyme-linked immunosorbent assay
<i>ERK</i>	Extracellular-signal-regulated kinase
<i>EthD</i>	Ethidium homodimer
F_{adh}	Force of adhesion
<i>FA</i>	Focal adhesion
<i>FACS</i>	Fluorescence-activated cell sorting
<i>FAK</i>	Focal adhesion kinase
<i>FBS</i>	Fetal bovine serum
<i>FCS</i>	Fetal calf serum
<i>FEED</i>	Focused electron beam induced deposition
<i>FIBID</i>	Focused ion beam induced deposition
<i>FIBL</i>	Focused ion beam lithography
<i>FTIR</i>	Fourier transform infrared spectroscopy
<i>GA</i>	Glutaraldehyde
<i>GWL</i>	General writing language
<i>hADSC</i>	Human adipose-derived stem cell
<i>hiMSC</i>	Human immortalized mesenchymal stem cell
<i>IFN-γ</i>	Interferon gamma

<i>IL-</i>	Interleukin-
<i>IM</i>	Immunomodulatory
<i>IPA</i>	Isopropyl alcohol
<i>ITO</i>	Indium tin oxide
<i>Lp</i>	Laser power
<i>LPS</i>	Lipopolysaccharide
<i>Mϕ</i>	Macrophage
<i>M1</i>	Pro-inflammatory macrophage
<i>M2</i>	Anti-inflammatory macrophage
<i>MAPK</i>	Mitogen-activated protein kinase
<i>MFI</i>	Mean fluorescence intensity
<i>Mg</i>	Magnesium
<i>MSC</i>	Mesenchymal stem/stromal cell
<i>NA</i>	Numerical aperture
<i>NF-κB</i>	Nuclear factor kappa-light-chain-enhancer of activated B cells
<i>NIL</i>	Nanoimprint lithography
<i>NO</i>	Nitric oxide
<i>NOS</i>	Nitric oxide synthase
<i>OB</i>	Preosteoblast
<i>OCN</i>	Osteocalcin
<i>OIM</i>	Osteoimmunomodulation
<i>OPN</i>	Osteopontin
<i>OSM</i>	Oncostatin M
<i>PBS</i>	Phosphate buffered saline
<i>PCL</i>	Polycaprolactone
<i>PDMS</i>	Polydimethylsiloxane
<i>Pen - strep</i>	Penicillin-Streptomycin
<i>PFA</i>	Paraformaldehyde

<i>PGE2</i>	Prostaglandin E2
<i>PGMEA</i>	Propylene glycol monomethyl ether acetate
<i>PI3K</i>	Phosphatidyl-inositide 3- kinase
<i>PLA</i>	Polylactic acid
<i>QI</i>	Quantitative imaging
<i>qPCR</i>	Quantitative polymerase chain reaction
<i>R_a</i>	Average roughness
<i>RhoA</i>	Ras homolog family member A
<i>ROCK</i>	Rho-associated protein kinase
<i>RPMI</i>	Roswell park memorial institute medium
<i>RUNX2</i>	Runt-related transcription factor 2
<i>SCFS</i>	Single-cell force spectroscopy
<i>SEM</i>	Scanning electron microscope
<i>SLA</i>	Stereolithography
<i>Sr</i>	Strontium
<i>STL</i>	Standard tessellation language
<i>TGF-β</i>	Transforming growth factor- β
<i>TLR - 4</i>	Toll-like receptor 4
<i>TNF-α</i>	Tumor necrosis factor α
<i>W_{adh}</i>	Work of adhesion
<i>XPS</i>	X-ray photoelectron spectroscopy
<i>YAP</i>	Yes-associated protein

1

Introduction

1.1. Regenerative biomaterials for bone implants

Bones have intrinsic healing and regeneration capabilities, but they cannot fully regenerate in some instances, especially when defects are too large such as those caused by severe trauma or the resection of bone tumors [1]. Unfortunately, the typical clinical treatment approaches (*e.g.*, autograft) have serious limitations such as condition of host tissue and donor site morbidity [2]. Such clinical challenges are being addressed within the context of “tissue engineering”, which was introduced in 1987 [3]. This field has opened up a new direction towards new strategies for bone tissue regeneration. Combining tissue engineering with advanced emerging sciences such as biomaterials, stem cell biology, and regenerative medicine creates the newly established multidisciplinary concept entitled “regenerative engineering” [3]. Implementing this concept in bone regeneration requires the development of biomaterials as one of its main pillars.

Regenerative biomaterials for bone applications should possess ideal properties to support the self-healing mechanisms of the bone. Upon implantation, the structure, composition, and biochemical cues of the biomaterial should modulate immune reactions, support the migration and differentiation of stem and progenitor cells, and enhance tissue regeneration [4]. Fabricating a biomaterial capable of regulating all aspects of the bone regeneration process is highly complicated.

The first generation of biomaterials, sometimes called “bioinert”, is biocompatible and provides sufficient mechanical support but may not specifically stimulate bone formation due to their insufficient interaction with the surrounding tissue [5, 6]. Non-biodegradable metallic biomaterials (*e.g.*, titanium or titanium alloys), synthetic polymers (*e.g.*, polymethyl methacrylate), and ceramics (*e.g.*, alumina) can be considered part of this category [3, 5]. The second generation of orthopedic biomaterials is bioactive/bioresorbable material that may induce tissue regeneration and make a bond with the tissue interface upon implantation [3, 7]. Examples are naturally derived polymers (*e.g.*, collagen and hyaluronic acid) that improve cell attachment [7], biodegradable synthetic polymers (*e.g.*, polylactide (PLA) and polycaprolactone (PCL)) that can customize the mechanical properties [7], and bioactive glass, which is the first artificial material known for its osseointegration potential [8]. The latest generation of orthopedic biomaterials possesses tailored physical (*e.g.*, porosity, geometry) and chemical properties (*e.g.*, (in)soluble factors such as growth factors, chemicals, immobilized adhesion ligands) [3, 9]. This type of materials is instructive, multifunctional, and capable of directing cell fate [3]. Although they induce different responses to multiple cell types [10] a close and effective interaction between the immune and skeletal cells is required to accomplish the formation of bone [11].

Understanding the sometimes unpredictable responses of various cells to the implanted biomaterials and the underlying signaling pathways is critical for unraveling the effects and possible modulatory role of biomaterials in the complex process of immunomodulation and bone regeneration.

1.2. Osteoimmunomodulatory biomaterials

Osteoimmunomodulation (OIM) has recently emerged as a potential biological characteristic of orthopedic biomaterials for regulating immune response and mediating bone regeneration [12, 13]. Three major elements, namely immune cells, bone cells, and biomaterials, are involved in OIM [14]. Understanding the interaction among immune and bone cells is essential as a first step. Due to the close communication between immune and bone regeneration processes, immune cells could significantly affect the bone formation in the presence of biomaterials that are considered foreign bodies [15]. These phenomena could be directed by the cytokines that immune cells express in their microenvironment, leading to either chronic inflammation or bone healing [15]. The impacts of biomaterials on the inflammatory reactions and osteogenesis should, therefore, be understood for optimal bone regeneration. The following emerging strategies should be considered when designing advanced OIM biomaterials:

- **Modification of the biomaterial's composition:** The integration of specific elements (*e.g.*, Mg, Sr) [16, 17] or inflammatory cytokines (*e.g.*, oncostatin M, (OSM)) may be used to modulate OIM [18].
- **Optimization of the particle size (from nano to macro scale), pore size, and porosity of scaffolds.** Nanoparticles [19, 20] and micropores between 30-40 μm [21] are reported to direct macrophages towards a pro-healing phenotype, but non-porous structures and random pore size may have an opposite effect.
- **Modification of biomaterials surface (chemistry or topography):** Nanoscale topographies [22, 23], surface roughness [24], and hydrophilicity [25] are found to direct the interaction of bone cells and macrophages.

Most of these approaches exploit specific underlying mechanisms involving single cells and biomaterials. Of those strategies, the ones conducive to osteogenesis [26, 27] may propose a set of design objectives for developing OIM orthopedic biomaterials.

At the early stage of implantation, cells rapidly perceive and react to the physiochemical characteristics of the biomaterial surface [28]. For example, modifying the surface of biomaterials using osteogenic agents is reported to enhance the osteogenic differentiation of stem cells *in vitro* [29, 30]. Even so, controlling the *in vivo* release of multiple molecules with the desired dose increases the complexity of biomaterials [30, 31]. On the other hand, the surface patterning of biomaterials not only allows them to mimic the native extracellular matrix (ECM) but may also help them regulate the immunogenic and osteogenic response of cells [29]. Together with the chemistry of the biomaterial, surface topographies, especially at the nano- and submicron scale, may influence the cascade of molecular interactions involved in the early inflammation [29] and the later differentiation of stem cells into the osteogenic lineage [32] via mechanotransduction pathways [31]. Therefore, biomaterials decorated with such patterns may be harnessed for

their osteogenic and immune-modulation potential, thereby broadening the range of surface cues that can be used to develop bone regenerative biomaterials. Nevertheless, not much is known about the influences of controlled surface patterns on early inflammation and subsequent osteogenesis.

The osteoimmunomodulatory effects of the surface topography of biomaterials have been unevenly studied [12]. The focus of previous research has been mainly on the osteogenic behavior of cells but not the OIM response. Surface roughness is considered a potent physical cue that could alter the response of both osteoblasts and immune cells. At the scale of micro, for example, the pro-healing response of macrophages is reported to be enhanced on hydrophilic microroughened surfaces [33]. Machine learning techniques have been recently used to identify the proper chemical and topographical features for immunomodulatory osteoconductive biomaterials [34]. Micropillars made of ethyl acrylate, with a diameter smaller than 6 μm and a height of 10 μm , have been found to cause macrophages to exhibit a prohealing response [34]. The highest upregulation of the ALP activity of human immortalized mesenchymal stem cells (hiMSCs) was observed on microfeatures with a diameter smaller than 7 μm and rotations $> 25^\circ$ relative to the x-axis [34]. At the nanoscale, increasing the roughness on the titanium surface from 6-12 nm upregulated the *in vivo* secretion of pro-inflammatory markers [35]. When gold particles with sizes of 16-68 nm are added on a chemically modified surface (with allylamine (AA) or acrylic acid (AC)), the level of inflammatory cytokines (*e.g.*, TNF- α , IL-1, IL-6) induced by murine-derived macrophages (Raw 264.7 cells) decreased as compared to the chemically modified flat substrate [29]. Furthermore, the AA-modified surfaces with 68 nm topographies boosted the osteogenic differentiation of bone marrow stromal cells (BMSCs) in the conditioned medium derived from materials/macrophages [29]. At the submicron scale, titanium grooves polarized macrophages to the M1 phenotype (inflammatory response) by increasing the surface roughness from 100 nm to 400 nm [36]. Moreover, a conditioned medium of material/macrophages was found to enhance the differentiation of preosteoblasts [36]. However, little is yet known about the regulation of the OIM response, especially by submicron pillars.

In addition to the abovementioned findings, it has been reported that specific pattern geometries could modulate the osteogenic [31] and immune [37] responses in monocultures. Among the various shapes of patterns, pillars, defined as high aspect ratio features protruding from a surface, are less investigated for bone regeneration. At the microlevel, the increased hydrophobicity of micropillared surfaces, as compared to flat ones, has been found to decrease the initial cell adhesion, spreading, and the expression of ECM proteins (BSP-2 (bone sialoprotein) and collagen-I) in human osteoblasts (MG-63) [38]. However, the effects of submicron pillars on bone regeneration and inflammatory responses are rarely studied.

One of the reasons for the limited understanding of the role of nano- and submicron scale patterns in regulating cellular functions has been the limited availability of fabrication techniques capable of producing patterns with controlled features (*i.e.*, dimensions, geometry, and spatial organization) on sufficiently large areas in a high-throughput manner. While the continuous progress of nanofabrica-

tion technologies is increasingly facilitating the study of the cascades of biological events involved in the dynamic process of bone regeneration at the interface with surface-modified biomaterials [39], engineering implants with controlled patterned surfaces is still challenging. That is due to the different manufacturing technologies needed to produce complex 3D biomaterials and the ones required for surface micro/nanopatterning [40]. The size of patterns is often 6 - 7 orders of magnitude smaller than the actual size of the orthopedic implants [31, 41]. There is still no single-step manufacturing technique that could produce biomaterials integrating such multiscale features. Moreover, the fabrication of well-defined micro and nanoscale structures in one single-step process is highly challenging since the fabrication technique requires great precision and sensitivity [42].

Additive manufacturing (AM) techniques have recently facilitated the fabrication of free-form geometries by reducing the fabrication steps and overcoming the limitations of traditional fabrication techniques [43]. For metals, the minimum feature sizes achieved by powder bed fusion technologies are around few tens of micrometers [44–46]. Micro- and submicron scale AM techniques are not currently well-developed for metals [44]. Although several high-resolution methods suitable for metals, such as focused electron/ion beam induced deposition (FEBID/FIBID), have been successful in fabricating features in the range of 0.05-10 μm [44], they tend to be very slow, making them unsuitable for the fabrication of actual orthopedic implants. For polymeric materials, stereolithography (SLA) machines can produce mesoscale structures with surface microfeatures at a writing speed of 20 mm/s [47]. Furthermore, direct laser writing (DLW) can generate centimeter-scale complex 3D structures with submicron resolutions at high speed in a single-step process [47]. However, producing uniform submicron scale features with a high speed over a large area remains challenging.

1.3. Aim, objectives, and outline of the thesis

This thesis aims to apply 3D printing techniques to create highly ordered submicron pillars over large areas and elucidate their effects on the bone and inflammatory cells by using *in vitro* mono- and co-culture models. The ultimate objective is to gain more insight into the OIM response of biomaterial surfaces covered by submicron pillars. Towards that aim, the following sub-objectives are defined (Figure 1.1):

- Obj. 1) 3D printing of submicron patterns:** To fabricate and characterize the 3D printed submicron pillars with controlled feature sizes for subsequent cellular studies.
- Obj. 2) Modulating the response of multiple cell types by submicron pillars with different dimensions:** To investigate the impact of submicron pillars on the bone and inflammatory cells.
- Obj. 3) Direct co-culture of osteogenic and inflammatory cells in the presence of submicron pillars:** To establish a direct co-culture model and investigate the OIM potential of submicron pillars.

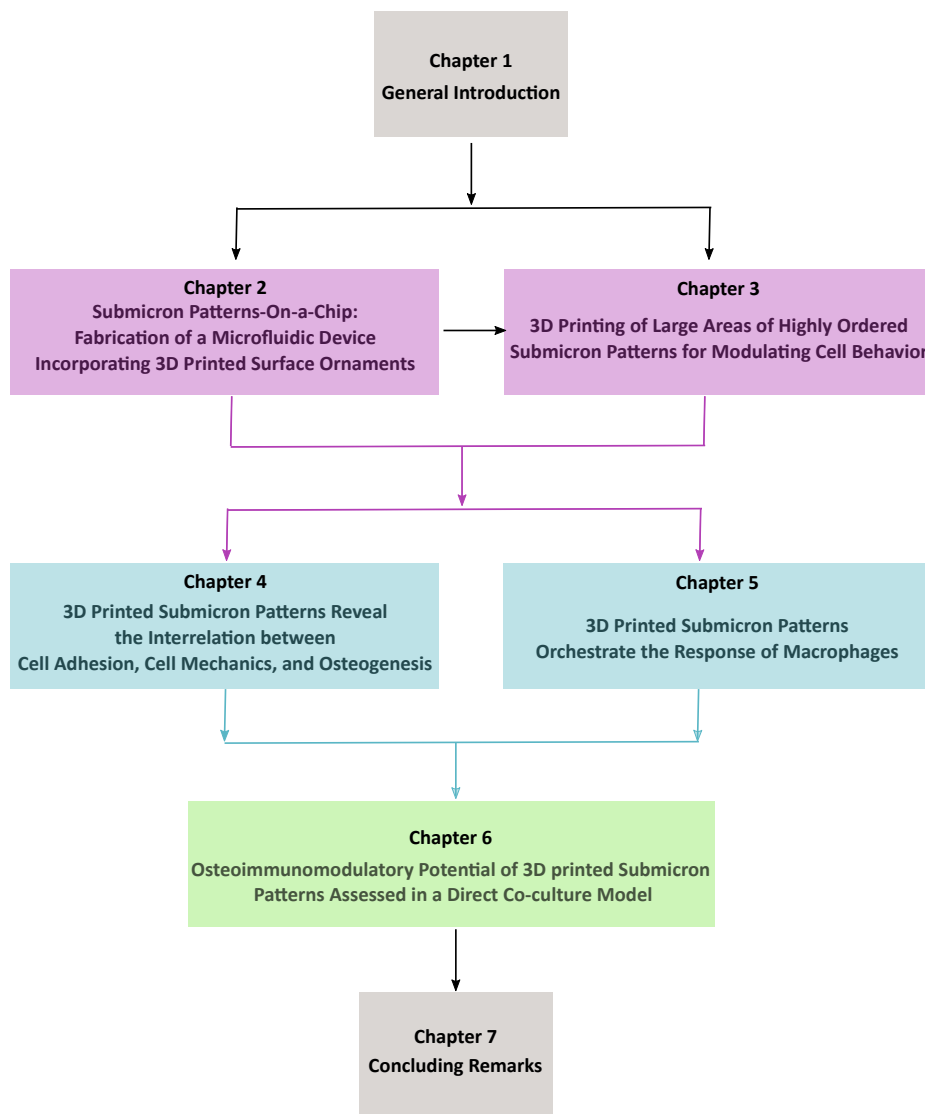


Figure 1.1: The outline of the thesis

The **challenges** associated with each sub-objective are discussed below:

1) Fabrication of submicron patterns:

The 2PP technique (Figure 1.2a) was chosen to fabricate pillars since it offers a single-step fabrication process. However, the 3D printing of highly ordered pillars in the submicron range using the 2PP method requires massive optimization of the printing parameters to create uniform pillars with controlled dimensions and interspacing with high speed. We tried to find answers to the following questions:

- “What would be the minimum feature sizes achievable by 2PP?”
- “Can we create highly ordered patterns over a large surface area?”
- “Can we speed up the printing process?”

In **Chapters 2** and **3**, we investigated the use of both main configurations (DiLL and conventional) used in 2PP (Figure 1.2a) to cover a large surface area with highly ordered pillars at high spatial resolutions. We assessed the cytocompatibility of the materials used with MSCs and preosteoblasts. Lastly, we engineered a multiscale scaffold and a microfluidic platform incorporated with submicron/nanoscale topographies, which can provide a promising model for 3D cell culture.

2) Interaction of multiple cell types with submicron pillars:

After successful printing of biocompatible patterns, the next research question was:

- “How do the dimensions and arrangement of the patterned surfaces regulate the behavior of osteogenic cells and immune cells?”

We investigated the effects of submicron patterns (Figure 1.2b) on preosteoblasts (**Chapter 4**) and macrophages (**Chapter 5**):

- **Osteogenic response:** We performed a comprehensive study with special attention to the adhesion phase of preosteoblasts on the patterned and non-patterned surfaces. We also developed a novel method to quantify the adhesion characteristics and the mechanical properties of the adherent cells. These techniques allowed us to study the possible interrelations between early cell adhesion, mechanics, and the late osteogenic activity of preosteoblasts.
- **Immunogenic response:** The cytocompatibility of biomaterials and the immunomodulatory potential of submicron pillars with various dimensions were investigated in **Chapter 5**. We studied the morphology and polarization of murine-derived macrophages interacting with 6 different types of submicron patterns (Figure 1.2b) in the presence of M1-inducing stimuli at multiple time points. Moreover, we explored whether the proposed submicron pillar dimensions can modulate the polarization of M1 macrophages towards a more favorable pro-healing phenotype.

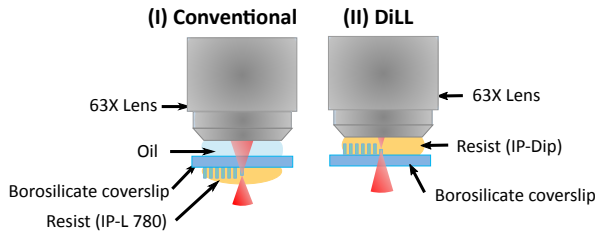
3) Cross-talk between immune and osteogenic cells in a direct co-culture model:

The interactions between the inflammatory and osteogenic cells in a direct co-culture model integrated with topographies has not been investigated before. Therefore, **Chapter 6** concludes the research presented in this thesis by studying the following question:

- “How do osteogenic and immune cells interact with submicron patterns in a direct co-culture model?”

We first established a direct co-culture model and used it to investigate the interactions between murine M1 macrophages (J774A.1) and murine preosteoblasts (MC3T3-E1) at various cell ratios and over different culturing times. The direct co-culture model was then applied to study the effects of 3D printed submicron pillars on both types of cells.

(a) Printing configurations in two-photon polymerization (2PP) technique



(b) The arrays of 3D printed submicron pillars interfaced with preosteoblasts and macrophages

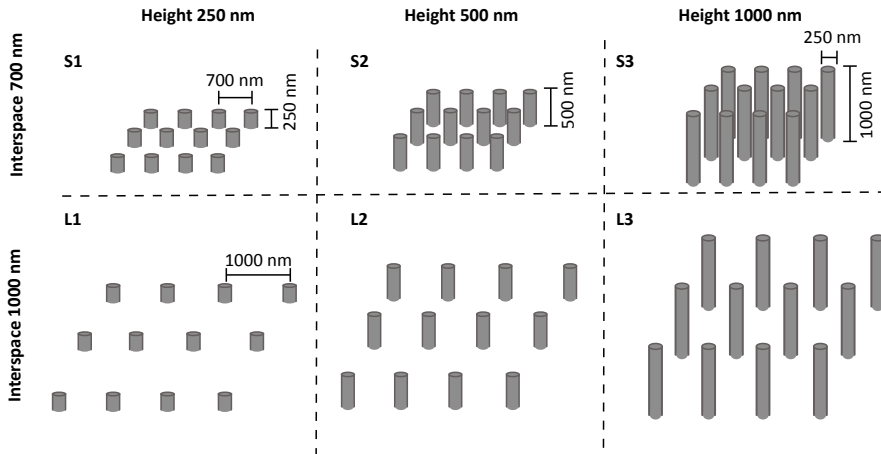


Figure 1.2: The fabrication of submicron pillars with (a) 2PP technique. (b) The geometries that are selected for the study of the OIM response.

2

Submicron Patterns-On-a-Chip: Fabrication of a Microfluidic Device Incorporating 3D Printed Surface Ornaments

Manufacturing high throughput *in vitro* models resembling the tissue microenvironment is highly demanded for studying bone regeneration. Tissues such as bone have complex multiscale architectures inside which cells reside. To this end, engineering a microfluidic platform incorporated with three-dimensional (3D) microscaffolds and submicron/nanoscale topographies can provide a promising model for 3D cell cultures. There are, however, certain challenges associated with this goal, such as the need to decorate large surfaces area with high-fidelity 3D submicron structures. Here, we succeeded in fabricating a microfluidic platform embedded with a large area (mm range) of reproducible submicron pillar-based topographies. Using the two-photon polymerization (2PP) as a 3D printing technique based on direct laser writing, uniform submicron patterns were created through optimization of the process parameters and writing strategy. To demonstrate the multiscale fabrication capabilities of this approach, submicron pillars of various heights were integrated onto the surfaces of a 3D microscaffold in a single-step 2PP process. The created submicron topography was also found to improve the hydrophilicity of the surface while being able to withstand flow rates of up to 8 mL/min. The material (IP-Dip resin) used for patterning did not have cytotoxic effects against human mesenchymal stromal cells after 3 days of dynamic culture in the microfluidic device. This proof-of-principle study, therefore, marks a significant step forward in manufacturing submicron structure-on-a-chip models for bone regeneration studies.

Published as: Nouri-Goushki, Mahdiyeh, *et al.*, "Submicron Patterns-On-a-Chip: Fabrication of a Microfluidic Device Incorporating 3D Printed Surface Ornaments." ACS Biomaterials Science & Engineering 5.11 (2019): 6127-6136, <https://doi.org/10.1021/acsbomaterials.9b01155>.

2.1. Introduction

Bone regeneration is a complex biological process that supports skeletal health throughout our lifetime. In this process, osteoprogenitor cells migrate, proliferate, and differentiate to restore and repair bone injuries [48, 49]. However, the bone regeneration capacity of the human body is either inadequate or is compromised in the case of large bony defects, infections, arthritis, and tumors [50–53]. The innate bone regeneration capacity should therefore be augmented through biomaterials that promote osteogenesis, thereby enhancing the performance of the bone regeneration process [53–55]. The vast majority of such biomaterials introduced to date work on the basis of locally delivering biomolecules such as bone morphogenic protein (BMP) to promote the osteogenic differentiation of human mesenchymal stromal cells (hMSCs) [30, 56]. There are, however, concerns regarding the size-dependent toxicity effects of some of these biomolecules [30, 57, 58] particularly in larger animals such as humans. In addition, such biomolecules are often expensive and may have undesired side effects [57, 59].

An alternative approach tries to exploit the effects of (nanoscale) topographies on cellular processes including migration, adhesion, proliferation, and differentiation to enhance the bone tissue regeneration performance of biomaterials [60, 61]. In particular, several studies have shown that very specific shapes and dimensions of nanopatterns could stimulate the osteogenic differentiation of stem cells [31, 62, 63]. Moreover, the same nanoscale patterns could be used to kill bacteria so as to minimize the risk of implant-associated infections [64–66]. However, it is still unclear how different design parameters of the surface nanopatterns affect the various cellular processes both for the host cells and bacteria [67, 68]. One therefore has to perform many experiments to systematically study the effects of a large number of design parameters on the different types of cellular responses. This challenge is further compounded by the fact that the experiments have to be repeated for different cell types including stem cells, immune cells, and different types of bacteria (*e.g.*, Gram-positive, Gram-negative). Therefore, high-throughput experimental setups that allow for such large systematic studies are required. Lab-on-a-chip devices that incorporate various nanopatterns inside a microfluidic chip are very attractive solutions for such an application. Such devices also allow improving the mass transfer of nutrients, metabolites, gases, and metabolic byproducts while controlling the temperature and pH [69]. However, fabrication of such devices would require a multiscale manufacturing approach to create the nanopatterned surfaces and to integrate them into the chip.

Micro- and nanoscale patterns can be fabricated by removing material from a bulk material using top-down nanopatterning techniques such as lithography [70] and etching [71, 72]. These structures can be also manufactured by deposition of atoms, molecules, or nanoparticles in processes by so-called bottom-up nanopatterning (*e.g.*, focused electron beam induced deposition (FEBID) [73], chemical vapor deposition (CVD) [74], and molecular self-assembly [75]). Although some of these techniques are capable of producing features with ultrafine resolutions (≤ 100 nm), they are often restricted in terms of surface quality, upscaling, and combination and alignment of multiple elements. To overcome these restrictions,

here, we use three-dimensional (3D) direct laser writing (DLW) [76, 77]. DLW works on the basis of two (or multiple) photon polymerization (2PP) and allows for printing 3D objects at the nanoscale and larger (up to mm) feature sizes [78]. Barata et al. [78] developed a microfluidic chip integrated with microstructures through a combination of photolithography, 2PP, and hot embossing. They studied the interaction of human osteosarcoma cells with the biomaterial under a low flow rate of continuous medium perfusion. In another study, Yong et al. [79] developed a microfluidic device incorporated with nanogratings through a stitching and micro-transfer assembly technique rooted in polymer thin film technologies. Despite the availability of these few studies, a versatile technique to fabricate microfluidic devices endowed with nanoscale features is still lacking [69].

Manufacturing a large area of nanopatterns for cell culture and preserving the geometrical accuracy after assembly are the two main challenges in the integration of nanopatterns within microfluidic devices [69]. In this study, we fabricated a large surface area with nanopillars made through the 2PP process and embedded them within a microfluidic chip (Figure 2.1).

The uniformity of the nanopillars was boosted by proper selection of the materials and writing mode, as well as by correcting for the substrate tilt. The morphologies of the nanopillars were first characterized and then upscaled to a larger area (mm range). We then fabricated a micro-scaffold covered with nanopillars of various heights. In addition to measuring the adhesion force and wettability, we performed dynamic culture of hMSCs to evaluate the biocompatibility of the nanopatterned surfaces.

2.2. Materials and methods

2.2.1. Nanopatterning using 2PP

We used the 2PP process for additive manufacturing of the surface nanopatterns using a Photonic Professional GT (Nanoscribe, Germany) machine. This machine works on the basis of a pulsed femtosecond laser (center wavelength = 780 nm, pulse duration = 100 fs, repetition rate = 80 MHz) and is equipped with a 63X objective lens (NA 1.4, numerical aperture). The Piezo writing strategy and dip-in laser lithography (DiLL) configuration were selected for writing the nanoscale features. The nanopillars were created using an acrylate-based resin (IP-Dip, Nanoscribe, Germany) atop an indium tin oxide (ITO) coated fused silica glass (ITO glass) (Nanoscribe, Germany). Before printing, the substrates were cleaned with acetone and isopropyl alcohol (IPA) (both Sigma-Aldrich, Germany). After writing, the samples were developed in propylene glycol monomethyl ether acetate (PGMEA, Sigma-Aldrich, Germany) for 25 min, followed by 5 min of development and rinsing in IPA.

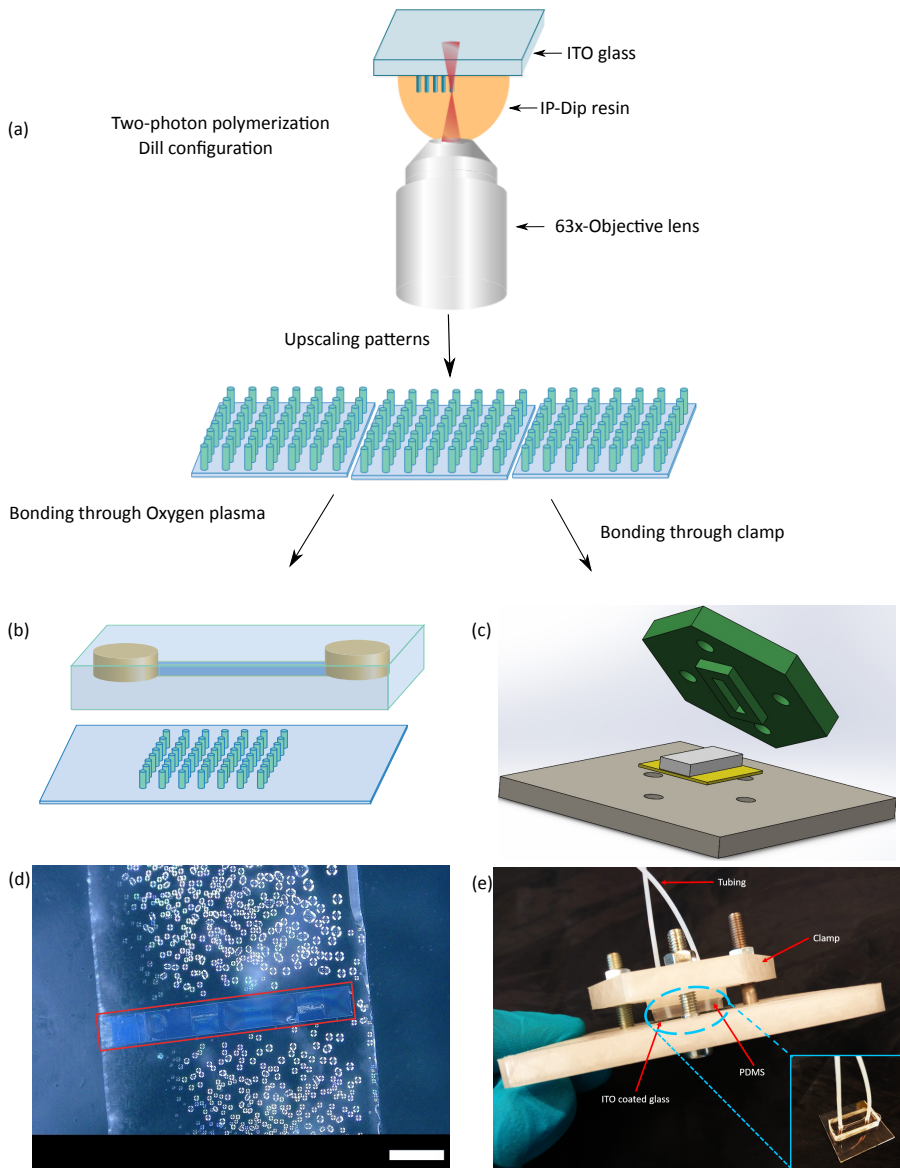


Figure 2.1: (a) A schematic illustration of the 2PP process to prototype a large area of nanopatterns. (b) Oxygen plasma bonding process for cell study. (c), (e) SolidWorks and real view models of the mechanical clamp set-up used to align the channel over the topography in the nanopattern delamination test. (d) Aligned nanopatterns along the channel edge. Microdroplets can be seen after the experiment. Scale bar is 200 μm .

2.2.2. Upscaling of nanopatterns and fabrication of a multiscale 3D scaffold

The writing parameters of the 2PP process were first optimized for printing reproducible nanopillars of known dimensions in an area of $100\ \mu\text{m} \times 100\ \mu\text{m}$. Larger areas of this nanotopography (up to $2\ \text{mm} \times 1.7\ \text{mm}$) were then achieved by repeat-printing the previously optimized area. The procedure was then extended to nanopillars with various heights on a 3D woodpile structure, which was fabricated using the machine's Galvo mode which has a larger throughput. Each woodpile had a cross section of $5\ \mu\text{m} \times 5\ \mu\text{m}$, a length of $55\ \mu\text{m}$, and a pitch of $10\ \mu\text{m}$.

2.2.3. Characterization of the nanopatterns

Nanotopographical surfaces were characterized using a scanning electron microscope (Jeol InTouchScope JSM-6010LA, Japan). All specimens were sputter-coated with a $\approx 10\ \text{nm}$ thick gold-palladium layer before imaging. Furthermore, an optical microscope (Keyence Digital Microscope VHX-6000, USA) was used to acquire pixel intensity maps and to evaluate the reproducibility and uniformity of the nanopillar dimensions. The wettability of the nanopatterned surfaces was assessed using a drop shape analyzer (KRUSS DSA100, Germany). First, the samples were cleaned with IPA (Sigma-Aldrich, Germany). Then, droplets of deionized water ($0.1\text{-}0.3\ \mu\text{L}$) were laid on the nanopatterned and non-patterned surfaces. The contact angles were recorded after $5\ \text{s}$ (three measurements per sample).

2.2.4. Image processing and quantification

The acquired SEM images were analyzed using ImageJ (open source image analysis software, <http://rsb.info.nih.gov/ij/index.html>) to measure the height, diameter, and uniformity of the nanopatterns over a large area. To do so, the height and diameter of the nanopillars were first quantified through high-magnification SEM images at 13000X from a few sample regions within the nanopatterned area that were then used to calibrate the mesoscale image of the nanopattern obtained from low-magnification images (taken at 850X via SEM and stitched together). Furthermore, optical images of the same area were taken to analyze their pixel intensity map. Finally, the pixel intensity map of the optical images was correlated with the data obtained from high-magnification SEM images using a custom-made MATLAB code (2017 b) to identify the numbers, dimensions (mean \pm SD), and uniformity of the printed nanopillars (Table 2.2).

2.2.5. Fabrication of the microfluidic device

A single microchannel of $200\ \mu\text{m}$ height, $1\ \text{mm}$ width, and $7.85\ \text{mm}$ length was fabricated via the mold replication technique. First, the mold was 3D printed using the stereolithography technique (Envisiontec Micro Plus HD, Germany). Then, a mixture of polydimethylsiloxane (PDMS) (Sigma Aldrich, Germany) and

the curing agent (10:1 w/w) (Sigma Aldrich, Germany) was poured into the 3D printed molds and desiccated for 1 h to remove any trapped air bubbles. After 3 h curing at 70 °C, the PDMS part was peeled off the molds. The PDMS layer was then placed over the substrate while aligning the channel with the nanopatterns (Figure 2.1b, d). The method of bonding PDMS to the substrate depended on the type of the experiment performed later. For the delamination test, PDMS was pressed onto the substrate through a mechanically designed clamp, while oxygen plasma was used in the case of the specimens prepared for cell culture.

2.2.6. Delamination test

The delamination of the nanopillars was tested with respect to the various flow rates of deionized water. Nanopatterned strips of 1 mm × 0.1 mm were integrated into the microfluidic chip and were held leak-tight with the help of the clamp. The CAD model and the actual 3D printed mechanical clamp (made with an Original Prusa I3 MK2S printer, Czech Republic) holding the chip are presented in Figure 2.1c and e, respectively. The different flow rates of deionized water (1, 3, 5, and 8 mL/min) were applied in the chip through a peristaltic pump (Ismatec ISM915, Germany). The nanopillars were observed before and after the experiments using optical microscope and SEM to check whether they were delaminated.

2.2.7. Dynamic cell culture

Two 1 mm × 0.3 mm areas of nanopatterned and non-patterned sheets (with a height of 3 μm) were printed in parallel and aligned along the channel edge. Both the nanopatterned surface and the channel side of the PDMS were exposed to air plasma (Low Cost System Atto, Diener Electronic, Germany) for 2 min (power level = 40 W, chamber pressure = 4 mbar) after which they were brought into contact.

hMCSs (passage 7; Lonza, Switzerland) were cultured in alpha minimal essential medium (αMEM: 10% (v/v) fetal calf serum (FCS), pH = 7.5, Phenol-red free; Life Technologies, USA) as previously described in detail by us [80]. A cell seeding concentration of approximately 1.1×10^6 cells/mL was used for the dynamic cell culture. The microfluidic device was flushed 3 times with αMEM medium followed by seeding into the microchannel. The cells were then incubated (at 37 °C, 5% CO₂) for 6 h before starting the flow of culture medium at 10 μL/h, using a NE-1200 syringe pump (KF Technology, Italy). After 3 days, the cells were rinsed 2 times with phosphate buffered saline (PBS, Life Technologies, USA) and incubated 10 min in a fixative solution (4% PFA and 1% GA (Sigma-Aldrich, Germany) in PBS) at room temperature. The fixed samples were washed 2 times with distilled water for 5 min and then immersed in a series of graded alcohol-PBS solution (50%, 70%, 96%) for 15 min, 20 min, and 20 min respectively. The samples were dried overnight at room temperature. At last, the specimens were gold-sputtered before obtaining SEM images.

2.2.8. Cell viability

A live/dead cell assay (ThermoFisher Scientific, USA) was performed to study the viability of the cultured cells. After 3 days of dynamic cell culture, hMSCs were washed 3 times with PBS and incubated in a mixture of 5 $\mu\text{g}/\text{mL}$ Hoechst 33342 (Nuclei Dye, Sigma-Aldrich, Germany) and 10 mg/mL propidium iodide (Dead Dye, Sigma-Aldrich, Germany) for 15 min at 37 °C. In this fluorescence-based assay, Nuclei Dye stains the nucleus of both live and dead cells in blue while Dead Dye penetrates the membrane of the dead cells (red). After staining, the cells were washed with PBS and viewed with a confocal microscope (Axiovert 200MOT, Zeiss, Germany).

2.3. Results and discussion

2.3.1. Fabrication of reproducible uniform nanopatterns

Selection of an appropriate print configuration and writing parameters within the 2PP process is necessary to produce uniform and reproducible topographical nanopatterns. To further enhance the uniformity of the nanopatterns, a tilt correction strategy for substrate was adopted and the effects of different configurations were evaluated. Lastly, a parametric study was conducted to assess the effects of 2PP writing parameters on the uniformity of the nanopatterns and the minimum feature size that could be reliably achieved.

2.3.1.1. Effects of print configurations

Different configurations and respective materials (resins and substrates) for the 2PP process were evaluated (Table 2.1).

Table 2.1: Configurations, materials, and the interface signal amplitude in the 2PP process.

Configuration	Materials	Interface signal amplitude
DiLL	IP-Dip + ITO coated fused silica glass	1000 – 2000
DiLL	IP-Dip + fused silica glass	600 - 700
Conventional	IP-L 780 + borosilicate glass	300 - 400

In comparison with the other types of substrates, a significant improvement (up to 86%) in the uniformity of the nanopatterns was achieved by printing over the ITO-coated fused silica glass when scaled up to a 2 mm \times 1.7 mm area in the DiLL configuration (Figure 2.2a). The ITO-coated fused silica substrate in combination with IP-Dip resin yielded a higher interface signal amplitude (a value directly proportional to the refractive index mismatch at the interface of

the resin and the substrate) in comparison with an uncoated fused silica substrate (Supplementary Figure 2.1). When using the conventional configuration (IP-L 780, borosilicate glass), the signal amplitude decreased even further (Supplementary Figure 2.2). Enhancing the interface signal amplitude decreased the noise and helped in more accurate detection of the substrate surface. This noise was decreased by increasing the refractive index difference between the two media (Supplementary Figures 2.1 and 2.2).

2.3.1.2. The effects of tilt correction

The Piezo writing strategy was selected among the available writing modes in the 2PP process to produce each nanopillar as a single voxel. At the nanoscale, a large variation in the nanopillar dimensions along the direction of writing was observed due to the angular motion of the scanner during the writing process (Supplementary Figure 2.3a). We used a tilt compensation method to reduce such effects where a correction accounting for the tilt of the substrate (accuracy in the range of 0.01°) was made to obtain a more uniform nanopattern (Supplementary Figure 2.3c). This procedure required measuring the interface position (in the z-direction) followed by fitting a linear plane to the measured position data points. The tilt angle of this fitted plane in the x- and y-direction were then input into the 2PP machine program to add the appropriate offsets in the z-coordinate while traversing in the x- and y-directions. The uniformity of the fabricated nanopillars increased after applying the tilt correction to the ITO-coated sample (Figure 2.2b). The uniformity of the nanopatterns written on manually tilt-corrected, auto tilt-corrected, and uncorrected substrates (ITO fused silica, DiLL configuration) are compared in the supplementary information (Supplementary Figure 2.3).

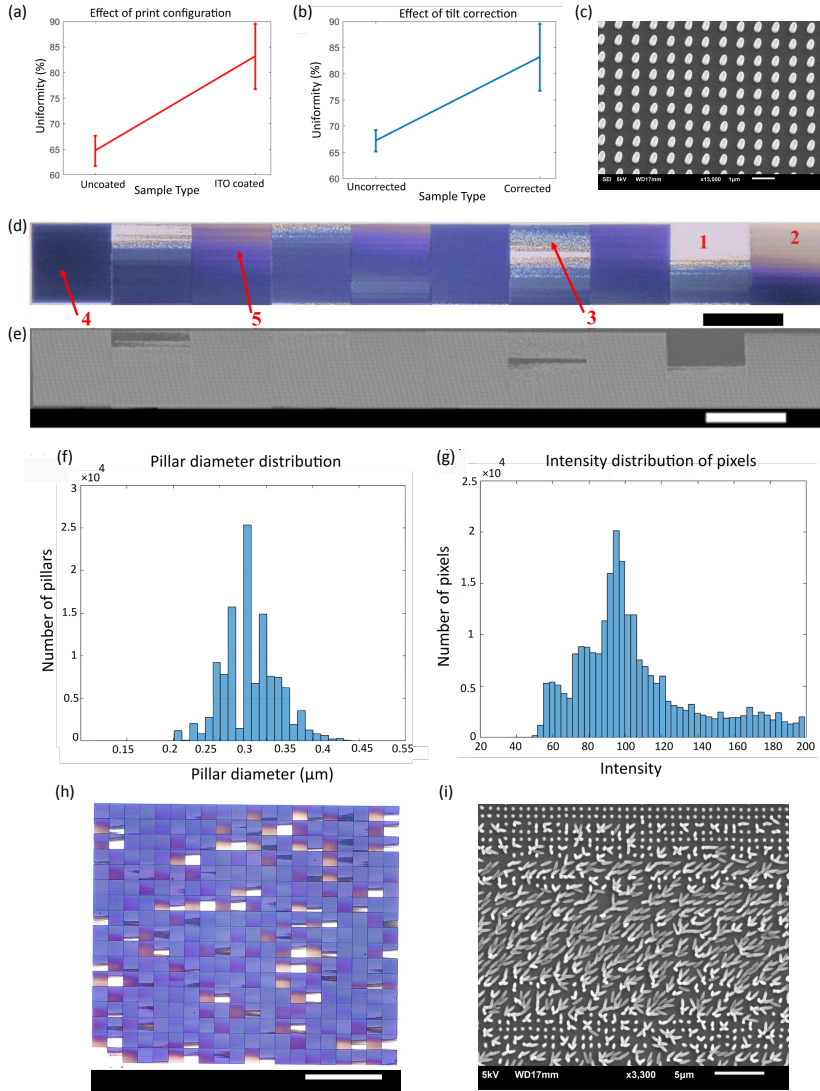


Figure 2.2: (a), (b) The effects of the print configuration and tilt compensation on the uniformity of the fabricated nanopatterns ($n = 4$). Both cases (a) and (b) were compensated for tilts. (c) Morphological characterization of uniform nanopillars (the scale bar is 1 μm while the tilt angle is 20°). (d) Optical image of the area depicting the different kinds of the regions covered by surface nanopatterns (the scale bar is 100 μm). (e) Stitching low-resolution SEM images to create an area of 1 mm \times 100 μm (the scale bar is 100 μm). (f) The frequency distribution of the diameters of the nanopillars determined using SEM image (Figure 2.2e). (g) The frequency distribution of the pixel intensities obtained from the optical image (Figure 2.2d). (h) The nanopatterned surface was extended to a 2 mm \times 1.7 mm area (the scale bar is 500 μm). (i) Morphological characterization of the nanopillars from the damaged area (region 3 in Figure 2.2d). The scale bar is 5 μm .

2.3.1.3. Effects of 2PP writing parameters

Achieving nanopatterns of specific dimensions involves optimizing a number of parameters such as the laser power, time of exposure, interface distance, and other Piezo writing-based parameters. Nanopillars as small as 160 nm in diameter and 300 nm in height could be fabricated using the Piezo writing strategy (Supplementary Figure 2.4). The height and diameter of the nanopillars change together with the laser parameters. It is therefore challenging to fix one of these dimensions, while varying the other. The higher values of the laser power and exposure time caused the diameters of the nanopillars to increase (Supplementary Figure 2.4), while the height and diameters of the nanopillars decreased with the interface distance (Supplementary Figure 2.5). The adhesion of the nanopillars to the substrate was also affected by the chosen value of the interface distance (Supplementary Figure 2.6). Increasing the interface distance, however, caused the printing process to start deeper into the substrate and reduced the uniformity and reproducibility of the nanopillars (Supplementary Figure 2.6). Moreover, the uniformity of the nanopillars improved with the laser power and exposure time (Supplementary Figure 2.7). After optimization of all these 2PP parameters, a laser power of 27.2 mW, an exposure time of 2400 s, and an interface distance of 0.3 μm were selected to achieve reproducible and uniform nanopatterns (Figure 2.2c). The ellipsoidal shape of the nanopillars (Figure 2.2c) were similar to that of the focal point of a focused laser beam. The focal point shape originates from the nature of the diffraction system and cannot be improved by lens design or through adjustment of the optical system [81].

2.3.2. Characterization of nanopatterns

2.3.2.1. Measuring uniformity over large area

An area of 1 mm \times 0.1 mm was nanopatterned using the above-mentioned optimal laser parameters (Figure 2.2d, e). The uniformity of this printed topography can be quantified through the pixel threshold intensity values. The pixel threshold intensity can be detected by correlating the histogram describing the distribution of the nanopillar diameters (Figure 2.2f) with the data regarding the distribution of the pixel intensity (Figure 2.2g). Here, the uniformity of the nanopatterns is defined as the percentage of the area in which the diameter of the nanopillars is larger than the cut-off value (*i.e.*, nanopillar diameter \geq (mean diameter - 50 nm)). An upper limit of about 500 nm was also applied on the diameter to avoid counting delaminated nanopillars stuck to the substrate in this analysis. Through this method, about 73% of the area (Figure 2.2d) has nanopillar diameters higher than 284 nm (uniformity is calculated using the data presented in Table 2.2).

These nanopatterns upscaled to an area of 2 mm \times 1.7 mm (Figure 2.2h) with a printing time of about 87 h and 50 min. This process is therefore not an ideal option for mass production of nanopatterned areas, but rather for the rapid nanopatterning of large areas. The uniformity of this area was measured to be about 86% ($n = 10$). Several types of regions can be seen after printing in larger areas (Figure 2.2d). Region 4 showed a uniform distribution of nanopillars, while

Table 2.2: The specifications of the nanopillars (obtained from image analysis).

Expected number of nanopillars	156250
Actual number of nanopillars	118966
Interspace (center to center)	800 nm
Mean diameter (d) \pm SD	334 ± 30 nm
Mean height (h) \pm SD	1541 ± 60 nm

the color intensity decreased in region 5, indicating a decrease in the nanopillar diameter. A further drop in the nanopillar diameter created areas similar to the region 2. There were also areas where there are no nanopillars (region 1) or areas where nanopillars were delaminated (Figure 2.2i and region 3 in Figure 2.2d) during the development process in PGMEA and IPA due to the weak adhesion to the substrate. This usually happens when the laser beam focuses far above the substrate surface or when the edge of the voxel that is going to be printed is too close to the surface of the substrate [81]. Although printing over large areas could not give us 100% uniform nanopatterns in this study, the uniformity significantly enhanced after optimization of 2PP parameters in the Piezo writing strategy, testing various print configurations, and applying a manual tilt correction.

2.3.2.2. Wettability

The water contact angle decreased from $81.84 \pm 3.15^\circ$ ($n = 9$) on the plain substrate to $41.7 \pm 3.9^\circ$ ($n = 9$) on the nanopatterned surface (Figure 2.3a). Previous studies [82–84] reported a water contact angle of $60^\circ - 80^\circ$ for the ITO glass. This variation indicates that the angle depends on the pre-cleaning procedure and may change due to the different solvent cleaning processes and plasma treatments [85]. An un-treated commercially available ITO glass has been found to exhibit a water contact angle of about 90° [85]. In this study, exposure to chemicals such as acetone, IPA, and PGMEA had been considered due to the involved sample development process. The Wenzel’s model [86] Equation 2.1, describing a homogeneous wetting regime, was used to estimate the contact angle of uniform nanopatterns wetted by droplets.

$$\cos \theta_w = R \cos \theta_y \quad (2.1)$$

Here, the apparent contact angle of the droplet on a nanopatterned and a smooth non-patterned surface is given by θ_w and θ_y , respectively [86]. On a rough surface, the roughness factor is determined by R which describes the ratio of the actual surface area to the apparent surface area of a rough surface. In this study, by assuming cylindrical nanopillars of height h , diameter d , and pitch p , the roughness factor can be calculated using Equation 2.2 as:

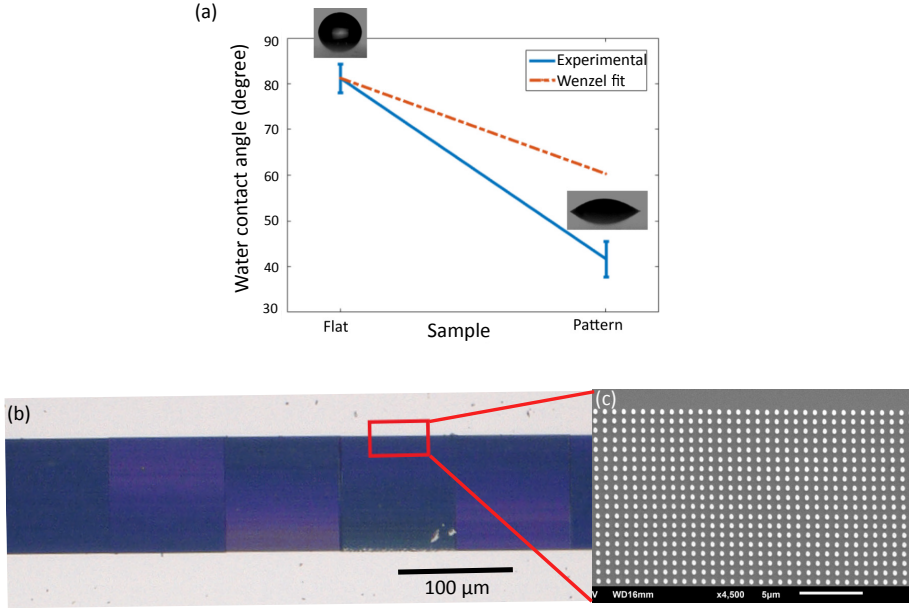


Figure 2.3: (a) Water contact angle measurement diagram. (b), (c) The optical and SEM images of the nanopillars after performing the microfluidic delamination tests at a flow rate of 8 mL/min. No signs of delamination were observed. The scale bar is 100 μm in (b) and 5 μm in (c). The tilt angle is 20° in (c).

$$R = 1 + \pi dh/p^2 \quad (2.2)$$

By substitution of the dimensions Table 2.2 in this equation, the roughness factor is calculated to be $R \approx 3.49$. Replacement of this value into Equation 2.1 yields $\theta_w = 60.3^\circ$, which is higher than the experimental value of the contact angle (47.1°). The deviation seen in the experimental value of the contact angle from the one predicted by the Wenzel's model could be attributed to the small non-homogeneity in nanopatterns (due to process limitation, there are few regions with imperfect nanopillars) and assuming nanopillars as cylindrical rather than using their actual truncated ellipsoid shape. This model, however, does correctly predict the increase in the hydrophilicity in such a case.

2.3.2.3. Adhesion force of the nanopillars

The shear stress on the microchannels walls of 7.85 mm length (l), 1 mm width (w), 200 μm height ($2h$), and a flow rate Q (liquid: water with a dynamic viscosity = 8.9×10^{-4} Pa.s) was measured through Equation 2.3 [87, 88] Table 2.3.

$$\tau = 3\mu Q/2wh^2 \quad (2.3)$$

Leakage was occasionally observed for a flow rate of 5 mL/min. Above this flow rate, keeping the chip leak tight was impossible (especially at the inlet and outlet connection points). The nanopillars, on the other hand, remained unaffected by flow rates of up to 8 mL/min. Figure 2.3b and c show pictures of pillars that had been exposed to such flow rates. It can therefore be concluded that the wall shear stress should be more than a few tens of Pascal to delaminate the nanopillars.

Table 2.3: The microfluidic testing conditions used to test the resistance of the nanopillars against delamination.

Flow rate (mL/min)	Shear stress (Pa)	Comments
1	2.2	Nanopillars unaffected, no leakage
3	6.7	Nanopillars unaffected, no leakage
5	11.2	Nanopillars unaffected, occasional leakage
8	17.9	Nanopillars unaffected, leakage via inlet/outlet

Equation 2.4 indicates the shear force applied to the nanopillars during the microfluidic flow studies.

$$F_s = \tau \pi r^2 \quad (2.4)$$

Here, the shear stress τ applied to the nanopillars has been estimated as the wall shear stress (Equation 2.3). Consequently, the drag force can be estimated to be in the order of 10^{-18} N and could therefore be neglected. Nanopillars were also experiencing a traction force by hMSCs cultured on them, which could lead to bending and delaminating the pillars (Figure 2.5e). The bending force on the nanopillars can be estimated using the following equation:

$$\delta = 4Fl^3/3\pi Er^4 \quad (2.5)$$

where δ is the linear horizontal displacement of the nanopillar tips, F is the horizontal bending force, l is the length of the nanopillar, r is the radius of the nanopillar, and E is the Young's modulus of the polymeric material. δ can be estimated to be in the range of a few hundred nanometers from the SEM images (Figure 2.5e), E to be in the range of a few GPa [89], $r \approx 167$ nm, and $l \approx 1.54$ μ m. These estimations resulted in calculated forces in the order of hundreds of

nN to a few μN . This estimated range of forces is in agreement with the values reported by Fu et al. [90].

The forces applied by the cells to the nanopillars are much higher than the drag forces. One could therefore conclude that the cell traction forces delaminated the nanopillars during the dynamic cell culture experiments.

2.3.3. Fabrication of multiscale structures

The possibility of printing 3D micro-architectures such as porous scaffolds with controlled porosities and nanotopographies using the 2PP process enables new approaches to the design of biomaterials. Although, it is not easy to print uniform nanopatterns onto large-scale 3D printed structures such as scaffolds and flat sheets, we succeeded in writing nanopillars with variable heights over a micro-scaffold (Figure 2.4). The potential of shifting between the Galvo and Piezo writing strategies in a single process allowed for this novelty. The Galvo writing strategy was used to fabricate the 3D woodpile structure, while the Piezo writing strategy (by applying the optimized parameters) was used to incorporate the nanopatterns on the woodpile layers. It is also worth mentioning that increasing the distance from the woodpiles surface leads to a gradient in the height and diameter of the nanopillars created on the surface of various woodpiles (Figure 2.4b and c). This approach could be used to create 3D cellular microenvironments that resemble more closely the native extracellular matrix or can provide novel surface physical cues to control cellular functions.

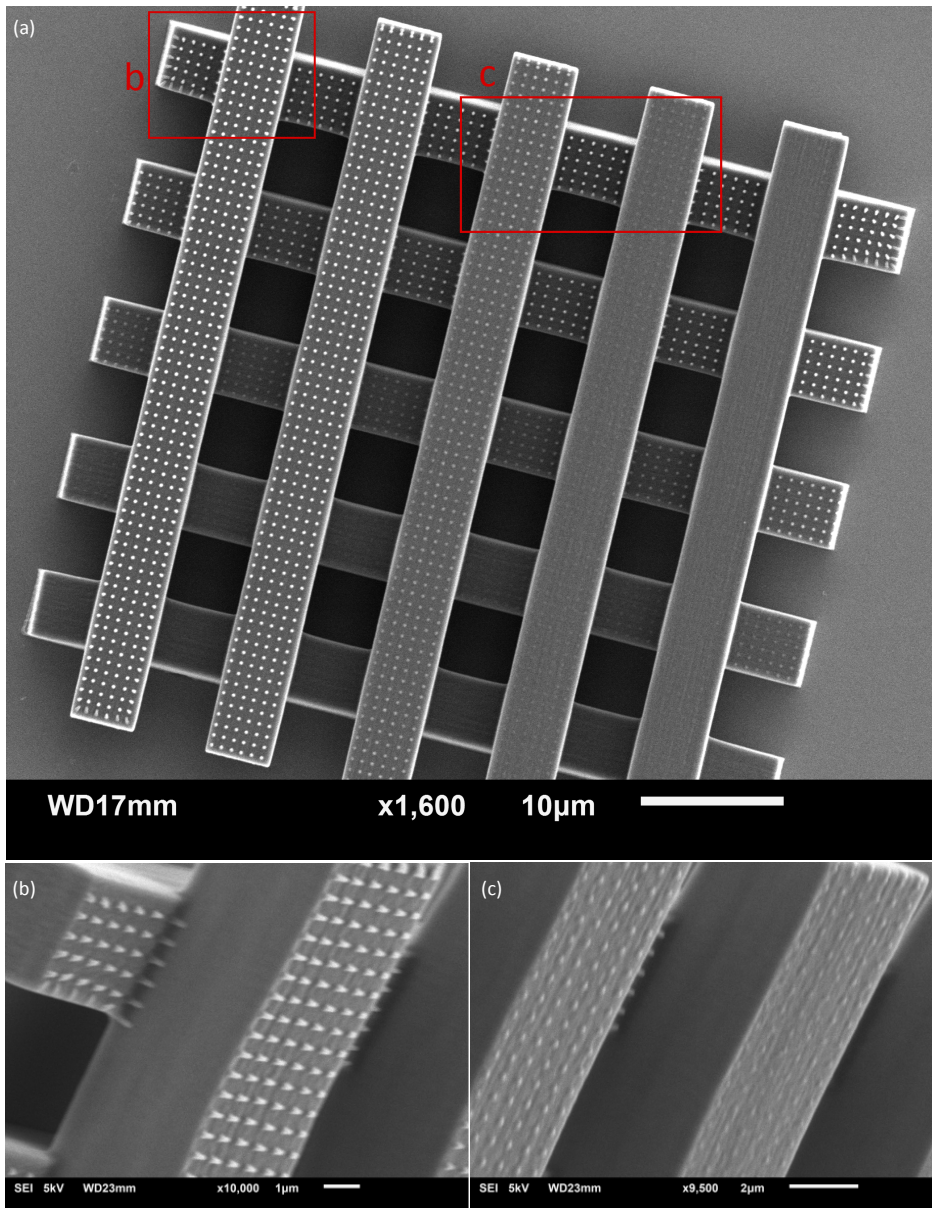


Figure 2.4: (a) SEM image of nanopatterns incorporated into a woodpile-based micro-scaffold. (b), (c) The nanopillars with different heights.

2.3.4. Cytocompatibility

The live/dead fluorescence microscopy images taken after 3 days of dynamic culture on the polymeric flat surface (Figure 2.5a) and nanopatterned surfaces (Figure 2.5b and c) indicated no visible signs of hMSCs death. In addition, cells could colonize and spread on the patterned area quite uniformly (Figure 2.5c). These preliminary findings suggest that the IP-Dip resin is not cytotoxic for these cells. Other studies have coated surfaces made from similar resin with biocompatible layers (*e.g.*, TiO₂, collagen, and fibronectin) [91–93] before cell culture while this resin can be used without any biocompatible coating.

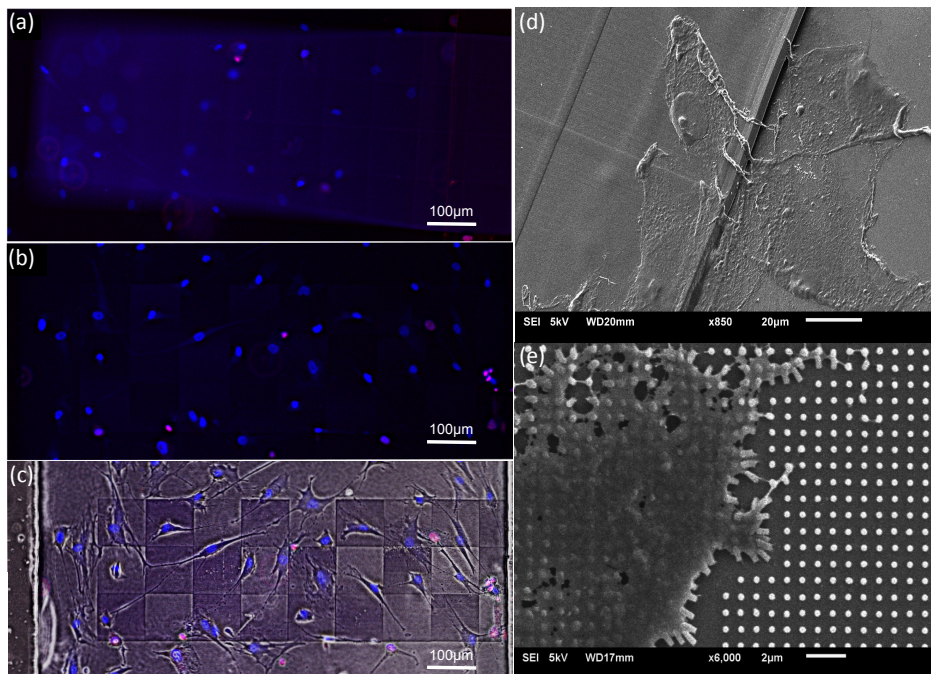


Figure 2.5: Live/dead staining of the hMSCs after 3 days of culture on (a) the control surface (*i.e.*, a printed flat surface with the same material used for the submicron pillars) and (b) submicron patterned surfaces. (c) Bright-field microscopy images of the cells shown in (b). (d, e) Cell-surface interface by SEM: (d) cells residing on the flat surface and (e) cells on submicron patterned area.

A closer look at the surface-cell interface by SEM showed a well spread morphology of the hMSCs on the flat polymeric surface (Figure 2.5d) and visible extensions interacting with the cells from the surrounding glass substrate. The cells on the nanopatterns (Figure 2.5e) exerted contractile forces on the nanopillars, which caused them to bend and delaminate. As calculated before, the estimated cell traction force is in the order of hundreds of nN to a few μN . It is therefore necessary to improve the nanopillar adhesion for cell studies. This could be achieved by increasing the diameter of the nanopillars, reducing their height, exploring other resins, and increasing the interface distance (which starts the printing process deeper into the substrate).

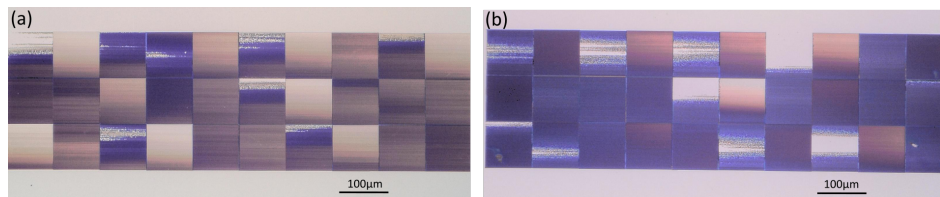
2.4. Conclusions

We developed a method to create microfluidic chips decorated with surface nanopatterns as well as to fabricate 3D porous scaffolds with a large area of nanopatterned surface areas. Both microfluidic chips and 3D porous scaffolds could be used in bone regeneration studies. The direct laser writing (*i.e.*, 2PP) process has the potential of creating bone scaffolds with optimal feature sizes and a bespoke topological design. Varying the processing parameters of 2PP resulted in direct changes in the feature sizes at the nanoscale. Furthermore, the created nanotopographies enhanced the surface hydrophilicity and, could withstand flow rates of up to a few mL/min. In addition, the results of hMSCs culture indicated no evident cytotoxicity of the material (IP-Dip resin). Although we succeeded in creating a large area of nanopatterns in a single step, the long printing time remains a major limitation in this approach.

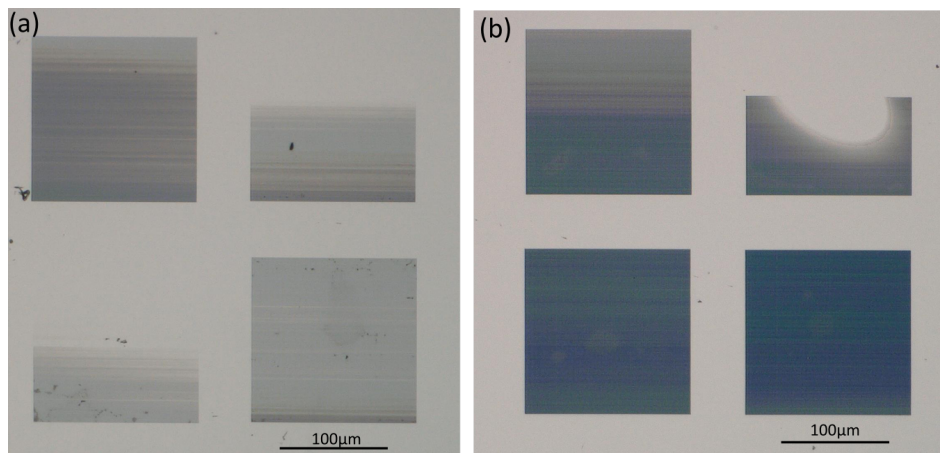
2.5. Supplementary information

2.5.1. Effects of substrate type and print configurations on the nanopatterns uniformity

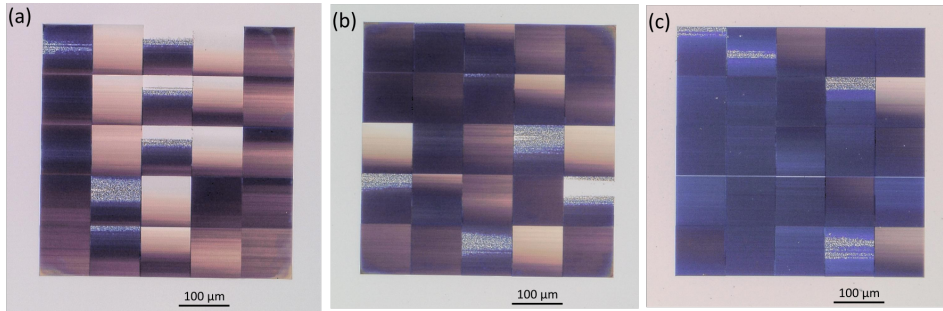
Different types of substrate (Supplementary Figure 2.1) and print configurations (Supplementary Figure 2.2) were assessed to fabricate uniform nanopatterns. It was found that ITO coated fused silica in combination with DiLL configuration resulted in printing more homogenous nanopatterns. These parameters were evaluated in Piezo writing strategy (Supplementary Figure 2.1, 2.2) .



Supplementary Figure 2.1: Increase in nanopatterns uniformity by using ITO coated fused silica (by about 15%) in comparison to a normal fused silica substrate. (a) Nanopatterns uniformity on the fused silica glass. (b) Nanopatterns uniformity on the ITO coated fused silica glass. The change in the substrate type increases the interface signal amplitude from 600-700 to 1500-1600. Tilt correction was conducted for both cases. The experiments were performed in Piezo writing strategy using DiLL configuration, a laser power of 27.2 mW, an exposure time of 2400 μ s, and an interface distance of 0.3 μ m.



Supplementary Figure 2.2: Increase in nanopatterns uniformity upon the transition from the conventional (IP-L 780, borosilicate glass) to DiLL configuration (IP-Dip, fused silica) in Piezo writing strategy. (a) Printing in the conventional configuration on borosilicate glass using IP-L 780. (b) Printing in the DiLL configuration on fused silica glass using IP-Dip. The change in configuration type increases the interface signal amplitude from approximately 300-350 to 600-700. Both samples were corrected against tilt. A laser power of 32 mW and an exposure time of 2000 μ s applied in both cases.



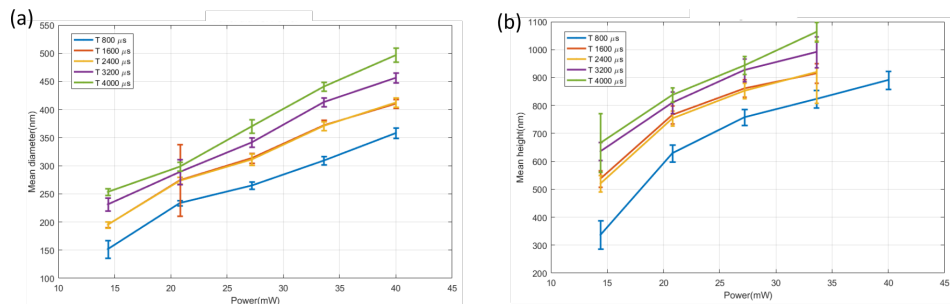
Supplementary Figure 2.3: Increase in nanopatterns uniformity on correcting the sample tilt. (a) Nanoattners uniformity without tilt correction. (b) Nanoattners uniformity using the auto tilt correction. (c) Nanoattners uniformity using manual tilt correction. This was done for IP-Dip and ITO glass combination by applying a laser power of 27.2 mW and time of exposure of 2400 μ s.

2.5.2. Effect of tilt correction on the nanopatterns uniformity

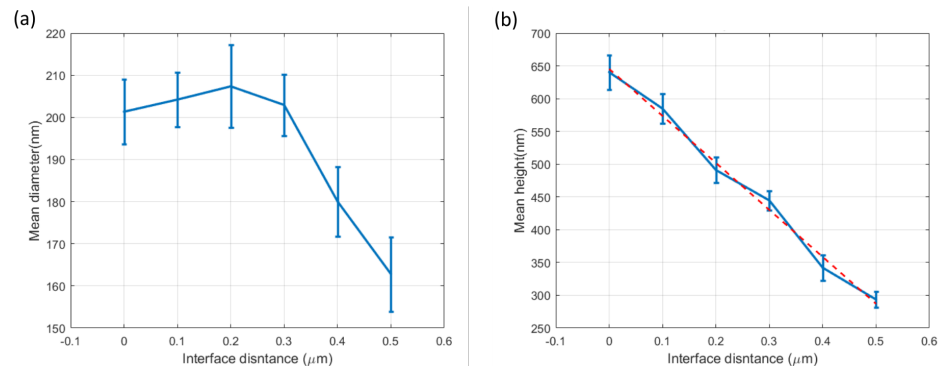
In Piezo writing strategy, the machine displays the substrate tilt in x and y directions and manipulates the z coordinate of the Piezo element to compensate for these tilts. However, it was found that the tilt values measured by the machine were not repeatable (even for the same sample) and hence produced unsatisfactory results. This lead to conduct a manual tilt correction through measuring the z position of the Piezo at different points to obtain the tilt angle of the substrate along x and y directions (Supplementary Figure 2.3).

2.5.3. Effect of 2PP parameters on the dimensions and uniformity of nanopatterns

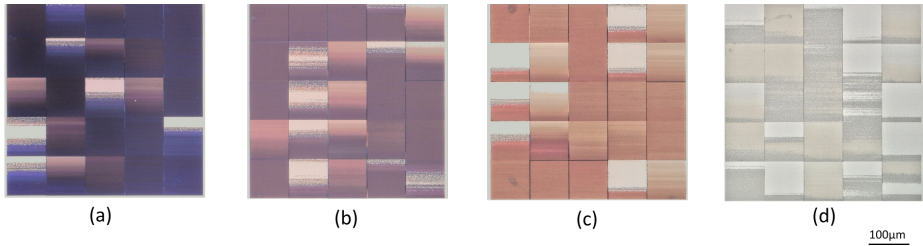
Effects of laser power, exposure time, and interface distances on the nanopatterns dimensions (height and diameter) and uniformity were evaluated in Piezo writing strategy. The pillars height as well as diameter increase with the laser powers and exposure time, while the dependence of nanopillars height and diameter on the interface distance shows a decreasing trend (Supplementary Figure 2.4, 2.5). It can be seen that the nanopatterns uniformity decreases with large unwritten areas appearing on increasing the interface distance (Supplementary Figure 2.6). It is interesting to note that the percentage of printed area also decreases as the laser power is decreased which indicates the dominating effects of laser fluctuations at lower laser powers (Supplementary Figure 2.7).



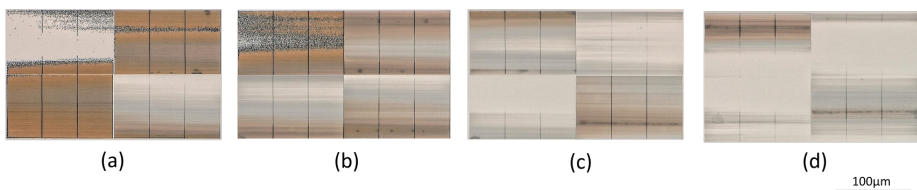
Supplementary Figure 2.4: Parametric study of nanopillars dimensions with laser parameters (a) Increasing nanopillar diameter with laser power (mW) for different times of exposure, T (μs) (b) Increasing nanopillar height with laser power (mW) for different times of exposure, T (μs). The measurements were done in the DiLL configuration using ITO coated glass substrate and at a constant interface distance of $0.1 \mu\text{m}$. The error bar denotes two standard deviation in both cases.



Supplementary Figure 2.5: Effects of interface distance on (a) nanopillars diameter (b) nanopillars height. The dependence of nanopillars diameter on the interface distance is not monotonically decreasing. However, the dependence of height shows a decreasing linear trend. The laser power and exposure time were fixed at 14.4 mW and $1600 \mu\text{s}$ respectively. The error bar denotes two standard deviation in both cases.



Supplementary Figure 2.6: Decrease in nanopatterns uniformity with increasing interface distance: (a) $0.1 \mu\text{m}$ (b) $0.3 \mu\text{m}$ (c) $0.6 \mu\text{m}$, and (d) $0.8 \mu\text{m}$. The pattern uniformity reduces by increasing interface distance (towards right). While on making interface distance smaller (right to left), areas containing eroded pillars can be seen thus indicating an insufficient attachment. The experiments were performed using the DiLL configuration with ITO coated glass substrate, a laser power of 14.4 mW , and a time exposure of $2400 \mu\text{s}$.



Supplementary Figure 2.7: Change in nanopatterns optical image with laser power: (a) 27.2 mW , (b) 24 mW , (c) 20.8 mW , and (d) 14.4 mW . The change in nanopatterns color represents the variation in nanopillar dimensions. The nanopatterns uniformity reduces for smaller nanopillar dimensions (towards the right). The experiments were performed using DiLL configuration with ITO coated glass substrate, an exposure time of $2400 \mu\text{s}$, and an interface of $0.3 \mu\text{m}$

3

3D Printing of Large Areas of Highly Ordered Submicron Patterns for Modulating Cell Behavior

Fabricating large areas of geometrically complex and precisely controlled topographies is required for the studies of cell behavior on patterned surfaces. Direct laser writing (DLW) is an advanced 3D-fabrication technique, which facilitates the manufacturing of structures within various scales (from a few hundred nanometers to millimeters). However, this method requires improvements in the accuracy and reproducibility of the submicron and nanoscale features that are printed over a large area. Here, we present a scheme to both improve the uniformity of the printed submicron patterns and decrease the printing time. The effects of various processing parameters (*e.g.*, laser power and writing field) on the dimensions and uniformity of submicron pillars as well as on their Young's modulus and surface wettability were assessed. Decreasing the writing field to $33 \times 33 \mu\text{m}^2$ significantly improved the uniformity of submicron pillars that were printed over an area of 4 mm^2 in a single-step process. Preosteoblast cells (MC3T3-E1) were used to assess the cytocompatibility of the used material (IP-L780 resin) with a focus on cell morphology, cell proliferation, cytoskeletal organization, and the elastic modulus of the cells. The cells cultured for 2 days on the submicron pillars showed a polarized shape and a higher Young's modulus of the area corresponding to the nucleus relative to those cultured on flat surfaces. Taken together, the results of the current study clearly show that the submicron patterns created using DLW are both cytocompatible and could modulate the morphology and mechanical properties of cells. This work paves the way for direct printing of submicron features with controlled Young's moduli over large areas in a single-step process, which is necessary for systematically studying how such patterns modulate cellular functions.

Published as: Nouri-Goushki, Mahdiyeh, *et al.*, "3D Printing of Large Areas of Highly Ordered Submicron Patterns for Modulating Cell Behavior" ACS Applied Materials & Interfaces 2020, 12, 1, 200–208, <https://doi.org/10.1021/acsami.9b17425>.

3.1. Introduction

Controlling cellular processes such as cell migration, proliferation, and differentiation is required for guiding and modulating tissue formation and regeneration [94–97]. In naturally occurring systems, the micro- and nanotopography of the extracellular matrix (ECM) plays an important role in this regard [98–100]. Mimicking the small-scale topography of the ECM and assessing the resulting cell-surface interactions are, therefore, necessary when developing novel biomaterials [101–105]. Indeed, recent studies have shown that nanoscale topographical features incorporated onto biomaterial surfaces could be used to guide the differentiation of stem cells towards the osteogenic lineage [31, 106, 107] and kill bacteria that may otherwise cause biomaterial-associated infections [65, 108]. Achieving the desired effects is, however, often contingent on decorating the entire surface of (usually porous) biomaterials with precisely defined and geometrically complex nanopatterns [98].

Fabricating porous biomaterials whose surface is covered by such types of nanopatterns remains a major unsolved challenge due to the inherent incompatibilities existing between the technologies required for the free-form fabrication of a complex porous structure and those required for free-form surface nanopatterning [109]. In fact, there is 5-6 orders of magnitude of difference between the length scale of the required nanopatterns (10-500 nm [31]) and that of the micro-architecture of the scaffold (10 – 900 μm [41]) used for bone implants. On the one hand, no single free-form fabrication technique could create precisely controlled structures over such a wide range of length scales. On the other hand, combining multiple techniques is not feasible given the huge internal surface of porous biomaterials that cannot be reached once they have been fabricated. To put this technical challenge in perspective, it is worth reviewing the length scales that can be achieved by different types of 3D printing techniques. On the side of large length scales, the techniques based on material extrusion (*e.g.*, fused deposition modeling [110]), powder bed fusion processes [111] (*e.g.*, selective laser sintering [112, 113] and electron beam melting [114]), and material jetting (*e.g.*, inkjet technology [115–117]) could achieve length scales between 250 μm and 1 mm. Stereolithography can reach somewhat higher resolutions (*i.e.*, down to 10 μm) while being capable of manufacturing large structures [118]. On the side of smaller length scales, electron beam induced deposition [119] could be used for free-form fabrication of structures with feature sizes between 10 nm and a few micrometers [120].

A notable exception to the above-mentioned rule is direct laser writing (DLW) working on the basis of two-photon polymerization (2PP) [121]. Although not capable of covering the entire range of the desired length scales, it covers a significant part of that range with features sizes as small as 200 nm and as large as 100 μm [122, 123]. Fine-tuning this technique to its limits has even allowed for achieving sub-20 nm feature sizes [124]. 2PP is therefore ideally positioned to address the challenge of free-form fabrication of nanopatterned porous biomaterials.

Incapability of tuning the defined geometries, particularly at high spatial resolutions and over specially large areas, has restricted the investigations of the

effects of nanostructures on the cellular behavior [107]. Even though DLW is a promising technology to fulfill these requirements, controlling this process over such a large range of length scales, to combine high enough speeds with high enough accuracy and repeatability, is technically extremely challenging. In fact, even submicron and nanoscale patterning of large surface areas has not been sufficiently addressed before. In a previous study [125], we demonstrated that the application of the piezo-mode DLW for the submicron patterning of large surface areas is associated with both a long printing time and high levels of inaccuracy (*i.e.*, non-uniformity) of the resulting pillars. Here, we followed an alternative DLW configuration (the so-called galvo-mode) for upscaling the area of patterned surfaces while decreasing the printing time and enhancing the uniformity of the fabricated features. Furthermore, we studied how different processing parameters influence the geometrical and mechanical properties of the resulting patterns. Finally, we created large patterned surface areas and studied the effects of patterns on the morphology, proliferation and mechanical properties of preosteoblast cells.

3.2. Materials and methods

3.2.1. Fabrication of the patterns

The geometry of individual pillars (diameter = 200 nm, height = 700 nm) was imported as a standard tessellation language (STL) file into a job preparation software (Describe, Nanoscribe, Germany). Describe then produced a general writing language (GWL) file from that STL file. The GWL code was modified to upscale the submicron pillars (pitch = 700 nm) so that they covered a large area of 4 mm². The file was then imported into the Photonic Professional GT machine (Nanoscribe, Germany) for 2PP exposure. The machine was equipped with a femtosecond (fs) laser source that emitted 100 fs pulses at 80 MHz with a wavelength of 780 nm (Figure 3.1a).

The galvo writing mode and conventional configuration were used for patterning similar surface areas (Figure 3.1aI). A droplet of photoresist (IP-L780, Nanoscribe, Germany) was placed atop a borosilicate coverslip (Nanoscribe, Germany). The laser beam was then focused within the resin using a 63x microscope objective (numerical aperture [NA] = 1.4). After exposing, the development process was performed in propylene glycol monomethyl ether acetate (PGMEA, Sigma-Aldrich, Germany) for 25 min followed by 5 min rinsing in isopropyl alcohol (IPA) (Sigma-Aldrich, Germany) and subsequent blow-drying with air.

The submicron pillars were written using a scanning speed of 1200 $\mu\text{m/s}$. The effects of different laser powers (Lp: 12-21% of the mean power value at the objective aperture) on the dimensions and Young's moduli of the submicron pillars were assessed accordingly. The water contact angle measurements, the measurement of the detachment force of the pillars, and the cells experiments were then performed on the pillars created using a Lp of 21%.

3.2.2. Microscopic characterization of the patterns

The features resulting from the writing processes were characterized using a scanning electron microscope (SEM, Nova Nano Lab 650 dual beam system, FEI company, USA) before and after culturin (≈ 5 nm) before imaging. Two-dimensional maps of the patterned areas were also acquired by an optical microscope (Keyence Digital Microscope VHX-6000, USA) to check the uniformity of the patterns. The dimensions of 100 different pillars were quantified from SEM images using ImageJ (<http://rsb.info.nih.gov/ij/index.html>).

3.2.3. Contact angle measurement

A drop shape analyzer (KRUSS DSA100, Germany) was used to measure the wettability of the patterned surfaces. Deionized water droplets (volume = $2 \mu\text{L}$) were placed on the non-patterned (borosilicate coverslips) and patterned surfaces. The contact angle was measured after 5 s (three measurements per specimen). The specimens were cleaned with IPA and dried with nitrogen gas prior to the measurements.

3.2.4. Mechanical characterization

3.2.4.1. Young's modulus

The mechanical experiments reported here were performed using an atomic force microscope (AFM) (JPK Nanowizard 4, Berlin, Germany) while the corresponding data post-processing was carried out with the JPK SPM data processing software (JPK instruments, v6.1, Berlin, Germany).

The Young's moduli of a number of large deposits of the IP-L780 resin (*i.e.*, pillars with a diameter of $1 \mu\text{m}$ and height of 500 nm) written at different laser powers were measured using the quantitative imaging (QI) mode, and an NM-TC probe (Bruker, Billerica, USA) with a nominal spring constant of 350 N/m. The deflection sensitivity of the cantilever was calibrated on a sapphire surface using the contact method and resulted in a value of 21.33 nm/V. The spring constant of the probe was assumed equal to the nominal value and the relative method of calibration was applied to estimate the corresponding tip radius. A polystyrene sample with a nominal Young's modulus of 3 GPa was used as the reference material. The tip radius was then adjusted to make the measured Young's modulus of the reference sample equal to the nominal value at an indentation depth of 10 nm. A Poisson's ratio of 0.4 was assumed. A tip radius of 10 nm was found to result in a Young's modulus of 3.1 GPa for the polystyrene. Then, a constant set point force of 500 nN was applied to each sample in order to obtain an indentation depth of 10 nm. The Hertz's contact mechanics model was used to calculate, from the force-distance curves recorded in each point of the scanned area, the Young's modulus corresponding to each scanned point. The Young's modulus of 3 pillars for each 2PP printing condition was calculated, from the Young's modulus map, as the average values in a selected area corresponding to the top of the pillar.

3.2.4.2. Detachment force of pillars

The measurement of the detachment force of the pillars was performed using the same instrument and a NCHV probe (Bruker) with a nominal spring constant of 40 N/m, a nominal cantilever length of 115 μm , a thickness of 3.5 μm , and a tip height of 10 μm . The thermal noise calibration technique was used to measure the spring constant and the sensitivity of the probe, which were found to be respectively 38.26 N/m and 19.51 nm/V.

Areas of 20 $\mu\text{m} \times 20 \mu\text{m}$ (containing 13 pillars) were scanned successively in QI mode, with a pixel time of 18 ms, a Z length of 500 nm, and increasing values of the lateral force (from 2 μN to 5.5 μN) obtained by setting increasing values of the set point deflection (from 52 nm to 130 nm). The number of detached pillars corresponding to each level of applied force and the eventual changes in the morphology of the scanned pillars due to the applied force were evaluated by acquiring, after the application of each force value, a QI image with a low set point deflection (*i.e.*, 1.5 nm).

The scanning direction was chosen such that the contact between the probe and the pillars occurred on one of the lateral faces on the front of the pyramidal AFM tip. The force (F_N) applied to the pillar is therefore directed along the normal to that surface. The magnitude of the lateral component of the force applied to the pillar was calculated as:

$$F_{lat} = \sqrt{F_{N,x}^2 + F_{N,y}^2} \quad (3.1)$$

where:

$$F_{N,x} = F_N \cos\beta \cos\gamma, \quad F_{N,y} = F_N \sin\beta \cos\gamma \cos\phi - F_N \sin\gamma \sin\phi \quad (3.2)$$

are the components of F_N along the two orthogonal directions (x and y) normal to the axis of the pillar (z). From the beam theory and after applying the geometry considerations, F_N , can be calculated as:

$$F_N = \frac{k^* d_z}{\sin\gamma - \frac{3(h_{tip} + \frac{t}{2})}{L} \sin\beta \cos\gamma} \quad (3.3)$$

where, d_z is the set point deflection of the cantilever, k^* is the equivalent spring constant of the system cantilever + pillar, β is the half front angle of the tip (measured by SEM imaging of the probe), and γ is the angle of inclination of the tip wall with respect of its axis and is calculated as $\gamma = \arctan \frac{l_{tip}}{\sin\beta}$, where l_{tip} is the length of the tip (measured by SEM imaging of the probe). The other parameters include ϕ that is the tilting angle of the cantilever holder with respect to the horizontal direction (10° in JPK systems), h_{tip} that is the height of the tip, and t that is the thickness of the cantilever. The parameter k^* was measured as the slope of the contact region of the force-distance curves when the tip was in contact with the pillar (*e.g.*, at a scan point before pillar failure).

3.2.5. Cell experiments

3.2.5.1. Cell seeding and culture

Preosteoblast cells (MC3T3-E1, Sigma Aldrich, Germany) at passage 11 were seeded on the control (borosilicate coverslips) and patterned surfaces ($n = 4$) at a concentration of 25×10^3 cells/mL. The samples were incubated in the alpha minimal essential medium (α -MEM without ascorbic acid: supplemented with 10% (v/v) fetal bovine serum (FBS), 1% (v/v) penicillin-streptomycin (10.000 units/mL), pH = 7.5, Life Technologies, USA) for 2 or 4 days (37 °C, 5% CO_2). The medium was refreshed after 2 days.

3.2.5.2. Cytoskeleton staining

Actin staining was performed on days 2 and 4. Therefore, the cells were washed two times with phosphate-buffered saline (PBS, Sigma Aldrich, Germany) and then fixated in 4% formaldehyde/PBS (Sigma Aldrich, Germany) at room temperature for 10 min. Then, the samples were rinsed with PBS and the cells were permeabilized with 0.5% Triton/PBS (Sigma Aldrich, Germany) at 4 °C for 15 min. The specimens were then incubated in 1% bovine serum albumin (BSA)/PBS (Sigma Aldrich, Germany) for 5 min at 37 °C followed by the addition of rhodamine conjugated phalloidin (1:1000 in 1% BSA/PBS, Life Technologies, USA) and incubation for 1 h at 37 °C. Subsequently, the samples were washed 3 times for 5 min with 0.5% Tween/PBS (Sigma-Aldrich, Germany) followed by washing with PBS for 5 min. Next, 70 μ L Prolong gold (containing 4',6-diamidino-2-phenylindole (DAPI), Life Technologies, USA) were added to the cells and the samples were mounted on glass slides and observed using a fluorescence microscope (ZOE fluorescent cell imager, Bio-Rad, USA).

Consequently, the stained specimens were rinsed 2 times with distilled water for 5 min. The cells were then dehydrated in a series of graded ethanol/PBS solutions (Sigma-Aldrich, Germany) as follows: 15 min in 50%, 20 min in 70%, and 20 min in 96%. The specimens were allowed to dry overnight and were gold sputtered for SEM imaging.

3.2.5.3. Image analysis

The images of the stained cells on days 2 and 4 were processed using ImageJ. First, the image overlay of the fluorescently stained F-actin and nucleus was split into channels to separate the nucleus from the F-actin network. The grayscale nucleus and F-actin images were thresholded to produce binary nucleus and F-actin images, respectively. The cell density was determined through counting the nuclei observed in four different 1 mm² areas of each specimen. The area of the cells was quantified through measuring the actin area of 150 single cells on four different 1 mm² area of the specimens. By fitting an ellipse to the actin area of each cell, which can be performed through particle analysing in ImageJ, the degree of anisotropy (DA) was calculated using the following equation:

$$DA = 1 - d_2/d_1 \quad (3.4)$$

where d_2 and d_1 are the minor and major diameters of the fitted ellipse (ImageJ, BoneJ2, <https://github.com/bonej-org/BoneJ2/tree/bonej-6.1.1>). $DA = 0$ means the cell is fully isotropic and does not have directionality, while $DA \sim 1$ indicates a strong preferential orientation in the cells.

3.2.5.4. AFM characterization

The morphology and mechanical properties (Young's modulus) of living cells at day 2 were characterized using an AFM (JPK Nanowizard 4, Berlin, Germany). The JPK Petri dish heater was used to maintain cells at 37 °C during the measurements. A MLCT-Bio probe (type B, rectangular) with a nominal spring constant of 0.02 N/m and a tip having the shape of a square-based pyramid (nominal front, side, and back angles of 35°) was used. The probe was calibrated using thermal noise method, resulting in a sensitivity of 23.29 nm/V and a spring constant of 0.017 N/m. A set-point force of 1 nN, a pixel time of 18 ms, and a Z length of 1.5 μm were used for the measurements on each cell. The Young's modulus was calculated by fitting the force-distance curves obtained in each point of the scanned area to the Hertz-Sneddon model considering a square-based pyramid as the indenter. The maximum height of the cells was measured in the region corresponding to the nucleus. The reported values of the Young's modulus are the average of the Young's moduli measured in selected areas corresponding to the cell nucleus.

3.2.6. Computational models

A nonlinear finite element solver (Abaqus 6.14) was used for the numerical simulations of the reaction force of the pillar under bending. The 3D geometries of a pillar and a glass plate were first created in the finite element program. Two different linear elastic material models were assigned to the pillar ($E_{np} = 4.55$ GPa, $\nu_{np} = 0.4$) and the glass plate ($E_g = 63$ GPa, $\nu_g = 0.2$ [126]). The Young's modulus of the pillar (printed with $L_p = 21\%$) was already measured through a nanomechanical system and explained in more details in section 3.2.4. The pillar was assumed to be attached to its glass base. Therefore, a tie constraint was used at their interface. A 20-node quadratic brick element with hybrid mode formulation (C3D20H) was used to create the 3D mesh.

To apply the displacement-controlled boundary conditions, a reference point was defined at the top surface of the pillar, which was kinematically coupled to the corresponding nodes of that surface. Different displacements (up to 235 nm at which point the submicron pillars partially detached from substrate, as it was obtained from the SEM images of the cells) normal to the main axis of the pillar was applied to the reference point. The reference point was free to rotate in three directions. A clamped boundary condition was applied to the base plate to constrain the possible rigid body motions of the submicron pillar and base

plate. The reaction force (along the direction of the applied displacement) at the reference point was calculated. We also performed a mesh sensitivity analysis for different minimum element sizes (*i.e.*, 80, 60, 40, 20 nm). An element size equal to 20 nm led to $< 1\%$ variations in the calculated value of the reaction force and was, therefore, used to obtain all of the results that are reported below.

3.3. Results and discussion

3.3.1. Pattern fabrication

The 2PP technique can accurately manufacture microscale structures (*i.e.*, with feature dimensions above one micron). The main challenge, therefore, is in printing submicron and nanoscale features with high precision over large areas of the surface [124, 125]. One of the important parameters affecting the uniformity of DLW objects at these length scales is the writing field, which was assessed by the optical imaging of the arrays of pillars printed with two different field sizes and analyzing the contrast of the images obtained for each field (Figure 3.1b, c). By decreasing the writing field from $100\ \mu\text{m} \times 100\ \mu\text{m}$ to $33\ \mu\text{m} \times 33\ \mu\text{m}$, the tilt and the astigmatism of the galvo scanning process were less pronounced, which led to more uniform pillars (Figure 3.1c). The variation in the pixel intensity shows the difference in the height of the printed pillars. The coefficient of pixel variation (*i.e.*, $\text{CV} = \text{SD}/\text{mean}$) was 3 times smaller after optimizing the printing process (*i.e.*, decreased from 17.6% to 5.25%, Figure 3.1d, e), meaning that the procedure proposed in this study resulted in multi-fold decrease in the variations observed in the height of the submicron pillars (Figure 3.1c, e). Furthermore, for the larger writing field (*i.e.*, $100\ \mu\text{m} \times 100\ \mu\text{m}$), a decrease in the pixel intensity was observed with the printing time (Figure 3.1f), which shows an increase in the height of the pillars (the lower the intensity, the larger the height of the pillars). In addition, larger variations were observed within each field. On the other hand, for the smaller writing field (*i.e.*, $33\ \mu\text{m} \times 33\ \mu\text{m}$), the pixel intensity inside various fields was more or less constant regardless of the printing time (Figure 3.1g), which suggests that the height of the pillars is uniform. In this study, the submicron patterns were uniformly reproduced over areas up to $4\ \text{mm}^2$. In terms of the printing time, the technique proposed here resulted in three times shorter printing times for the same area as compared to the piezo printing mode reported in our previous study [125]. Obviously, the printing time depends on the dimensions and density of the printed pillars, and the area to be patterned. For example, the printing time was 6-8 h for covering an area of $1\ \text{mm}^2$ with pillars whose diameter and height are presented in Figure 3.2e.

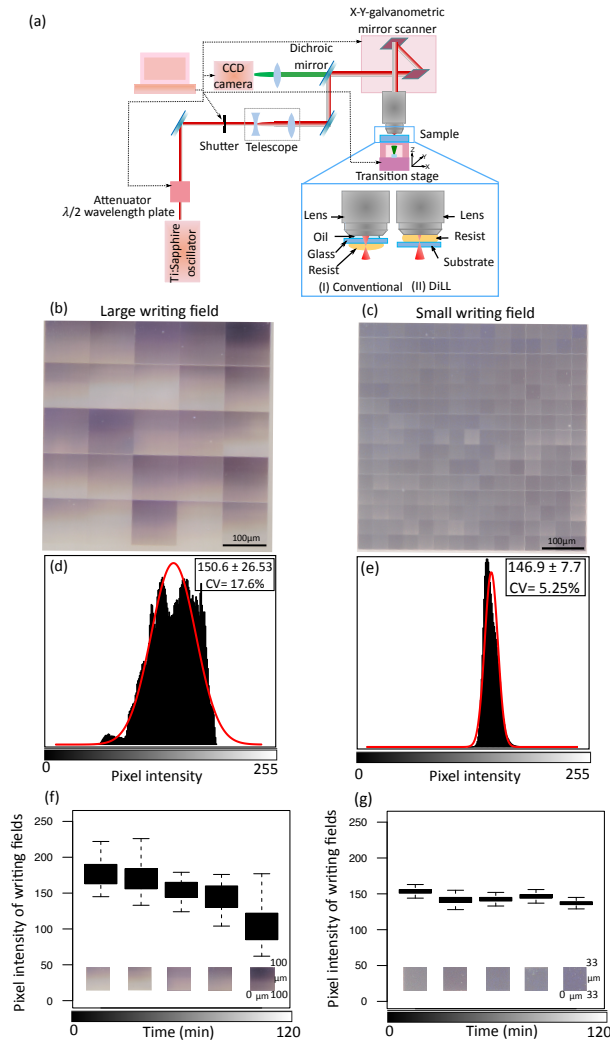


Figure 3.1: A schematic drawing of the applied nanoscale 3D printing technique and the results of the writing field optimization process. (a) A schematic illustration of the 2PP system: the system consists of an exposure source (Ti Sapphire laser, pulse duration: 100 fs, wavelength: 780 nm, and repetition rate: 80 MHz) and a $\lambda/2$ wavelength plate and a cube polarizer for attenuating the laser power. The beam is expanded by a telescope and positioned into the resin either by the galvo scanner or the 3D transition stage. The CCD camera placed behind a dichroic mirror displays the printing process online. Either a conventional (I) or a Dill configuration (II) can be used for the printing process. (b)-(c) Optical microscopy images showing the uniformity of the DLW submicron pillars for writing fields of $100 \times 100 \mu\text{m}^2$ and $33 \times 33 \mu\text{m}^2$, respectively. (d), (e) The frequency distribution of the pixel intensity obtained from optical images (subfigures b, c). Gaussian functions (red curves) were fitted to the pixel intensity data. (f), (g) The pixel intensity of large ($100 \times 100 \mu\text{m}^2$) and small ($33 \times 33 \mu\text{m}^2$) writing fields vs. the printing time.

The laser power significantly influenced the dimensions of the pillars including both diameter and height (Figure 3.2a-e). Increasing the laser power will increase size of the volume around the focal point of the focused laser beam, where the intensity is high enough to initiate two-photon processes. This affects the feature dimensions at the submicron scale (*i.e.*, feature sizes $\leq 1\mu\text{m}$). Therefore, to control the dimensions of such small features, a fine-tuning of the printing parameters in general and the laser power in particular is needed. Figure 3.2e indicates how the diameter and height of pillars in the submicron range can be controlled through the adjustment of the laser power. As the laser power (L_p) increased from 12% to 21%, the mean diameter of the submicron pillars almost doubled (from 222 to 426 nm) while their mean height increased from ≈ 600 nm to ≈ 900 nm (Figure 3.2e). The standard deviation of the diameter of the pillar was particularly low (*i.e.*, 4-8 nm), while height showed somewhat higher levels of variation (*i.e.*, 30-50 nm) (Figure 3.2e). Furthermore, the small coefficient of variation in diameter and height (2% and 5%, respectively) for different laser powers underlined the reproducibility of the process. A proper selection of the laser power is therefore essential for the fabrication of pillars with controlled dimensions in the submicron to nanoscale range.

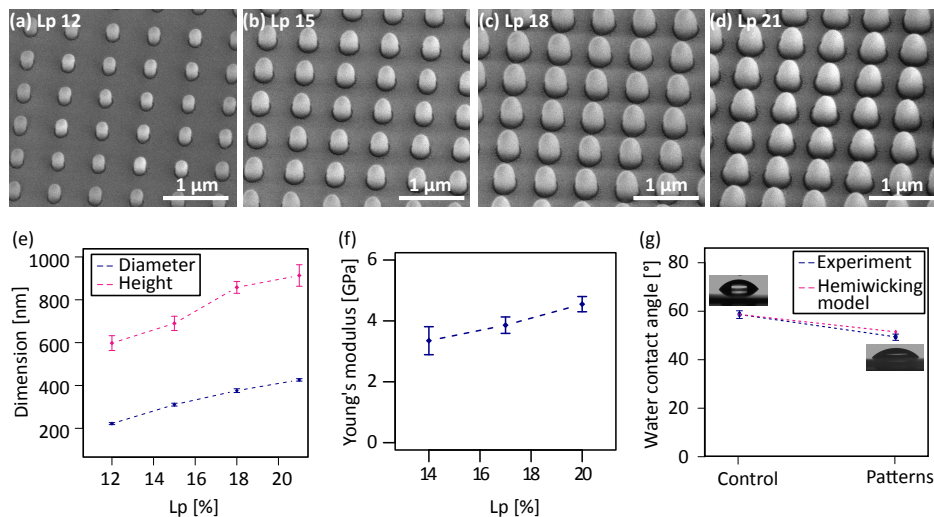


Figure 3.2: Submicron pillars characterization. (a-d) SEM images of the submicron pillars printed using laser powers of 12%, 15%, 18%, and 21%, respectively. (e) The dimensions of the submicron pillars as a function of the laser power. (f) The Young's modulus of the submicron pillars as a function of laser power. (g) The experimental and theoretical measurements of the water contact angle on the flat and patterned surfaces ($L_p = 21\%$). The dotted lines are included to guide the eye.

3.3.2. Mechanical properties

An increase in the Young's modulus from 3.35 GPa to 4.55 GPa was also observed for the used material (IP-L780) with increasing the laser power from 14% to 20% (Figure 3.2f). This could be explained by a higher degree of crosslinking and, thus, increased Young's modulus resulting from a higher laser power (at a constant writing speed)[127]. The possibility to tune the Young's modulus of DLW material using the laser processing parameters and within the same single-step fabrication process can be of great utility when trying to manufacture 3D structures with gradient stiffnesses at microscale. It would, however, be increasingly more challenging to achieve the same with submicron features, because the laser power will affect both the Young's modulus and the size of the structures. That said, the dimensions of submicron patterns can be controlled even when the laser power and writing speed are kept constant (to ensure the Young's modulus remains unchanged).

3.3.3. Water contact angle

According to previous studies [86, 128], both chemical composition and geometric parameters affect the wettability of patterned surfaces. In this study, the contact angle decreased from $58 \pm 1.35^\circ$ ($n = 6$) on the non-patterned substrate to $48.9 \pm 2.29^\circ$ ($n = 6$) on the patterned surface, indicating a shift towards hydrophilicity as a result of patterning (Figure 3.2g). This observation can be explained through the Hemiwicking's phenomenon [86] according to which a patterned surface can absorb the water droplet due to its surface roughness. Therefore, the water penetration propagates through pillars beyond the droplet and a liquid film forms over the surface. The Hemiwicking' phenomenon occurs when the contact angle of a non-patterned surface (Young's angle = θ) is smaller than a critical value θ_c given by the following relationship [86]:

$$\cos \theta_c = (1 - \phi_s) / (r - \phi_s) \quad (3.5)$$

where ϕ_s is the density of the submicron pillars and r is the roughness factor on rough surfaces. The roughness factor is defined as the ratio of the rough surface area to that of the flat surface area (for a smooth surface $r = 1$, and for a rough surface $r > 1$). Approximating pillars as cylinders, for the square pillar arrays, ϕ_s and r are given as [86, 129]:

$$\phi_s = \pi d^2 / 4p^2, \quad r = \frac{A_r}{A_f} = \frac{p^2 + 4 \times (\frac{\pi dh}{4})}{p^2} = 1 + \pi dh / p^2 \quad (3.6)$$

Substituting the dimensions of the submicron pillars ($d = 426$ nm, $h = 913$ nm, $p = 700$ nm, p is defined as the distance between the center of two adjacent pillars) into Equations 3.5 and 3.6, yields $\phi_s = 0.3$, $r = 3.49$, and $\theta_c = 77^\circ$. As θ_c is higher than the Young's angle (58°), the water contact angle on the submicron pillars can be calculated as [86]:

$$\cos \theta^* = 1 - (1 - \phi_s) \cos \theta \quad (3.7)$$

This equation accurately predicts both a theoretical contact angle ($\theta^* = 51^\circ$) that agrees with the experimental value of the contact angle (49°) and an increase in hydrophilicity that is also observed in our experiments (Figure 3.2g).

3.3.4. Response of MC3T3-E1 cells to the 2PP patterns

The pillars made with the highest laser power (*i.e.*, $L_p = 21\%$) were selected for the preliminary cell experiments, because they showed the highest Young's moduli (Figure 3.2f). Moreover, a stiffer substrate is known to stimulate the osteogenic differentiation of osteoprogenitor cells [130]. Firstly, the MC3T3-E1 cells cultured on the patterned surfaces showed no signs of death indicating that the polymer is not cytotoxic for these cells and time of exposure. From the second day of culture, the cells residing on the non-patterned surfaces developed a well-spread, polygonal morphology with areas around $3000 \mu\text{m}^2$ (as determined from the actin cytoskeleton staining) (Figure 3.3a, c, I, III). Furthermore, the number of cells increased from day 2 to day 4 on this surface while cell morphology and degree of anisotropy did not change significantly (Figure 3.3a, c, e, f).

By comparison, the cells cultured on the patterned surfaces appeared highly polarized on day 2 with clear filopodia developed for attachment and significantly smaller cell area, resulting in higher anisotropy (Figure 3.3b, II, f, g). Over time, the cells grew in size and adopted a more well-spread stellate morphology on the patterned surfaces (Figure 3.3d, IV, g). Consequently, the degree of anisotropy of the cells significantly decreased from day 2 to day 4 on the patterned surfaces (Figure 3.3f). In addition, the proliferative capacity of the cells was found to be at least similar to that of the cells cultured on the non-patterned surfaces, as indicated by the measurement of the cell density (Figure 3.3e). The actin fibers were oriented parallel to the stretching direction on both non-patterned and patterned surfaces, but they were less organized on the patterned surfaces due to the stretching in all directions (stellate shape) (Figure 3.3d, IV). The morphological analysis of living cells performed using AFM on day 2 revealed a number of other interesting findings. First, the heights of the cells cultured on patterned surfaces were lower as compared to the cells cultured on non-patterned surfaces, confirming the highly polarized morphology of the cells interacting with the patterns (Figure 3.3h, i, j). In addition, for the cells interacting with the patterned surfaces, the presence of perinuclear actin cap fibers was observed in the mechanical maps (Figure 3.3l). This could contribute to the higher value of the Young's modulus (Figure 3.3l, m) measured in the area corresponding to the nucleus of these cells. By comparison, thicker and peripheral actin fibers were observed on the non-patterned surfaces (Figure 3.3k, m).

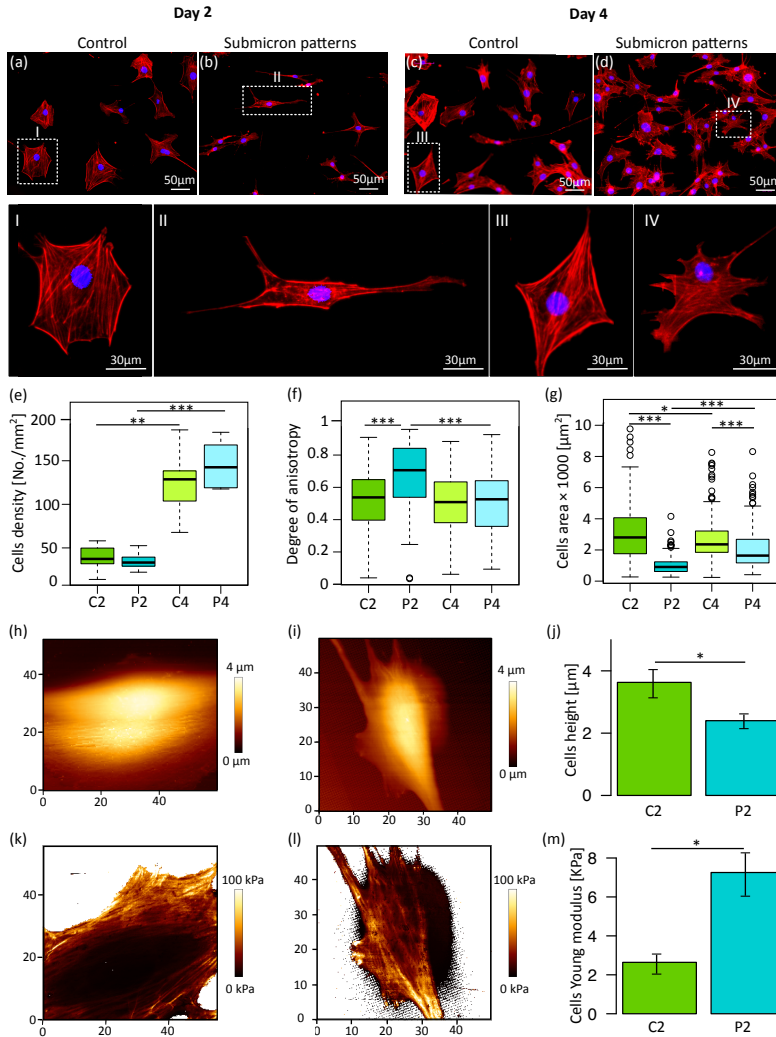


Figure 3.3: The fluorescence microscopy images of the MC3T3-E1 cells cultured on the flat control and patterned surfaces (a), (b) F-actin (red) and nucleus (blue) staining of cells on the control (*i.e.*, glass) and patterned surface ($L_p=21\%$) on day 2. (c), (d) F-actin and nucleus of the cells cultured on the control (*i.e.*, glass) and patterned surfaces ($L_p=21\%$) on day 4. (I-IV) The magnified views of the indicated regions in a-d. (e-g) The cell density, degree of anisotropy, and F-actin area measured on the control (C2, C4) and patterned (P2, P4) surfaces on days 2 and 4, as determined from the fluorescence images. (h-j) The AFM-measured morphological images of the cells cultured on the control and patterned surfaces on day 2 (h-i) and the values of the cells maximum height (j). (k-m) The AFM mechanical maps on the control and patterned surfaces on day 2 (k,l) and the values of the Young's modulus measured in the area corresponding to the nucleus (m). The Student's t-test was used to compare the statistical significance of the differences between both groups. A p value below 0.05 was considered statistically significant (* $p < 0.05$, ** $p < 0.01$, *** $p < 0.001$).

A closer look at the cell-surface interface by SEM revealed that the cells' filopodia used the pillars as anchoring sites and that some of the pillars bent, especially at the local regions around the edge of the cells (Figure 3.4a-d). This implies that the cell adhesion forces differed locally, with possibly higher forces at the leading front than at the rear of the cell. Based on the SEM image analysis, the lateral displacement of the pillars by cells was estimated to be between 0 and 235 nm (Figure 3.4c, d). Our computational model of the pillars was then used to estimate the corresponding reaction force of the pillars given the measured Young's modulus of the material (Figure 3.4e). We found that forces around 2.5 μN corresponded to the maximum measured displacement. AFM nanomechanical experiments indicated detachment forces of the pillars from the substrate in the range between 2.5 μN and 5.5 μN . Few completely detached pillars were actually visible around the edges of some cells (Figure 3.4c, d) indicating that those cells exerted forces $\geq 4 \mu\text{N}$ locally on some pillars. Further studies are required to exactly measure the adhesion force of the cells on the substrate. The adhesion of pillars to the substrate can be enhanced by increasing the diameter of the pillars, decreasing the height of the pillars, and increasing the interface distance during the printing process [125].

These findings suggest that cells on the patterns initially required a period of adaptation to the surface but once attached, their migration, proliferation, and spreading were supported by the patterned surfaces probably with the contribution of the enhanced hydrophilicity of these surfaces [125, 131–133]. The effects of different cell morphologies observed at the early time points on the later cellular functions such as osteogenic differentiation need to be further investigated.

The ability of the presented methodology to generate large areas covered by submicron patterns with a controlled height, diameter, interspacing and Young's modulus in a single-step process is unique among 3D printing techniques. Furthermore, the possibility of creating 3D structures decorated with such surface nanopatterns allows to approach the complexity of stem cell niche with regards to the extracellular matrix characteristics. Together with the shown cytocompatibility of the used resins for mouse preosteoblasts (IP-L780 resin, in this study) and human stem cells (IP-Dip resin, in our previous study [125]), the 2PP process enables the systematic studies of the effects of these complex structures on cellular functions.

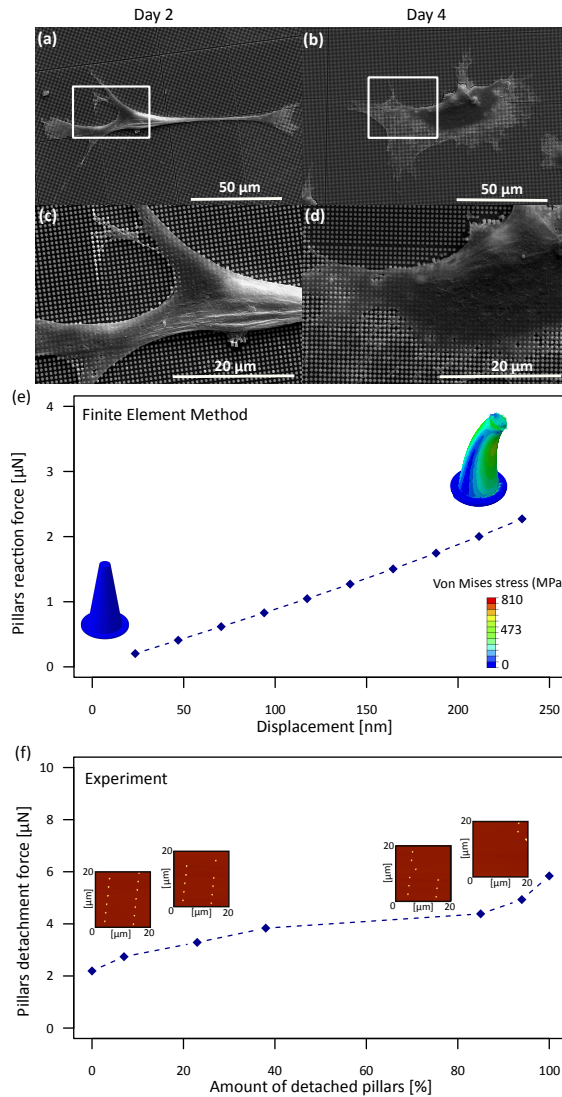


Figure 3.4: Cell-surface interactions. (a), (b) The SEM images of the cells cultured on the patterned surfaces ($L_p=21\%$) after 2 and 4 days, respectively. (c), (d) The magnified views of the indicated regions in subfigures a and b. (e) The results of the computational model which represent the pillars reaction force (F) vs. displacement. The inset figures visualize the von Mises stress distribution within the submicron pillars for lateral displacement of 0 and 235 nm. (f) The AFM experimental results of submicron pillars detachment force. The bright dots in the micrographs represent the pillars remaining after the application of a certain force. This indicates that the pillars “peeled off” from the substrate, suggesting that the failure occurred at the interface between the substrate and the pillar.

3.4. Conclusions

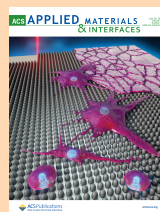
In summary, we presented a comprehensive study on an advanced 3D printing method for generation of patterns with controlled morphology and mechanical properties in a single-step process, relevant for modulating cell behavior. Our results led to an optimized 2PP method for a fast and improved reproducibility of DLW submicron features over large areas by modifying the writing mode and field while optimizing the laser power of the DLW system. More specifically, we could achieve a three-fold decrease in the printing time and uniform patterns (coefficient of variation $\approx 5\%$) over an area of 4 mm^2 . Increasing the laser power not only increased the polymerized volume but also resulted in a higher Young's modulus of the structure. Both experimental and simulation data showed that forces in the range of $2.5\text{-}5.5 \mu\text{N}$ could detach the pillars from the substrate. The hydrophilicity of the surface was enhanced by patterning. Importantly, our cell experiments confirmed that the IP-L780 resin used here is compatible with MC3T3-E1 cells. The surface patterns significantly influenced the morphology of these cells as compared to the non-patterned surfaces while proliferation showed a similar trend over the 4 days of culture. In addition, the Young's modulus corresponding to the nucleus area of the cells cultured on the patterned surfaces for 2 days was significantly higher than of those cultured on the non-patterned surfaces. This study indicates that the 2PP process provides unique possibilities for studying the effects of highly controlled submicron patterns on the bone tissue regeneration process.

4

3D Printed Submicron Patterns Reveal the Interrelation between Cell Adhesion, Cell Mechanics, and Osteogenesis

The surface topography of implantable devices is of crucial importance for guiding the cascade of events that starts from the initial contact of the cells with the surface and continues until the complete integration of the device in its immediate environment. There is, however, limited quantitative information available regarding the relationships between the different stages of such cascade(s) and how the design of surface topography influences them. We, therefore, used direct laser writing to 3D-print submicron pillars with precisely controlled dimensions and spatial arrangements to perform a systematic study of such relationships. Using single-cell force spectroscopy, we measured the adhesion force and the work of adhesion of the preosteoblast cells residing on the different types of surfaces. Not only the adhesion parameters (after 2–60 s) but also the formation of focal adhesions was strongly dependent on the geometry and arrangement of the pillars: sufficiently tall and dense pillars enhanced both adhesion parameters and the formation of focal adhesions. Our morphological study of the cells (after 24 h) showed that those enhancements were associated with a specific way of cell settlement onto the surface (*i.e.*, “top state”). The cells interacting with tall and dense pillars were also characterized by numerous thick actin stress fibers in the perinuclear region and possibly high internal stresses. Furthermore, living cells with highly organized cytoskeletal networks exhibited greater values of the elastic modulus. The early responses of the cells predicted their late response including matrix mineralization: tall and dense submicron pillars significantly upregulated the expression of osteopontin after 21 days of culture under both osteogenic and nonosteogenic conditions. Our findings paint a detailed picture of at least one possible cascade of events that starts from initial cell adhesion and continues to subsequent cellular functions and eventual matrix mineralization. These observations could inform the future developments of instructive surfaces for medical devices based on physical surface cues and early markers.

Published as: Nouri-Goushki, Mahdiyeh, *et al.*, “3D Printed Submicron Patterns Reveal the Interrelation between Cell Adhesion, Cell Mechanics, and Osteogenesis”, *ACS Applied Materials & Interfaces*, 2021, 13, 29, 33767–33781, <https://doi.org/10.1021/acsaami.1c03687>.



4.1. Introduction

The micro- and nanotopographical features of a biomaterial surface influence cellular responses, including cell adhesion [134], bactericidal activity [65, 66, 135–137], and immunoregulatory effects [138, 139]. The roles of a wide range of topographical characteristics in eliciting specific cellular responses have been investigated. Those include surface roughness [140], the aspect ratio of the surface features [141], their shape, and dimensions [32], which could be exploited to improve the treatment of bony defects. For example, micro- and nanostructured surfaces with certain characteristics have been found to promote osteogenic response [31, 142] of stem cells, thereby expediting the osseointegration and improving the service life of implants.

While the isolated effects of surface micro- and nanofeatures on the bone tissue regeneration process remain mainly elusive, some trends have been already identified. At the microscale (*i.e.*, feature size $> 1.0 \mu\text{m}$), for example, surface micro pillars with greater heights (*i.e.*, $\geq 1.6 \mu\text{m}$) and smaller diameters and interspacing (*i.e.*, 1, 2, 4, and $6 \mu\text{m}$) have been found to enhance the expression of osteogenic markers (*e.g.*, osteopontin (OPN)) [143]. At the nanoscale (*i.e.*, feature size $< 100 \text{ nm}$), previous studies [63, 144] have reported a decreased level of OPN and osteocalcin (OCN) expression for nanopillars with greater heights. Despite the presence of these individual studies, the landscape of how the design parameters of surface patterns affect the osteogenic response remains largely unknown: (i) how the cell adhesion properties (*e.g.*, cell adhesion work and force) are regulated via interactions with patterns at different scales (from nano to micro scale) and (ii) whether the initial cell adhesion force promotes the osteogenic differentiation of the cells.

It is becoming increasingly clear that cellular receptors, such as integrins, can sense small topographical features during the adhesion phase and activate topography-induced mechanotransduction pathways. These involve integrin clustering, the formation of focal adhesions (FA), and the reorganization of the cytoskeleton and nucleus [16–20]. There are, therefore, many mechanobiological pathways that are directly or indirectly involved in how surface features influence cell response. Quantification of the adhesion force of the cell during its early interactions with patterned surfaces could enhance our understanding of how mechanics-related factors influence cell-surface interactions. However, most previous studies have used qualitative approaches, such as flow shear stress assays [145, 146], stretching devices [147, 148], and microscopy techniques [149] to evaluate the adhesion of cells to the substrate.

Among experimental force-sensitive techniques for mechanical probing of cells [150], single-cell force spectroscopy (SCFS) can quantitatively measure the early stage [151–153] of cellular adhesion force in the range of a few to tens of nanonewton [154] while precisely manipulating the cell attachment positions. To date, few studies have applied SCFS to measure the initial cellular adhesion force of osteoblasts [151, 153, 155–158] and mesenchymal stem cells (MSCs) [154, 159, 160] on various surfaces. Quantitative SCFS analyses have revealed that the adhesion force of the human osteoblasts increases with the surface roughness on selected

laser melted titanium surfaces, reaching a value of 8.5 nN on the roughest surface relative to surfaces treated with different blasting agents [28]. This finding was associated with a higher degree of osteoblast colonization. In another SCFS study, partially denatured collagen surfaces were found to increase the initial cellular adhesion relative to native collagen and promote spreading, migration, and osteogenic differentiation of preosteoblasts [153].

SCFS has not yet been applied to surfaces decorated with precisely controlled micro- and nanopatterns. Understanding the impact of the design parameters of surface micro- and nanopatterns and their length scale on cell adhesion and the interrelation between the adhesion forces and subsequent cell functions necessitates systematic studies of such effects [161]. One of the main factors that limit such systematic investigations has been the unavailability of fabrication methods for creating precisely controlled patterns. Direct laser writing (DLW) via two-photon polymerization (2PP) has been recently shown to be a powerful technique for generating submicron patterns with high degrees of reproducibility and geometric fidelity [40, 125]. Moreover, this technique facilitates the surface engineering of implantable devices, since it is capable of printing structures with a wide range of length scales (*i.e.*, 200 nm – 100 μ m) in a single-step process. In our previous studies [40, 125], we have demonstrated the 3D printing of highly controllable submicron patterns over a large area and the cytocompatibility of the applied materials (IP-DIP and IP-L780) for the human mesenchymal stem cells (hMCS) and MC3T3-E1 preosteoblast cells.

To reveal the relationships between the various steps of cell-surface interactions and to identify the early markers of the osteogenic potential of surface-decorated biomaterials, we studied the effects of height and interspace of submicron pillars on the response of MC3T3-E1 cells from the adhesion phase up to matrix mineralization under both osteogenic and non-osteogenic conditions. Towards that aim, we applied quantitative methods, such as SCFS, atomic force microscopy (AFM), as well as a host of biological assays. Particular attention was paid to the spatiotemporal changes in cell morphology, cytoskeletal organization, the formation of FAs, and the mechanical characterization of living cells during the adhesion phase (from few seconds to 24 h). Moreover, the relevant properties of the patterns (dimensions, wettability, and roughness) and the cell-pattern interface were assessed to better elucidate the underlying mechanisms.

4.2. Materials and methods

4.2.1. Fabrication of the patterns

Submicron pillars with a diameter of 250 nm, different heights (*i.e.*, 250 nm, 500 nm, and 1000 nm) and interspaces (*i.e.*, center-to-center distances of 700 nm and 1000 nm) were designed and printed using a Photonic Professional GT machine (Nanoscribe, Germany) following our previously described protocol [40]. Briefly, six different patterns were designed and imported into a job preparation program (Describe, Nanoscribe, Germany). Arrays (1.0 mm²) of pillars were manufactured with a laser power of 14% and a scanning speed of 1200 μ m/s using the

conventional configuration and the Galvo writing strategy. A droplet of IP-L780 resin (Nanoscribe, Germany) was placed on a glass coverslip and then exposed to a femtosecond infrared laser beam (wavelength of 780 nm) to fabricate the designed patterns. After printing, the specimens were developed in propylene glycol monomethyl ether acetate (PGMEA) (Sigma-Aldrich, Germany) and rinsed in isopropyl alcohol (IPA) (Sigma-Aldrich, Germany) for 25 and 5 min, respectively, followed by blow-drying.

We refer to the patterns with a “small” interspace (designed value = 700 nm) with the letter “S” and the patterns with a “large” interspace (designed value = 1000 nm) with the letter “L”. The lowest height (designed value = 250 nm) will be identified with the number “1”, the intermediate height (designed value = 500 nm) with the number “2”, and the highest height (designed value = 1000 nm) with the number “3”. Thus, groups S1, S2, and S3 were patterned using a “small” (*i.e.*, 700 nm) interspace and the designed heights of 250 nm, 500 nm, and 1000 nm, respectively. Similarly, groups L1, L2, and L3 were patterned with a “large” (*i.e.*, 1000 nm) interspace and the designed heights of 250 nm, 500 nm, and 1000 nm, respectively. For all groups, the flat substrate (glass) was considered as the control group.

4.2.2. Characterization of the patterns

4.2.2.1. Morphological analysis

The morphology of the patterns was characterized by using scanning electron microscopy (SEM) (Helios Nano Lab 650, FEI, USA). The specimens were coated with gold (coating thickness ≈ 5 nm) using a sputter coater (JFC-1300, JEOL, Japan) and then imaged by SEM. To acquire the height of the pillars, the samples were tilted 30 degrees during imaging. The average diameter and height of 100 pillars from the different areas of each sample were quantified using ImageJ (<http://rsb.info.nih.gov/ij/index.html>). The reported height values of the pillars were corrected for the measurement tilt angle.

3D topographical images of the patterns were acquired in tapping mode using an AFM (JPK Nanowizard 4, Germany) and a high aspect ratio probe (TESPA-HAR, Bruker, Germany). Three images of $10\ \mu\text{m} \times 10\ \mu\text{m}$ for each sample were recorded and analyzed. The average surface roughness (R_a) was determined using the JPK SPM data processing software (JPK instruments, v6.1, Germany).

4.2.2.2. Wettability

The wettability of the patterned surfaces was measured using a drop shape analyzer (KRUSS DSA100, Germany). Briefly, deionized water droplets ($2.0\ \mu\text{L}$) were placed on the flat (glass without patterns) and patterned surfaces (with an area of $9.0\ \text{mm}^2$) and the contact angle was recorded after 5 s ($n = 3$) at room temperature.

4.2.2.3. Surface chemistry analysis

Fourier transform infrared spectroscopy (FT-IR, Thermo Fisher Scientific Nicolet FTIR Spectrometer 6700, US) was performed to identify the functional group of the IP-L780 photoresist and the submicron pillars. Four scans in the range of $4000 - 650 \text{ cm}^{-1}$ were performed to acquire each spectrum using the Attenuated Total Reflection (ATR) Element. X-ray photoelectron spectroscopy (XPS, ThermoFisher K-Alpha, Rockford, IL, USA) was performed to analyze the chemical composition of the 3D printed pillars submicron pillars on the glass substrate. 10 scans were acquired with energy steps of 0.2 eV using an Al K Alpha source gun with a spot size of $400 \mu\text{m}^2$ in a standard lens mode. Due to the small size of the pillars and the space between the individual pillars, XPS measured both, the pillars and the substrate. The apparent disturbance of the potassium (K2p) signal within a carbon (C1s) scan was used to calculate and subtract the amount of the carbon signal that originated from the substrate.

4.2.3. Cell experiments

4.2.3.1. Cell culture condition

The specimens were first sterilized by immersion in 70% ethanol (Sigma-Aldrich, Germany) followed by UV light exposure for 20 min. Then, 5.0×10^4 preosteoblast cells (MC3T3-E1; Sigma-Aldrich, Germany, passage 11) were seeded on each sample in a 6-well plate (Greiner Bio-One, Netherlands) and incubated at 37°C , 5% CO_2 in an alpha minimum essential medium (α -MEM) (ThermoFisher, US) supplemented with 10% (v/v) fetal bovine serum (FBS, ThermoFisher, US) and 1% (v/v) penicillin-streptomycin (ThermoFisher, US). For the long-term experiments (*i.e.*, 21 days of culture), the medium was refreshed every 2 days. For the cases where osteogenic conditions were desired, ascorbic acid and β -glycerophosphate (both from Sigma-Aldrich, Germany) were added to α -MEM (1:1000 and 1:500, respectively) from day 2.

4.2.3.2. Cell adhesion measurements by SCFS

SCFS experiments were performed using a JPK Nanowizard IV AFM (JPK Instruments, Germany) mounted on a Zeiss Axio Observer optical microscope (Carl Zeiss AG, Germany) and equipped with the JPK CellHesion module (JPK Instruments, Germany), which allows for an extended $100 \mu\text{m}$ Z-range. The specimens were glued to Petri dishes (TPP, Switzerland), which were compatible with the JPK Petri dish heater (JPK Instruments, Germany) that maintained the temperature constant at 37°C during the experiments. Arrow TL-tipless cantilevers (NanoWorld, Switzerland) with a nominal spring constant of 0.03 N/m were incubated in phosphate-buffered saline (PBS, ThermoFisher, US) containing $10 \mu\text{g/mL}$ fibronectin (Sigma-Aldrich, Germany) for 30 min at room temperature. After functionalization, the cantilevers were rinsed twice in PBS and were calibrated using the thermal noise method.

For the SCFS experiments, 5.0×10^4 MC3T3-E1 cells were pre-cultured in a standard 6-well plate. When the cells reached confluence, the culture medium was removed, the cells were rinsed twice with 2.0 mL PBS, and were detached from the well using 100 μL of 0.5% Trypsin-EDTA (ThermoFisher Scientific, US) solution (37 °C, 3 min). The trypsinized cells were suspended in 1.0 mL of culture media and were used for the SCFS experiments. 100 μL of the cell suspension was directly injected in a Petri dish containing the sample and 2.0 mL culture medium, relatively far from the patterned area. Single round cells were identified by the optical microscope and were individually picked up by the functionalized probe. To pick the cells, the free end of the cantilever was carefully aligned with the cell and a force-distance cycle was performed using the following parameters: a setpoint force of 3 nN, a Z length of 50 μm , approach and retract speeds of 2 $\mu\text{m}/\text{s}$, and a contact time of 10 s. The cantilever with cell attached to the tip is referred to as “cell probe”. The cell adhesion measurements with surfaces were then performed by acquiring force-distance curves with the “cell probe” using the following parameters: a setpoint force of 1 nN, a Z length of 80 μm , and approach / retract speeds of 5 $\mu\text{m}/\text{s}$. Since the first phase of cell adhesion, characterized by single-integrin adhesion events, takes place during the first 60 s of contact with a surface [162–164], 2 s and 60 s contact times were tested.

Since immunostaining analysis showed that cells interacting with L1 and S1 patterns did not have different behavior (in terms of cell area, cell morphology and FAs) as compared to the control samples, SCFS experiments were performed only on S2, S3, L2, L3 and on the control (flat glass) surfaces. Three force-distance curves on the pattern and three force-distance curves on the glass control surface were acquired with each “cell probe”. Between 7 and 9 cells were tested on each specimen. The reported normalized values of the adhesion force and the work of adhesion were obtained by normalizing the values from each cell on the patterns to the values obtained for the same cell on the glass control surface. The nonparametric KruskalWallis test was used to compare the measurements obtained on the different patterns.

4.2.3.3. Immunocytochemistry analyses

The actin filaments, nucleus, and FAs of the cells were stained after 4 h and 1 day. As previously described [40], the specimens were first rinsed with PBS and the cells were fixated using a 4% (v/v) formaldehyde solution (Sigma-Aldrich, Germany). After permeabilization with 0.5% Triton X-100/PBS (Sigma-Aldrich, Germany) at 4 °C for 5 min, the cells were incubated in 1% BSA/PBS (Sigma-Aldrich, Germany) at 37 °C for 5 min. Then, the specimens were incubated in rhodamine-conjugated phalloidin (1:1000 in 1% BSA/PBS, ThermoFisher, US) and anti-vinculin mouse monoclonal primary antibody (1:100 in 1% BSA/PBS, Sigma-Aldrich, Germany) for 1 h at 37 °C. The cells were then rinsed thrice with 0.5% Tween-20/PBS (Sigma-Aldrich, Germany) and incubated in Alexa Fluor 488, donkey anti-mouse polyclonal secondary antibody (1:200 in BSA/PBS, ThermoFisher, US) for 1 h at room temperature. The specimens were again rinsed thrice with 0.5% Tween-20/PBS for 5 min each time, followed by 5 min rins-

ing with 1x PBS. Afterward, a droplet of 10 μL Prolong gold (containing 4',6-diamidino-2-phenylindole (DAPI), ThermoFisher, US) was laid on the cells and the specimens were flipped over on microscopic glass slides and were imaged using a fluorescence microscope (ZOE fluorescent cell imager, Bio-Rad, Netherlands). For SEM observations, the stained specimens were rinsed twice with distilled water for 5 min and were dehydrated in 50%, 70%, and 96% ethanol solutions for 15 min, 20 min, and 20 min, respectively. Finally, the samples were dried overnight at room temperature and were coated with gold by sputtering prior to being imaged by SEM.

The cells matrix mineralization was analyzed on day 21 in both non-osteogenic and osteogenic media. Therefore, the cells were washed with PBS and were fixed with a 4% (v/v) formaldehyde solution for 15 min. Next, the samples were prepared for staining by a process similar to cytoskeleton staining (see above). The cells were incubated with osteopontin (OPN) antibody conjugated to Alexa fluor 488 (1:100 in BSA/PBS, Santa Cruz Biotechnology, US) for 1 h at 37 °C. Then, the cells were rinsed thrice with 0.5% Tween-20/PBS for 5 min followed by a subsequent 5 min rinsing with 1x PBS. Prolong gold was added to the specimens and they were mounted on glass slides to be imaged using the fluorescence microscope.

4.2.3.4. Mechanics of living cells by AFM

Mechanical mapping of living cells after 1 day of culture was performed using an AFM (JPK Nanowizard III, JPK Instruments, Germany) in the quantitative imaging (QI) mode and a qp-BioAC-CB3 probe (Nanosensors, Switzerland) with a nominal spring constant of 0.06 N/m. The instrument allowed for a maximum scan area of 30 μm \times 30 μm . During the experiments, the temperature was maintained at 37 °C using the JPK Petri dish heater (JPK Instruments, Germany). The probe was calibrated using the thermal noise method [165]. The applied set-point force was 1 nN, which corresponded to an indentation depth in the range of 300-900 nm. The cells were evaluated using a pixel time of 20 ms and a Z length of 2.0 μm . The maps of the elastic modulus were obtained by fitting the force-distance curves measured at each point of the scanned area to the Hertz-Sneddon model [166] considering a paraboloid tip with a nominal tip radius of 10 nm. The reported values of the elastic modulus were calculated as the average elastic modulus value in a certain area of interest (*e.g.*, the periphery or center of the cells).

4.2.3.5. Image analysis

ImageJ was used to process the fluorescent images. First, the image overlay was split into channels to separate the nucleus, F-actin, and other proteins (*i.e.*, vinculin and osteopontin). The grayscale images of F-actin and osteopontin were thresholded. The cell area, the degree of anisotropy (DA , $DA \sim 1$ presents polarization in cells and $DA \sim 0$ indicates the fully isotropic cells) of 20 cells per sample ($n = 4$), and the osteopontin area ($n = 4$) were then quantified through the Analyse Particle command [40].

To count and measure the FAs area, a previously described method was used [167]. Briefly, the background was subtracted from the greyscale images under the Sliding Paraboloid option with a rolling ball radius of 50 pixels. The local contrast of the image was then enhanced by running the CLAHE plugin (<https://imagej.nih.gov/ij/plugins/clahe/index.html>) with a block size of 19, histogram bins of 256, and a maximum slope of 6. To further minimize the background, the mathematical exponential (EXP) was applied through the process menu. Next, the brightness, contrast, and threshold were automatically adjusted. Finally, the area and number of FAs were measured using the Analyze Particle command [167]. The measurements were performed only on fully separated focal points. The Unpaired *t*-test with Welch's correction was used to determine the significant level of difference with cells on control sample (flat glass).

4.2.3.6. Statistical analysis

To determine whether there were significant differences between the means of different experimental groups, one-way ANOVA followed by the Tukey's multiple pairwise-comparisons post-hoc test was performed using Prism (version 8.0.1, GraphPad, CA, USA). A p-value below 0.05 was considered to indicate statistical significance.

4.2.4. Computational models

We used a commercial non-linear finite element code (Abaqus, v6.21) for our computational simulations to study the mechanics of the submicron pillars interacting with cells. We used isotropic linear elastic material properties for the modeling of the submicron pillars ($E = 3.35$ GPa, $\nu = 0.4$) and the glass substrates ($E = 63$ GPa, $\nu = 0.2$). Using a tie-constraint, the pillar and the substrate were attached. Two pillars with different heights ($h = 500$, and 1000 nm) and similar boundary conditions were modeled. A reference point was defined at the center of the top surface of the pillars. This reference point was kinematically coupled to the nodes on the top surface of the pillars. A displacement boundary condition along the x-axis (U_x) was applied to the reference point. The magnitude of the displacement of the tip of the bent pillars was extracted from SEM images of the cells on different patterns using ImageJ. The displacements of the pillars were applied to the pillars present in each computational model (*i.e.*, $U_x = 0 - 70$ nm for $h = 500$ nm, and $U_x = 0 - 190$ nm for $h = 1000$ nm). Clamped boundary conditions were applied to the glass substrate. 3D quadratic hexahedral elements (C3D20) with a minimum mesh size of 20 nm were used in all of our models. A standard non-linear analysis was used for the simulations. The average local traction forces were calculated from the experimental displacement observations.

4.3. Results and discussion

4.3.1. Characterization of the patterns

The diameter and the interspacing of the pillars were generally very controllable (Table 4.2, Figure 4.1a). The deviations observed in the height of the pillars could be attributed to the fluctuations of the laser intensity during the printing process, as previously reported [38]. The printing time varied between 4.5 – 11.5 h/mm² depending on the height and areal density of the pillars (Table 4.2). The average roughness (R_a) of the series S and L was measured by AFM and varied between 79 – 236 nm and 29 - 213 nm, respectively (Table 4.2). As expected, the surface roughness increased with the height of the pillars, while increasing the interspacing of the pillars reduced the measured roughness of the patterned surface, particularly for the pillars with the smaller heights (Table 4.2, Figure 4.1b). The hydrophilicity of the substrate increased with the height of the pillars (Figure 4.1c). This behavior is in agreement with the previous studies [168, 169] that have shown that rougher surfaces tend to increase the wettability of the surface if the contact angle of the initial surface (48° in our study) is below 60°.

We have analyzed the functional groups of photoresists before and after polymerization via FTIR test. C=C stretch bonds were found in the region of 1680 cm⁻¹ in the resin but disappeared in the polymer spectrum, indicating no signs of monomer after polymerization (Figure 4.1d). Peaks at 1720 cm⁻¹ showed the ester groups in IP-L780 before and after polymerization (Figure 4.1d). Since polymerized nanopillars are printed over a small area, the absorbance value of the ester peak in polymer is less than the one appearing in the monomer. Furthermore, we have quantified the binding energy and percentage of carbon bonds in the polymerized IP-L (Table 4.1). C-C, C=O, and C-O bonds were present in the XPS spectra of nanopillars showing the presence of acrylic structures in the polymer (Figure 4.1e).

Table 4.1: The energy binding of C1s species in the 3D printed submicron pillars (made of IP-L780).

Bond	Energy binding [eV]	Atomic %
C-C	284.9	33.1
C-O	286.2	43.4
C=O	288.8	23.5

Table 4.2: The characteristics of the submicron pillars, the printing times, and the average roughness of the patterned surfaces.

Groups	Diameter [nm]		Interspacing [nm]		Height [nm]		Aspect ratio	Density [/ $100\mu\text{m}^2$]	Print time [h/ mm^2]	Roughness R_a [nm]
	design	measured	design	measured	design	measured				
S1	250	235± 16	700	716± 12	250	251± 24	1	205	5.5	79± 13
S2	250	288± 9	700	714± 9	500	540± 46	2	205	7.5	114± 2
S3	250	305± 14	700	706± 9	1000	928± 32	4	205	11.5	236± 11
L1	250	211± 21	1000	1012± 13	250	253± 30	1	100	4.5	29± 2
L2	250	265± 17	1000	1010± 14	500	498± 28	2	100	5.5	91± 8
L3	250	297± 4	1000	1012± 15	1000	973± 44	4	100	7.5	213± 13

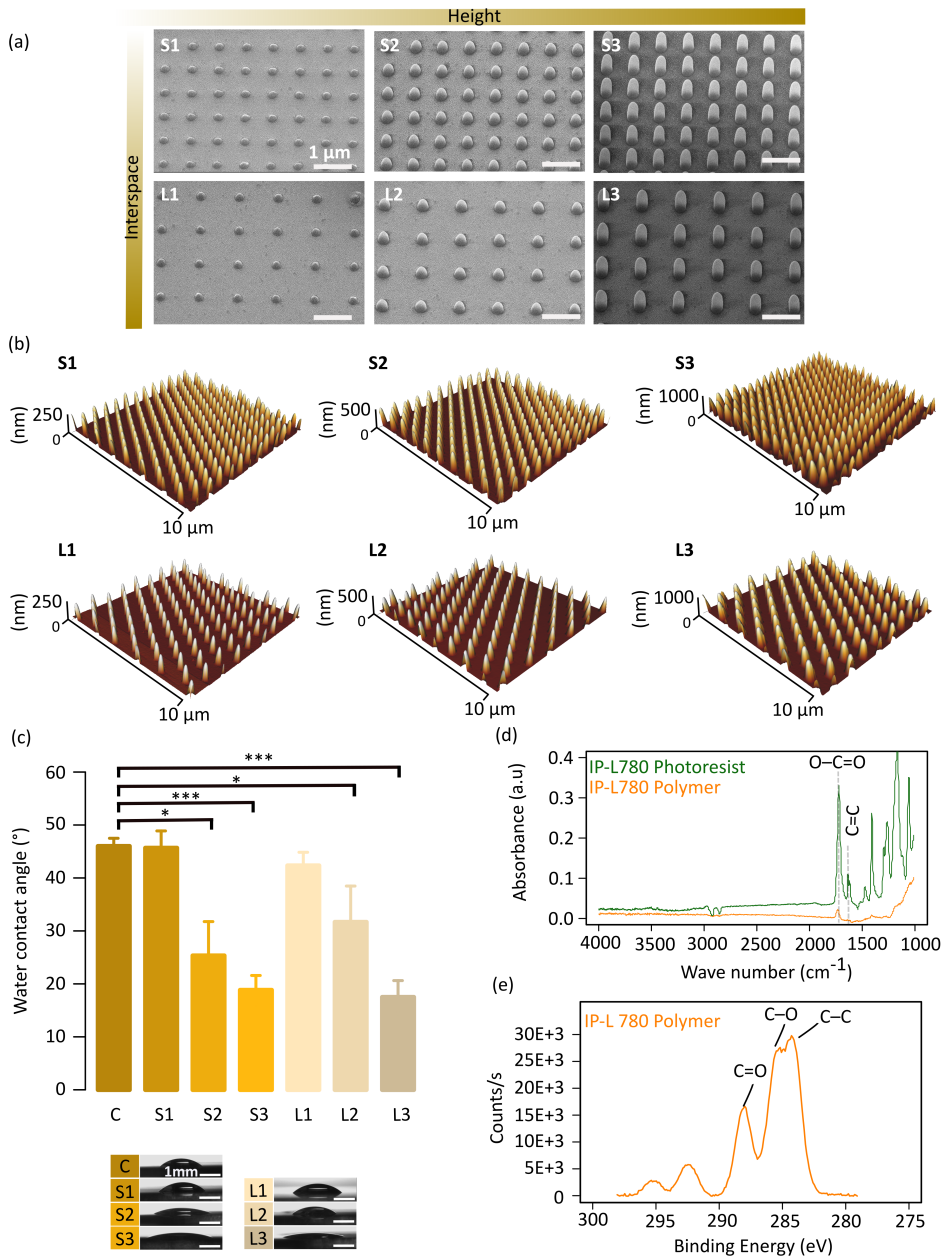


Figure 4.1: Characterization of the submicron pillars. (a) SEM and (b) AFM images of submicron pillars 3D printed using 2PP. (c) A comparison of the wettability of the patterned and control (glass) (C) specimens characterized through water contact angle measurement. (d) FTIR spectra in the ATR mode of the IP-L780 photoresist and polymer (after 2PP). (e) The XPS spectra of C1s peaks in IP-L780 after polymerization. (* $p < 0.05$, ** $p < 0.01$, *** $p < 0.001$).

4.3.2. Differential effects of the patterns on cell adhesion, morphology, and elastic modulus

4.3.2.1. Cell adhesion

The representative force-distance (F-D) curves acquired at 2 s and 60 s on the S2, S3, L2, L3 patterns (Figure 4.2a) showed the typical shape observed when a cell interacts with a surface, indicating the proper functioning of our “cell probes” in terms of cell viability and the positioning of the cantilever. The maximum force peak on the retrace curve, indicating the cell detachment force (*i.e.*, F_{adh}), was followed by step-like events, which were either preceded by a ramp-like change in force (jumps) or by a plateau region (tethers) [164, 170, 171].

The adhesion force (F_{adh}) and the work of adhesion (W_{adh}) increased for all groups after 60 s of contact time as compared to the values recorded after 2 s of contact. This can be explained by the fact that a longer contact time enables the formation of more and possibly stronger (more mature) adhesion sites between the cellular receptors and the surface. The type of pattern influenced the cellular adhesion too (Figure 4.2b and c). After both 2 s and 60 s of contact time, the patterns with the tallest pillars (*i.e.*, S3 and L3) exhibited significantly higher F_{adh} as compared to the patterns with the shorter pillars (*i.e.*, S2 and L2) and the control surface (Figure 4.2b). The F_{adh} values measured for the S2 and L2 groups were not significantly different from those of the control surface (Figure 4.2b).

Furthermore, the patterns with the highest areal density of pillars (*i.e.*, S3 and S2) exhibited a higher W_{adh} as compared to the patterns having similar heights but lower areal densities (*i.e.*, L3 and L2). S3 exhibited higher W_{adh} as compared to L3 (Figure 4.2c). A less clear difference was observed between S2 and L2 where S2 exhibited slightly (but not significantly) higher W_{adh} as compared to L2 after both 2 s and 60 s of contact time.

The curves acquired for the patterns with similar heights (and comparable roughness and contact angle) indicated similar values of F_{adh} after 60 s (*e.g.*, 3.8 nN for S2, 4.8 nN for L2; 8.1 nN for S3, and 9.8 nN for L3 in the examples reported in Figure 4.2a). The adhesion force increased almost linearly with the height of the pillars. For example, the adhesion force corresponding to a pillar height of 1000 nm was around 2 times higher than the one corresponding to a pillar height of 500 nm. The work of adhesion, W_{adh} , was higher on the surfaces decorated with the denser patterns (*e.g.*, 47.5 fJ for S2 vs. 20.6 fJ for L2; 43.5 fJ for S3 vs. 33.8 fJ for L3 in the examples reported in Figure 4.2a).

In summary, the pattern with the tallest and densest pillars (S3), exhibited the highest values of the adhesion parameters (*i.e.*, adhesion force and adhesion work). The L3 pattern, which has a similar height of pillars but a lower pillar density, exhibited an adhesion force that was similar to S3 but a lower work of adhesion. By comparison, the adhesion characteristics of the shorter S2 and L2 patterns were close to the control surface with S2 showing a slightly higher work of adhesion as compared to L2 and the control group.

Hydrophilicity and roughness are known to impact the initial attachment of cells to various kinds of non-patterned surfaces [131, 153, 156, 172, 173]. We

found that the patterns with the tallest pillars (S3 and L3), which are also the most hydrophilic and roughest patterns (Figure 4.1c), result in the highest values of the adhesion force.

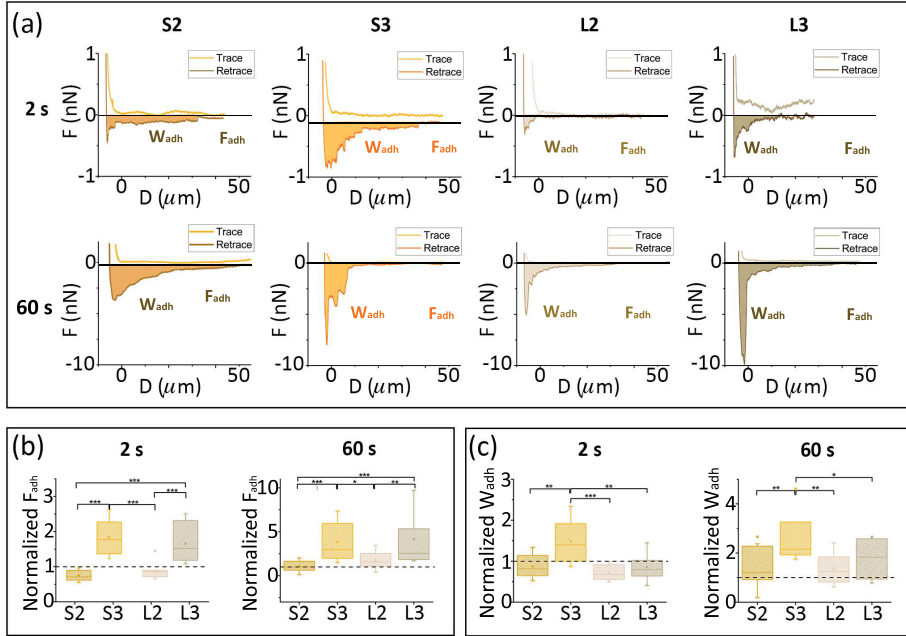


Figure 4.2: Characterization of cell adhesion: (a) Representative F-D curves obtained by SCFS on S2, S3, L2, and L3 patterns after 2 s (first line) and 60 s (second line) of contact. (b) The adhesion force (normalized with respect to that of the control surface) was measured by SCFS on the patterned surfaces after 2 s (left) and 60 s (right) of contact. (c) The work of adhesion (normalized with respect to that of the control surface) measured by SCFS on the patterned surfaces after 2 s (left) and 60 s (right) of contact. The nonparametric one-way ANOVA (KruskalWallis) test was used to evaluate the statistical significance of the differences between the various experimental groups (* $p < 0.1$, ** $p < 0.05$, *** $p < 0.01$).

The interspacing between the pillars affected the mechanism of the early adhesion of cells to the analyzed submicron patterns: lower interspacing resulted in a greater work of adhesion. The work of adhesion depends, among such factors as the adhesion force and the characteristics of the cell type, on the number of the anchoring points (*i.e.*, detachment events) of the cell to the surface [171]. Our results, therefore, suggest that the number of cellular anchoring points on the patterns increases with the areal density of the pillars. This increase was particularly clear for the patterns with the tallest pillars (*i.e.*, S3 as compared to L3).

4.3.2.2. Cell morphology and cytoskeleton organization

After 4 h of culture, round cells with an average area of $1900 \pm 719 \mu\text{m}^2$ and diameters around $49 \mu\text{m}$ were visible on all the patterns and the control specimens (Figure 4.3a, c). Nevertheless, the cells on the S3 pattern developed clearly visible membrane extensions rich in vinculin, indicating their ability to more easily spread and interact with the pillars on this pattern. Therefore, the largest variation in the cell area was encountered for this pattern (Figure 4.3c). The presence of relatively well-developed membrane extensions (mainly lamellipodia) around the periphery of the cells (Figure 4.3a) suggests the start of FAs maturation followed by the formation of actin bundles, indicating that the cells are in the contractile spreading phase [174]. On the contrary, the cells cultured on the control specimens and the specimens from other groups had nascent vinculin sites around the periphery of the cells and the protrusive activity was not yet started (Figure 4.3a), indicating that the cells were not yet in the contractile spreading phase [174] but rather in an earlier phase of the development of FAs [174].

The faster development of FAs on the substrates exhibiting high hydrophilicity and initial adhesion force (measured by SCFS experiments) has been observed in studies performed on non-patterned surfaces as well [153]. In our case, the formation of FAs on the S3 pattern was promoted not only by enhanced hydrophilicity but also by a higher areal density of pillars relative to the other patterns (*e.g.*, L3) that could favor integrin clustering [45-47]. This was also supported by our SCFS experiments (Figure 4.1), which indicated that a high areal density of the pillars results in the formation of more discrete attachment sites already after 2 s and 1 min of contact with these patterned surfaces. Furthermore, integrin clustering may have been further favored by the lower stiffness of the taller pillars in the case of the S3 pattern. Indeed, taller pillars could undergo enhanced bending, thereby further approaching each other when subjected to the interaction forces with the cells [175].

After the first day of culture, the cells significantly grew in size regardless of the experimental group (Figure 4.3b, c). The cells cultured on the patterned surfaces were, however, smaller than those residing on the control surface. In both S and L series, the cell area decreased with the height of the pillar from $\approx 2800 - 2900 \mu\text{m}^2$ for the shorter pillars (S2 and L2) to $\approx 2100 - 2200 \mu\text{m}^2$ for the taller pillars (L3 and S3). By comparison, the pillar interspacing did not affect the area of the cells (Figure 4.3b, c). This observation is in line with the previous studies that have reported a decrease in the cell area for an increased roughness in the submicron range [140].

On day 1, the density and area of FAs per cell increased with the height of the pillars (Figure 4.3d, e). However, the pillar interspacing did not significantly influence the area and density of vinculin-rich plaques. The cells cultured on the S2, S3, and L3 specimens formed the largest FAs areas with an average area of $6.5 \pm 0.03 \mu\text{m}^2$, which was significantly higher than the one found on the control sample (*i.e.*, $5.5 \pm 0.7 \mu\text{m}^2$) (Figure 4.3d, e). Furthermore, the cells residing on taller patterns (S3 and L3) exhibited the highest FA density (Figure 4.3e).

After 1 day of culture, three different cell shapes with different cytoskeletal

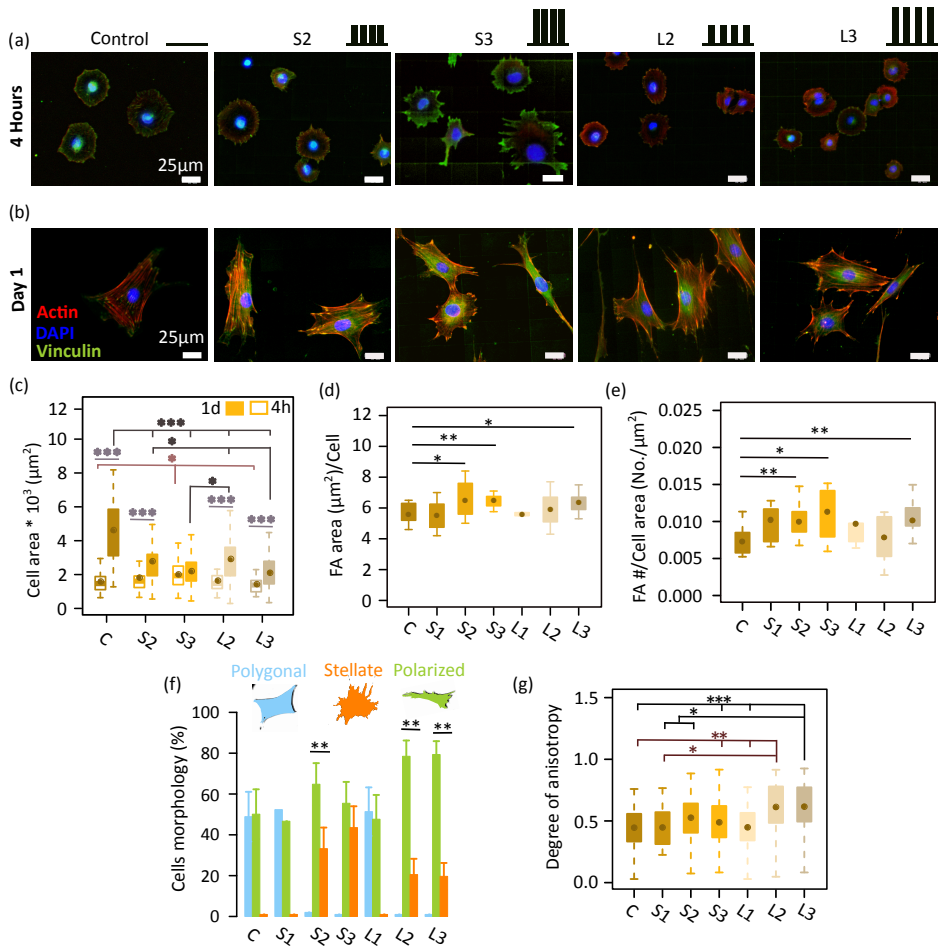


Figure 4.3: Cells spreading and the early response of the MC3T3-E1 cells cultured on the patterned and control surfaces at different time points. (a, b) F-actin, vinculin, and nucleus of the cells cultured on the control and different patterned surfaces after 4 h (b) and 1 day. (c) The cell areas were measured on the patterned and control samples after 4 h and 1 day. (d, e) The FA area and FA density of the cells residing on the patterned and control surfaces on day 1. (f, g) The different types of cell morphology and the degree of anisotropy of the cells residing on the patterned and control surfaces on day 1 (* $p < 0.05$, ** $p < 0.01$, *** $p < 0.001$).

organizations were visible on the specimens (Figure 4.3b, f): (1) polygonal cells with peripherally organized actin fibers, (2) polarized cells with perinuclear actin cap fibers, and (3) stellate cells characterized by the presence of actin fibers in the perinuclear region and multidirectional membrane extensions (mostly filopodia). The polygonal cells were isotropic ($DA \sim 0.4$) and were found on the control spec-

imens as well as on the specimens from the S1 and L1 groups (Figure 4.3b, f, g). The majority of the cells residing on the S2, L2, and L3 specimens were polarized ($DA \sim 0.7$) with wider leading edges showing the motile behavior of the cells (Figure 4.3b, f, g). The cells grown on the S3 pattern adopted a half-polarized, half-stellate morphology and had a DA value close to 0.5 (Figure 4.3b, f, g). In the stellate cells, F-actin stress fibers were stretched towards the protrusions and FA sites. Taken together, the degree of anisotropy and the number of polarized cells were enhanced as the height and interspacing of the pillars increased. However, the influence of the pillar interspacing on the shape and the degree of anisotropy of the cells was more pronounced than that of the height (Figure 4.3f, g).

Cells with different morphologies exhibited qualitatively different spatial organizations of the FAs and F-actin bundles (Figure 4.3b). A coupling between the FAs and the F-actin bundles was more visible for the cells with multidirectional protrusions (*e.g.*, stellate cells on S3 and L3 in Figure 4.3b), which exhibited mature and long-lasting FA sites mainly at the proximity of the cell edge (mostly present in the S3 group) (Figure 4.3b). The coupling of F-actin with FAs around the periphery of cells tends to enhance cellular adhesion [176]. The coupling of vinculin with the actin bundles was less visible on the polarized cells than on the stellate cells, and they were mainly located in the front and rear of the cells (Figure 4.3b). On the polarized cells, the actin stress fibers were aligned and stretched along the direction of the protrusions, suggesting that the cells were migrating and indicating a higher destabilization of the cell adhesion as well as presumably short-lasting FA points [177].

Furthermore, we observed three different settling states of the cells on the patterned surfaces (Figure 4.4a, b) that we categorized as follows: i) a “top state” [178] in which the entire cell body resides on top of the submicron pillars, ii) a “bottom state” [178] in which the submicron pillars fully penetrate the cell body, and iii) a “mixed state” [178] where some areas of the cell sink into the submicron pillars (bottom state) whereas other areas reside on top of the pillars (top state) (Figure 4.4a, b).

On the shortest pillars (*i.e.*, S1 and L1), the bottom state was observed. The cells fully engulfed the pillars and came into contact with the entire available surface of the pillars (top and lateral) and the substrate (Figure 4.4a, b). The body of the cells appeared very thin as the tip of the pillars was almost visible through the entire cell (Figure 4.4a, b). The pillar interspacing did not influence the settling state on those two patterns.

On the taller pillars, the effects of the pillar interspacing on the cell settling state were more pronounced. The cells cultured on the S2 patterns exhibited a mixed state, with a dominant top state. Indeed, the bottom state was observed only in some regions at the periphery of the cell. Moving towards the nucleus, the cell body appeared thicker, resulting in a top state (Figure 4.4a, b). On the L2 patterns, the bottom state was dominant and was observed almost for the entire body of the cells (Figure 4.4a, b). This may have been caused by the larger pillar interspacing, which helps the cells to easily fill the space between the submicron pillars.

In the case of the S3 patterns characterized by the maximum height and

the minimum interspacing, the top state was always observed, suggesting that the cells come into contact only with the top of the pillars without touching the substrate (Figure 4.4a, b). On the L3 patterns, with the maximum height and interspacing, the mixed state was observed. The bottom state was observed only in very small regions around the cell periphery, especially at the rear and front ends of the cells, while the top state was dominant for the rest of the cell body (Figure 4.4a, b).

Previous studies have already shown the effects of the density of nanostructures on how cells “settle” onto a patterned surface and have demonstrated that a high areal density of nanostructures (ρ (/100 μm^2) ≥ 80) and a large diameter of nanopillars ($d \geq 200$ nm) energetically promote the top state [178–181]. The small interspacing between the nanopillars leads to intense stretching and unfolding deformation of the cell membranes while they adhere to the sidewalls [178]. Consequently, the cells adhere to the tip of the pillars. Here, we observed a combined effect of both the density and height of the pillars with a diameter of 250 nm. Indeed, both height and interspacing in the range investigated in this study had an impact on the interactions between the cells and the underlying pillars. The cells that were cultured on the pillars with smaller heights and large interspacing distances (*i.e.*, S1, L1, and L2) came into contact with both pillars and substrate (the dominant bottom state) while increasing the height of the pillars and decreasing their interspacing (*i.e.*, S2, L3, and S3 patterns) caused the cells to mostly interact with the top of the pillars without touching the substrate, hence, the dominant top state.

Interestingly, the cells were able to bend the pillars locally after 1 day of residing on the substrate. The bending was more prominent in the vicinity of the edge of the cells settled in the top state (S2, S3, L3 in Figure 4.4a, b). The pillars were deflected towards the center of the cells (S2, S3, L3 in Figure 4.4a, b). The lateral displacement of the pillar tips was measured by analyzing the SEM images of the dehydrated cells on the patterns (Figure 4.4c). The corresponding local traction forces in the proximity of the cell border were estimated through computational modeling (Figure 4.4c). The cells applied average local traction forces of 144 ± 38 nN to the pillars with a height of 1000 nm. A higher force value (429 ± 62 nN) was calculated for the pillars with a height of 500 nm. As the traction forces are exerted to the extracellular matrix by FAs [182], we further assessed the relationship between the traction forces and FAs area. Although we observed no significant differences between the area of FAs on the pillars with the height of 1000 nm and 500 nm, the estimated local traction forces were different on those pillars (height 500 nm and 1000 nm). These findings suggest that mature FAs with the same area can withstand a wide range of force values (100 - 429 nN estimated in Figure 4.4c), and the results of [182, 183] support our findings. These observations were made for preosteoblasts and are in line with the previous studies that have found direct correlations between the FAs size and the traction forces only during the initial growth phase of FAs, and not for mature FAs [182, 183]. It is, nevertheless, important to realize that the fixation protocol might affect the deformation of the pillars and, thus, the estimated forces.

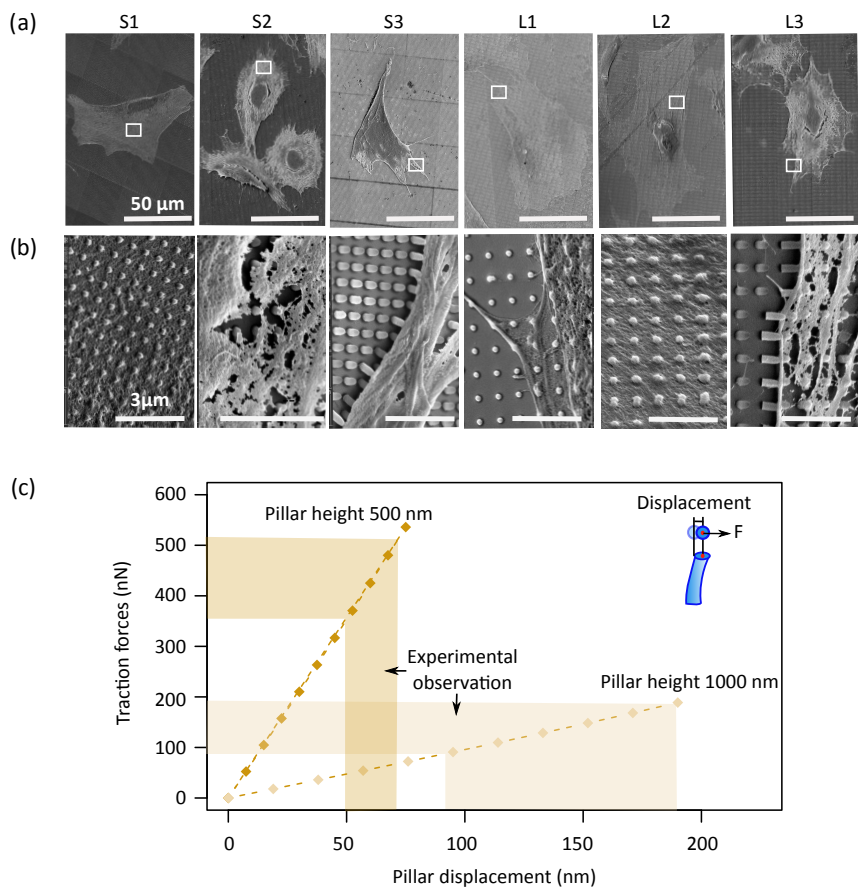


Figure 4.4: Visualization of the cell interactions with the patterned surfaces using SEM and computational modeling. (a, b) Low and high magnification SEM images of the cells on the patterned surfaces. (c, d) The reaction force (applied by cells to the pillars) and von Mises stress in the submicron pillars calculated using the computational models. Lateral displacements of 58, 140, and 289 nm were applied to the pillars with the heights of 250, 500, and 1000 nm, respectively.

4.3.2.3. The elastic modulus of the cells

The different shapes and cytoskeletal organizations found on the different patterns together with the observations on the cell-pattern interfaces indicated that cells residing on different patterns may also have different mechanical properties. Therefore, the elastic moduli of the living cells interacting with the patterned (S2, S3, L2, L3) and control surfaces were analyzed by acquiring AFM mechanical maps of the cells after 1 day of culture (Figure 4.5). Exploiting the capability of AFM-based stiffness measurements to perform subsurface imaging of soft bio-

logical samples up to a depth of 900 nm [184, 185] also allows for a more detailed analysis of the organization of cortical actin, especially in the perinuclear region.

On the control surfaces (Figure 4.5a, b), the presence of thick peripheral actin fibers was observed in the cells with both polygonal and polarized shapes, while no or few perinuclear actin fibers were detected. This type of cytoskeletal organization resulted in a high elastic modulus at the periphery of the cells ($E = 25.8$ kPa for the polygonal cell in Figure 4.5a and $E = 42.5$ kPa for the polarized cell shown in Figure 4.5b) and low elastic modulus at the center of the cells, corresponding to the perinuclear region ($E = 6.1$ kPa in the case of polygonal cell in Figure 4.5a and $E = 4.9$ kPa for the polarized cell in Figure 4.5b).

On all the patterned surfaces, the cells with polarized shape presented aligned (almost parallel) fibers crossing the perinuclear region of the cells from the leading edge to the cell rear, suggesting a motile state where, in general, actin fibers tend to align in the direction of cell movement. This type of cytoskeletal organization can be ascribed to the actin cap formation [186] and gave rise to an elastic modulus, in the perinuclear region, in the range of 6-8 kPa for the cells cultured on the S2, L2, and L3 patterns (*i.e.*, $E = 7.6$, 6.1, and 6.2 kPa for the cells shown in Figure 4.5d, h, and j, respectively). A significantly higher elastic modulus in the perinuclear region was observed for the elongated cells residing on the S3 pattern (*e.g.*, $E = 14.45$ kPa for the region shown in Figure 4.5f), which may be due to a more organized cytoskeleton formed by the thick bundles of actin fibers. This organization can be the result of a faster formation of perinuclear stress fibers in the polarized cells grown on the S3 pattern and suggests higher cell contractility and tension.

Stellate cells exhibited a different type of cytoskeletal organization in the perinuclear region, which in the case of the specimens from the S2, S3, and L3 groups resulted in a branched network of thick bundles of actin fibers and, thus, higher values of the elastic modulus ($E = 14.6$, 13.9, and 14.5 kPa respectively for the cells residing on the S2, S3 and L3 patterns, Figure 4.5c, e, i). This type of organization indicates that the stress fibers in these cells were stretched in different directions. The presence of actin star sites (*e.g.*, the small green arrows in Figure 4.5c, e, i) were associated with the highest values of the elastic modulus and suggested the entanglement of several actin bundles coming from different directions [187, 188].

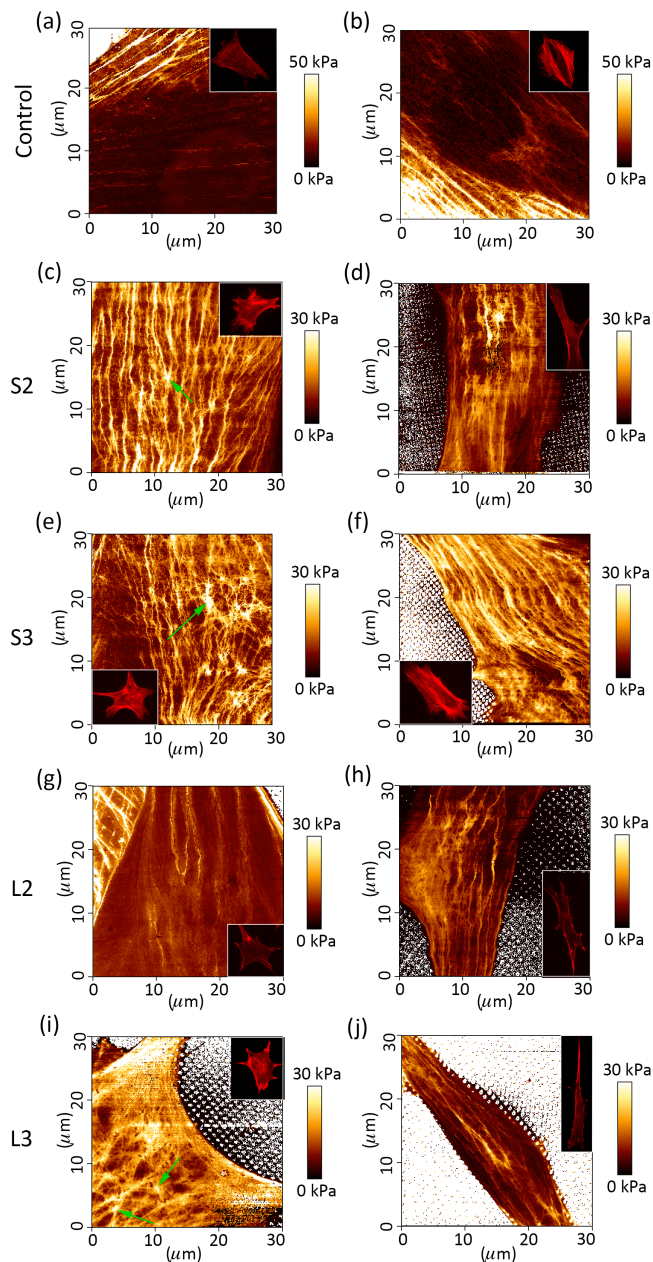


Figure 4.5: AFM-based mechanical characterization of the cells cultured on the patterned and control surfaces on day 1. Some examples of the maps of the elastic modulus obtained for a polygonal cell on the control surface (a), a polarized cell on the control surface (b), stellate cells on the S2, S3, L2, and L3 patterns (c, e, g, i), and polarized cells on the S2, S3, L2, and L3 patterns (d, f, h, j), respectively.

The formation of these actin patterns, such as asters or stars, has been hypothesized to be associated with high levels of intrinsic mechanical stress within the cortical network [189–191]. They may, therefore, indicate a high-tension state for the stellate cells residing on the S2, S3, and L3 patterns.

The stellate cells cultured on the L2 patterns exhibited a different type of cytoskeletal organization as compared to the stellate cells grown on the other patterns. Big peripheral actin stress fibers were observed, while the nuclear region was characterized by a very limited presence of actin fibers or filaments and, thus, a low value of the elastic modulus (*i.e.*, 8.5 kPa for the sample cell shown in Figure 4.5g). This suggests lower contractility and tension of the stellate cells on the L2 pattern as compared to the other patterns. Interestingly, the cells residing on the L2 patterns, in contrast with those cultured on the other patterns (S2, S3, L3), exhibited mostly a “bottom settling state” (*i.e.*, contact not only with the top of the pillars but also with the substrate between them) (Figure 4.4a, b). This observation suggests a correlation between the way cells adhere to and settle onto the patterns (*i.e.*, top state or bottom state) and their response in terms of cytoskeletal organization and mechanical properties.

4.3.3. Summary of the early cellular responses on submicron pillars

We found a direct relationship between the cell adhesion, surface wettability, and surface roughness. S3 and L3 were the roughest and most hydrophilic surfaces and the cells on those patterns exhibited the highest initial adhesion force and the most abundant focal adhesion sites after 1 day. Our results are in line with the previous studies showing the positive impact of hydrophilicity [40] and intermediate roughness (*i.e.*, $R_a \sim 200$ nm) in the submicron range on cell adhesion [140, 192, 193].

Furthermore, our results suggest a faster FA formation process on the S3 pattern (Figure 4.3a). The faster formation of vinculin-rich sites may have been caused not only by the high initial adhesion force on such surfaces but also by the geometry of the pillars (height and interspace). Tall and dense pillars provide a large number of anchoring points (higher work of adhesion), as observed in our SCFS experiments. The high density of the anchoring points could result in a high density of integrin binding sites, which could more easily cluster and develop mature FAs [194].

The morphology and cytoskeletal organization of the cells on day 1 support the statement regarding the faster formation of mature FAs. The S3 patterns exhibited the highest numbers of stellate cells at day 1, implying the greater coupling of the focal points with F-actin, which normally form in presence of mature FAs [102, 177] and, thus, indicate a more advanced state of the FAs formation process.

The cells cultured on the S3 surfaces with both elongated and stellate morphologies exhibited the highest values of the elastic modulus and the highest degree of cytoskeletal organization, characterized by the presence of thick and dense actin stress fibers in the perinuclear region. This observation suggests higher con-

tractility and higher tension as compared to the cells interacting with the other patterns, which may be attributed to the different adhesion behavior of the cells residing on this type of surface as indicated by the initial force and work of adhesion as well as the development and distribution of FAs. This may lead to a higher level of nuclear tension [140, 195] and affect subsequent cellular functions. Indeed, previous studies have shown that the presence of dense actin cap fibers is associated with elevated levels of nuclear tension, high chromatin condensation, and YAP nuclear accumulation, resulting in the osteogenic differentiation of MSCs on catecholic polyglycerol coatings with roughness values (R_a) in the range of 150-300 nm [140].

The next question was whether our findings regarding the early adhesion, morphology, and mechanical properties of preosteoblasts affect the subsequent cellular functions. Therefore, a long-term experiment was performed to investigate the ECM formation by preosteoblast cells.

4.3.4. Effects of the patterns on the ECM

One of the essential ECM proteins expressed by mature osteoblasts is OPN [196], which is further enhanced by applying mechanical stress [197]. We, therefore, analyzed the level of OPN expression for the specimens from different experimental groups using both osteogenic and non-osteogenic media after 21 days of cell culture. On flat controls, OPN was expressed only in the osteogenic medium (Figure 4.6b). In the osteogenic condition, the surfaces patterned with the tallest pillars (*i.e.*, S3 and L3, height = 1000 nm) significantly upregulate the expression of OPN as compared to the other patterns and the control group (Figure 4.6a, b). In addition, a slight (not significant) increase in the OPN expression compared to the control surface was observed for the S2 group, while the other patterns did not show any difference as compared to the control group (Figure 4.6c). A difference in the OPN expression after 21 days was observed only on those patterns (S2, S3, and L3) for which an increased area and density of FAs were observed after 1 day (Figure 4.6f) and where cells mostly interacted with the top region of the pillars (dominant top state). This finding supports the presence of a relationship between the capability of the cells to rapidly form mature FAs and the subsequent matrix mineralization process. The S3 pattern, for which we found the strongest cell adhesion and the highest elastic modulus values in the perinuclear areas, also exhibited the highest level of OPN expression, further supporting the hypothesis that a direct relationship exists between the early cell adhesion behavior and the late matrix mineralization process. We did not, however, detect a significant difference between S3 and L3 (pillars with a larger interspacing of 1000 nm) under the osteogenic conditions (Figure 4.6a, c).

To isolate the effects of the surface patterns from those of the osteogenic supplements, we repeated the experiments for the S3, L3, and control groups under non-osteogenic conditions. The difference between the OPN expression of the S3 and L3 groups was statistically significant when using a non-osteogenic medium (Figure 4.6d, e). The differential effects of the patterns with different geometries on the OPN expression could, therefore, be more easily detected when

the influence of the osteogenic supplements was removed. These findings reveal possible osteoinductive properties of the S3 pattern.

The combined use of different techniques allowed us to unravel the relationships between the early and late indicators of the response of preosteoblasts to submicron surface patterns. On the most potent pattern, *i.e.*, the S3 pattern, the initial work of adhesion and the area of focal adhesion sites (vinculin) were upregulated, which in turn increased the elastic modulus of the cells by stretching actin stress fibers in all directions (Figure 4.6e). As a result, the highest amount of OPN expression was observed (Figure 4.6e). Thus, the quantitative and systematic approach used in our study suggests that the earlier markers related to the adhesion phase (*e.g.*, adhesion strength, cell mechanical properties) may be useful for predicting the osteogenic potential of patterned biomaterials.

The geometry and spacing of the submicron and nanopillars are known to influence the extracellular proteins expressed by preosteoblasts [198]. At the submicron scale, we observed that the tall and dense submicron pillars were the most potent physical stimuli to alter the response and function of preosteoblast cells. Furthermore, the roughness of the osteogenic pattern identified in our study is in the range of the roughness values (150 nm - 450 nm) that have been found in the literature to enhance the osteogenic differentiation of osteoblasts and MSCs [199, 200].

In addition to the surface design, the substrate stiffness can influence the response of cells. It is known that in soft materials like hydrogels, a higher stiffness is needed to favor osteogenic differentiation in hMSC and preosteoblasts [201, 202]. On the other hand, the scale of surface topographies affects osteogenic differentiation on very stiff substrates, such as titanium. For example, at the nanoscale, short titania pillar (around 15 nm in height) have been found to be effective for the mineralization of MSCs [191]. At the submicron scale, roughness values around 150 nm - 450 nm have been shown to stimulate the adhesion and osteogenesis of osteoblasts and MSCs [199, 200]. By comparison, macroscale roughness (1050 nm) tend to attenuate the osteogenic mineralization of MSCs [199] and the formation of focal adhesions in osteoblasts ($R_a = 2.190 - 3.400 \mu\text{m}$) [203]. Substrate stiffness and topographies can induce intracellular tension by promoting the polymerization of actin and increasing actomyosin forces [204, 205]. Increasing the stiffness of the substrate activates RhoA/ROCK signaling pathways, leading to the enhanced osteogenesis of hMSCs [205, 206].

The presence of stretch and tension in the osteoblast cytoskeleton leads to the activation of the mechanocoupling phase [197] and is a messenger of the mechanotransduction process [207]. A direct mechanotransduction pathway may be activated by the S3 pattern via integrin clustering, followed by signal transduction through the cytoskeleton elements toward the nucleus where mechanoactuators activate the mechanosensitive genes. These mechanotransduction pathways include kinase pathways that involve the phosphorylation of kinase proteins, such as focal adhesion kinase (FAK) and subsequent upregulation of late osteogenic markers, such as OPN gene in preosteoblasts [197, 208]. Further research is required to gain insights into the mechanotransduction pathways activated by such a patterned surface.

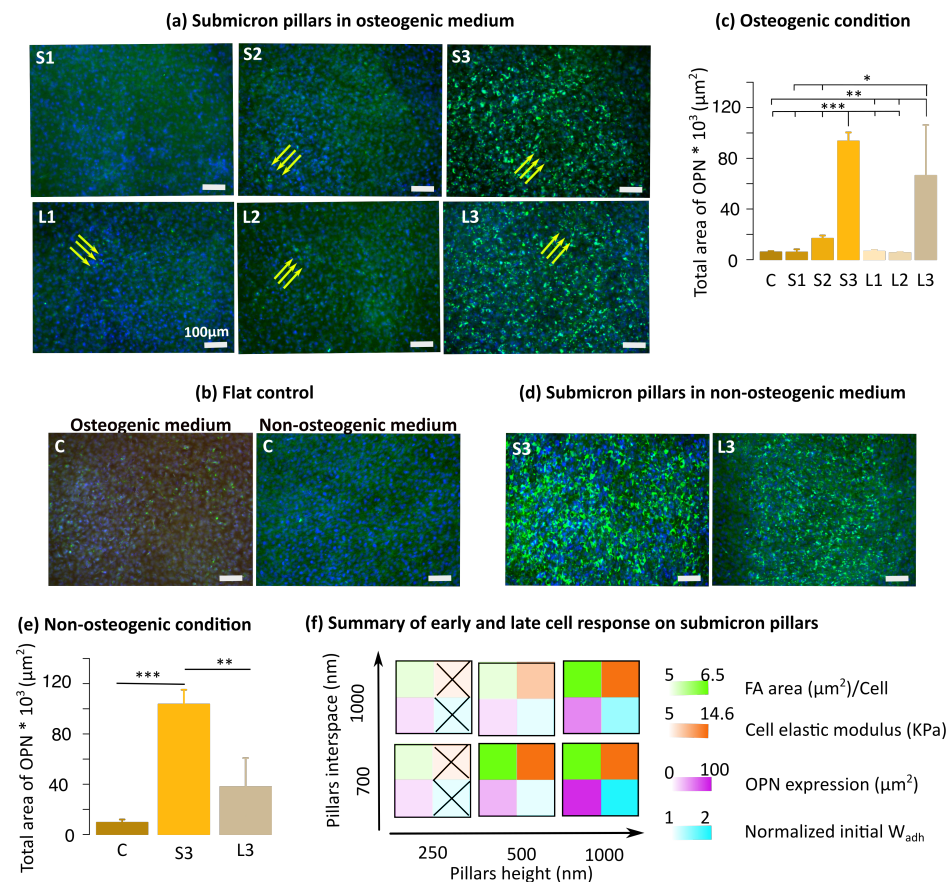


Figure 4.6: OPN expression in the MC3T3-E1 matrix after 21 days of culture. The experiments were performed under both osteogenic (a, c) and non-osteogenic (d, e) conditions. (b) expression of OPN on the flat control in both osteogenic and non-osteogenic media. (f) The response of the preosteoblast cells as a function of the height and interspacing of the pillars s (* $p < 0.05$, ** $p < 0.01$, *** $p < 0.001$).

4.4. Conclusions

We performed a systematic study on the effects of the design parameters of 3D printed submicron pillars on the response of preosteoblasts from initial adhesion to the formation of the extracellular matrix. This included single-cell measurement of the adhesion parameters (*i.e.*, adhesion force and work of adhesion), a study of cell morphology and cytoskeletal organization, mapping of the elastic modulus within individual cells, and expression of late osteogenic markers (*i.e.*, OPN). The adhesion of cells and subsequent formation of FAs were positively modulated by

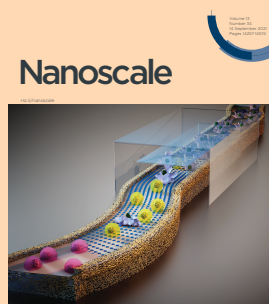
the surface topography only when the pillars were tall and dense enough, in which case the cells settled onto the surface in the “top state”. Furthermore, the cells interacting with tall and dense pillars were characterized by numerous thick actin stress fibers in the perinuclear region and upregulation of OPN. Our findings reveal previously undocumented mechanistic pathways through which submicron pillars with specific geometries and spatial organizations initiate a cascade of events that regulate the cell response starting from initial adhesion and continuing all the way to matrix mineralization. These findings pave the way towards the discovery of early and quantifiable markers capable of predicting the osteogenic potential of biomaterials. This improved understanding of how the design parameters of submicron pillars influence the bone tissue regeneration process could inform the future designs of instructive surfaces, thereby enhancing the osseointegration of future orthopedic implants.

5

3D Printed Submicron Patterns Orchestrate the Response of Macrophages

The surface topography of engineered extracellular matrices is one of the most important physical cues regulating the phenotypic polarization of macrophages. However, not much is known about the ways through which submicron (*i.e.*, 100–1000 nm) topographies modulate the polarization of macrophages. In the context of bone tissue regeneration, it is well established that this range of topographies stimulates the osteogenic differentiation of stem cells. Since the immune response affects the bone tissue regeneration process, the immunomodulatory consequences of submicron patterns should be studied prior to their clinical application. Here, we 3D printed submicron pillars (using two-photon polymerization technique) with different heights and interspacings to perform the first ever systematic study of such effects. Among the studied patterns, the highest degree of elongation was observed for the cells cultured on those with the tallest and densest pillars. After 3 days of culture with inflammatory stimuli (LPS/IFN- γ), sparsely decorated surfaces inhibited the expression of the pro-inflammatory cellular marker CCR7 as compared to day 1 and to the other patterns. Furthermore, sufficiently tall pillars polarized the M1 macrophages towards a pro-healing (M2) phenotype, as suggested by the expression of CD206 within the first 3 days. As some of the studied patterns are known to be osteogenic, the osteoimmunomodulatory capacity of the patterns should be further studied to optimize their bone tissue regeneration performance.

Published as: Nouri-Goushki, Mahdiyeh, *et al.*, "3D Printed Submicron Patterns Orchestrate the Response of Macrophages", *Nanoscale*, 2021, 13, 14304-14315, <https://doi.org/10.1039/D1NR01557E>.



5.1. Introduction

The successful integration of the biomaterials within their host tissues is mediated by immune responses [209, 210]. The core regulators of the immune responses are macrophages, which play a major role in host defense and bone tissue healing [211, 212]. The behavior of these cells is known to be modulated by soluble factors existing in the microenvironment of the host tissue [213]. In the presence of inflammatory substances, macrophages are activated towards their pro-inflammatory (M1) phenotype to defend the host against pathogens and inflammation [214]. In contrast, pro-healing factors actuate the M2 phenotype by expressing wound healing cytokines, contributing to tissue repair [215]. While the effects of soluble factors on macrophage polarization have been studied before, the mechanisms through which the physical cues of biomaterials influence macrophage polarization remain largely elusive [216].

Among physical cues, those associated with the surface topography of implants are known to be capable of eliciting a favorable immune response [37, 217]. Other studies have shown that the features of implant surfaces affect the trade-off between M1/M2 phenotypic polarization at the early stages of bone formation [218, 219]. Topographies that prolonged the expression of the M1 cytokines caused chronic inflammation while a timely switch to the M2 phenotype promoted the osseointegration of the implant [218–222]. Recent studies suggest that submicron and nanoscale topographies could better regulate the pro-healing response than microscale topographies [223–225] since the size of the receptor of cells is in the nanoscale range [226]. However, the role of the dimensions of submicron (100 – 1000 nm) features on the polarization states of macrophages remains poorly understood. That is partially due to the difficulties associated with the fabrication of surfaces with precise micro-/nanoscale surface ornaments. Advanced micro- and nanofabrication techniques, such as 3D nanoprinting (*e.g.*, two-photon polymerization (2PP) [40, 125], electron beam induced deposition (EBID) [227]), and lithography-based techniques (*e.g.*, electron beam lithography (EBL) [228], nanoimprint lithography (NIL) [229], and focused ion beam lithography (FIBL) [230]), that have been relatively recently applied for biomedical applications [210], have offered a path forward.

The study of the effects of submicron and nanoscale topographies on modulating the immune response is often performed with the ultimate aim of enhancing osteogenesis [14, 231]. The osteoimmune response triggered by disordered patterns [29], pores [232], tubular motifs [233], and groove-like [234] features have, therefore, been investigated both *in vivo* [233] and *in vitro* [29, 232, 234]. For example, titanium implants covered with semispherical nanoprotusions (diameter: 80 nm, interspacing: 165 nm) fabricated by colloidal lithography are found to hinder the initial inflammatory cytokines and enhance the osteogenic response *in vivo* [235]. However, there is still a lack of information on whether pillar arrays in the submicron range (*i.e.*, 100 nm - 1000 nm) promote osteoimmune responses. In fact, submicron pillars with a diameter of 200 - 300 nm and an interspacing of 450 - 700 nm (fabricated by NIL and 2PP) are shown to upregulate the osteogenic response of human adipose-derived stem cells (hADSCs) *in vivo* [236] and

preosteoblast cells *in vitro* [237] without any osteogenic supplements. However, systematic studies that reveal the effects of the design parameters of submicron patterns on the immune response they elicit remain unavailable.

Here, we used an advanced 3D nanoprinting technique (*i.e.*, two-photon polymerization) to comprehensively study the effects of the height and spacing of submicron pillars on the immune response they cause. The cytokines secreted by a variety of cells in response to infection or tissue damage [238] can influence the response of macrophages and activate certain signaling pathways [238, 239]. The role of such cytokines in modulating the (osteo)immune response triggered by submicron patterns have not been studied before. To bridge this knowledge gap, we investigated the morphology and polarization of murine-derived macrophages interacting with 6 different types of submicron patterns in the presence of M1-inducing stimuli at multiple time points. Moreover, we explored whether the proposed submicron pillars dimensions can modulate the polarization M1 macrophages towards a more favorable pro-healing phenotype. This study was performed to examine the immunomodulatory potential of the osteogenic pillars that we have reported recently [237], thereby portraying a more complete picture of the osteoimmunomodulatory potential of submicron patterns.

5.2. Materials and methods

5.2.1. Fabrication of the patterns

Six different patterns of submicron pillars (diameter = 250 nm, heights = 250, 500, 1000 nm, and interspacing = 700, 1000 nm) were designed in a computer aided design (CAD) program and were imported into Photonic Professional GT machine (Nanoscribe, Germany) according to a previously described method [40]. A laser power of 14% and a scanning speed of 1200 $\mu\text{m/s}$ were applied to print the patterns atop a borosilicate coverslip substrate (Thermo Fisher Scientific, US) using the IP-L780 resin (Nanoscribe, Germany). The samples were then developed for 25 min in propylene glycol monomethyl ether acetate (PGMEA) (Sigma-Aldrich, Germany), rinsed with isopropyl alcohol (IPA) (Sigma-Aldrich, Germany) for 5 min, and dried with an air-blowing gun. We categorized the patterns (with a printed area of $500 \times 500 \mu\text{m}^2$) into two groups (*i.e.*, “S” and “L”). The interspaces between the pillars in groups S and L were 700 nm and 1000 nm, respectively. Each group contained patterns with 3 different heights (*i.e.*, S1= 250 nm, S2= 500 nm, S3 = 1000 nm). In all experiments, we used non-patterned borosilicate coverslip as the control group.

5.2.2. Characterization of the patterns

The homogeneity of the patterns was evaluated with an optical microscope (Keyence Digital Microscope VHX-6000, USA). The histograms of the optical images of the printed areas were extracted using ImageJ (<http://rsb.info.nih.gov/ij/index.html>). The coefficient of variation (CV) of pixel intensity, which is defined as the standard deviation divided by the mean pixel intensity for each histogram

was calculated to evaluate the uniformity of the patterns. A full geometrical characterization of the patterns was performed using scanning electron microscopy (SEM) (Helios Nano Lab 650, FEI, USA). The specimens were gold-sputtered (coating thickness ≈ 5 nm) using a gold-coater (JFC-1300, JEOL, Japan). The images of the specimens were acquired with a tilt angle of 30° . The images were further processed in ImageJ to determine the height and diameter of the pillars (36 - 45 pillars originating from 3 different samples were analyzed for each pattern type).

5.2.3. Cell culture conditions

A concentration of 7×10^5 cells/mL Murine macrophages (at passage 15, J774A.1, Merck KGaA, Germany) were cultured in 75 cm^2 flasks (Greiner Bio-One GmbH, Austria) with 20 mL of the Dulbecco's Modified Eagle's medium (DMEM: 10% (v/v) fetal bovine serum and 1% of penicillin-streptomycin, ThermoFisher Scientific, US) and were incubated at 37°C and 5.0% CO_2 . After 3 days of culture, the cells were centrifuged and seeded onto the experimental substrates at a concentration of 5×10^4 cells/mL. The medium was refreshed every two to three days.

One day after the seeding of the cells onto the surfaces, the morphologies of the cells residing on the substrate were investigated with SEM. Towards that end, the DMEM culture medium was discarded, the specimens were rinsed twice with PBS, and were consequently fixated in a 4% (v/v) formaldehyde/PBS solution (PFA, Sigma-Aldrich, Germany) at room temperature for 15 min. The specimens were then rinsed with distilled water for 5 min and were incubated with 50%, 70%, and 96% ethanol (Sigma-Aldrich, Germany) solutions for 15 min, 20 min, and 20 min, respectively. The specimens were then allowed to dry overnight at room temperature, were gold-sputtered for 40 s, and were imaged with SEM.

5.2.4. Cell viability

The viability of macrophages was investigated using a live/dead assay (ThermoFisher Scientific, US). After 48 h of seeding, the cells were rinsed with phosphate-buffered saline (PBS) 10x, PBS 1x, and were incubated in a mixture of $0.1 \mu\text{L}/\text{mL}$ Calcein acetoxymethyl (AM)/PBS, and $1.5 \mu\text{L}/\text{mL}$ Ethidium homodimer 1 (EthD-1)/PBS. After 30 min, the solution was replaced with PBS and the cells were imaged with a fluorescent microscope (ZOE Fluorescent Cell Imager, BioRad, US). EthD-1 dye (in red) binds to the DNA of the cells with a disrupted membrane, while calcein AM binds to the cellular membrane and can be transported inside living cells where it becomes green fluorescent after the acetoxymethyl is hydrolyzed by intracellular esterases (according to the ThermoFisher guideline).

5.2.5. Seeding cells on the patterns with inflammatory cytokines

The control groups and patterned substrates were first sterilized with 70% ethanol followed by rinsing with PBS. Next, a concentration of 5×10^4 cells/mL was seeded onto the samples, and the cells were incubated in DMEM (37 °C, 5% CO_2). After 6 h of incubation, a concentration of 100 ng/mL of lipopolysaccharide (LPS, Sigma-Aldrich, Germany) and 10 ng/mL of interferon gamma (IFN- γ , Sigma-Aldrich, Germany) were added to the culture medium. The samples were immunostained on days 1 and 3, followed by imaging with a confocal microscope (ZEISS LSM 900, Germany).

5.2.6. M1/M2 macrophages controls

A concentration of 5×10^5 cells/mL macrophages (at passage 15) were cultured in 6 well-plate on control samples and were incubated at 37 °C, 5% CO_2 in DMEM. The medium was refreshed after 3 days. The cells were stimulated towards the M1 phenotype through the addition of 100 ng/mL LPS and 10 ng/mL of IFN- γ to the culture medium for 72 h. For the M2 stimulation, the same cell seeding procedure was performed and 10 ng/mL of IL-4 (Sigma-Aldrich, Germany) was added to the culture medium for 72 h before immunostaining analysis.

5.2.7. Immunoassay of IL-10

The expression of mouse interleukin 10 (IL-10) by M0, M1 and M2 cells was measured using a Victor X3 microplate reader (PerkinElmer, Groningen, The Netherlands). We followed the protocol provided by Abcam company (SimpleStep ELISA kit, Abcam, UK). Briefly, after centrifugation, the culture media of (non)activated cells was diluted with a 50x cell extraction enhancer solution to reach a 1x solution. 50 μ L of the 1x supernatant was then incubated with 50 μ L mixture of mouse IL-10 antibodies (“Capture” and “Detector”) for 1 h at room temperature. Thereafter, the wells were washed three times with 340 μ L of 1x wash buffer (PT, abcam, UK) and 100 μ L development solution was then added to each well and incubated on a plate shaker (400 rpm) at room temperature. After 10 min, 100 μ L of “Stop” solution was added to each well and the OD was measured at 450 nm.

5.2.8. Griess assay of NO

The secretion of nitric oxide (NO) was measured according to the protocol provided in the Griess reagent kit (Abcam, US). Briefly, the culture media of (non)activated cells was collected and centrifuged for 5 min. 100 μ L of the supernatant was added to each well and then mixed with 100 μ L reaction. The microplate was incubated for 10 min at room temperature. Then, the absorbance of wells was read at the wavelength of 540 nm using the same Victor X3 microplate reader.

5.2.9. Culturing of M1 stimulated macrophages on the patterns

A similar M1 stimulation protocol (described above) was performed in 75 cm² flask. A concentration of 7×10^5 cells/mL macrophages (at passage 15) were cultured in flasks with 20 mL of DMEM and were incubated at 37 °C, 5% CO₂, followed by the addition of 100 ng/mL of LPS and 10 ng/mL of IFN- γ to the culture medium and incubation for another 72 h. Three days before immunostaining, the M1 stimulated cells were seeded on the patterned and control specimens at a concentration of 5×10^5 cells/mL.

5.2.10. Immunofluorescence imaging

The specimens were washed twice with PBS and were then fixated with a 4% (v/v) formaldehyde solution for 15 min at room temperature. After another washing step with PBS, the macrophages were permeabilized through the addition of 0.5% Triton/PBS (Sigma-Aldrich, Germany) for 15 min at 4 °C. The membrane of the cells was blocked with 1% bovine serum albumin (BSA)/PBS (Sigma-Aldrich, Germany) for 5 min at 37 °C. Next, the specimens were overnight incubated (at 4 °C) in a mixture of the primary antibodies C-C chemokine receptor type 7 (CCR7) and the macrophage mannose receptor (CD206) (both 1:100 in 1% BSA/PBS, Abcam, UK). After 3 times of rinsing with 0.5% Tween/PBS, the samples were incubated in the secondary antibodies Alexa-Fluor 488 (1:50 in 1% BSA/PBS, ThermoFisher Scientific, US) and Alexa-Fluor 594 (1:150 in 1% BSA/PBS, ThermoFisher Scientific, US) for 1 h at room temperature. Finally, the specimens were washed with PBS and were mounted on microscope glass slides with 10 μ L of Prolong gold (containing 4,6-diamidino-2-phenylindole (DAPI), Life Technologies, USA). The imaging of stained cells was performed using a confocal microscope (ZEISS LSM 900, Germany).

5.2.11. Image analysis

We used ImageJ to analyze the cell area, degree of elongation (*DE*), and expression levels of the biomarkers. The fluorescent images were split into single-colored channels, and the grayscale images were analyzed to quantify the data, as described in our previous studies [40, 237]. Here, *DE* was calculated as the ratios of the major to the minor axes of the ellipses fitted to single cells. Between 86 - 303 cells were analyzed per experimental group ($n = 4$). The mean fluorescent intensity of the biomarkers was quantified for at least 15 cells on day 1 and 50 cells on day 3 within a fixed area of $500 \times 500 \mu\text{m}^2$. Cell clusters were neglected in all evaluations.

5.2.12. Statistical analysis

The data are presented as mean \pm standard deviation (SD). Depending on the number of the experimental groups being compared, either the Wilcoxon test or one-way ANOVA followed by the Tukey's post-hoc analysis were used (software: R, significance threshold: $p < 0.05$).

5.3. Results

5.3.1. Characterization of the patterns

5.3.1.1. Microscopic characterization

The microscopic visualization of the patterned surfaces showed different pixel intensities among specimens (Figure 5.1a, b). The mean pixel intensity of the patterned areas decreased as the height and density of the pillars increased (Figure 5.1b, Table 5.1), leading to darker images. The CV was $< 10\%$ for all the patterned surfaces (Table 5.1), indicating the high accuracy and uniformity of the printed pillars. The dimensions of the pillars were quantified by analyzing the captured SEM images (Figure 5.1 c, d, e). A slight variation ($SD \approx 24$ nm) in the diameter of the pillars was observed as compared to the designed value (250 nm) (Figure 5.1d), which could be attributed to the slight fluctuations in the laser power that the resin receives during the printing process. This laser power fluctuation led to a slight variation in the height of the pillars compared to design value (Figure 5.1e).

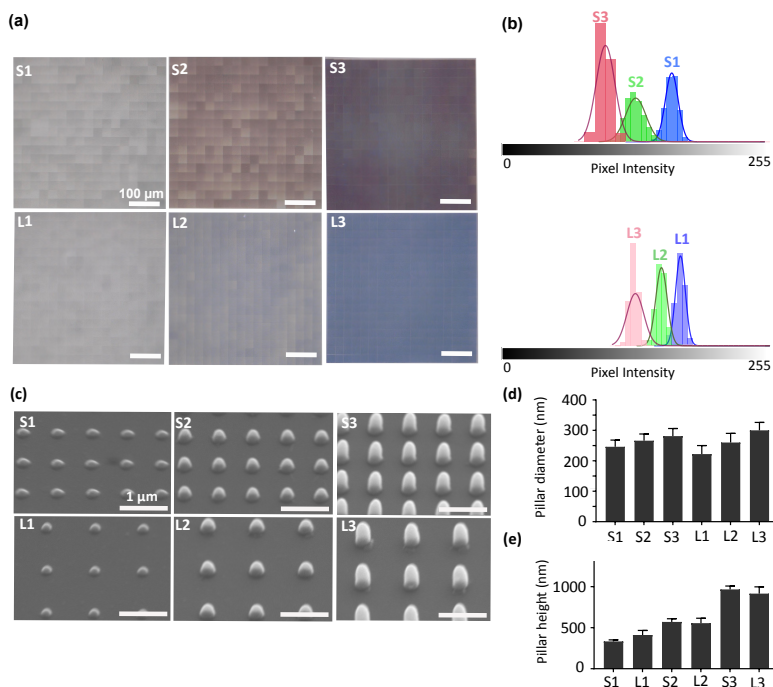


Figure 5.1: The characterization of the submicron pillars. (a) The optical microscopy images of the patterned area showing the uniformity of the printed pillars. (b) The histograms of the pixel intensity values obtained from the optical images. (c) The SEM images of the 6 different types of patterns studied here. (d) The quantified values of the diameter and (e) height of the pillars.

Table 5.1: The uniformity of the printed area is reported by the mean and coefficient of variation (CV) in the pixel intensity of the optical images.

Groups	Mean pixel intensity	CV (%)
S1	165 ±6	4
S2	130 ±10	8
S3	100 ±9	9
L1	168 ±5	3
L2	150 ±6	4
L3	124 ±8	7

5.3.1.2. Cytocompatibility

The live/dead fluorescence microscopy images of the J774A.1 macrophages cultured on the control (non-patterned glass) and patterned surfaces (S2) (Figure 5.2a, b) showed that the cells were alive after 48 h of culture on both control and patterned surfaces. Moreover, the cells were colonized close to the center and edges of the patterned area, showing the cellular interaction and migration of cells on the patterns and confirming the cytocompatibility of the IP-L780 material for this specific cell type.

5.3.2. Macrophages morphology on submicron pillars with(out) inflammatory cytokines

Two types of macrophage shapes (*i.e.*, round and polarized) were observed on both the control and patterned surfaces after 1 day of culture (Figure 5.2c, d) in the absence of inflammatory cytokines. Furthermore, on the control specimens, the cells appeared well-spread with numerous long cytoplasmic extensions (Figure 5.2c) whereas on the patterned surfaces, they were shrunk, with short membrane protrusions attached to the pillars, indicative of a more tense state (Figure 5.2d). The average area of the cells residing on the different types of specimens was around 281 - 417 μm^2 . Furthermore, the largest cells with an average area of $\approx 400 \mu\text{m}^2$ were mainly observed on the denser pillars (S2, S3) (Figure 5.2e). The *DE* of the cells cultured on different patterned surfaces was between 1.6 – 2.6. Within 1 day, the cells residing on the tallest and densest pillars (S3) appeared to be significantly more elongated ($DE \approx 2.6$) as compared to the cells present on the other types of patterned and control surfaces (Figure 5.2f).

In the presence of M1 stimulators, the same mix of cell shapes, namely round and polarized, were observed on all the patterns and the control surfaces. Also, no difference in cell area and degree of elongation was observed between different patterns (Figure 5.2g, h). However, the area of the cells residing on the L2 ($473 \pm 256 \mu\text{m}^2$) and L3 ($612.5 \pm 225 \mu\text{m}^2$) patterns was significantly higher as

compared with the area of the cells on the control specimens ($338 \pm 157 \mu\text{m}^2$) (Figure 5.2g).

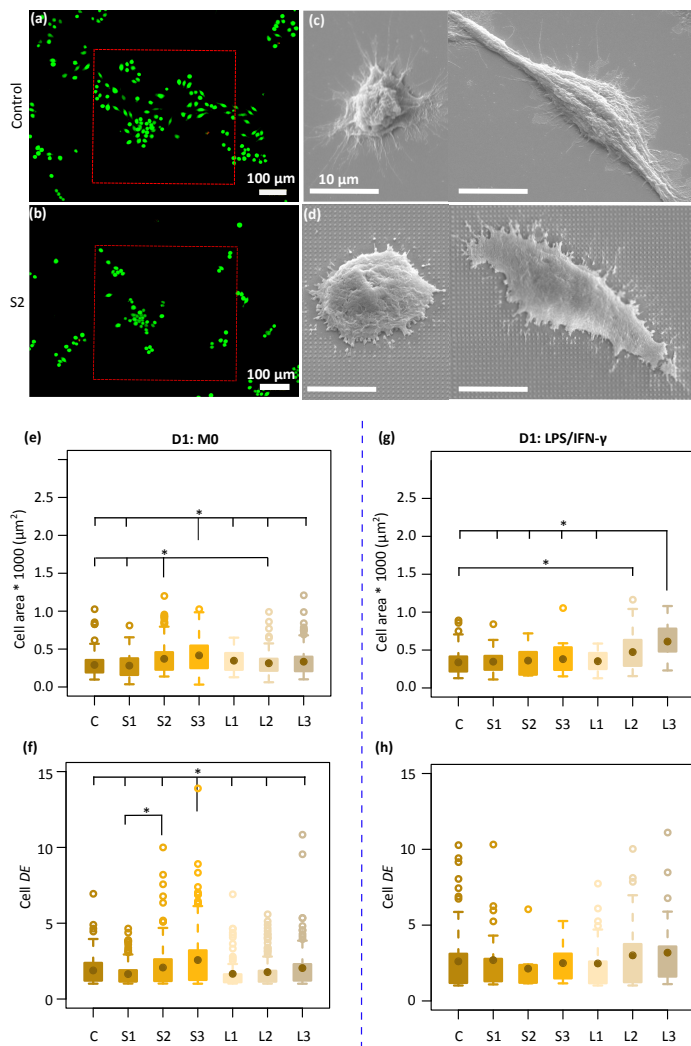


Figure 5.2: Cell viability and morphology on the patterned surfaces. The live/dead staining of J774A.1 cells after 2 days of culture on the (a) control and (b) a representative patterned specimen (S2). The SEM images of the cell-surface interaction: the different types of cell morphology (M0) observed after 1 day on (c) a control specimen and (d) a representative patterned surface (S2). The quantification area of (e) non-treated and (g) LPS/IFN- γ treated cells residing on the control and patterned surfaces after 1 day of culture. The quantification of cell elongation (*DE*) for (f) non-treated and (h) LPS/IFN- γ treated macrophages on the control and patterned surfaces after 1 day of culture (* $p < 0.05$).

5.3.3. Macrophage polarization on submicron pillars

We first analyzed the effect of cytokines, LPS/IFN- γ (for M1 phenotype), and IL-4 (for M2 phenotype) on the polarization and morphology of macrophages cultured on the control specimens (Figure 5.3a-f). After three days, the activation of M1 cells was examined by a pro-inflammatory (M1) surface marker, CCR7 and secretion of NO (Figure 5.3a, b). A considerable amount of NO was expressed by M1 cells (Figure 5.3b), showing the presence of an inflammatory microenvironment [240]. On the other hand, the orange color in M2 cells (Figure 5.3a) showed both CCR7 and CD206 markers (the latter being representative of pro-healing (M2) phenotype). To check the activation of M2 cells, we have measured the expression of an M2-prohealing cytokine, interleukin-10 (IL-10). IL-10 was significantly upregulated in the M2 cells (Figure 5.3c), indicating the anti-inflammatory microenvironment [241]. After 3 days of stimulation, the morphology of the cells stimulated to the M1 phenotype (referred to as the M1 cells) was markedly different from that of the cells stimulated to the M2 phenotype (referred to as the M2 cells) (Figure 5.3a, d, e). M1 cells exhibited an elongated ($DE \approx 3.3 \pm 2$) and spread morphology with a significantly larger area ($\approx 3133 \pm 1667 \mu\text{m}^2$) (Figure 5.3a, d, e) than the M2 cells, which were rounder ($DE \approx 1.8 \pm 0.8$) and smaller in area ($\approx 398 \pm 157 \mu\text{m}^2$) (Figure 5.3a, d, e). The polarization state of the cells on the flat control surfaces was evaluated on day 1 and day 3 using the CCR7 and CD206 surface markers (Figure 5.3f). The cells stimulated with LPS/IFN- γ secreted noticeably higher levels of CCR7 on day 3 as compared to day 1 (Figure 5.3f). However, the expression of CD206 was relatively low on both days and did not change over time (Figure 5.3f).

After 1 day of cell culture on the patterned surfaces without any inflammatory cytokines, the expression of CCR7 was significantly enhanced with the height of the pillars but not with their interspacing, indicating that pillars taller than 500 nm (S2, S3, L2, L3) tend to stimulate the pro-inflammatory phenotype (Figure 5.3g). In comparison, the expression of CD206 remained at the same level on the various patterned surfaces and was lower than the control specimens (Figure 5.3j). By the addition of the LPS/IFN- γ to the culture medium, both markers seem to be downregulated after day 1 (Figure 5.3h, k). When comparing different patterns, for CCR7 (Figure 5.3h), the effects of pillar height was still present but the interspacing also showed an effect on the expression of CCR7. More specifically, the taller pillars with a larger interspacing (L2, L3) significantly promoted the expression of CCR7 relative to the corresponding denser patterns (S2, S3), indicating a pro-inflammatory response induced by these patterns in the presence of inflammatory stimuli (Figure 5.3h).

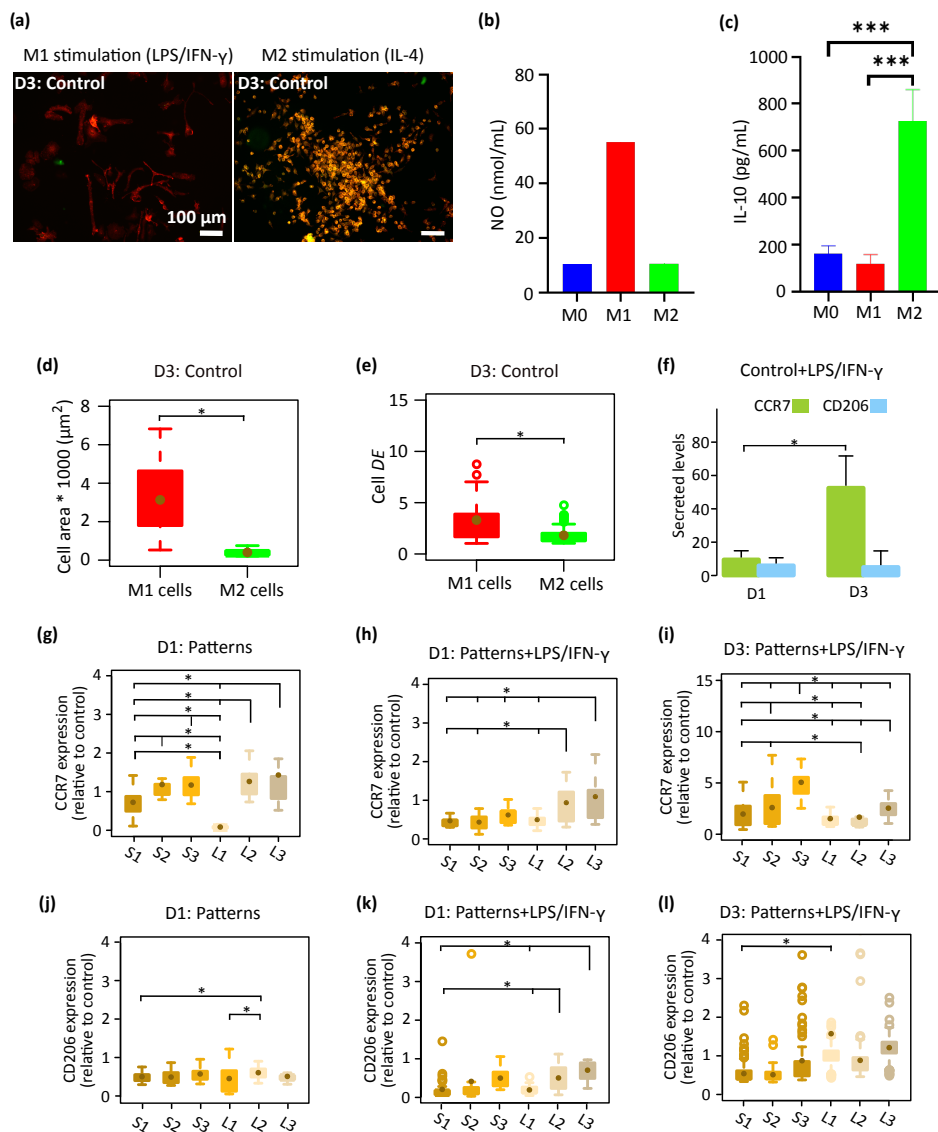


Figure 5.3: (a) The immunofluorescent images of LPS/IFN- γ and IL-4 treated macrophages stained for CCR7 (M1 phenotype in red) and CD206 (M2 phenotype in green) after 3 days of culture on the control substrate. (b, c) Expression of NO and IL-10 in M0, M1, and M2 activated cells. (d) The area and (e) elongation degree (*DE*) of M1 and M2 stimulated cells after 3 days of culture on the control surface. (f) Secreted markers in LPS/IFN- γ treated cells after 1 and 3 days of culture on the control surface. The expression level of (g) CCR7 and (j) CD206 in macrophages cultured on the patterned surfaces for 1 day (relative to cells cultured on the control surface). (h, i) The expression level of CCR7 and (k, l) CD206 in LPS/IFN- γ treated cells cultured on the patterned surfaces for 1 and 3 days, respectively. (relative to cells residing on the control surface) (* $p < 0.05$).

Increasing the time of cell culture to 3 days in the presence of LPS/IFN- γ (Figure 5.3i and 3l) changed the expression levels of the two markers. Thus, for the CCR7 the trend reversed as the levels increased on S1-S3 patterns relative to day 1 while on L1-L3 patterns the levels were not really changing with time. This finding indicates the potential of the L1-L3 patterns to inhibit the M1 polarization of macrophages with time (Figure 5.3i). In such an inflammatory environment, an insignificant difference in the amount of CD206 was observed between cells that resided on different submicron pillars (Figure 5.3l). A statistically significant difference was observed between L1 and S1 patterns.

In summary, during the 3 days of culture in medium containing pro-inflammatory stimuli (LPS/IFN- γ) the pillars with a height of 500 and 1000 nm, and an interspacing of 1000 nm (L2, L3) inhibited the expression of CCR7 M1 marker and promoted the M2 CD206 marker by the macrophages. By comparison, the corresponding denser patterns (S2 and S3) stimulated the expression of both markers during the 3 days of culture.

5.3.4. Morphology and polarization of M1 macrophages on submicron pillars

To better delineate the effects of the patterns on macrophage polarization, the starting cells were first stimulated to M1 and then cultured on the patterns and the control surfaces for 3 days (Figure 5.4a). The average area of the cells cultured on the patterned surfaces and control specimens was in the range of 280 - 560 μm^2 (Figure 5.4b). Furthermore, a wider distribution of the cell area was observed on the patterns with a larger interspace (L series) (Figure 5.4b). Moreover, the average *DE* of the cells residing on different patterned surfaces and control samples was in the same range (*i.e.*, 1.4 - 2), indicating two types of cell shapes (*i.e.*, round and polarized) on the different surfaces. Furthermore, both surface phenotype markers (*i.e.*, CCR7 and CD206) were expressed in both populations: CCR7 (in red) was observed at the boundary of the cells while CD206 (in green) was detected at the center of the cells and around the nucleus (Figure 5.4a). The fluorescence signal of CCR7 remained similar across all the experimental groups, which was almost twice as much as the control specimens (Figure 5.4d). The expression of the M2 marker (CD206) was also upregulated in the macrophages cultured on all six types of patterned substrates as compared to the control specimens but more differences were observed between the various patterns. The height of the pillars was correlated with the levels of the CD206 expression by the cells cultured on the densely patterned surfaces (*i.e.*, S series). The interspacing of the higher pillars did not change the expression level of CD206 (Figure 5.4e). For example, similar levels of CD206 expression were observed on (S2 and L2) and (S3 and L3). In summary, these results indicated that the patterns modulated the polarization of M1 macrophages after 3 days of culture and that the effective sizes for the height and interspacing of submicron pillars to promote the polarization of M1 macrophages towards a prohealing M2 phenotype are 500 and 1000 nm, and 700 and 1000 nm, respectively.

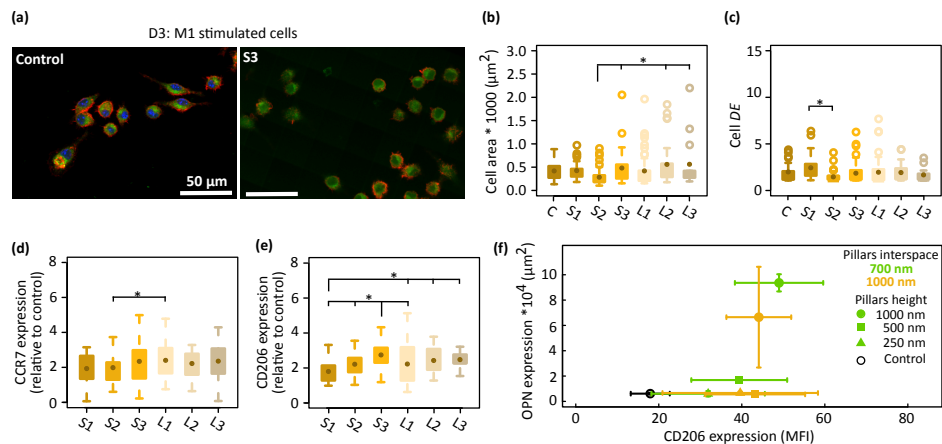


Figure 5.4: (a) The fluorescent images of immunostained M1 stimulated macrophages for CCR7 (red) and CD206 (green) after 3 days of culture on the control and a representative pattern (S3). (b) The cell area and (c) degree of elongation (DE) of the M1 cells cultured on patterned and control surfaces. The expression level of (d) CCR7 and (e) CD206 in the M1 cells cultured on patterned surfaces for 3 days (relative to the control surfaces). (f) The expression of OPN in preosteoblasts after 21 days of culture on the patterns [32] and that of CD206 in M1 cells residing on the patterned surfaces for 3 days. The averaged mean fluorescence intensity (MFI) of the CD206 is reported (* $p < 0.05$).

5.4. Discussion

In the *in vivo* microenvironment of tissues, cytokines can be secreted naturally by a variety of cells in response to infection or cellular damage [238]. For example, the type II activated murine macrophages secretes IL-4 [242], and human macrophages produces IFN- α [243]. These cytokines are known to manipulate the macrophages morphology and activation through binding to cell receptors and consequently transducing signals to the nucleus [238, 239]. Studying the role of submicron pillars on the macrophage phenotype in the presence of the critical cytokines mediators is of crucial importance and has not been investigated before.

Although the effects of surface topography on the behavior of macrophages have been extensively studied in the literature, there is limited information on how surface topographies modulate both the osteogenic and immune responses. Most current topographies are being assessed only for one cell type, either immune [218, 221, 224] or osteogenic [226]. A potent physical cue should be capable of modulating immunogenic response without affecting the osteogenic activity but rather promoting it. In the context of osteoimmunomodulatory biomaterials, mainly macrophage conditioned medium was used for osteoblasts differentiation [244]. However, both macrophages and osteoblast are in direct contact with the biomaterials *in vivo*.

We systematically studied the role of the design parameters of 3D printed submicron pillars on the morphology and polarization of macrophages in different testing conditions: 1. in the presence of inflammatory stimuli added in the medium and 2. using M1 phenotype cells. When macrophages were cultured with LPS/IFN- γ (inflammatory stimuli) on the control specimens, a longer culture time (3 days) was required for an effective polarization towards M1 (a pro-inflammatory response) (Figure 5.3f). Moreover, the M1 phenotype was associated with a highly elongated and more spread shape, which is in line with the observations reported in previous studies [245]. The same transition time point (*i.e.*, 3 days) was observed for the cells cultured on submicron pillars in the presence of LPS/IFN- γ . In this condition, cells residing on the shortest pillars (L1) expressed higher CD206 relative to the ones settling on the corresponding pattern with smaller interspace (S1) (Figure 5.3l). Although the expression of CD206 on the other patterns did not change significantly after 3 days of culture with LPS/IFN- γ (Figure 5.3l), the pillars with a larger interspacing (*i.e.*, L series) inhibited the secretion of the M1 marker in the presence of inflammatory stimuli (Figure 5.3i). Interestingly, when M1 macrophages were cultured on submicron pillars (Figure 5.4), the polarization towards the M2 phenotype was stimulated by the tallest pillars (S3, L3) (Figure 5.4e), while no visible changes in the area and elongation of the cells residing on different patterned surfaces were observed (Figure 5.4c). A possible reason might be the increase in the surface hydrophilicity with increasing the height of the pillars which we observed in our previous study [237]. Surface hydrophilicity steers the polarization of the macrophages towards an anti-inflammatory response by mediating the adsorption of fibronectin and fibrinogen proteins [246]. Macrophages adhered on a hydrophilic surface interact with the absorbed fibronectin through integrin $\beta 1$ which in turn enhances the phosphorylation levels of phosphoinositide 3-kinase (PI3K) and serine/threonine kinase (Akt) and consequently enhances the secretion of anti-inflammatory cytokines and M2 surface markers (*e.g.*, CD206) [246, 247].

In a previous study [32], we evaluated the expression of OPN on the same 6 patterned surfaces. We found that taller and denser pillars (S3) stimulate the expression of OPN in both osteogenic and non-osteogenic conditions. Our results, here, reveal the role of interspacing in suppressing the pro-inflammatory phenotype of macrophages in the presence of LPS/IFN- γ (potent patterns: L2 and L3 patterns) as well as the role of the pillar height in promoting the polarization of M1 macrophages towards a pro-healing phenotype (potent patterns: S3, L3). Therefore, in the submicron range, sufficiently tall pillars could have osteoimmunomodulatory properties (Figure 5.4f).

Unraveling the role of ECM topographies in the polarization of macrophages has motivated researchers to use patterning techniques for the development of ECM-mimicking implant surfaces. The surface topography of implants influences the adhesive interactions [51], cell morphology [52, 53] and gene expression [54-56] of the cells that come into contact with them. The type and dimensions of surface features play a crucial role in modulating the response of both immune (*e.g.*, monocytes and macrophages) [57] and bone (*e.g.*, osteoblasts and osteoclasts) cells [58] existing in the tissue microenvironment. Submicron-/nanofeatures are

known to more effectively influence the response of cells as compared to microfeatures. That is often attributed to their size, which is closer to the cell receptors [11, 26]. Given the fact that multiple cell types are present in the extracellular microenvironment and that they respond differently to topographies as well as existing cytokines in their surroundings, it is crucial to precisely control and carefully optimize the dimensions of micro-/nanofeatures present on implant surfaces [26].

5.5. Conclusions

For the first time, we investigated the effects of the height (250 – 1000 nm) and interspacing (700 nm, 1000 nm) of 3D printed submicron pillars on the response of murine macrophages (J77A.1) in the presence of soluble inflammatory factors (LPS/IFN- γ). Driven by the advances in nanofabrication techniques, we produced submicron pillars with high accuracy in a single-step procedure. The cytocompatibility of the material from which the patterns were made was confirmed in our experiments. Both round and elongated cells were observed on the patterned and control surfaces. The M1-stimulated cells were significantly larger in their area and degree of elongation than the M2-stimulated cells. Furthermore, the proposed submicron pillars modulated the macrophage responses even in the presence of LPS/IFN- γ . In this condition, the patterns effects also changed over time: on day 1, pillars with a higher (lower) pillar density impeded (boosted) the expression of the pro-inflammatory marker, while opposite results were observed on day 3. Moreover, in the absence of inflammatory solubles, the tallest pillars with higher pillar densities encouraged a switch of M1 macrophages to the pro-healing M2 phenotype after 3 days and improved the osteogenic activity of preosteoblast cells. This work provides the basis for future exploration of the osteoimmunomodulatory phenomena that are associated with submicron topographies and are of relevance for the development of orthopedic implants.

6

Osteoimmunomodulatory Potential of 3D Printed Submicron Patterns Assessed in a Direct Co-culture Model

Modulation of the immune response following the implantation of biomaterials can have beneficial effects on bone regeneration. This involves complex interactions between the inflammatory and osteogenic cells. Therefore, the study of cell-cell interactions using direct co-culture models integrated with biomaterials is of great interest. In this chapter we studied the viability, morphology, and osteogenic activity of preosteoblasts (OBs) co-cultured with pro-inflammatory macrophages (M1s) on the (non)patterned surfaces. OBs and M1s remained alive and proliferated actively for 14 days in the mixture of DMEM and α -MEM (1:1), regardless of the cell ratio in the co-cultures. The spatial organization of the two types of cells changed with the time of culture from an initially uniform cell distribution to the formation of a thick sheet of OBs covered by clusters of M1s. On day 7, the expression of PGE2 and TNF- α were upregulated in the co-culture relative to the mono-culture of OBs and M1s. The inflammation decreased the differentiation and matrix mineralization of OBs after 28 days of culture. Interestingly, the incorporation of 3D printed submicron pillars into the direct co-culture model enhanced the differentiation of preosteoblasts, as revealed by relatively higher RUNX2 expression. Our findings highlight the importance of direct co-culture models and the role of submicron patterns in the osteoimmunomodulation process.

Under review: Nouri-Goushki, Mahdiyeh, *et al.* "Osteoimmunomodulatory Potential of 3D Printed Submicron Patterns Assessed in a Direct Co-culture Model"

6.1. Introduction

Upon implantation, biomaterials invariably elicit an inflammatory response. The properties of the implanted biomaterials may affect the type, severity, and evolution of the inflammatory response [248]. Recently, there has been increasing evidence suggesting that biomaterials can actively modulate the response of inflammatory cells with potentially favorable effects on osteogenesis [249]. Such an osteoimmunomodulatory (OIM) process involves complex surface-cell and cell-cell interactions that require suitable *in vitro* cell culture models to be studied [248].

Among the various kinds of cells involved in OIM, macrophages play a major role. Since both pro-inflammatory (M1) and pro-healing (M2) phenotypes can be observed in macrophages, a timely M1-to-M2 switch is required to prevent acute inflammation and promote tissue healing [249]. The specific molecules secreted by M1/M2 macrophages, such as transforming growth factor β (TGF- β), prostaglandin E2 (PGE2), and tumor necrosis factor α (TNF- α) can influence the fate of bone cells [249]. TNF- α has been shown to hinder the differentiation of preosteoblast cells (OBs) by binding to TNF- α receptors in OBs [250] and suppressing the level bone morphogenetic protein 2 (BMP2) [251, 252]. Furthermore, a high concentration of TNF- α in conditioned medium (CM) is reported to enhance the production of PGE2 in preosteoblasts, thereby promoting bone resorption [253]. At physiological concentrations, however, the matrix mineralization by mesenchymal stromal cells (MSCs) has been shown to be upregulated in the presence of four inflammatory cytokines, namely TNF- α , IFN- γ , IL-17, and TGF- β [254]. Under such physiological conditions, TNF- α activates the NF- κ B pathway, consequently promoting the expression of osteogenic proteins, such as BMP2 and ALP [11, 254–256]. The influences of inflammatory cytokines on bone regeneration are, therefore, sensitive to both dose and time [254]. Unraveling the landscape of such dependencies requires co-culture models that are geared towards the study of such OIM responses.

Indirect and direct co-culture models are currently being used to study OIM [257]. In indirect co-culture models, either the target cells are exposed to the conditioned media of the other cell type [213] or a barrier, such as a membrane [258], hydrogel [259], or transwell systems [260], is used to physically separate the different cell types [29, 213]. This type of models have been most widely used due to their simplicity and effectiveness in studying paracrine signaling pathways [213]. Indirect co-culture models, however, exclude any direct communications between different cell types. Furthermore, it is difficult to reproduce the concentration of secreted factors in the conditioned medium [29, 257]. In direct co-culture models, different cell types can be seeded simultaneously or in sequence [257]. Direct co-culture models can, therefore, more closely resemble the *in vivo* conditions. Nevertheless, distinguishing the function of each cell type is more complicated in such models and the distributions of all cell types need to be controlled [257].

Direct co-culture studies of the interactions between macrophages and (pre)osteoblasts/MSCs in the presence of biomaterials are currently very limited [261, 262]. In one such study, the adhesion of osteoblasts on the titania surface is found to be inhibited in direct co-culture with macrophages [262]. The same study

found that titania surfaces coated with non-mulberry silk fibroin enhance the mineralization of osteoblasts and reduce the expression of the inflammatory cytokine TNF- α in macrophages [262]. Surface topographies can provide physical cues that have been found to affect the paracrine interactions of MSCs with macrophages [261]. For example, MSCs seeded on microporous topographies ($2 \mu\text{m} < \text{pores diameter} < 25 \mu\text{m}$) have been shown to promote the level of anti-inflammatory cytokines (IL-10) in macrophages and attenuate the activity of bone resorption mediators [261]. However, the effects of 3D printed submicron pillars on the osteogenic differentiation of preosteoblasts directly co-cultured with macrophages have not been studied yet. In this chapter, we first established a direct co-culture model and used it to investigate the interactions between murine M1 macrophages (J774A.1) and murine preosteoblasts (MC3T3-E1) at various cell ratios and over different culturing times. The direct co-culture model was then applied to study the influences of 3D printed submicron pillars on both types of cells.

6.2. Materials and methods

6.2.1. Cell preculture

6.2.1.1. Macrophages preculture and polarization

Murine macrophages (J774A.1, passage 15, Merck KGaA, Germany) were incubated in 75 cm^2 flasks ($1 \times 10^4 \text{ cells/cm}^2$) (Greiner Bio-One GmbH, Austria) containing 10 mL Dulbecco's Modified Eagle's medium (DMEM: 10% (v/v) fetal bovine serum and 1% penicillin-streptomycin, ThermoFisher Scientific, US). The culture medium was refreshed every 2-3 days until the cells reached confluency. Confluent cells, at a density of around $1 \times 10^5 \text{ cells/cm}^2$, were stimulated towards the pro-inflammatory phenotype (M1s) by the addition of 100 ng/mL LPS (Sigma-Aldrich, Germany) and 10 ng/mL IFN- γ (Sigma-Aldrich, Germany) for 3 days [263]. Polarization towards anti-inflammatory cells (M2s) was stimulated by adding 10 ng/mL IL-4 (Sigma-Aldrich, Germany) for 3 days [263]. Next, (non)polarized macrophages were scraped and seeded alone or with OBs on the substrates. Day 3 of M1 polarization is considered as day 0 in experiments that the M1 cells co-cultured with osteoblasts. Unstimulated macrophages (M0) (Figure 6.1a) were used as a control group.

6.2.1.2. Preosteoblasts preculture

Murine preosteoblasts MC3T3-E1 (OBs; passage 13) were incubated in a 25 cm^2 culture flask ($5 \times 10^3 \text{ cells/cm}^2$) in alpha Minimum Essential Medium (α MEM; ThermoFisher Scientific, US) without ascorbic acid (AA) but supplemented with 10% FBS and 1% pen-strep. The culture medium was refreshed every 2-3 days until confluency was reached. Next, the osteoblasts were trypsinized and seeded alone or with macrophages subsets.

6.2.2. Direct co-culture of macrophages and OBs

Co-cultures of OBs and M1s at the ratio of 1:1 (CO11) and at the ratio of 1:2 (CO12) were studied in a direct co-culture system. For CO11 co-cultures, 5×10^3 cells/cm² of OBs were mixed with 5×10^3 cells/cm² M1s and seeded simultaneously in a 48-well plate in mixed medium (α MEM: DMEM (1:1), 10% FBS, and 1% pen-strep). The cells were incubated at 37 °C and 5% CO₂. For the CO12 co-cultures, 5×10^3 cells/cm² OBs were mixed with 10^4 cells/cm² M1s and were cultured in α MEM:DMEM (1:1) under similar conditions. As controls, M0s, M1s, M2s, and OBs (5×10^3 cells/cm²) were seeded in the mixed medium. After 2 days, the mixed medium was supplemented with 50 μ g/mL AA (Sigma-Aldrich, Germany) and 4 mM β -Glycerolphosphate (β -GL; Sigma-Aldrich, Germany) to induce osteogenic differentiation. The culture medium was refreshed every 2-3 days until day 14.

6.2.3. Direct co-culture of M1s and OBs on the patterned surfaces

6.2.3.1. 3D printing of submicron pillars

A Nanoscribe Photonic Professional GT laser lithography system (Nanoscribe, Germany) working on the basis of two-photon polymerization was used to fabricate the patterns. The general writing language (GWL) file of the designed pillars (diameter = 300 nm, height = 500 nm, and interspacing = 700 nm) was prepared as previously described [40, 125, 237]. A curable acrylate-based photosensitive resin, namely IP-L780, was polymerized under the exposure of an infrared laser beam, and submicron pillars were fabricated using a previously described protocol [263]. After polymerization, the samples were immersed in propylene glycol monomethyl ether acetate (PGMEA) (Sigma-Aldrich, Germany) for 25 min followed by 5 min rinsing with isopropyl alcohol (IPA) (Sigma-Aldrich, Germany) and blow-drying with air.

The dimensions of the pillars was characterized by scanning electron microscopy (SEM) (Helios Nano Lab 650, FEI, USA). A gold-coater (JFC-1300, JEOL, Japan) was used to sputter a thin layer of gold (layer thickness \approx 5 nm) on the specimens before imaging.

6.2.3.2. Cell seeding on the submicron pillars

The patterned samples were disinfected with 70% ethanol (Sigma-Aldrich, Germany) followed by rinsing twice with 1x phosphate-buffered saline (PBS) (ThermoFisher Scientific, US). OBs and CO12 co-cultures were prepared as mentioned earlier and were seeded on the sterile patterned substrates (referred to as OBp and CO12p hereafter) and non-patterned control surfaces (referred to as OB and CO12 hereafter). In the mono-cultures, 5×10^3 cells/cm² of OBs were seeded on the patterned and control surfaces. In the co-cultures, 5×10^3 cells/cm² OBs and 1×10^4 cells/cm² M1s were cultured on the specimens. A mixed medium

of α MEM:DMEM (1:1, supplemented with AA and β -GL) was used, which was refreshed every 2-3 days.

6.2.4. Cytokines profile

The secretion of cytokines by the macrophages (M0s, M1s, and M2s) in response to the stimulating factors and preosteoblast cells were measured using a VICTOR X3 Multimode Plate Reader (PerkinElmer, Groningen, The Netherlands) on days 0, 1, 3, and 7. The amount of TNF- α , IL-10, and PGE-2 expressed in the supernatant of cells was measured by enzyme-linked immunosorbent assay (ELISA) according to the manufacturer's protocol (Abcam, UK). A mixed culture medium was used as a control. Each experimental condition was repeated 4 times ($n = 4$).

6.2.5. Cells viability

The viability of cells in both mono and co-culture conditions was measured by a LIVE/DEAD™ Viability/Cytotoxicity Kit (ThermoFisher Scientific, US) on days 3, 7, 10, and 14. In short, 48-well plates containing mono- and co-culture cells were retrieved from the incubator and were washed with 1x PBS (ThermoFisher Scientific, US) and 1x PBS. Next, a live/dead solution of 2 μ M calcein AM and 3 μ M EthD diluted in PBS were added to the OB, CO11, and CO12 cultures. For M0s, M1s, and M2s, a live/dead solution of 0.8 μ M calcein AM and 3 μ M EthD was used. The samples were incubated at 37 °C for 30 min. Subsequently, the solution was discarded and was replaced by 1x PBS. Fluorescent images were taken with a ZOE Fluorescent Cell Imager (BioRad, US) at 5 random locations. For each condition, four different samples were analyzed ($n = 4$).

6.2.6. Osteogenic and mineralization markers

6.2.6.1. RUNX2 staining

The effects of the M1 cells and patterned surfaces on the osteogenic of preosteoblasts were assessed using Runt-related transcription factor (RUNX2) and alkaline phosphatase (ALP) assays. For RUNX2, the cells were washed twice with 1x PBS and were fixed with 4% paraformaldehyde (PFA; Sigma-Aldrich, Germany) for 15 min at room temperature. After rinsing twice with 1x PBS, the cells were permeabilized with 0.5% Triton/PBS (Sigma-Aldrich, Germany) for 5 min at 4 °C and then blocked with 1% bovine serum albumin in PBS (BSA/PBS; Sigma-Aldrich, Germany) for 5 min at 37 °C. Primary rabbit RUNX2 antibody (Abcam, UK) was diluted in BSA/PBS (1:250) and was added to the wells. After 1 hour incubation at 37 °C, the cells were rinsed 3 times with 0.5% Tween/PBS (Sigma-Aldrich, Germany). Alexa 488 donkey anti-rabbit (ThermoFisher Scientific, US) was added to the wells as a secondary antibody in 1% BSA/PBS (1:200), which were then incubated for 1 hour at room temperature. Subsequently, the cells were washed 3 times with 0.5% Tween/PBS (Sigma-Aldrich, Germany) and

once with 1x PBS. The samples were fixed on a glass slide using Prolong gold antifade reagent (containing 4,6-diamidino-2-phenylindole (DAPI); ThermoFisher Scientific, US). Fluorescent images were taken using a ZOE Fluorescent Cell Imager (BioRad, US) at 5 random locations of each sample. For each condition, two different specimens were analyzed (n=2).

6.2.6.2. ALP activity

The analysis was performed according to the manufacturer's instruction kit (ALP Assay Fluoremetric kit, Abcam, UK). Briefly, 100 μ L culture supernatant was collected on days 7, 11, 14, 21, and 28 and was added to a 96-well plate (n = 4/group). The mixed medium was considered as a control sample. Next, 20 μ L of the ALP enzyme solution was added to the standard wells; 20 μ L of the ALP reaction mixture (2 μ L of 5mM non-fluorescent 4-methylumbelliferyl phosphate disodium (MUP) + 18 μ L ALP assay buffer) was added to the specimens and incubated for 30 min at 25 °C. Next, the stop solution was added to all the samples. After thorough mixing, the fluorescent absorbance was read (Ex/Em = 360/440 nm) using a VICTOR X3 Multimode Plate Reader (PerkinElmer, Groningen, The Netherlands).

6.2.6.3. Alizarin red staining

After 28 days of culture, the samples were washed twice with 1x PBS and were fixed with 4% paraformaldehyde (PFA; Sigma-Aldrich, Germany) for 15 min at room temperature. Next, the cells were washed twice with distilled water. A 2% Alizarin Red S/PBS solution was added to the specimens, which were then shaken with a thermal shake Lite plate shaker (VWR, USA) at 300 rpm for 20 minutes. Next, the cells were washed 5 times with distilled water on a plate shaker at 300 rpm for 5 min. At last, the specimens were dried at room temperature and were imaged with a WIFI digital microscope (Rotek, China) at five random locations for each specimen. The average mineralized area (%) was reported (n=4).

6.2.7. Image analysis

Image processing was performed using the open-source software FIJI (<https://imagej.net/software/fiji/downloads>). For counting live and dead cells, the living cells were selected by thresholding the green fluorescent images. The threshold was altered to fit all the green-stained cells present. The remaining part of the image was then segmented using the "watershed" function. Finally, all the particles bigger than the smallest cell present in the image were counted. The dead cells were counted by applying the same method to the red fluorescent images.

RUNX2 expression was quantified as the sum of the green fluorescence intensity in the cells present in a fixed area ($234.4 \times 234.4 \mu\text{m}^2$). Firstly, the cells were selected using the same thresholding method as the one applied to the live/dead images. Secondly, the intensity of the green marker was measured within each cell. Finally, the results of all the cells were summed up to obtain the total amount of RUNX2 expression in the area. The mean and standard deviation

(SD) of the 5 random images were included in the graph. For all the images, the background noise was measured as well. The mean value of the background noise was subsequently subtracted from the measured values. In order to quantify the mineralized area, the bright field images were color thresholded in Fiji (HUE= 0-30, Saturation, 0-255, Brightness 0-255).

6.2.8. Statistical analysis

Data are reported as mean \pm (SD). One-way ANOVA using the Sidak's multiple comparisons test was performed in GraphPad Prism version 8.0.1 for Windows (GraphPad Software, USA) to analyze the differences between mono- and co-cultures. For the tests with multiple conditions at multiple days, two-way ANOVA was used followed by the Sidak's multiple comparisons test. Probability values < 0.05 were assumed statistically significant. The outliers in the ELISA results were removed using the ROUT test with $Q = 1\%$.

6.3. Results and discussion

6.3.1. Macrophage activation

After 3 days of macrophage polarization, elongated and flatter morphologies were mainly observed for the M1 cells while the M2 cells were less polarized (Figure 6.1a). Similar morphologies of activated cells have been observed before [263, 264]. The expressions of TNF- α , PGE2, and IL-10 were measured in the (non)activated macrophages. The M1 cells expressed significantly higher levels of TNF- α and PGE2, confirming the pro-inflammatory phenotype of the M1 cells (Figure 6.1b, c) [265]. As expected, IL-10 was predominantly expressed in the M2 cells, which is in agreement with their pro-healing state (Figure 6.1d) [266].

6.3.2. Direct co-culture of M1 macrophages and MC3T3-E1 cells

The viability of M0, M1, M2, OB in mono-culture and of the OB-M1 in co-cultures (OB:M1= 1:1 1:2, Table 6.1) was very high and constant during the entire 14-days period of incubation, indicating that the proposed mixed culture medium provided the needed nutrients for both cell types (Figure 6.2a, b). Finding a suitable culture medium is essential in the direct co-culture models. Depending on the type, origin, and ratio of the (pre)osteoblasts and macrophages, different types of media have been used in previous studies [267–269]. For example, a mixture of α -MEM and RPMI 1640 (ratio 1:1) was applied for the direct co-culture of MC3T3-E1 preosteoblasts and murine bone marrow M1, followed by IL-4 treatment [267, 268]. On the other hand, in indirect co-cultures, the conditioned medium of macrophages seeded on the biomaterials was used to analyze its effect on bone cells [270]. However, reproducing the desired level of cytokines in the conditioned medium is problematic at the first step. It requires further dilution with a medium suitable for other cell types at the second step, leading to a

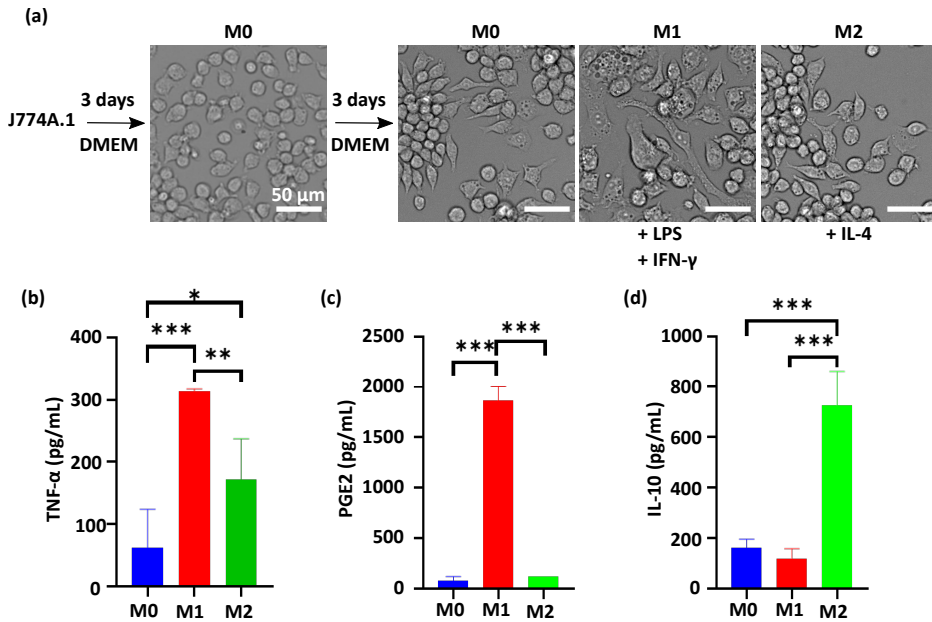


Figure 6.1: Macrophages subsets. (a) Stimulation of macrophages (M0) to M1 and M2. Expression of (b) TNF- α , (c) PGE2, and (d) IL-10 in macrophages subsets (* $p < 0.05$, ** $p < 0.01$, *** $p < 0.001$).

prolonged *in vitro* procedure [249]. On the other hand, the advantage of an indirect model is the flexibility it offers regarding the origin of preosteoblasts and immune cells. By comparison, cells should be from the same species in direct co-cultures to prevent unwanted immune reactions that are caused by xenogeneic cells [14].

After 3 days in mono-cultures, the preosteoblasts adopted a fully spread morphology whereas the M1 cells seemed to show a mixture of M1 and M2 morphologies in their colonies (Figure 6.2c). In the co-cultures (CO11 and CO12), the preosteoblasts and the macrophages were clearly distinguishable and seemed to nicely co-exist. Both M1- and M2-like morphologies were observed with macrophages appearing smaller and thicker than the preosteoblasts (Figure 6.2c). After 10 days of culture, thick and dense layers of cells were visible in all the cultures. The macrophages formed clusters of cells. In the co-cultures, they were present mostly on top of the preosteoblast cell layer. These results are in line with the live/dead data, indicating the ability of both cell types to proliferate in the co-culture conditions of this study.

Due to the different types of macrophage morphology observed and the high cell density, recognizing the dominant phenotype of macrophages was not feasible. Therefore, we further analyzed the inflammatory cytokines in the culture media.

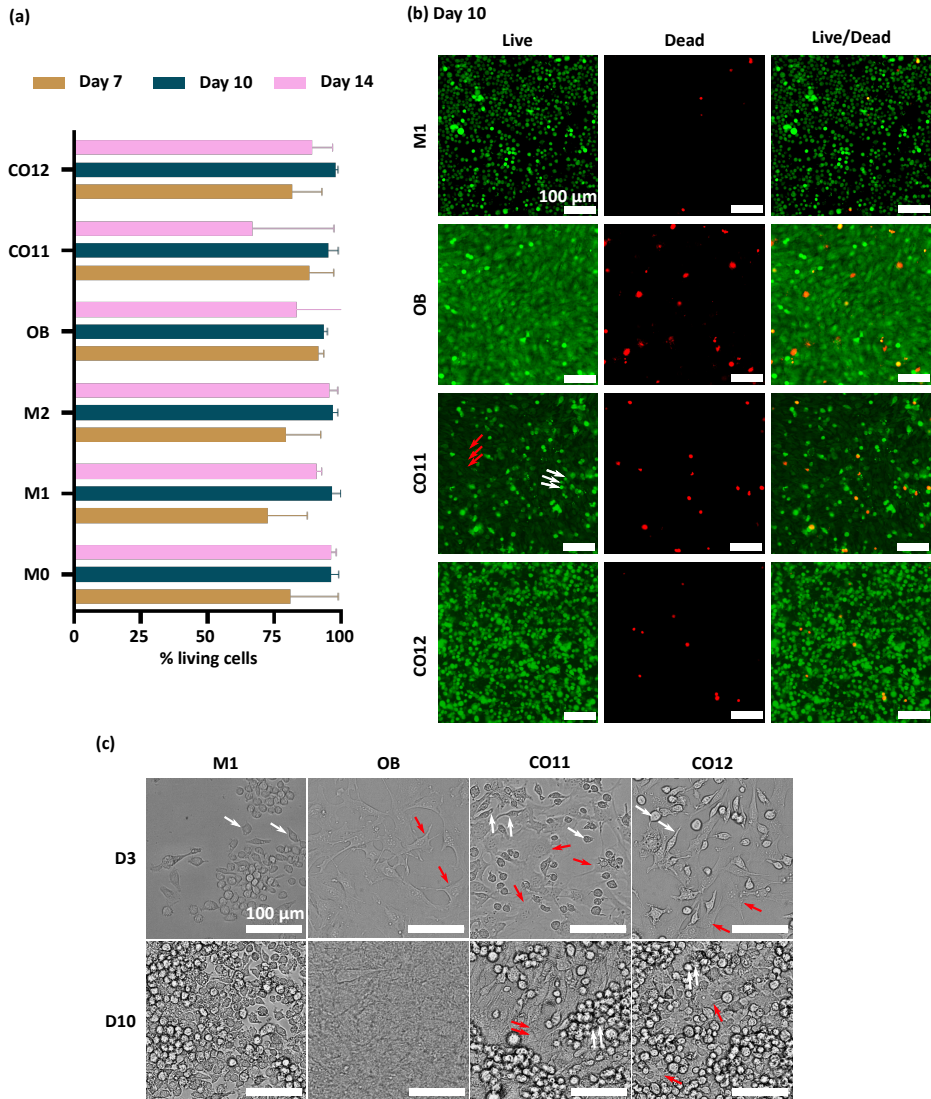


Figure 6.2: Cell viability and proliferation in the mono and direct co-cultures. (a) percentage of living cells on days 7, 10, and 14. (b) Live/dead staining of M1s and OBs in the mono and co-cultures (CO11 and CO12) after 10 days of culture. (c) Morphological arrangement of OBs and M1s after 3 and 10 days of seeding. White and red arrows indicate M1 and OB cells respectively (* $p < 0.05$, ** $p < 0.01$, *** $p < 0.001$).

6.3.2.1. Inflammatory response

The pro- and anti-inflammatory cytokines secreted in the mono- and co-cultures were measured to determine whether the M1 macrophages retained their phenotype. At 1 and 3 days after seeding, the expression of TNF- α was similar in mono- and co-cultures (Figure 6.3a), which was threefold lower than the amount of TNF- α expressed by the M1 cells on day 0 (*i.e.*, day 3 of M1 polarization presented in Figure 6.1b). Furthermore, the amounts of IL-10 expressed on days 1 and 3 (Figure 6.3b) in all culture conditions were comparable with the levels produced by the M0 cells on day 0 (Figure 6.1d), suggesting that M1 cells switched their phenotype to M0 during the first 3 days of culture. This transition from M1 to M0 phenotype that was observed in both the mono- and co-culture conditions may be related to the mechanical (scraping) stress that the cells experienced during the harvesting procedure [271]. To maintain the phenotypic stability of cells, the presence of polarization stimuli is required [266, 271]. Interestingly, after 7 days of seeding, we noted a significant boost in the expression of TNF- α in mono- and co-cultures as compared to days 1 and 3 (Figure 6.3a), verifying the continued M1 phenotype. The highest level of TNF- α was observed in the co-cultures (CO11, CO12). The concentration of IL-10 did not change during the first 7 days of culture, confirming the inflammatory conditions in co-cultures. Although inflammatory cytokines are primarily expressed by M1 cells, bone cells (*e.g.*, OBs and MSCs) are known to produce pro-inflammatory cytokines too. Here, the expression of PGE2 in OBs increased in the pro-inflammatory environment of day 7 (Figure 6.3c, a). The amount of PGE2 released in the mono-culture was highest on day 1 and then significantly dropped over time (Figure 6.3c). While the level of PGE2 in the co-culture (CO11, CO12) was high on day 1, it decreased on day 3 but then rose again on day 7 (Figure 6.3c). The high level of PGE2 on day 1 was most likely caused by the trypsinization of OBs before seeding, which could quickly stimulate the synthesis of PGE2 [272].

Table 6.1: The density of M1 and OB cells in the direct co-culture model

Groups	M1 density (#/cm ²)	OB density (#/cm ²)
M1	5×10^3	-
OB	-	5×10^3
CO11	5×10^3	5×10^3
CO12	10×10^3	5×10^3

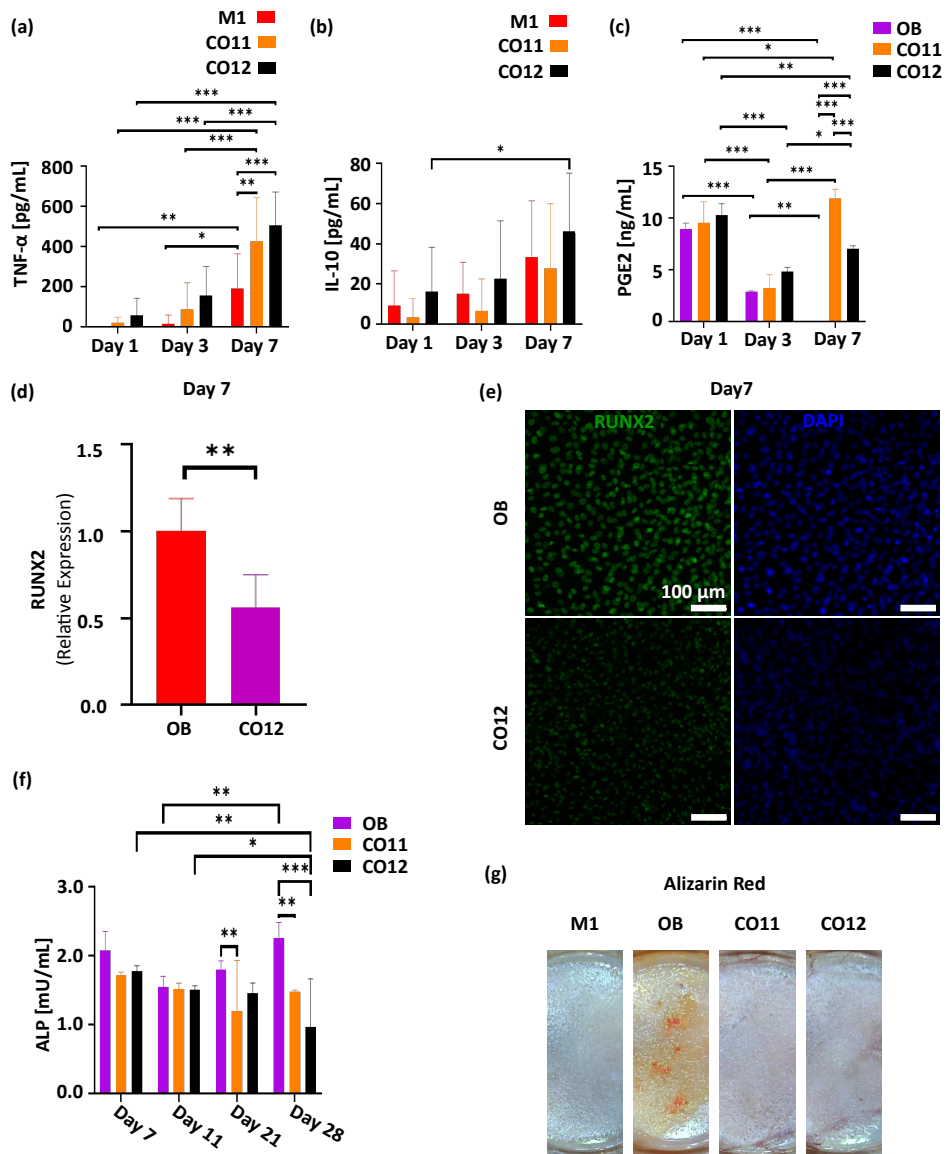


Figure 6.3: An enhancement in the inflammatory cytokines on day 7 led to a decrease in the osteoblasts' activity in the direct co-culture models. (a) Secretion of pro-inflammatory, TNF- α , (b) anti-inflammatory cytokine, IL-10, and (c) PGE2 after 1, 3, and 7 days of co-culturing OBs with M1s. (d) The expression level of RUNX2 and (e) immunostaining of RUNX2 differentiation marker in OBs co-cultured with M1s. The expression level is normalized to the expression of RUNX2 in osteoblasts in the mono-culture. (f) ALP activity and (g) mineralization of osteoblasts in mono and co-cultures over a time span of 28 days (* $p < 0.05$, ** $p < 0.01$, *** $p < 0.001$).

6.3.2.2. Osteogenic response

We assessed the impact of inflammatory cells on the osteogenic activity of pre-osteoblasts. On day 7 after seeding, the expression of RUNX2 in the mono-culture of OBs was two times higher than the one expressed in the co-culture CO12 (Figure 6.3d), indicating that the inflammatory M1 cells attenuated the differentiation of preosteoblasts. The ALP activity of OBs on days 21 and 28 was significantly higher than the level of ALP secretion in the co-cultures (Figure 6.3f). In contrast, the ALP activity of preosteoblasts on day 7 and 11 was similar in both mono- and co-cultures (Figure 6.3f). Furthermore, preosteoblasts deposited a higher amount of calcium in the mono-culture (Figure 6.3g). The reduced matrix mineralization in the co-cultures can be explained by the increased secretion of TNF- α and PGE2 after 7 days of culture. The effect of PGE2 on the activity of preosteoblasts is dependent on the concentration of TNF- α [250, 265]. At high TNF- α concentrations (*i.e.*, pro-inflammatory conditions), PGE2 stimulates the activity of osteoclasts, whereas in the presence of low concentrations of inflammatory cytokines, PGE2 enhances the proliferation of osteoblasts [250, 265]. Ideally, an M1 to M2 polarization will shift high levels of TNF-alpha towards low concentrations, and thus an improved osteogenic activity will occur accordingly. However, we did not observe the M1-M2 polarization in co-cultured samples and thus prolonged inflammatory response resulted in reduced osteogenesis in CO11 and CO12. The addition of exogenous growth factors to the culture media may be required to promote OIM [273, 274]. In the presence of biomaterials, surface modification may help in modulating the response of macrophages and osteoblasts [258, 275].

6.3.3. Modulation of OIM response via submicron pillars

We further investigated the effect of specific physical patterns on the response of both types of cells in the co-culture model established above. In our previous studies, we have extensively examined the effects of the spatial arrangement of submicron pillars on preosteoblasts [237] and macrophages [263]. Here, we studied whether submicron pillars can modulate the pro-inflammatory response observed in the co-culture towards stimulating the osteogenic response. Therefore, the growth of both cell types (CO12) on the patterned surfaces was assessed (Figure 6.4a). On day 3 of culture, both macrophages and preosteoblasts were observed on the patterned area (CO12p). M1 macrophages in the co-culture tended to migrate to the patterned surface. On day 7 of culture, a monolayer of preosteoblasts covered the patterned area and the macrophages, with a dominant round morphology (indicative of the M2 phenotype [263]), were located on top of the preosteoblast layer. The level of RUNX2 expression on day 7 was significantly upregulated on the submicron patterned surface as compared with the flat control (Figure 6.4b, c), indicating the potential of such nano-engineered surfaces to promote the differentiation of preosteoblast in inflammatory conditions possibly enabled through M1-to-M2 switching.

The main signaling pathway revealed so far in OIM biomaterials is the TLR4-NF- κ B pathway, in which toll-like receptor 4 (TLR-4) identifies the biomaterials

and nuclear factor κ B (NF- κ B) regulates the inflammation and improves bone regeneration [24]. In the monocultures, titania nanotubes (diameter \sim 78 nm) suppressed the NF- κ B pathway and reduced the inflammation in M1 macrophages (RAW 264.7) [276]. When macrophages (RAW 264.7) were co-cultured with MSCs (in transwells), titania nanotubes with a diameter of 110 nm activated the NF- κ B pathway, leading to high inflammation [277]. As a result, MSCs were actively engaged in stimulating prohealing response, leading to higher matrix mineralization and ALP activity than nanotubes of 30 nm and 70 nm diameter [277].

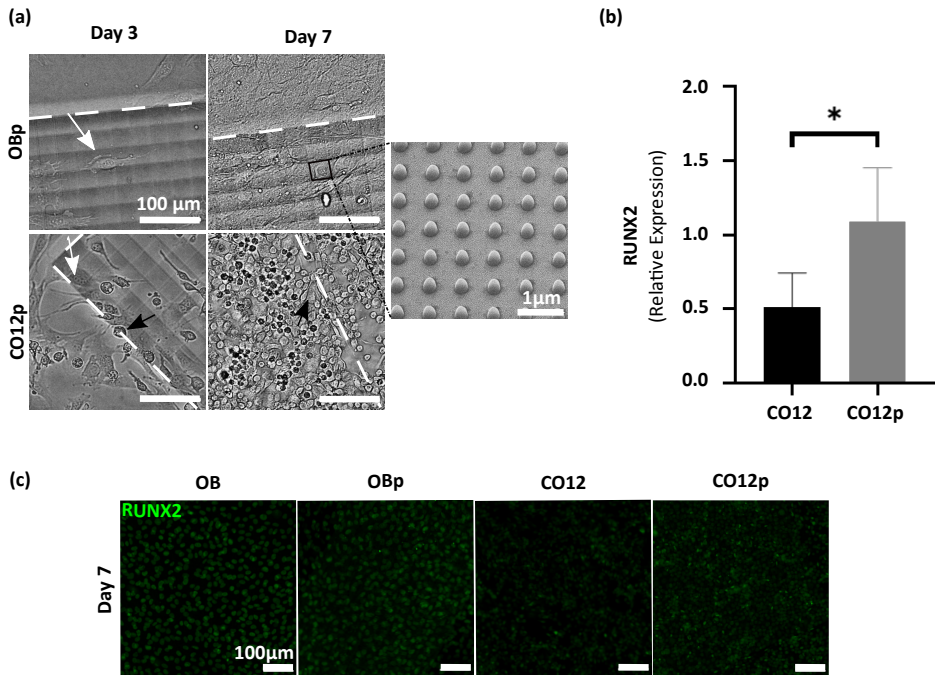


Figure 6.4: Submicron patterns upregulated the differentiation of OBs in the direct co-culture. (a) Interaction of OBs and M1s in the mono and co-cultures on the patterned and non-patterned surfaces. Black and white arrows indicate M1s and OBs, respectively. The dotted lines indicate the edge between the patterned and non-patterned area. (b) The expression level of RUNX2 in the OBs co-cultured with M1s on the non-patterned (CO12) vs. patterned (CO12p) surfaces. The expression level is normalized to the expression of RUNX2 in osteoblasts in the mono-culture. (c) Immunostained images of RUNX2 expressed in mono and co-cultures on the patterned and non-patterned substrates (* $p < 0.05$, ** $p < 0.01$, *** $p < 0.001$).

To date, the research on osteoimmunomodulatory biomaterials has been predominantly performed using indirect *in vitro* co-cultures models. This type of models facilitates assessing the paracrine effects of different cell types while neglecting the effects of direct cell-cell interactions. Using such indirect models, it

has been found that while nano-engineered topographies may promote the expression of osteogenic factors (such as BMP2/6) in macrophages, the resulting conditioned medium containing higher BMPs does not necessarily stimulate the mineralization of bone marrow-derived mesenchymal stem cells (BMSCs) [29]. Another approach for indirect co-culturing of bone and immune cells utilizes transwell systems that enable the co-culturing of two cell types by separating them via a membrane [258]. BMSCs seeded on titania nanowires in transwells have been found to decrease the level of inflammatory cytokines and polarize the M1 macrophages towards an M2 pro-healing phenotype [258]. The titania nanowires were found to activate the ROCK-mediated cyclooxygenase-2 (COX2) pathway that modulates the secretion of PGE2, thereby enhancing the osteogenic activity of the BMSCs [258].

Despite the complexity of direct co-culture models, they are essential to closely mimic the *in vivo* conditions [29]. Although mono-culture and in direct co-culture models revealed some of the mechanisms behind cells biomaterials interactions [258], the direct interaction between different cell and biomaterials should be also considered to improve the design of biomaterials for *in vivo* studies.

6.4. Conclusions

We developed a direct co-culture model incorporating bone and inflammatory cells to more closely mimic the interaction of those cell types *in vivo*. The spatial distribution of both cell types was homogeneous until day 3, while from day 7 a layered distribution was observed with preosteoblasts occupying the space underneath the macrophages. Although preosteoblasts were cultured with inflammatory M1 cells, we barely observed inflammatory cytokines in the co-culture microenvironment up until day 7, indicating the switch in polarization state from M1 to M0. On day 7, the high level of PGE2 in the inflammatory condition attenuated the preosteoblast differentiation, as revealed by a lower level of RUNX2 measured in the co-cultures as compared to the mono-culture. Consequently, the ALP activity and mineralization of preosteoblast decreased on day 28 of co-culture. The integration of submicron pillars in the co-culture system enhanced the differentiation of preosteoblasts, indicating the potential of submicron topographies in modulating the osteoimmune responses in direct co-culture models.

7

Concluding Remarks

7.1. General discussion

From tissue replacement to repair and, more recently, regeneration, the role of biomaterials is becoming increasingly complex. This is enabled by the advances in medicine and cell pathophysiology on the one hand and in materials science and engineering on the other. Particularly, multiscale fabrication and characterization methods have enabled the conception and creation of new categories of biomaterials. In orthopedics, examples include regenerative biomaterials that aim to treat large bony defects originating from severe trauma injuries, bone tumors, and non-union fractures. The other examples are the components of joint replacement implants, including those used for both primary and revision surgeries.

Given the relatively recent findings regarding the function of the immune system and stem cells in the complex process of bone regeneration, one approach to improve the performance of regenerative orthopedic biomaterials is to develop biomaterials with osteoimmunomodulatory properties. To achieve this, the surface properties of biomaterials can be harnessed, as they significantly influence the inflammation and subsequent tissue repair phases through direct interactions with relevant cells and soluble factors.

While surface chemistry is the main focus of most studies performed to date, surface topography at the submicron and nanoscales provides an alternative route for controlling the fate of stem/osteoprogenitor and inflammatory cells. The advantages of surface topography over chemical cues include better stability and control of the cell-surface interface and the fact that no extra materials are needed, meaning that there are fewer issues regarding chemical biocompatibility. Moreover, it is possible to incorporate the physical characteristics of the extracellular matrix into the surface of biomaterials. Designing topographies that can enhance bone regeneration via OIM, therefore, constitutes a new strategy that can be used both alone and in combination with surface chemistry in the development of the generations of regenerative orthopedic biomaterials. However, much research is still needed to understand how such topographies can orchestrate the response of multiple cell types before we can rationally design OIM topographies. Towards this aim, in this thesis, several challenges and research questions were addressed, including the 3D printing of submicron patterns, a study of the effects of submicron patterns on preosteoblast cells, a study of the immunomodulatory potential of submicron patterns, and an investigation of the interactions between preosteoblasts, inflammatory cells, and patterns in a direct co-culture model.

7.1.1. 3D printing of submicron patterns

Although DLW based on 2PP is amongst the most accurate 3D printing techniques for the fabrication of intricate microscale structures for a wide range of applications [124], there are several challenges that need to be addressed to further broaden its applications. These include printing highly uniform submicron and nanoscale patterns over large areas in a reasonable time and the use of materials and additives that are compatible with the designed (bio)functionality of the final product [124]. In this research, several solutions were proposed to address

these challenges in the context of the specific application at hand (*i.e.*, creating submicron pillars with controlled height, diameter, and spatial organization on sufficiently large areas to enable systematic studies with cells).

The selection of an appropriate print configuration, scanning mode, and writing parameters for the 2PP process was necessary to produce uniform and reproducible submicron patterns. We used two print configurations, namely “DiLL” and “Conventional”, and succeeded in fabricating reproducible pillars as small as 160 nm in diameter and 250 nm in height. However, the uniformity and the printing time depended on the scanning modes (*i.e.*, Galvo or Piezo). The Piezo scan mode is recommended for fabricating high-resolution structures (a positioning accuracy of around 10 nm), while the writing speed in the Galvo scanning mode (100 - 20000 $\mu\text{m/s}$ using a 63x objective) is much faster than that of the Piezo (25 - 300 $\mu\text{m/s}$).

Furthermore, the uniformity of the nanofeatures over a large surface area was highly dependent on the printing parameters in each scanning mode. When using the DiLL configuration and Piezo scanning mode, the uniformity of the print was improved by compensating for the substrate tilt and coating the glass with ITO [125]. As for the conventional configuration and the Galvo scanning mode, the area of the writing field played the dominant role in the uniformity of the patterned area. Since the tilt correction is not supported in the Galvo scanning mode, reducing the writing field to around $33\ \mu\text{m} \times 33\ \mu\text{m}$ diminished the effects of sample tilt and reduced the print time three folds (as compared to Piezo) [40].

Controlling the dimension of the pillars at the submicron range (*i.e.*, feature sizes $\leq 1\ \mu\text{m}$) is highly challenging in the 2PP technique. In the Piezo writing mode, the laser power and exposure time are the primary factors influencing the dimensions of submicron pillars. In the Galvo mode, the laser power was the most important parameter. Increasing the laser power will increase the size of the volume surrounding the focal point of the focused laser beam, where the intensity is sufficiently high to trigger two-photon polymerization. Consequently, the height and diameter of the pillars increase with the laser power, making it challenging to keep one dimension constant while varying the other one. Therefore, to control the dimensions of such small features, the fine-tuning of the printing parameters in general and the laser power, in particular, is needed. Finally, with a proper selection of the laser power (*i.e.*, $L_p \approx 14\%$ in the DiLL configuration and using the Galvo scanning mode), we successfully fabricated reproducible submicron pillars with a minimum diameter of 250 nm, a minimum interspacing of 200 nm (end to end), and a minimum height of 250 nm.

The integration of nanopillars into microfluidic chips and 3D porous structures can be used to study bone regeneration. We developed a method to create microfluidic chips decorated with submicron surface patterns which withstood flow rates of up to 8 mL/min. In addition, we succeeded in printing submicron pillars with diameters down to 200 nm and a height gradient on the surface of our microscaffolds. Shifting between the Galvo and Piezo writing strategies in a single process enabled these achievements. This approach could create 3D cellular microenvironments that are more similar to the native ECM or can provide novel surface physical cues to control cellular functions.

Our findings showed that the commercial photo-sensitive materials (*i.e.*, IP-Dip and IP-L780, containing reactive acrylate groups in their structures) are compatible with hMSCs, preosteoblasts MC3T3-E1, and murine macrophages J774A.1. Other studies coated the surfaces made from similar resins with biocompatible layers (*e.g.*, TiO_2 , collagen, and fibronectin) before cell culture [91, 92]. As the materials did not have cytotoxic effects and the geometry of the pillars are known to alter the cells' functions, in the following section, we discussed the impacts of the dimensions of the submicron pillars on the osteogenic and healing responses of bone and immune cells.

7.1.2. Modulating the response of multiple cell types by submicron patterns

7.1.2.1. Effects of submicron patterns on preosteoblasts response

Although the micro-/ nanotopographical features of biomaterials are known to influence the osteogenic response of cells, there is limited quantitative information available regarding (i) how the cell adhesion properties (*e.g.*, cell adhesion work and force) are regulated via interactions with patterns at different length scales and, (ii) whether the initial cell adhesion force promotes the osteogenic differentiation of the cells.

In this thesis (Chapter 4, [237]), we performed a systematic study to assess the effects of the height and interspacing of submicron pillars on the early response (cell morphology, mechanics, and adhesion) and the late response (osteogenic activity) of osteoblast cells.

We found a correlation between the initial phase of cell adhesion and the settling state of the cells on the patterned surfaces. While the cells residing on the S2, S3, and L3 surfaces generally only interacted with the tip of the pillars (*i.e.*, exhibited a dominant top settling state), those on the L2 surface interacted both with the pillars and the substrate (*i.e.*, exhibited a dominant bottom settling state). This is most likely caused by the spatial organization of these pillars, which enables the cells to partially occupy the space between them. Our SCFS results suggest that a similar type of cell-pattern interaction may occur during the initial adhesion phase. Assuming that cells come into contact only with the tip of the pillars when interacting with the S3 and L3 patterns, the significantly higher work of adhesion detected in the case of S3 as compared to L3 can be justified by the increase in the available surface caused by a higher areal density of the pillars. The increased density of the initial anchoring points could result in a higher density of integrin binding sites, which could give rise to a different, potentially faster FAs development process [175, 194, 278]. We did not see a considerable change in the work of adhesion of the S2 and L2 patterns. This observation, in combination with the results of the SEM analysis, indicates no direct correlation between the density of the pillars and the binding sites in the case of the S2 and L2 patterns. That is because the cells settle differently onto the surface (*i.e.*, dominant top state in the case of S2 and dominant bottom state in the case of L2).

Interestingly, the effects of topography on the initial adhesion force, FAs area,

and density were visible only on those patterns that exhibited a dominant top state (S2, S3, and L3). No significant difference in the FAs area and density as compared to the control surface was observed for the patterns with a dominant bottom state. Therefore, the patterns influenced the adhesion process and FAs development only when the contact between the cells and the pillars was concentrated around the tip of the pillars.

The shape of the cells residing on the nanopatterned substrate was monitored over time (4 h and 1 day). After 4 h of culture, the patterned surfaces did not induce any difference in the morphology of the cells. Cells adopted a round morphology with an average area of $1900 \mu\text{m}^2$, and the cortical actin networks were organized on the periphery of the cells, meaning that cells were in a non-contractile spreading phase [174]. Furthermore, the most extensive distribution of the cells' area was observed on the highest and densest pillars (S3). The cells residing on this pattern more rapidly developed their membrane extensions (mostly lamellipodia), a sign of initiating FAs maturation and forming actin stress fibers, suggesting that cells on the S3 pattern had already entered the contractile spreading phase [174].

After 1 day of culture, the cell area was more influenced by the height of the pillars and not so much by their interspacing. The smaller cells ($2100 - 2200 \mu\text{m}^2$) were settled on the taller pillars (L3, S3), indicating the effects of roughness on the cell area in the submicron range. Furthermore, among the three types of cell morphologies observed on the patterned surfaces, the stellate cells mainly resided on the denser and taller pillars (*i.e.*, S2 and S3). These cells were rich in mature FA sites (vinculin), exhibited multidirectional thick actin stress fibers, tangled up in the perinuclear area, and formed actin star sites with the highest values of the elastic modulus [188]. The observations confirm the high levels of tension and stress in the stellate cells.

The geometry and spacing of the submicron and nanopillars influence the extracellular proteins expressed by preosteoblasts [198]. At the nanoscale, shorter pillars have been reported to enhance the bone matrix nodules in hMCSs [63]. At the submicron scale, we observed an opposite trend. The tall and dense submicron pillars were the most potent physical stimuli to enhance the formation of a bone matrix protein (*i.e.*, OPN) after 21 days of cell seeding. The reason could be the tension in the cells that enhances the formation of bone matrix protein [190, 197]. In addition to the intracellular tension, we found that the initial work and force of cell adhesion could be another key factor determining whether or not a surface pattern is osteogenic. Hydrophilic surfaces cause more robust cell adhesion [153]. OPN, which is a late osteogenic marker, is therefore significantly upregulated in the cells residing on the most hydrophilic surfaces (*i.e.*, S3 and L3), which also exhibited the highest force and work of cell adhesion. The mechanism underlying these observations could be the enhancement of $\alpha_5\beta_1$ integrin at the early stage of adhesion, which regulates cell adhesion strength, and consequently activates $\alpha_v\beta_3$ integrin (which enables mechanotransduction)[163].

Substrate topographies and stiffness can induce intracellular tension by promoting the polymerization of actin and increasing actomyosin forces [204, 205]. Increasing the stiffness of the substrate activates RhoA/ROCK signaling path-

ways, leading to the enhanced osteogenesis of hMSCs [205, 206]. The presence of stretch and tension in the osteoblast cytoskeleton leads to the activation of the mechanocoupling phase and is a messenger of the mechanotransduction process [197]. The S3 pattern may activate a direct mechanotransduction pathway via integrin clustering, followed by signal transduction through the cytoskeleton elements towards the nucleus, where mechanoactuators activate the mechanosensitive genes. These mechanotransduction pathways include kinase pathways that involve the phosphorylation of kinase proteins, such as FA kinase, and the subsequent upregulation of late osteogenic markers, such as the OPN gene in pre-osteoblasts [197, 208]. Further research is required to gain insights into the mechanotransduction pathways activated by such patterned surfaces.

7.1.2.2. Effects of submicron patterns on the macrophage response (IM effects)

Although the impact of topographical features on the response of macrophages has been extensively studied in the literature, there is limited information on how surface topographies modulate both the osteogenic and immune responses. Most current topographies are being assessed only for one cell type, either immune [218, 221, 224] or osteogenic [226]. An ideal physical cue should be capable of modulating the immunogenic response while also promoting the osteogenic differentiation of stem cells.

In Chapter 5 [237], we further explored the influences of submicron pillars on the response of macrophages in two different testing conditions: **(i)** in the presence of inflammatory stimuli added to the medium and **(ii)** using M1 phenotype cells. The M1 cells were associated with a highly elongated and more spread shape, which is aligned with the observations reported in previous studies [245]. Macrophages revealed a dynamic phenotype when seeded on the patterned surface in the presence of inflammatory inducers (LPS/IFN- γ). The pro-inflammatory phenotype was first attenuated on the densely distributed pillars (S series, spacing = 700 nm) on day 1. While later (day 3), sparsely distributed pillars (interspacing = 1000 nm) inhibited the secretion of inflammatory markers. No considerable change was observed in the expression level of pro-healing cytokines CD206 on the other patterns after 3 days of cell culture with LPS/IFN- γ .

To determine the effects of patterns on the polarization of inflammatory cells, M1 activated cells were cultured on the patterns for 3 days. In this condition, the height of pillars (500 nm and 1000 nm) positively affected the transition of the M1 macrophages towards the pro-healing M2 type. Among the multiple types of patterns [14, 31, 279, 280] that were studied in terms of their osteo(immuno)modulatory properties, pillars having 200 nm – 300 nm diameter are known to enhance the expression of osteogenic factors [236]. In Chapter 4, we showed that the same S3 patterns (pillars with a diameter in this range) promote the matrix mineralization of preosteoblasts by enhancing cell adhesion, regulating the cell shape, and modulating the mechanical properties of the cytoskeleton. Here, we found that those pillars also cause macrophages to shrink, which is a sign of intracellular tension, and upregulate the pro-healing response

of M1 macrophages. Regulating the polarization of macrophages is associated with tension and contraction in the cytoskeleton of the cells [139]. Cytoskeletal tension, as measured by the level of ROCK-activity, can lead to the upregulation of anti-inflammatory genes in macrophages [139, 281, 282]. The underlying mechanisms involve the elongation and tension in actin fibers directly affecting the organization of the nucleus and the condensation of chromatin that eventually influence the macrophage phenotype [139].

7.1.3. Co-culture of osteogenic and inflammatory cells on submicron pillars

Mimicking the *in vivo* dynamics of bone regeneration entails studying cell-cell interactions in a direct co-culture model *in vitro*. However, direct co-culture studies of the interactions between macrophages and (pre)osteoblasts/MSCs in the presence of biomaterials are currently very limited [261, 262]. To date, the research on osteoimmunomodulatory biomaterials has been predominantly performed using indirect co-culture models. Although this model facilitates the assessment of the paracrine effects of different cell types, the impact of direct cell-cell interactions is neglected in indirect models.

In the last chapter of this thesis, we established a direct co-culture setup incorporating bone and inflammatory cells to more closely mimic the interaction of those cell types *in vitro*. Finding a suitable culture medium is essential in direct co-culture models. Depending on the type, origin, and ratio of the (pre)osteoblasts and macrophages, different types of media have been used in previous studies [267–269]. For example, a mixture of α -MEM and RPMI 1640 (ratio 1:1) has been applied for the direct co-culture of MC3T3-E1 preosteoblasts and murine bone marrow M1, followed by IL-4 treatment [267, 268]. In this research, the mixture of α -MEM and DMEM (ratio 1:1) was suitable for M1 cells cultured with OB cells. The cell viability remained between 80-95% during 14 days of culture.

We observed that M1 inflammatory macrophages co-cultured with osteoblasts lost their inflammatory phenotype after 3 days of culture and possessed characteristics of both M1 and M2 phenotypes, while signs of inflammation appeared on day 7. This indicates that osteoblasts directed the continuum between M1 and M2 phenotypes towards an inflammatory state. OBs, hMSCs, and chondrocytes produce IL-6, which has been reported to promote bone resorption in response to IL-1 and TNF- α both *in vitro* [283] and *in vivo* [284]. It should be noted that MSCs are considered the regulator of inflammation at the very early stages. MSCs are activated in response to inflammation, convert pro-inflammatory macrophages to anti-inflammatory ones, and reduce the inflammation through the expression of PGE2 via the COX2 signaling pathway [285].

Current research recommends adding exogenous growth factors to the culture media to promote OIM [273, 274]. However, physical and/or chemical modification of biomaterial surfaces may help modulate the response of macrophages and osteoblasts [258, 275]. When the submicron topographies were integrated into our direct co-culture setup, preosteoblasts differentiation was enhanced (measured by

RUNX2), which may be attributed to the regulation of the local inflammatory milieu. In Chapters 4 and 5, this particular design of submicron pillars was observed to promote the matrix mineralization by preosteoblasts and the pro-healing response of macrophages. In the direct co-culture model used in this thesis, the pillars may have played a similar role, effectively activating the anti-inflammatory state and enhancing the differentiation of preosteoblasts.

Upon integrin bindings, focal adhesions in MCSs and preosteoblasts, and podosomes (possessing adhesive molecules) in macrophages activate the mechanotransduction pathways [286]. Inhibition of FAK in macrophages may reduce the migration of macrophages to the inflammation sites. Biophysical features of ECM, substrate stiffness and topographies, may activate FAK in macrophages and bone cells [287]. Soft materials (elastic modulus < 1 kPa) were found to reduce the polymerization of actin in macrophages, preventing activation of YAP, a mechanosensor protein, and damping inflammation *in vitro* and *in vivo* [288]. The microtopographies influenced the mechanotransduction pathways in hASCs [282]. Aligned fibers activated FAK and YAP signaling in hASCs, and later hASCs-microfibers conditioned medium stimulated the anti-inflammatory transition in macrophages [282]. Gold nanospheres (diameter 40 nm and 70 nm) upregulated the YAP activity in hMSCs, leading to enhanced osteogenic differentiation and calcium depositions [289].

7.2. Main findings of this thesis

In this dissertation, we systematically studied, for the first time, the potential of 3D printed submicron topographies in promoting the OIM response *in vitro*. We 3D printed submicron patterns with a single-step nanofabrication technique (*i.e.*, DLW) to investigate the osteogenic and immunogenic response of cells to such surface patterns. Since decorating the large surface area with uniform and reproducible patterns were highly challenging, we first focused on reproducing uniform submicron patterns and expediting the fabrication process by optimizing the printing parameters and writing strategies. The cytotoxicity and Young's modulus of the used materials, as well as the uniformity, wettability, morphology, and roughness of the patterned surfaces were further analyzed. In the second phase, a comprehensive study was performed to explore the early and late response of preosteoblast cells to different types of submicron patterns. The interrelations between the cell adhesion, cell mechanics, and osteogenesis on the topographical features were extensively explored. We found that sufficiently tall and dense pillars at the submicron scale modulate the adhesion and elastic modulus of living cells, leading to enhanced mineralization. Interestingly, the osteoinductive pillars could also regulate the immune responses of macrophages. In the last phase of this project, a direct co-culture model was developed to assess the cross-talk among immune and bone cells with and without topographies. The integration of submicron pillars in the co-culture system enhanced the differentiation of the preosteoblasts, indicating the potential of submicron topographies in modulating the osteoimmune response in direct co-culture models. The most remarkable

findings of this research are summarized below:

1. 3D printing of submicron patterns

- Submicron patterns with controlled dimension and mechanical properties can be fabricated via an advanced 3D nanoprinting technique, namely DLW. The optimized 2PP method enhanced the uniformity and reproducibility of DLW submicron features over large areas with a three-fold reduction of the printing time. A large area of patterns with controlled heights was further incorporated over a porous scaffold and fabricated via DLW in one step.
- We fabricated a microfluidic chip incorporating 3D printed surface ornaments to assess cell proliferation in a multiscale microenvironment as a proof of concept. The submicron patterns could tolerate high flow rates (up to 8 mL/min).
- The cell experiments confirmed that the materials used in this study (*i.e.*, IP-Dip and IP-L resins) are compatible with murine preosteoblasts (MC3T3E1), hMSCs, and murine macrophages (J774A.1).
- Surface patterning enhanced the surface roughness and subsequently augmented the wettability of the surfaces. Increasing the height of the submicron pillars boosted the hydrophilicity of the surface.

2. Modulating the response of multiple cell types by submicron patterns

- The osteoblasts residing on the most hydrophilic surfaces applied significantly higher initial adhesion force and rapidly formed larger and denser focal adhesion sites (vinculin). Furthermore, the tallest and densely distributed pillars (S3 pattern) caused the cells to form numerous thick actin stress fibers, eventually resulting in a high elastic modulus in the perinuclear region. Consequently, the osteogenic marker (OPN) was expressed even in the absence of osteogenic supplements. This is likely due to the activation of the mechanotransduction pathways induced by the S3 pattern.
- The most hydrophilic surfaces (*i.e.*, the S3 and L3 patterns) also steered the polarization of the M1 macrophages towards an anti-inflammatory phenotype after 3 days. On the other hand, the proposed submicron pillars modulated the macrophage responses even in the presence of soluble inflammatory factors (LPS/IFN- γ). Under such conditions, the effects of the patterns also changed with time. On day 1, pillars with a higher (lower) pillar density impeded (boosted) the expression of the pro-inflammatory marker (CCR7), while opposite results were observed on day 3.

3. Co-culture of osteogenic and inflammatory cells on submicron pillars

- In the direct co-culture of murine osteoblasts and macrophages, the spatial distribution of both cell types was homogenous until day 3. From day 7, a layered distribution was observed with preosteoblasts occupying the space underneath the macrophages. Although preosteoblasts were cultured with inflammatory M1 cells, we barely observed inflammatory cytokines in the co-culture microenvironment up until day 7, indicating the switch in polarization from M1 to M0. On day 7, the high level of PGE2 in the inflammatory condition attenuated the preosteoblast differentiation, as revealed by a lower level of RUNX2 measured in the co-cultures as compared to the monoculture.
- The integration of submicron pillars in the co-culture system enhanced the differentiation of preosteoblasts, indicating the potential of submicron topographies in modulating the osteoimmune responses in direct co-culture models.

Our findings highlight the importance of direct co-culture models and the role of submicron patterns in the osteoimmunomodulation process.

7.3. Future research directions

We suggest the following broad areas for future research:

- **Processing view-point**
 - *Manufacturing*: Despite the unique design freedom that 2PP offers, the area of the nanopatterned surface needs to be further scaled up. Nanoimprinting (*e.g.*, NIL) can be combined with 2PP to scale up the desired nanopatterned surface.
 - *Materials*: The materials used in 2PP are limited to the photo-sensitive polymers. It would be interesting to fabricate nanopatterned stamps via 2PP and use it to imprint its patterns into a desired material (metals, plastics and ceramics) using NIL technique [290].
 - *Characterization*: Measuring the overall stiffness of the patterned surfaces was limited by the availability of a proper nanoindentation probe. It would be useful to further investigate the influences of substrate stiffness on cellular responses. The integration of force-sensitive sensors into nanopatterned substrates/scaffolds may help to measure the actual force that cells apply to the substrate.
- **Biological view-point**
 - *Cell type*: In addition to macrophages, MSCs are present at the injury site. Investigating the effects of the proposed submicron pillars on the response of MSCs is highly recommended.
 - *Osteogenic assays*: The mechanotransduction pathways promoting osteogenesis should be further studied. Notably, the kinase pathway,

which involves the phosphorylation of kinase proteins, such as FAK, is recommended to be investigated.

- *Immunogenic assays:* The level of the ROCK-activity, which can lead to the upregulation of anti-inflammatory genes in macrophages, should be measured to study the cytoskeletal tension in the macrophages.

Macrophages could possess the characteristics of both M1 and M2 phenotypes. Therefore, relying solely on surface markers may not give reliable data to detect the polarization state of macrophages. Further gene expression tests and qPCR analysis are required to prove the OIM potential of submicron pillars.

Labeling the proteins of living cells and using fluorescence-activated cell sorting (FACS) techniques may help detecting the specific population of cells in the co-culture systems.

- **Suggestions for co-culture models**

- *Cell Seeding order:* In this study, we seeded a mixed concentration of cells and osteoblasts. It is worth studying the effects of seeding order on co-culture experiments.
- *Dynamic co-culture:* *In vivo* cells sense physiological shear stress. It is, therefore, essential to research the OIM efficiency of biomaterials in a dynamic co-culture system. We did a preliminary research on the effects of flow in our culture system. The high proliferation rate of osteoblast (5000 cells/cm²) in a microfluidic chip blocked microchannels (width = 200 μm , length = 10000 μm , depth = 50 μm) after 7 days of culture. However, the differentiation of osteoblasts enhanced in the dynamic condition compared with the static ones. The initial cell seeding density and the shear stress should be optimized to design a reliable dynamic co-culture setup. Fluid shear stress (FSS) of 0.6-3.0 Pa is estimated in the canaliculi channels (0.1 μm radius) in the mineralized bone surrounding osteocytes [291, 292]. However, osteoblasts might be subjected to lower fluid shear stress since they are located in regions with larger pore sizes [292]. Low flow shear stress (< 0.5 Pa) is reported to better stimulate the osteogenic activity of osteoblasts as compared to high FSS (0.5 -2 Pa) *in vitro* [292]. In our preliminary study in the dynamic co-culture, few macrophages were presented in the channel after 7 days of seeding, indicating the high sensitivity of the macrophages to the shear stress. In other words, a lower adhesion strength was observed in macrophages as compared to osteoblasts under a flow rate of 1 $\mu\text{L}/\text{min}$. It is, therefore, necessary to investigate the influence of shear stress on the adhesion of each cell type and the further consequences on the OIM responses.

References

- [1] M. Alonzo, F. Alvarez Primo, S. Anil Kumar, J. A. Mudloff, E. Dominguez, G. Fregoso, N. Ortiz, W. M. Weiss, and B. Joddar, “Bone tissue engineering techniques, advances, and scaffolds for treatment of bone defects,” *Current Opinion in Biomedical Engineering*, vol. 17, p. 100248, 2021.
- [2] J. G. Lyons, M. A. Plantz, W. K. Hsu, E. L. Hsu, and S. Minardi, “Nanostructured biomaterials for bone regeneration,” *Frontiers in bioengineering and biotechnology*, vol. 8, pp. 922–922, 2020.
- [3] X. Yu, X. Tang, S. V. Gohil, and C. T. Laurencin, “Biomaterials for bone regenerative engineering,” *Advanced Healthcare Materials*, vol. 4, no. 9, pp. 1268–1285, 2015.
- [4] S. Minardi, B. Corradetti, F. Taraballi, M. Sandri, J. Van Eps, F. J. Cabrera, B. K. Weiner, A. Tampieri, and E. Tasciotti, “Evaluation of the osteoinductive potential of a bio-inspired scaffold mimicking the osteogenic niche for bone augmentation,” *Biomaterials*, vol. 62, pp. 128–137, 2015.
- [5] L. L. Hench, “Biomaterials: a forecast for the future,” *Biomaterials*, vol. 19, no. 16, pp. 1419–1423, 1998.
- [6] M. Tirrell, E. Kokkoli, and M. Biesalski, “The role of surface science in bioengineered materials,” *Surface Science*, vol. 500, no. 1, pp. 61–83, 2002.
- [7] B. D. Ulery, L. S. Nair, and C. T. Laurencin, “Biomedical applications of biodegradable polymers,” *Journal of Polymer Science Part B: Polymer Physics*, vol. 49, no. 12, pp. 832–864, 2011.
- [8] L. L. Hench, “The story of bioglass®,” *Journal of Materials Science: Materials in Medicine*, vol. 17, no. 11, pp. 967–978, 2006.
- [9] E. Alsberg, H. A. von Recum, and M. J. Mahoney, “Environmental cues to guide stem cell fate decision for tissue engineering applications,” *Expert opinion on biological therapy*, vol. 6, no. 9, pp. 847–866, 2006.
- [10] J. M. Sadowska, F. Wei, J. Guo, J. Guillem-Marti, Z. Lin, M.-P. Ginebra, and Y. Xiao, “The effect of biomimetic calcium deficient hydroxyapatite and sintered -tricalcium phosphate on osteoimmune reaction and osteogenesis,” *Acta Biomaterialia*, vol. 96, pp. 605–618, 2019.
- [11] Y. Xie, C. Hu, Y. Feng, D. Li, T. Ai, Y. Huang, X. Chen, L. Huang, and J. Tan, “Osteoimmunomodulatory effects of biomaterial modification strategies on macrophage polarization and bone regeneration,” *Regenerative Biomaterials*, vol. 7, no. 3, pp. 233–245, 2020.
- [12] A. Diez-Escudero, M. Espanol, M. Bonany, X. Lu, C. Persson, and M.-P. Ginebra, “Heparinization of beta tricalcium phosphate: Osteoimmunomodulatory effects,” *Advanced Healthcare Materials*, vol. 7, no. 5, p. 1700867, 2018.
- [13] Z. Wang, Y. Niu, X. Tian, N. Yu, X. Yin, Z. Xing, Y. Li, L. Dong, and

- C. Wang, “Switching on and off macrophages by a “bridge-burning” coating improves bone-implant integration under osteoporosis,” *Advanced Functional Materials*, vol. 31, no. 7, p. 2007408, 2021.
- [14] Z. Chen, T. Klein, R. Z. Murray, R. Crawford, J. Chang, C. Wu, and Y. Xiao, “Osteoimmunomodulation for the development of advanced bone biomaterials,” *Materials Today*, vol. 19, no. 6, pp. 304–321, 2016.
- [15] A. Vishwakarma, N. S. Bhise, M. B. Evangelista, J. Rouwkema, M. R. Dokmeci, A. M. Ghaemmaghami, N. E. Vrana, and A. Khademhosseini, “Engineering immunomodulatory biomaterials to tune the inflammatory response,” *Trends in Biotechnology*, vol. 34, no. 6, pp. 470–482, 2016.
- [16] C. Wu, Z. Chen, Q. Wu, D. Yi, T. Friis, X. Zheng, J. Chang, X. Jiang, and Y. Xiao, “Clinoenstatite coatings have high bonding strength, bioactive ion release, and osteoimmunomodulatory effects that enhance in vivo osseointegration,” *Biomaterials*, vol. 71, pp. 35–47, 2015.
- [17] C. Wu, Z. Chen, D. Yi, J. Chang, and Y. Xiao, “Multidirectional effects of sr-, mg-, and si-containing bioceramic coatings with high bonding strength on inflammation, osteoclastogenesis, and osteogenesis,” *ACS Applied Materials Interfaces*, vol. 6, no. 6, pp. 4264–4276, 2014.
- [18] N. A. Sims and J. M. Quinn, “Osteoimmunology: oncostatin m as a pleiotropic regulator of bone formation and resorption in health and disease,” *BoneKEY reports*, vol. 3, 2014.
- [19] J. J. Moon, B. Huang, and D. J. Irvine, “Engineering nano- and microparticles to tune immunity,” *Advanced Materials*, vol. 24, no. 28, pp. 3724–3746, 2012.
- [20] M. O. Oyewumi, A. Kumar, and Z. Cui, “Nano-microparticles as immune adjuvants: correlating particle sizes and the resultant immune responses,” *Expert Review of Vaccines*, vol. 9, no. 9, pp. 1095–1107, 2010.
- [21] A. J. MARSHALL, “Biomaterials with tightly controlled poresize that promote vascular in-growth,” *Polymer Preprints*, vol. 45, pp. 100–101, 2004.
- [22] L. Liang, Q. Huang, H. Wu, H. He, G. Lei, D. Zhao, and K. Zhou, “Engineering nano-structures with controllable dimensional features on microtopographical titanium surfaces to modulate the activation degree of m1 macrophages and their osteogenic potential,” *Journal of Materials Science Technology*, vol. 96, pp. 167–178, 2022.
- [23] B. S. Smith, P. Capellato, S. Kelley, M. Gonzalez-Juarrero, and K. C. Papat, “Reduced in vitro immune response on titania nanotube arrays compared to titanium surface,” *Biomaterials Science*, vol. 1, no. 3, pp. 322–332, 2013.
- [24] H. Xing, R. Li, Y. Qing, B. Ying, and Y. Qin, “Biomaterial-based osteoimmunomodulatory strategies via the tlr4-nf-b signaling pathway: A review,” *Applied Materials Today*, vol. 22, p. 100969, 2021.
- [25] J. A. Jones, D. T. Chang, H. Meyerson, E. Colton, I. K. Kwon, T. Matsuda, and J. M. Anderson, “Proteomic analysis and quantification of cytokines and chemokines from biomaterial surface-adherent macrophages and for-

- eign body giant cells,” *Journal of Biomedical Materials Research Part A*, vol. 83A, no. 3, pp. 585–596, 2007.
- [26] Z. Chen, R. M. Visalakshan, J. Guo, F. Wei, L. Zhang, L. Chen, Z. Lin, K. Vasilev, and Y. Xiao, “Plasma deposited poly-oxazoline nanotextured surfaces dictate osteoimmunomodulation towards ameliorative osteogenesis,” *Acta Biomaterialia*, vol. 96, pp. 568–581, 2019.
- [27] J. M. Sadowska, F. Wei, J. Guo, J. Guillem-Marti, M.-P. Ginebra, and Y. Xiao, “Effect of nano-structural properties of biomimetic hydroxyapatite on osteoimmunomodulation,” *Biomaterials*, vol. 181, pp. 318–332, 2018.
- [28] N. Gui, W. Xu, D. Myers, R. Shukla, H. Tang, and M. Qian, “The effect of ordered and partially ordered surface topography on bone cell responses: a review,” *Biomaterials science*, vol. 6, no. 2, pp. 250–264, 2018.
- [29] Z. Chen, A. Bachhuka, S. Han, F. Wei, S. Lu, R. M. Visalakshan, K. Vasilev, and Y. Xiao, “Correction to “tuning chemistry and topography of nano-engineered surfaces to manipulate immune response for bone regeneration applications”,,” *ACS Nano*, vol. 13, no. 3, pp. 3739–3739, 2019.
- [30] J. van der Stok, M. Koolen, M. de Maat, S. A. Yavari, J. Alblas, P. Patka, J. Verhaar, E. van Lieshout, A. A. Zadpoor, and H. Weinans, “Full regeneration of segmental bone defects using porous titanium implants loaded with bmp-2 containing fibrin gels,” *Eur. Cells Mater.*, vol. 2015, no. 29, pp. 141–154, 2015.
- [31] S. Dobbenga, L. E. Fratila-Apachitei, and A. A. Zadpoor, “Nanopattern-induced osteogenic differentiation of stem cells—a systematic review,” *Acta Biomater.*, vol. 46, pp. 3–14, 2016.
- [32] M. J. Dalby, N. Gadegaard, R. Tare, A. Andar, M. O. Riehle, P. Herzyk, C. D. Wilkinson, and R. O. Oreffo, “The control of human mesenchymal cell differentiation using nanoscale symmetry and disorder,” *Nature materials*, vol. 6, no. 12, pp. 997–1003, 2007.
- [33] K. M. Hotchkiss, G. B. Reddy, S. L. Hyzy, Z. Schwartz, B. D. Boyan, and R. Olivares-Navarrete, “Titanium surface characteristics, including topography and wettability, alter macrophage activation,” *Acta Biomaterialia*, vol. 31, pp. 425–434, 2016.
- [34] L. Burroughs, M. H. Amer, M. Vassey, B. Koch, G. P. Figueredo, B. Mukonoweshuro, P. Mikulskis, A. Vasilevich, S. Vermeulen, I. L. Dryden, D. A. Winkler, A. M. Ghaemmaghami, F. R. A. J. Rose, J. de Boer, and M. R. Alexander, “Discovery of synergistic material-topography combinations to achieve immunomodulatory osteoinductive biomaterials using a novel in vitro screening method: The chemotopochip,” *Biomaterials*, vol. 271, p. 120740, 2021.
- [35] Q.-L. Ma, L.-Z. Zhao, R.-R. Liu, B.-Q. Jin, W. Song, Y. Wang, Y.-S. Zhang, L.-H. Chen, and Y.-M. Zhang, “Improved implant osseointegration of a nanostructured titanium surface via mediation of macrophage polarization,” *Biomaterials*, vol. 35, no. 37, pp. 9853–9867, 2014.
- [36] X. Li, Q. Huang, T. A. Elkhooly, Y. Liu, H. Wu, Q. Feng, L. Liu, Y. Fang,

- W. Zhu, and T. Hu, "Effects of titanium surface roughness on the mediation of osteogenesis via modulating the immune response of macrophages," *Biomedical Materials*, vol. 13, no. 4, p. 045013, 2018.
- [37] S. Franz, S. Rammelt, D. Scharnweber, and J. C. Simon, "Immune responses to implants – a review of the implications for the design of immunomodulatory biomaterials," *Biomaterials*, vol. 32, no. 28, pp. 6692–6709, 2011.
- [38] C. Matschegewski, S. Staehlke, R. Loeffler, R. Lange, F. Chai, D. P. Kern, U. Beck, and B. J. Nebe, "Cell architecture–cell function dependencies on titanium arrays with regular geometry," *Biomaterials*, vol. 31, no. 22, pp. 5729–5740, 2010.
- [39] M. Ermis, E. Antmen, and V. Hasirci, "Micro and nanofabrication methods to control cell-substrate interactions and cell behavior: A review from the tissue engineering perspective," *Bioactive Materials*, vol. 3, no. 3, pp. 355–369, 2018.
- [40] M. Nouri-Goushki, M. J. Mirzaali, L. Angeloni, D. Fan, M. Minneboo, M. K. Ghatkesar, U. Staufer, L. E. Fratila-Apachitei, and A. A. Zadpoor, "3d printing of large areas of highly ordered submicron patterns for modulating cell behavior," *ACS Applied Materials Interfaces*, vol. 12, no. 1, pp. 200–208, 2020.
- [41] S. M. M. Roosa, J. M. Kemppainen, E. N. Moffitt, P. H. Krebsbach, and S. J. Hollister, "The pore size of polycaprolactone scaffolds has limited influence on bone regeneration in an in vivo model," *J. Biomed. Mater. Res. A*, vol. 92A, no. 1, pp. 359–368, 2010.
- [42] M. G. Stanford, P. D. Rack, and D. Jariwala, "Emerging nanofabrication and quantum confinement techniques for 2d materials beyond graphene," *npj 2D Materials and Applications*, vol. 2, no. 1, p. 20, 2018.
- [43] R. Winkler, J. D. Fowlkes, P. D. Rack, and H. Plank, "3d nanoprinting via focused electron beams," *Journal of Applied Physics*, vol. 125, no. 21, p. 210901, 2019.
- [44] L. Hirt, A. Reiser, R. Spolenak, and T. Zambelli, "Additive manufacturing of metal structures at the micrometer scale," *Advanced Materials*, vol. 29, no. 17, p. 1604211, 2017.
- [45] M. Vaezi, H. Seitz, and S. Yang, "A review on 3d micro-additive manufacturing technologies," *The International Journal of Advanced Manufacturing Technology*, vol. 67, no. 5-8, pp. 1721–1754, 2013.
- [46] W. Zhang, M. Tong, and N. M. Harrison, "Resolution, energy and time dependency on layer scaling in finite element modelling of laser beam powder bed fusion additive manufacturing," *Additive Manufacturing*, vol. 28, pp. 610–620, 2019.
- [47] C. Barner-Kowollik, M. Bastmeyer, E. Blasco, G. Delaittre, P. Müller, B. Richter, and M. Wegener, "3d laser micro- and nanoprinting: Challenges for chemistry," *Angewandte Chemie International Edition*, vol. 56, no. 50, pp. 15828–15845, 2017.

- [48] P. V. Giannoudis, H. Dinopoulos, and E. Tsiridis, "Bone substitutes: an update," *Injury*, vol. 36, no. 3, pp. S20–S27, 2005.
- [49] K. H. Kraus and C. Kirker-Head, "Mesenchymal stem cells and bone regeneration," *Vet. Surg.*, vol. 35, no. 3, pp. 232–242, 2006.
- [50] Y. Li and C. Liu, "Nanomaterial-based bone regeneration," *Nanoscale*, vol. 9, no. 15, pp. 4862–4874, 2017.
- [51] T. Gong, J. Xie, J. Liao, T. Zhang, S. Lin, and Y. Lin, "Nanomaterials and bone regeneration," *Bone Res.*, vol. 3, p. 15029, 2015.
- [52] J. Henkel, M. A. Woodruff, D. R. Epari, R. Steck, V. Glatt, I. C. Dickinson, P. F. Choong, M. A. Schuetz, and D. W. Huttmacher, "Bone regeneration based on tissue engineering conceptions—a 21st century perspective," *Bone Res.*, vol. 1, no. 3, p. 216, 2013.
- [53] X. Zhang, C. Zhang, Y. Lin, P. Hu, Y. Shen, K. Wang, S. Meng, Y. Chai, X. Dai, and X. Liu, "Nanocomposite membranes enhance bone regeneration through restoring physiological electric microenvironment," *ACS Nano*, vol. 10, no. 8, pp. 7279–7286, 2016.
- [54] B.-D. Sui, C.-H. Hu, A.-Q. Liu, C.-X. Zheng, K. Xuan, and Y. Jin, "Stem cell-based bone regeneration in diseased microenvironments: Challenges and solutions," *Biomaterials*, 2017.
- [55] Y. Yan, B. Cheng, K. Chen, W. Cui, J. Qi, X. Li, and L. Deng, "Enhanced osteogenesis of bone marrow-derived mesenchymal stem cells by a functionalized silk fibroin hydrogel for bone defect repair," *Adv. Healthcare Mater.*, p. 1801043, 2018.
- [56] S. A. Yavari, J. van der Stok, Y. C. Chai, R. Wauthle, Z. T. Birgani, P. Habibovic, M. Mulier, J. Schrooten, H. Weinans, and A. A. Zadpoor, "Bone regeneration performance of surface-treated porous titanium," *Biomaterials*, vol. 35, no. 24, pp. 6172–6181, 2014.
- [57] M. Dang, L. Saunders, X. Niu, Y. Fan, and P. X. Ma, "Biomimetic delivery of signals for bone tissue engineering," *Bone Res.*, vol. 6, 2018.
- [58] Z. Gorgin Karaji, M. Speirs, S. Dadbakhsh, J.-P. Kruth, H. Weinans, A. Zadpoor, and S. Amin Yavari, "Additively manufactured and surface biofunctionalized porous nitinol," *ACS Appl. Mater. Interfaces*, vol. 9, no. 2, pp. 1293–1304, 2017.
- [59] A. A. Zadpoor, "Current trends in metallic orthopedic biomaterials: From additive manufacturing to bio-functionalization, infection prevention, and beyond," *Int. J. Mol. Sci.*, vol. 19, no. 9, p. 2684, 2018.
- [60] E. H. Ahn, Y. Kim, S. S. An, J. Afzal, S. Lee, M. Kwak, K.-Y. Suh, D.-H. Kim, and A. Levchenko, "Spatial control of adult stem cell fate using nanotopographic cues," *Biomaterials*, vol. 35, no. 8, pp. 2401–2410, 2014.
- [61] J. K. Hohmann and G. von Freymann, "Influence of direct laser written 3d topographies on proliferation and differentiation of osteoblast-like cells: Towards improved implant surfaces," *Adv. Funct. Mater.*, vol. 24, no. 42, pp. 6573–6580, 2014.

- [62] C. Hammann, C. T. H. Heerkens, C. Hagen, A. Zadpoor, and L. Fratila-Apachitei, "Direct submicron patterning of titanium for bone implants," *Microelectron. Eng.*, vol. 195, pp. 13–20, 2018.
- [63] T. Sjöström, M. J. Dalby, A. Hart, R. Tare, R. O. Oreffo, and B. Su, "Fabrication of pillar-like titania nanostructures on titanium and their interactions with human skeletal stem cells," *Acta Biomater.*, vol. 5, no. 5, pp. 1433–1441, 2009.
- [64] S. Amin Yavari, L. Loozen, F. L. Paganelli, S. Bakhshandeh, K. Lietaert, J. A. Groot, A. C. Fluit, C. Boel, J. Alblas, and H. C. Vogely, "Antibacterial behavior of additively manufactured porous titanium with nanotubular surfaces releasing silver ions," *ACS Appl. Mater. Interfaces*, vol. 8, no. 27, pp. 17080–17089, 2016.
- [65] M. Mirzaali, I. Van Dongen, N. Tümer, H. Weinans, S. A. Yavari, and A. Zadpoor, "In-silico quest for bactericidal but non-cytotoxic nanopatterns," *Nanotechnology*, vol. 29, no. 43, p. 43LT02, 2018.
- [66] K. Modaresifar, S. Azizian, M. Ganjian, L. E. Fratila-Apachitei, and A. A. Zadpoor, "Bactericidal effects of nanopatterns: a systematic review," *Acta Biomater.*, 2018.
- [67] K. Anselme, P. Davidson, A. Popa, M. Giazzon, M. Liley, and L. Ploux, "The interaction of cells and bacteria with surfaces structured at the nanometre scale," *Acta Biomater.*, vol. 6, no. 10, pp. 3824–3846, 2010.
- [68] L. Ploux, K. Anselme, A. Dirani, A. Ponche, O. Soppera, and V. Roucoules, "Opposite responses of cells and bacteria to micro/nanopatterned surfaces prepared by pulsed plasma polymerization and uv-irradiation," *Langmuir*, vol. 25, no. 14, pp. 8161–8169, 2009.
- [69] Y. Yang and K. W. Leong, *Microfluidic platforms with nanoscale features*, pp. 65–90. Elsevier, 2019.
- [70] Y. Chen, "Nanofabrication by electron beam lithography and its applications: a review," *Microelectron. Eng.*, vol. 135, pp. 57–72, 2015.
- [71] S. Cleuvenbergen, "Direct fabrication of complex 3d hierarchical nanostructures by reactive ion etching of hollow sphere colloidal crystals," *Nanoscale*, vol. 8, no. 35, pp. 15845–15849, 2016.
- [72] E. F. Pecora, N. Lawrence, P. Gregg, J. Trevino, P. Artoni, A. Irrera, F. Priolo, and L. Dal Negro, "Nanopatterning of silicon nanowires for enhancing visible photoluminescence," *Nanoscale*, vol. 4, no. 9, pp. 2863–2866, 2012.
- [73] B. B. Lewis, B. A. Mound, B. Srijanto, J. D. Fowlkes, G. M. Pharr, and P. D. Rack, "Growth and nanomechanical characterization of nanoscale 3d architectures grown via focused electron beam induced deposition," *Nanoscale*, vol. 9, no. 42, pp. 16349–16356, 2017.
- [74] G. Zhang, X. Xiao, B. Li, P. Gu, H. Xue, and H. Pang, "Transition metal oxides with one-dimensional/one-dimensional-analogue nanostructures for advanced supercapacitors," *J. Mater. Chem. A*, vol. 5, no. 18, pp. 8155–8186, 2017.
- [75] S. Luo, P. Zhang, T. Yuan, J. Ruan, C. Peng, Y. Pang, H. Sun, J. Yang,

- and S. Zheng, “Molecular self-assembly of a nanorod n-li 4 ti 5 o 12/tio 2/c anode for superior lithium ion storage,” *J. Mater. Chem. A*, vol. 6, no. 32, pp. 15755–15761, 2018.
- [76] M. Malinauskas, M. Farsari, A. Piskarskas, and S. Juodkazis, “Ultrafast laser nanostructuring of photopolymers: A decade of advances,” *Phys. Rep.*, vol. 533, no. 1, pp. 1–31, 2013.
- [77] M. Malinauskas, A. Žukauskas, S. Hasegawa, Y. Hayasaki, V. Mizeikis, R. Buividas, and S. Juodkazis, “Ultrafast laser processing of materials: from science to industry,” *Light Sci. Appl.*, vol. 5, no. 8, p. e16133, 2016.
- [78] D. Barata, E. Provaggi, C. van Blitterswijk, and P. Habibovic, “Development of a microfluidic platform integrating high-resolution microstructured biomaterials to study cell–material interactions,” *Lab Chip*, vol. 17, no. 23, pp. 4134–4147, 2017.
- [79] Y. Yang, K. Kulangara, J. Sia, L. Wang, and K. W. Leong, “Engineering of a microfluidic cell culture platform embedded with nanoscale features,” *Lab Chip*, vol. 11, no. 9, pp. 1638–1646, 2011.
- [80] C. Bruedigam, M. van Driel, M. Koedam, J. van de Peppel, B. C. van der Eerden, M. Eijken, and J. P. van Leeuwen, “Basic techniques in human mesenchymal stem cell cultures: differentiation into osteogenic and adipogenic lineages, genetic perturbations, and phenotypic analyses,” *Curr. Protoc. Stem Cell Biol.*, vol. 17, no. 1, pp. 1H. 3.1–1H. 3.20, 2011.
- [81] H.-B. Sun, T. Tanaka, and S. Kawata, “Three-dimensional focal spots related to two-photon excitation,” *Appl. Phys. Lett.*, vol. 80, no. 20, pp. 3673–3675, 2002.
- [82] R. A. Afre, Y. Hayashi, and T. Soga, “Enhanced photovoltaic device performance upon modification of indium tin oxide coated glass by liquid nitrogen treatment,” *J. Phys. D: Appl. Phys.*, vol. 42, no. 4, p. 042002, 2009.
- [83] M.-H. Piao, D.-S. Yang, K.-R. Yoon, S.-H. Lee, and S.-H. Choi, “Development of an electrogenerated chemiluminescence biosensor using carboxylic acid-functionalized mwcnt and au nanoparticles,” *Sensors*, vol. 9, no. 3, pp. 1662–1677, 2009.
- [84] Z. Zhong, Y. Zhong, C. Liu, S. Yin, W. Zhang, and D. Shi, “Study on the surface wetting properties of treated indium-tin-oxide anodes for polymer electroluminescent devices,” *Phys. Status Solidi A*, vol. 198, no. 1, pp. 197–203, 2003.
- [85] S. Besbes, H. B. Ouada, J. Davenas, L. Ponsonnet, N. Jaffrezic, and P. Alcouffe, “Effect of surface treatment and functionalization on the ito properties for oleds,” *Mater. Sci. Eng. C*, vol. 26, no. 2-3, pp. 505–510, 2006.
- [86] D. Quéré, “Wetting and roughness,” *Annu. Rev. Mater. Res.*, vol. 38, pp. 71–99, 2008.
- [87] B. Boyan, A. Cheng, R. Olivares-Navarrete, and Z. Schwartz, “Implant surface design regulates mesenchymal stem cell differentiation and maturation,” *Adv. Dent. Res.*, vol. 28, no. 1, pp. 10–17, 2016.
- [88] S. Tunma, K. Inthanon, C. Chaiwong, J. Pumchusak, W. Wongkham, and

- D. Boonyawan, "Improving the attachment and proliferation of umbilical cord mesenchymal stem cells on modified polystyrene by nitrogen-containing plasma," *Cytotechnology*, vol. 65, no. 1, pp. 119–134, 2013.
- [89] E. D. Lemma, F. Rizzi, T. Dattoma, B. Spagnolo, L. Sileo, A. Qualtieri, M. De Vittorio, and F. Pisanello, "Mechanical properties tunability of three-dimensional polymeric structures in two-photon lithography," *IEEE Trans. Nanotechnol.*, vol. 16, no. 1, pp. 23–31, 2017.
- [90] J. Fu, Y.-K. Wang, M. T. Yang, R. A. Desai, X. Yu, Z. Liu, and C. S. Chen, "Mechanical regulation of cell function with geometrically modulated elastomeric substrates," *Nat. Methods*, vol. 7, no. 9, p. 733, 2010.
- [91] M. M. Nava, N. Di Maggio, T. Zandrini, G. Cerullo, R. Osellame, I. Martin, and M. T. Raimondi, "Synthetic niche substrates engineered via two-photon laser polymerization for the expansion of human mesenchymal stromal cells," *J. Tissue Eng. Regener. Med.*, vol. 11, no. 10, pp. 2836–2845, 2017.
- [92] B. Spagnolo, V. Brunetti, G. Leménager, E. De Luca, L. Sileo, T. Pellegrino, P. P. Pompa, M. De Vittorio, and F. Pisanello, "Three-dimensional cage-like microcaffolds for cell invasion studies," *Sci. Rep.*, vol. 5, p. 10531, 2015.
- [93] R. Wittig, E. Waller, G. von Freymann, and R. Steiner, "Direct laser writing-mediated generation of standardized topographies for dental implant surface optimization," *J. Laser Appl.*, vol. 24, no. 4, p. 042011, 2012.
- [94] E. A. Cavalcanti-Adam and D. Missirlis, "Nanoscale control of cell behavior on biointerfaces," *Biomimetic Approaches Biomater. Dev.*, pp. 213–236, 2012.
- [95] C. Cha, W. B. Liechty, A. Khademhosseini, and N. A. Peppas, "Designing biomaterials to direct stem cell fate," *ACS nano*, vol. 6, no. 11, pp. 9353–9358, 2012.
- [96] M. P. Lutolf, P. M. Gilbert, and H. M. Blau, "Designing materials to direct stem-cell fate," *Nature*, vol. 462, no. 7272, pp. 433–441, 2009.
- [97] S. Yin, W. Zhang, Z. Zhang, and X. Jiang, "Recent advances in scaffold design and material for vascularized tissue-engineered bone regeneration," *Adv. Healthcare Mater.*, vol. 8, no. 10, p. 1801433, 2019.
- [98] K. S. Brammer, C. Choi, C. J. Frandsen, S. Oh, and S. Jin, "Hydrophobic nanopillars initiate mesenchymal stem cell aggregation and osteo-differentiation," *Acta Biomater.*, vol. 7, no. 2, pp. 683–690, 2011.
- [99] M. J. Dalby, N. Gadegaard, and R. O. Oreffo, "Harnessing nanotopography and integrin–matrix interactions to influence stem cell fate," *Nat. Mater.*, vol. 13, no. 6, pp. 558–569, 2014.
- [100] M. Rizwan, W. T. John, A. Nori, K. W. Leong, and E. K. Yim, *Cell–substrate interactions*, pp. 437–468. Elsevier, 2019.
- [101] I. A. Janson and A. J. Putnam, "Extracellular matrix elasticity and topography: Material-based cues that affect cell function via conserved mechanisms," *J. Biomed. Mater. Res., Part A*, vol. 103, no. 3, pp. 1246–1258, 2015.

- [102] K. Kulangara and K. W. Leong, "Substrate topography shapes cell function," *Soft Matter*, vol. 5, no. 21, pp. 4072–4076, 2009.
- [103] M. S. Lord, M. Foss, and F. Besenbacher, "Influence of nanoscale surface topography on protein adsorption and cellular response," *Nano Today*, vol. 5, no. 1, pp. 66–78, 2010.
- [104] R. R. Resende, E. A. Fonseca, F. M. Tonelli, B. R. Sousa, A. K. Santos, K. N. Gomes, S. Guatimosim, A. H. Kihara, and L. O. Ladeira, "Scale/topography of substrates surface resembling extracellular matrix for tissue engineering," *J. Biomed. Nanotechnol.*, vol. 10, no. 7, pp. 1157–1193, 2014.
- [105] E. Santos, G. Orive, R. M. Hernández, and J. L. Pedraz, *Cell-Biomaterial Interaction: Strategies to Mimic the Extracellular Matrix*. IntechOpen, 2011.
- [106] R. J. McMurray, N. Gadegaard, P. M. Tsimbouri, K. V. Burgess, L. E. McNamara, R. Tare, K. Murawski, E. Kingham, R. O. Oreffo, and M. J. Dalby, "Nanoscale surfaces for the long-term maintenance of mesenchymal stem cell phenotype and multipotency," *Nat. Mater.*, vol. 10, no. 8, pp. 637–644, 2011.
- [107] C. R. Pedrosa, D. Arl, P. Gryan, I. Khan, S. Durrieu, S. Krishnamoorthy, and M.-C. Durrieu, "Controlled nanoscale topographies for osteogenic differentiation of mesenchymal stem cells," *ACS Appl. Mater. Interfaces*, vol. 11, no. 9, pp. 8858–8866, 2019.
- [108] D. Widyaratih, P.-L. Hagedoorn, L. Otten, M. Ganjian, N. Tumer, I. Apachitei, C. W. K. Hagen, L. Fratila-Apachitei, and A. A. Zadpoor, "Towards osteogenic and bactericidal nanopatterns?," *Nanotechnology*, vol. 30, p. 20LT01, 2019.
- [109] W. Tang, D. Lin, Y. Yu, H. Niu, H. Guo, Y. Yuan, and C. Liu, "Bioinspired trimodal macro/micro/nano-porous scaffolds loading rhbmp-2 for complete regeneration of critical size bone defect," *Acta biomater.*, vol. 32, pp. 309–323, 2016.
- [110] P. Zorlutuna, N. Annabi, G. Camci-Unal, M. Nikkhah, J. M. Cha, J. W. Nichol, A. Manbachi, H. Bae, S. Chen, and A. Khademhosseini, "Microfabricated biomaterials for engineering 3d tissues," *Adv. Mater.*, vol. 24, no. 14, pp. 1782–1804, 2012.
- [111] A. A. Zadpoor and J. Malda, "Additive manufacturing of biomaterials, tissues, and organs," *J. Ann. Biomed. Eng.*, vol. 45, pp. 1–11, 2017.
- [112] J. Van der Stok, O. P. Van der Jagt, S. Amin Yavari, M. F. De Haas, J. H. Waarsing, H. Jahr, E. M. Van Lieshout, P. Patka, J. A. Verhaar, and A. A. Zadpoor, "Selective laser melting-produced porous titanium scaffolds regenerate bone in critical size cortical bone defects," *J. Orthop. Res.*, vol. 31, no. 5, pp. 792–799, 2013.
- [113] S. Zhang, S. Vijayavenkataraman, W. F. Lu, and J. Y. Fuh, "A review on the use of computational methods to characterize, design, and optimize tissue engineering scaffolds, with a potential in 3d printing fabrication," *J. Biomed. Mater. Res., Part B*, vol. 107, no. 5, pp. 1329–1351, 2018.

- [114] S. Bsati, S. Yavari, M. Munsch, E. Valstar, and A. Zadpoor, "Effect of alkali-acid-heat chemical surface treatment on electron beam melted porous titanium and its apatite forming ability," *Materials*, vol. 8, no. 4, pp. 1612–1625, 2015.
- [115] J. H. Jordahl, L. Solorio, H. Sun, S. Ramcharan, C. B. Teeple, H. R. Haley, K. J. Lee, T. W. Eyster, G. D. Luker, and P. H. Krebsbach, "3d jet writing: Functional microtissues based on tessellated scaffold architectures," *Adv. Mater.*, vol. 30, no. 14, p. 1707196, 2018.
- [116] M. Mirzaali, M. Edens, A. H. de la Nava, S. Janbaz, P. Vena, E. Doubrovski, and A. Zadpoor, "Length-scale dependency of biomimetic hard-soft composites," *Sci. Rep.*, vol. 8, no. 1, p. 12052, 2018.
- [117] M. J. Mirzaali, A. H. d. l. Nava, D. Gunashekar, M. Nouri-Goushki, E. Doubrovski, and A. A. Zadpoor, "Fracture behavior of bio-inspired functionally graded soft–hard composites made by multi-material 3d printing: The case of colinear cracks," *Materials*, vol. 12, no. 17, p. 2735, 2019.
- [118] S. Vijayavenkataraman, L. Zhang, S. Zhang, J. Y. Hsi Fuh, and W. F. Lu, "Triply periodic minimal surfaces sheet scaffolds for tissue engineering applications: An optimization approach toward biomimetic scaffold design," *ACS Appl. Bio Mater.*, vol. 1, no. 2, pp. 259–269, 2018.
- [119] S. Janbaz, N. Noordzij, D. S. Widyaratih, C. W. Hagen, L. E. Fratila-Apachitei, and A. A. Zadpoor, "Origami lattices with free-form surface ornaments," *Sci. Adv.*, vol. 3, no. 11, p. eaao1595, 2017.
- [120] D. Brodoceanu and T. Kraus, *Micro-and Nanopatterning of Biomaterial Surfaces*, book section 10, pp. 285–309. 2013.
- [121] M. Emons, K. Obata, T. Binhammer, A. Ovsianikov, B. N. Chichkov, and U. Morgner, "Two-photon polymerization technique with sub-50 nm resolution by sub-10 fs laser pulses," *Opt. Mater. Express*, vol. 2, no. 7, pp. 942–947, 2012.
- [122] A. J. Gross and K. Bertoldi, "Additive manufacturing of nanostructures that are delicate, complex, and smaller than ever," *Small*, vol. 15, p. 1902370, 2019.
- [123] T. Weiß, G. Hildebrand, R. Schade, and K. Liefeth, "Two-photon polymerization for microfabrication of three-dimensional scaffolds for tissue engineering application," *Eng. Life Sci.*, vol. 9, no. 5, pp. 384–390, 2009.
- [124] S. Wang, Y. Yu, H. Liu, K. T. Lim, B. M. Srinivasan, Y. W. Zhang, and J. K. Yang, "Sub-10-nm suspended nano-web formation by direct laser writing," *Nano Futures*, vol. 2, no. 2, p. 025006, 2018.
- [125] M. Nouri-Goushki, A. Sharma, L. Sasso, S. Zhang, B. C. Van der Eerden, U. Staufer, L. E. Fratila-Apachitei, and A. A. Zadpoor, "Submicron patterns-on-a-chip: fabrication of a microfluidic device incorporating 3d printed surface ornaments," *ACS Biomaterials Science Engineering*, vol. 5, no. 11, pp. 6127–6136, 2019.
- [126] M. Barlet, J.-M. Delaye, T. Charpentier, M. Gennisson, D. Bonamy, T. Rouxel, and C. L. Rountree, "Hardness and toughness of sodium borosil-

- icate glasses via vickers's indentations," *J. Non-Cryst. Solids*, vol. 417, pp. 66–79, 2015.
- [127] L. E. Nielsen and R. F. Landel, *Mechanical Properties of Polymers and Composites*. New York, NY, USA: Marcel Dekker, 2nd ed., 1994.
- [128] G. Vereecke, X. Xu, W.-K. Tsai, H. Yang, S. Armini, T. Delande, G. Doumen, F. Kentie, X. Shi, and I. Simms, "Wetting behavior of aqueous solutions on high aspect ratio nanopillars with hydrophilic surface finish," *ECS Transactions*, vol. 58, no. 6, pp. 171–182, 2013.
- [129] L. Courbin, E. Denieul, E. Dressaire, M. Roper, A. Ajdari, and H. A. Stone, "Imbibition by polygonal spreading on microdecorated surfaces," *Nat. Mater.*, vol. 6, no. 9, pp. 661–664, 2007.
- [130] A. J. Engler, S. Sen, H. L. Sweeney, and D. E. Discher, "Matrix elasticity directs stem cell lineage specification," *Cell*, vol. 126, no. 4, pp. 677–689, 2006.
- [131] M. N. Goushki, S. A. Mousavi, M. J. Abdekhodaie, and M. Sadeghi, "Free radical graft polymerization of 2-hydroxyethyl methacrylate and acrylic acid on the polysulfone membrane surface through circulation of reaction media to improve its performance and hemocompatibility properties," *J. Membr. Sci.*, vol. 564, pp. 762–772, 2018.
- [132] A. Ranella, M. Barberoglou, S. Bakogianni, C. Fotakis, and E. Stratakis, "Tuning cell adhesion by controlling the roughness and wettability of 3d micro/nano silicon structures," *Acta biomaterialia*, vol. 6, no. 7, pp. 2711–2720, 2010.
- [133] S. Y. Yang, E.-S. Kim, G. Jeon, K. Y. Choi, and J. K. Kim, "Enhanced adhesion of osteoblastic cells on polystyrene films by independent control of surface topography and wettability," *Mat. Sci. Eng. C*, vol. 33, no. 3, pp. 1689–1695, 2013.
- [134] D. Khang, J. Lu, C. Yao, K. M. Haberstroh, and T. J. Webster, "The role of nanometer and sub-micron surface features on vascular and bone cell adhesion on titanium," *Biomaterials*, vol. 29, no. 8, pp. 970–983, 2008.
- [135] M. Ganjian, K. Modaresifar, M. R. O. Ligeon, L. B. Kunkels, N. Tümer, L. Angeloni, C. W. Hagen, L. G. Otten, P.-L. Hagedoorn, I. Apachitei, L. E. Fratila-Apachitei, and A. A. Zadpoor, "Nature helps: Toward bioinspired bactericidal nanopatterns," *Advanced Materials Interfaces*, vol. 6, no. 16, p. 1900640, 2019.
- [136] K. Modaresifar, L. B. Kunkels, M. Ganjian, N. Tümer, C. W. Hagen, L. G. Otten, P.-L. Hagedoorn, L. Angeloni, M. K. Ghatkesar, L. E. Fratila-Apachitei, and A. A. Zadpoor, "Deciphering the roles of interspace and controlled disorder in the bactericidal properties of nanopatterns against staphylococcus aureus," *Nanomaterials*, vol. 10, no. 2, p. 347, 2020.
- [137] A. Rifai, N. Tran, P. Reineck, A. Elbourne, E. Mayes, A. Sarker, C. Dekiwadia, E. P. Ivanova, R. J. Crawford, T. Ohshima, B. C. Gibson, A. D. Greentree, E. Pirogova, and K. Fox, "Engineering the interface: Nanodiamond coating on 3d-printed titanium promotes mammalian cell growth

- and inhibits staphylococcus aureus colonization,” *ACS Applied Materials Interfaces*, vol. 11, no. 27, pp. 24588–24597, 2019.
- [138] S. N. Christo, A. Bachhuka, K. R. Diener, A. Mierczynska, J. D. Hayball, and K. Vasilev, “The role of surface nanotopography and chemistry on primary neutrophil and macrophage cellular responses,” *Advanced healthcare materials*, vol. 5, no. 8, pp. 956–965, 2016.
- [139] F. Y. McWhorter, T. Wang, P. Nguyen, T. Chung, and W. F. Liu, “Modulation of macrophage phenotype by cell shape,” *Proceedings of the National Academy of Sciences*, vol. 110, no. 43, pp. 17253–17258, 2013.
- [140] Y. Hou, W. Xie, L. Yu, L. C. Camacho, C. Nie, M. Zhang, R. Haag, and Q. Wei, “Surface roughness gradients reveal topography-specific mechanosensitive responses in human mesenchymal stem cells,” *Small*, vol. 16, no. 10, p. 1905422, 2020.
- [141] S. G. Higgins, M. Becce, A. Belessiotis-Richards, H. Seong, J. E. Sero, and M. M. Stevens, “High-aspect-ratio nanostructured surfaces as biological metamaterials,” *Advanced Materials*, p. 1903862, 2020.
- [142] H. Wu, T. Liu, Z. Xu, J. Qian, X. Shen, Y. Li, Y. Pan, D. Wang, K. Zheng, A. R. Boccaccini, and J. Wei, “Enhanced bacteriostatic activity, osteogenesis and osseointegration of silicon nitride/polyetherketoneketone composites with femtosecond laser induced micro/nano structural surface,” *Applied Materials Today*, vol. 18, p. 100523, 2020.
- [143] J. Lovmand, J. Justesen, M. Foss, R. H. Lauridsen, M. Lovmand, C. Modin, F. Besenbacher, F. S. Pedersen, and M. Duch, “The use of combinatorial topographical libraries for the screening of enhanced osteogenic expression and mineralization,” *Biomaterials*, vol. 30, no. 11, pp. 2015–2022, 2009.
- [144] L. E. McNamara, T. Sjöström, K. E. V. Burgess, J. J. W. Kim, E. Liu, S. Gordonov, P. V. Moghe, R. M. D. Meek, R. O. C. Oreffo, B. Su, and M. J. Dalby, “Skeletal stem cell physiology on functionally distinct titania nanotopographies,” *Biomaterials*, vol. 32, no. 30, pp. 7403–7410, 2011.
- [145] K. W. Kwon, S. S. Choi, B. Kim, S. N. Lee, M. C. Park, P. Kim, S. H. Lee, S. H. Park, and K. Y. Suh, “A microfluidic flow sensor for measuring cell adhesion,” in *SENSORS, 2006 IEEE*, pp. 105–108, IEEE.
- [146] P. Zorlutuna, Z. Rong, P. Vadgama, and V. Hasirci, “Influence of nanopatterns on endothelial cell adhesion: Enhanced cell retention under shear stress,” *Acta biomaterialia*, vol. 5, no. 7, pp. 2451–2459, 2009.
- [147] C. G. Galbraith and M. P. Sheetz, “A micromachined device provides a new bend on fibroblast traction forces,” *Proceedings of the National Academy of Sciences*, vol. 94, no. 17, pp. 9114–9118, 1997.
- [148] J. L. Tan, J. Tien, D. M. Pirone, D. S. Gray, K. Bhadriraju, and C. S. Chen, “Cells lying on a bed of microneedles: an approach to isolate mechanical force,” *Proceedings of the National Academy of Sciences*, vol. 100, no. 4, pp. 1484–1489, 2003.
- [149] P. Roy, Z. Rajfur, P. Pomorski, and K. Jacobson, “Microscope-based tech-

- niques to study cell adhesion and migration,” *Nature Cell Biology*, vol. 4, no. 4, pp. E91–E96, 2002.
- [150] G. Bao and S. Suresh, “Cell and molecular mechanics of biological materials,” *Nature Materials*, vol. 2, no. 11, pp. 715–725, 2003.
- [151] M. Grau, J. Matena, M. Teske, S. Petersen, P. Aliuos, L. Roland, N. Grabow, H. Murua Escobar, N.-C. Gellrich, and H. Haferkamp, “In vitro evaluation of pcl and p (3hb) as coating materials for selective laser melted porous titanium implants,” *Materials*, vol. 10, no. 12, p. 1344, 2017.
- [152] G. Longo, C. A. Ioannidu, A. Scotto d’Abusco, F. Superti, C. Misiano, R. Zanoni, L. Politi, L. Mazzola, F. Iosi, and F. Mura, “Improving osteoblast response in vitro by a nanostructured thin film with titanium carbide and titanium oxides clustered around graphitic carbon,” *PLoS One*, vol. 11, no. 3, p. e0152566, 2016.
- [153] A. V. Taubenberger, M. A. Woodruff, H. Bai, D. J. Muller, and D. W. Huttmacher, “The effect of unlocking rgd-motifs in collagen i on pre-osteoblast adhesion and differentiation,” *Biomaterials*, vol. 31, no. 10, pp. 2827–2835, 2010.
- [154] L. Jiang, Z. Sun, X. Chen, J. Li, Y. Xu, Y. Zu, J. Hu, D. Han, and C. Yang, “Cells sensing mechanical cues: Stiffness influences the lifetime of cell–extracellular matrix interactions by affecting the loading rate,” *ACS Nano*, vol. 10, no. 1, pp. 207–217, 2016.
- [155] E. Lamers, J. t. Riet, M. Domanski, R. Luttmge, C. G. Figdor, J. G. Gardeniens, X. F. Walboomers, and J. Jansen, “Dynamic cell adhesion and migration on nanoscale grooved substrates,” 2012.
- [156] J. Markwardt, J. Friedrichs, C. Werner, A. Davids, H. Weise, R. Lesche, A. Weber, U. Range, H. Meißner, G. Lauer, and B. Reitemeier, “Experimental study on the behavior of primary human osteoblasts on laser-cused pure titanium surfaces,” *Journal of Biomedical Materials Research Part A*, vol. 102, no. 5, pp. 1422–1430, 2014.
- [157] T. Naganuma, “The relationship between cell adhesion force activation on nano/micro-topographical surfaces and temporal dependence of cell morphology,” *Nanoscale*, vol. 9, no. 35, pp. 13171–13186, 2017.
- [158] P. Wysotzki, A. Sancho, J. Gimsa, and J. Groll, “A comparative analysis of detachment forces and energies in initial and mature cell-material interaction,” *Colloids and Surfaces B: Biointerfaces*, vol. 190, p. 110894, 2020.
- [159] P. Bertoncini, S. Le Chevalier, S. Lavenus, P. Layrolle, and G. Louarn, “Early adhesion of human mesenchymal stem cells on tio2 surfaces studied by single-cell force spectroscopy measurements,” *Journal of Molecular Recognition*, vol. 25, no. 5, pp. 262–269, 2012.
- [160] C. Herranz-Diez, Q. Li, C. Lamprecht, C. Mas-Moruno, S. Neubauer, H. Kessler, J. M. Manero, J. Guillem-Martí, and C. Selhuber-Unkel, “Bioactive compounds immobilized on ti and tinbhf: Afm-based investigations of biofunctionalization efficiency and cell adhesion,” *Colloids and Surfaces B: Biointerfaces*, vol. 136, pp. 704–711, 2015.

- [161] C. Cimmino, L. Rossano, P. A. Netti, and M. Ventre, “Spatio-temporal control of cell adhesion: Toward programmable platforms to manipulate cell functions and fate,” *Frontiers in Bioengineering and Biotechnology*, vol. 6, no. 190, 2018.
- [162] R. Changede, X. Xu, F. Margadant, and M. Sheetz, “Nascent integrin adhesions form on all matrix rigidities after integrin activation,” *Developmental Cell*, vol. 35, no. 5, pp. 614–621, 2015.
- [163] N. Strohmeyer, M. Bharadwaj, M. Costell, R. Fässler, and D. J. Müller, “Fibronectin-bound 51 integrins sense load and signal to reinforce adhesion in less than a second,” *Nature Materials*, vol. 16, no. 12, pp. 1262–1270, 2017.
- [164] A. Taubenberger, D. A. Cisneros, J. Friedrichs, P.-H. Puech, D. J. Muller, and C. M. Franz, “Revealing early steps of 21 integrin-mediated adhesion to collagen type i by using single-cell force spectroscopy,” *Molecular Biology of the Cell*, vol. 18, no. 5, pp. 1634–1644, 2007.
- [165] S. Belikov, J. Alexander, C. Wall, I. Yermolenko, S. Magonov, and I. Malovichko, “Thermal tune method for afm oscillatory resonant imaging in air and liquid,” in *2014 American Control Conference*, pp. 1009–1014.
- [166] I. N. Sneddon, “The relation between load and penetration in the axisymmetric boussinesq problem for a punch of arbitrary profile,” *International Journal of Engineering Science*, vol. 3, no. 1, pp. 47–57, 1965.
- [167] U. Horzum, B. Ozdil, and D. Pesen-Okvur, “Step-by-step quantitative analysis of focal adhesions,” *MethodsX*, vol. 1, pp. 56–59, 2014.
- [168] H. Busscher, A. Van Pelt, P. De Boer, H. De Jong, and J. Arends, “The effect of surface roughening of polymers on measured contact angles of liquids,” *Colloids and surfaces*, vol. 9, no. 4, pp. 319–331, 1984.
- [169] M. Lampin, R. Warocquier-Clérout, C. Legris, M. Degrange, and M. Sigot-Luizard, “Correlation between substratum roughness and wettability, cell adhesion, and cell migration,” *Journal of Biomedical Materials Research: An Official Journal of The Society for Biomaterials and The Japanese Society for Biomaterials*, vol. 36, no. 1, pp. 99–108, 1997.
- [170] M. Benoit and H. E. Gaub, “Measuring cell adhesion forces with the atomic force microscope at the molecular level,” *Cells Tissues Organs*, vol. 172, no. 3, pp. 174–189, 2002.
- [171] J. Friedrichs, K. R. Legate, R. Schubert, M. Bharadwaj, C. Werner, D. J. Müller, and M. Benoit, “A practical guide to quantify cell adhesion using single-cell force spectroscopy,” *Methods*, vol. 60, no. 2, pp. 169–178, 2013.
- [172] M. Ferrari, F. Cirisano, and M. C. Morán, “Mammalian cell behavior on hydrophobic substrates: influence of surface properties,” *Colloids and Interfaces*, vol. 3, no. 2, p. 48, 2019.
- [173] A. A. Khalili and M. R. Ahmad, “A review of cell adhesion studies for biomedical and biological applications,” *International journal of molecular sciences*, vol. 16, no. 8, pp. 18149–18184, 2015.
- [174] N. C. Gauthier, T. A. Masters, and M. P. Sheetz, “Mechanical feedback

- between membrane tension and dynamics,” *Trends in Cell Biology*, vol. 22, no. 10, pp. 527–535, 2012.
- [175] C. W. Kuo, D.-Y. Chueh, and P. Chen, “Investigation of size-dependent cell adhesion on nanostructured interfaces,” *Journal of Nanobiotechnology*, vol. 12, no. 1, p. 54, 2014.
- [176] R. Zaidel-Bar, M. Cohen, L. Addadi, and B. Geiger, “Hierarchical assembly of cell–matrix adhesion complexes,” *Biochemical Society Transactions*, vol. 32, no. 3, pp. 416–420, 2004.
- [177] Y. Zhukova, C. Hiepen, P. Knaus, M. Osterland, S. Prohaska, J. W. C. Dunlop, P. Fratzl, and E. V. Skorb, “The role of titanium surface nanostructuring on preosteoblast morphology, adhesion, and migration,” *Advanced Healthcare Materials*, vol. 6, no. 15, p. 1601244, 2017.
- [178] J. Zhou, X. Zhang, J. Sun, Z. Dang, J. Li, X. Li, and T. Chen, “The effects of surface topography of nanostructure arrays on cell adhesion,” *Physical Chemistry Chemical Physics*, vol. 20, no. 35, pp. 22946–22951, 2018.
- [179] M. A. Bucaro, Y. Vasquez, B. D. Hatton, and J. Aizenberg, “Fine-tuning the degree of stem cell polarization and alignment on ordered arrays of high-aspect-ratio nanopillars,” *ACS Nano*, vol. 6, no. 7, pp. 6222–6230, 2012.
- [180] N. Buch-Månson, D.-H. Kang, D. Kim, K. E. Lee, M.-H. Yoon, and K. L. Martinez, “Mapping cell behavior across a wide range of vertical silicon nanocolumn densities,” *Nanoscale*, vol. 9, no. 17, pp. 5517–5527, 2017.
- [181] N. Buch-Månson, A. Spangenberg, L. P. C. Gomez, J.-P. Malval, O. Sopera, and K. L. Martinez, “Rapid prototyping of polymeric nanopillars by 3d direct laser writing for controlling cell behavior,” *Scientific Reports*, vol. 7, no. 1, p. 9247, 2017.
- [182] J. Stricker, Y. Aratyn-Schaus, P. Oakes, and M. Gardel, “Spatiotemporal constraints on the force-dependent growth of focal adhesions,” *Biophysical Journal*, vol. 100, no. 12, pp. 2883–2893, 2011.
- [183] L. Trichet, J. Le Digabel, R. J. Hawkins, S. R. K. Vedula, M. Gupta, C. Ribault, P. Hersen, R. Voituriez, and B. Ladoux, “Evidence of a large-scale mechanosensing mechanism for cellular adaptation to substrate stiffness,” *Proceedings of the National Academy of Sciences*, vol. 109, no. 18, p. 6933, 2012.
- [184] C. Roudit, S. Sekatski, G. Dietler, S. Catsicas, F. Lafont, and S. Kasas, “Stiffness tomography by atomic force microscopy,” *Biophysical Journal*, vol. 97, no. 2, pp. 674–677, 2009.
- [185] L. Angeloni, M. Reggente, D. Passeri, M. Natali, and M. Rossi, “Identification of nanoparticles and nanosystems in biological matrices with scanning probe microscopy,” *WIREs Nanomedicine and Nanobiotechnology*, vol. 10, no. 6, p. e1521, 2018.
- [186] M. Maninova, J. Caslavsky, and T. Vomastek, “The assembly and function of perinuclear actin cap in migrating cells,” *Protoplasma*, vol. 254, no. 3, pp. 1207–1218, 2017.
- [187] M. Fritzsche, D. Li, H. Colin-York, V. T. Chang, E. Moeendarbary, J. H.

- Felce, E. Sezgin, G. Charras, E. Betzig, and C. Eggeling, “Self-organizing actin patterns shape membrane architecture but not cell mechanics,” *Nature Communications*, vol. 8, no. 1, p. 14347, 2017.
- [188] C. R. Guerrero, P. D. Garcia, and R. Garcia, “Subsurface imaging of cell organelles by force microscopy,” *ACS Nano*, vol. 13, no. 8, pp. 9629–9637, 2019.
- [189] L. Haviv, Y. Brill-Karniely, R. Mahaffy, F. Backouche, A. Ben-Shaul, T. D. Pollard, and A. Bernheim-Groswasser, “Reconstitution of the transition from lamellipodium to filopodium in a membrane-free system,” *Proceedings of the National Academy of Sciences of the United States of America*, vol. 103, no. 13, p. 4906, 2006.
- [190] Y. Ideses, Y. Brill-Karniely, L. Haviv, A. Ben-Shaul, and A. Bernheim-Groswasser, “Arp2/3 branched actin network mediates filopodia-like bundles formation in vitro,” *PLoS one*, vol. 3, no. 9, pp. e3297–e3297, 2008.
- [191] M. Soares e Silva, M. Depken, B. Stuhmann, M. Korsten, F. C. MacKintosh, and G. H. Koenderink, “Active multistage coarsening of actin networks driven by myosin motors,” *Proceedings of the National Academy of Sciences*, vol. 108, no. 23, p. 9408, 2011.
- [192] A. Lerebours, P. Vigneron, S. Bouvier, A. Rassineux, M. Bigerelle, and C. Egles, “Additive manufacturing process creates local surface roughness modifications leading to variation in cell adhesion on multifaceted tial6v4 samples,” *Bioprinting*, vol. 16, p. e00054, 2019.
- [193] C. Wu, M. Chen, T. Zheng, and X. Yang, “Effect of surface roughness on the initial response of mc3t3-e1 cells cultured on polished titanium alloy,” *Bio-medical materials and engineering*, vol. 26, no. s1, pp. S155–S164, 2015.
- [194] K. A. Jansen, D. M. Donato, H. E. Balcioglu, T. Schmidt, E. H. J. Danen, and G. H. Koenderink, “A guide to mechanobiology: Where biology and physics meet,” *Biochimica et Biophysica Acta (BBA) - Molecular Cell Research*, vol. 1853, no. 11, Part B, pp. 3043–3052, 2015.
- [195] A. Buxboim, J. Irianto, J. Swift, A. Athirasala, J.-W. Shin, F. Rehfeldt, and D. E. Discher, “Coordinated increase of nuclear tension and lamin-a with matrix stiffness outcompetes lamin-b receptor that favors soft tissue phenotypes,” *Molecular Biology of the Cell*, vol. 28, no. 23, pp. 3333–3348, 2017.
- [196] M. Zhu, H. Ye, J. Fang, C. Zhong, J. Yao, J. Park, X. Lu, and F. Ren, “Engineering high-resolution micropatterns directly onto titanium with optimized contact guidance to promote osteogenic differentiation and bone regeneration,” *ACS Applied Materials Interfaces*, vol. 11, no. 47, pp. 43888–43901, 2019.
- [197] S. Stewart, A. Darwood, S. Masouros, C. Higgins, and A. Ramasamy, “Mechanotransduction in osteogenesis,” *Bone Joint Research*, vol. 9, no. 1, pp. 1–14, 2020.
- [198] B. Ghezzi, P. Lagonegro, N. Fukata, L. Parisi, D. Calestani, C. Galli, G. Salviati, G. M. Macaluso, and F. Rossi, “Sub-micropillar spacing modu-

- lates the spatial arrangement of mouse mc3t3-e1 osteoblastic cells,” *Nanomaterials*, vol. 9, no. 12, p. 1701, 2019.
- [199] E. Martinez, K. Seunarine, H. Morgan, N. Gadegaard, C. D. Wilkinson, and M. O. Riehle, “Air-trapping on biocompatible nanopatterns,” *Langmuir*, vol. 22, no. 26, pp. 11230–11233, 2006.
- [200] D. Khang, J. Choi, Y.-M. Im, Y.-J. Kim, J.-H. Jang, S. S. Kang, T.-H. Nam, J. Song, and J.-W. Park, “Role of subnano-, nano- and submicron-surface features on osteoblast differentiation of bone marrow mesenchymal stem cells,” *Biomaterials*, vol. 33, no. 26, pp. 5997–6007, 2012.
- [201] M. Sun, G. Chi, J. Xu, Y. Tan, J. Xu, S. Lv, Z. Xu, Y. Xia, L. Li, and Y. Li, “Extracellular matrix stiffness controls osteogenic differentiation of mesenchymal stem cells mediated by integrin 5,” *Stem Cell Research Therapy*, vol. 9, no. 1, p. 52, 2018.
- [202] H.-S. Lee, J.-I. Kang, W.-J. Chung, D. H. Lee, B. Y. Lee, S.-W. Lee, and S. Y. Yoo, “Engineered phage matrix stiffness-modulating osteogenic differentiation,” *ACS Applied Materials Interfaces*, vol. 10, no. 5, pp. 4349–4358, 2018.
- [203] K. Anselme, M. Bigerelle, B. Noel, E. Dufresne, D. Judas, A. Iost, and P. Hardouin, “Qualitative and quantitative study of human osteoblast adhesion on materials with various surface roughnesses,” *Journal of Biomedical Materials Research*, vol. 49, no. 2, pp. 155–166, 2000.
- [204] M. Ghibaudo, A. Saez, L. Trichet, A. Xayaphoummine, J. Browaeys, P. Silberzan, A. Buguin, and B. Ladoux, “Traction forces and rigidity sensing regulate cell functions,” *Soft Matter*, vol. 4, no. 9, pp. 1836–1843, 2008.
- [205] Y. Yang, K. Wang, X. Gu, and K. W. Leong, “Biophysical regulation of cell behavior—cross talk between substrate stiffness and nanotopography,” *Engineering*, vol. 3, no. 1, pp. 36–54, 2017.
- [206] A. J. Keung, E. M. de Juan-Pardo, D. V. Schaffer, and S. Kumar, “Rho gtpases mediate the mechanosensitive lineage commitment of neural stem cells,” *STEM CELLS*, vol. 29, no. 11, pp. 1886–1897, 2011.
- [207] F. Martino, A. R. Prestrelo, V. Vinarský, S. Pagliari, and G. Forte, “Cellular mechanotransduction: From tension to function,” *Frontiers in physiology*, vol. 9, pp. 824–824, 2018.
- [208] J. E. Gautrot, J. Malmström, M. Sundh, C. Margadant, A. Sonnenberg, and D. S. Sutherland, “The nanoscale geometrical maturation of focal adhesions controls stem cell differentiation and mechanotransduction,” *Nano Letters*, vol. 14, no. 7, pp. 3945–3952, 2014.
- [209] C. R. Arciola, D. Campoccia, and L. Montanaro, “Implant infections: adhesion, biofilm formation and immune evasion,” *Nature Reviews Microbiology*, vol. 16, no. 7, pp. 397–409, 2018.
- [210] G. Mendonça, D. B. S. Mendonça, F. J. L. Aragão, and L. F. Cooper, “Advancing dental implant surface technology – from micron- to nanotopography,” *Biomaterials*, vol. 29, no. 28, pp. 3822–3835, 2008.
- [211] J. Pajarinen, T. Lin, E. Gibon, Y. Kohno, M. Maruyama, K. Nathan, L. Lu,

- Z. Yao, and S. B. Goodman, “Mesenchymal stem cell-macrophage crosstalk and bone healing,” *Biomaterials*, vol. 196, pp. 80–89, 2019.
- [212] D. G. Russell, L. Huang, and B. C. VanderVen, “Immunometabolism at the interface between macrophages and pathogens,” *Nature Reviews Immunology*, vol. 19, no. 5, pp. 291–304, 2019.
- [213] L. Saldaña, F. Bensiamar, G. Vallés, F. J. Mancebo, E. García-Rey, and N. Vilaboa, “Immunoregulatory potential of mesenchymal stem cells following activation by macrophage-derived soluble factors,” *Stem Cell Research Therapy*, vol. 10, no. 1, p. 58, 2019.
- [214] G. L. Seim, E. C. Britt, S. V. John, F. J. Yeo, A. R. Johnson, R. S. Eisenstein, D. J. Pagliarini, and J. Fan, “Two-stage metabolic remodelling in macrophages in response to lipopolysaccharide and interferon- stimulation,” *Nature Metabolism*, vol. 1, no. 7, pp. 731–742, 2019.
- [215] D. Hachim, S. T. LoPresti, R. D. Rege, Y. Umeda, A. Iftikhar, A. L. Nolfi, C. D. Skillen, and B. N. Brown, “Distinct macrophage populations and phenotypes associated with il-4 mediated immunomodulation at the host implant interface,” *Biomaterials Science*, vol. 8, no. 20, pp. 5751–5762, 2020.
- [216] Y. Jia, W. Yang, K. Zhang, S. Qiu, J. Xu, C. Wang, and Y. Chai, “Nanofiber arrangement regulates peripheral nerve regeneration through differential modulation of macrophage phenotypes,” *Acta Biomaterialia*, vol. 83, pp. 291–301, 2019.
- [217] H. Rostam, S. Singh, N. Vrana, M. Alexander, and A. Ghaemmaghami, “Impact of surface chemistry and topography on the function of antigen presenting cells,” *Biomaterials science*, vol. 3, no. 3, pp. 424–441, 2015.
- [218] T. U. Luu, S. C. Gott, B. W. K. Woo, M. P. Rao, and W. F. Liu, “Micro- and nanopatterned topographical cues for regulating macrophage cell shape and phenotype,” *ACS Applied Materials Interfaces*, vol. 7, no. 51, pp. 28665–28672, 2015.
- [219] E. Saino, M. L. Focarete, C. Gualandi, E. Emanuele, A. I. Cornaglia, M. Imbriani, and L. Visai, “Effect of electrospun fiber diameter and alignment on macrophage activation and secretion of proinflammatory cytokines and chemokines,” *Biomacromolecules*, vol. 12, no. 5, pp. 1900–1911, 2011.
- [220] H. Cao, K. Mchugh, S. Y. Chew, and J. M. Anderson, “The topographical effect of electrospun nanofibrous scaffolds on the in vivo and in vitro foreign body reaction,” *Journal of Biomedical Materials Research Part A*, vol. 93A, no. 3, pp. 1151–1159, 2010.
- [221] S. Chen, J. A. Jones, Y. Xu, H.-Y. Low, J. M. Anderson, and K. W. Leong, “Characterization of topographical effects on macrophage behavior in a foreign body response model,” *Biomaterials*, vol. 31, no. 13, pp. 3479–3491, 2010.
- [222] K. Wang, W.-D. Hou, X. Wang, C. Han, I. Vuletic, N. Su, W.-X. Zhang, Q.-S. Ren, L. Chen, and Y. Luo, “Overcoming foreign-body reaction through nanotopography: Biocompatibility and immunoisolation properties of a nanofibrous membrane,” *Biomaterials*, vol. 102, pp. 249–258, 2016.

- [223] V. Malheiro, F. Lehner, V. Dinca, P. Hoffmann, and K. Maniura-Weber, "Convex and concave micro-structured silicone controls the shape, but not the polarization state of human macrophages," *Biomaterials science*, vol. 4, no. 11, pp. 1562–1573, 2016.
- [224] S. Singh, D. Awuah, H. M. Rostam, R. D. Emes, N. K. Kandola, D. Onion, S. S. Htwe, B. Rajchagool, B.-H. Cha, D. Kim, P. J. Tighe, N. E. Vrana, A. Khademhosseini, and A. Ghaemmaghami, "Unbiased analysis of the impact of micropatterned biomaterials on macrophage behavior provides insights beyond predefined polarization states," *ACS Biomaterials Science Engineering*, vol. 3, no. 6, pp. 969–978, 2017.
- [225] W.-W. Yue, H.-J. Li, T. Xiang, H. Qin, S.-D. Sun, and C.-S. Zhao, "Grafting of zwitterion from polysulfone membrane via surface-initiated atp with enhanced antifouling property and biocompatibility," *Journal of membrane science*, vol. 446, pp. 79–91, 2013.
- [226] R. A. Gittens, T. McLachlan, R. Olivares-Navarrete, Y. Cai, S. Berner, R. Tannenbaum, Z. Schwartz, K. H. Sandhage, and B. D. Boyan, "The effects of combined micron-/submicron-scale surface roughness and nanoscale features on cell proliferation and differentiation," *Biomaterials*, vol. 32, no. 13, pp. 3395–3403, 2011.
- [227] M. Ganjian, L. Angeloni, M. J. Mirzaali, K. Modaresifar, C. W. Hagen, M. K. Ghatkesar, P.-L. Hagedoorn, L. E. Fratila-Apachitei, and A. A. Zadpoor, "Quantitative mechanics of 3d printed nanopillars interacting with bacterial cells," *Nanoscale*, 2020.
- [228] A. Klymov, L. Prodanov, E. Lamers, J. A. Jansen, and X. F. Walboomers, "Understanding the role of nano-topography on the surface of a bone-implant," *Biomaterials Science*, vol. 1, no. 2, pp. 135–151, 2013.
- [229] L.-S. Wang, B. Duncan, R. Tang, Y.-W. Lee, B. Creran, S. G. Elci, J. Zhu, G. Yesilbag Tonga, J. Doble, M. Fessenden, M. Bayat, S. Nonnenmann, R. W. Vachet, and V. M. Rotello, "Gradient and patterned protein films stabilized via nanoimprint lithography for engineered interactions with cells," *ACS Applied Materials Interfaces*, vol. 9, no. 1, pp. 42–46, 2017.
- [230] T. Limongi, L. Tirinato, F. Pagliari, A. Giugni, M. Allione, G. Perozziello, P. Candeloro, and E. Di Fabrizio, "Fabrication and applications of micro/nanostructured devices for tissue engineering," *Nano-Micro Letters*, vol. 9, no. 1, p. 1, 2016.
- [231] T. M. Valentin, S. E. Leggett, P.-Y. Chen, J. K. Sodhi, L. H. Stephens, H. D. McClintock, J. Y. Sim, and I. Y. Wong, "Stereolithographic printing of ionically-crosslinked alginate hydrogels for degradable biomaterials and microfluidics," *Lab on a Chip*, vol. 17, no. 20, pp. 3474–3488, 2017.
- [232] Z. Chen, S. Ni, S. Han, R. Crawford, S. Lu, F. Wei, J. Chang, C. Wu, and Y. Xiao, "Nanoporous microstructures mediate osteogenesis by modulating the osteo-immune response of macrophages," *Nanoscale*, vol. 9, no. 2, pp. 706–718, 2017.
- [233] Q. Ou, K. Huang, C. Fu, C. Huang, Y. Fang, Z. Gu, J. Wu, and Y. Wang,

- “Nanosilver-incorporated halloysite nanotubes/gelatin methacrylate hybrid hydrogel with osteoimmunomodulatory and antibacterial activity for bone regeneration,” *Chemical Engineering Journal*, vol. 382, p. 123019, 2020.
- [234] C. Li, L. Yang, X. Ren, M. Lin, X. Jiang, D. Shen, T. Xu, J. Ren, L. Huang, and W. Qing, “Groove structure of porous hydroxyapatite scaffolds (has) modulates immune environment via regulating macrophages and subsequently enhances osteogenesis,” *JBIC Journal of Biological Inorganic Chemistry*, vol. 24, no. 5, pp. 733–745, 2019.
- [235] D. Karazisis, A. M. Ballo, S. Petronis, H. Agheli, L. Emanuelsson, P. Thomsen, and O. Omar, “The role of well-defined nanotopography of titanium implants on osseointegration: cellular and molecular events in vivo,” *International journal of nanomedicine*, vol. 11, pp. 1367–1382, 2016.
- [236] S. Zhang, B. Ma, F. Liu, J. Duan, S. Wang, J. Qiu, D. Li, Y. Sang, C. Liu, D. Liu, and H. Liu, “Polylactic acid nanopillar array-driven osteogenic differentiation of human adipose-derived stem cells determined by pillar diameter,” *Nano Letters*, vol. 18, no. 4, pp. 2243–2253, 2018.
- [237] L. M. K. M. M. B. P. M. M. J. F.-A. L. E. Z. A. A. Nouri-Goushki, Mahdiyeh; Angeloni, “3d printed submicron patterns reveal the interrelation between cell adhesion, cell mechanics, and osteogenesis,” *ACS Applied Materials Interfaces*, vol. 13, no. 29, pp. 33767–33781, 2021.
- [238] J. M. Daley, J. S. Reichner, E. J. Mahoney, L. Manfield, W. L. Henry, B. Mastrofrancesco, and J. E. Albina, “Modulation of macrophage phenotype by soluble product (s) released from neutrophils,” *The Journal of Immunology*, vol. 174, no. 4, pp. 2265–2272, 2005.
- [239] L. C. Borish and J. W. Steinke, “2. cytokines and chemokines,” *Journal of Allergy and Clinical Immunology*, vol. 111, no. 2, Supplement 2, pp. S460–S475, 2003.
- [240] K. Yang, Y. Wu, H. Xie, M. Li, S. Ming, L. Li, M. Li, M. Wu, S. Gong, and X. Huang, “Macrophage-mediated inflammatory response decreases mycobacterial survival in mouse mscs by augmenting no production,” *Scientific Reports*, vol. 6, no. 1, p. 27326, 2016.
- [241] Y. Bi, J. Chen, F. Hu, J. Liu, M. Li, and L. Zhao, “M2 macrophages as a potential target for antiatherosclerosis treatment,” *Neural Plasticity*, vol. 2019, p. 6724903, 2019.
- [242] A. C. La Flamme, M. Kharkrang, S. Stone, S. Mirmoeini, D. Chuluundorj, and R. Kyle, “Type ii-activated murine macrophages produce il-4,” 2012.
- [243] L. Darwich, G. Coma, R. Peña, R. Bellido, E. J. J. Blanco, J. A. Este, F. E. Borrás, B. Clotet, L. Ruiz, A. Rosell, F. Andreo, R. M. E. Parkhouse, and M. Bofill, “Secretion of interferon- by human macrophages demonstrated at the single-cell level after costimulation with interleukin (il)-12 plus il-18,” *Immunology*, vol. 126, no. 3, pp. 386–393, 2009.
- [244] J. Wang, Y. Su, L. Xu, and D. Li, “Micro-patterned surface construction on bcp ceramics and the regulation on inflammation-involved osteogenic

- differentiation,” *Materials Science and Engineering: C*, vol. 116, p. 111220, 2020.
- [245] M. Weber, A. B. Mackenzie, S. D. Bull, and T. D. James, “Fluorescence-based tool to detect endogenous peroxynitrite in m1-polarized murine j774.2 macrophages,” *Analytical Chemistry*, vol. 90, no. 17, pp. 10621–10627, 2018.
- [246] L. Lv, Y. Xie, K. Li, T. Hu, X. Lu, Y. Cao, and X. Zheng, “Unveiling the mechanism of surface hydrophilicity-modulated macrophage polarization,” *Advanced Healthcare Materials*, vol. 7, no. 19, p. 1800675, 2018.
- [247] S. Gao, R. Lu, X. Wang, J. Chou, N. Wang, X. Huai, C. Wang, Y. Zhao, and S. Chen, “Immune response of macrophages on super-hydrophilic tio2 nanotube arrays,” *Journal of Biomaterials Applications*, vol. 34, no. 9, pp. 1239–1253, 2020.
- [248] H. Takayanagi, “Osteoimmunology: shared mechanisms and crosstalk between the immune and bone systems,” *Nature Reviews Immunology*, vol. 7, no. 4, pp. 292–304, 2007.
- [249] G. Mestres, S.-S. D. Carter, N. P. Hailer, and A. Diez-Escudero, “A practical guide for evaluating the osteoimmunomodulatory properties of biomaterials,” *Acta Biomaterialia*, 2021.
- [250] J. M. Curran, J. A. Gallagher, and J. A. Hunt, “The inflammatory potential of biphasic calcium phosphate granules in osteoblast/macrophage co-culture,” *Biomaterials*, vol. 26, no. 26, pp. 5313–5320, 2005.
- [251] M. Feldmann and R. N. Maini, “Anti-tnf therapy, from rationale to standard of care: What lessons has it taught us?,” *Journal of Immunology*, vol. 185, no. 2, pp. 791–794, 2010.
- [252] L. Gilbert, X. He, P. Farmer, S. Boden, M. Kozlowski, J. Rubin, and M. S. Nanes, “Inhibition of osteoblast differentiation by tumor necrosis factor-,” *Endocrinology*, vol. 141, no. 11, pp. 3956–3964, 2000.
- [253] J. B. Gonzales, M. A. Purdon, and S. M. Horowitz, “In vitro studies on the role of titanium in aseptic loosening,” *Clinical Orthopaedics and Related Research®*, vol. 330, 1996.
- [254] K. Hess, A. Ushmorov, J. Fiedler, R. E. Brenner, and T. Wirth, “Tnf promotes osteogenic differentiation of human mesenchymal stem cells by triggering the nf-b signaling pathway,” *Bone*, vol. 45, no. 2, pp. 367–376, 2009.
- [255] J. Ding, O. Ghali, P. Lencel, O. Broux, C. Chauveau, J. C. Devedjian, P. Hardouin, and D. Magne, “Tnf- and il-1 inhibit runx2 and collagen expression but increase alkaline phosphatase activity and mineralization in human mesenchymal stem cells,” *Life Sciences*, vol. 84, no. 15, pp. 499–504, 2009.
- [256] L. Rifas, “T-cell cytokine induction of bmp-2 regulates human mesenchymal stromal cell differentiation and mineralization,” *Journal of Cellular Biochemistry*, vol. 98, no. 4, pp. 706–714, 2006.
- [257] K. Sakthivel, A. O’Brien, K. Kim, and M. Hoorfar, “Microfluidic analysis of heterotypic cellular interactions: A review of techniques and applications,” *TrAC Trends in Analytical Chemistry*, vol. 117, pp. 166–185, 2019.

- [258] K. Li, S. Liu, T. Hu, I. Razanau, X. Wu, H. Ao, L. Huang, Y. Xie, and X. Zheng, “Optimized nanointerface engineering of micro/nanostructured titanium implants to enhance cell–nanotopography interactions and osseointegration,” *ACS Biomaterials Science Engineering*, vol. 6, no. 2, pp. 969–983, 2020.
- [259] M. D. Swartzlander, A. K. Blakney, L. D. Amer, K. D. Hankenson, T. R. Kyriakides, and S. J. Bryant, “Immunomodulation by mesenchymal stem cells combats the foreign body response to cell-laden synthetic hydrogels,” *Biomaterials*, vol. 41, pp. 79–88, 2015.
- [260] L. A. Córdova, F. Loi, T.-H. Lin, E. Gibon, J. Pajarinen, A. Nabeshima, L. Lu, Z. Yao, and S. B. Goodman, “Ccl2, ccl5, and igf-1 participate in the immunomodulation of osteogenesis during m1/m2 transition in vitro,” *Journal of Biomedical Materials Research Part A*, vol. 105, no. 11, pp. 3069–3076, 2017.
- [261] G. Vallés, F. Bensiamar, L. Crespo, M. Arruebo, N. Vilaboa, and L. Saldaña, “Topographical cues regulate the crosstalk between mscs and macrophages,” *Biomaterials*, vol. 37, pp. 124–133, 2015.
- [262] D. Naskar, S. Nayak, T. Dey, and S. C. Kundu, “Non-mulberry silk fibroin influence osteogenesis and osteoblast-macrophage cross talk on titanium based surface,” *Scientific Reports*, vol. 4, no. 1, p. 4745, 2014.
- [263] D. E. M. M. Q. L. P. B. M. M.-L. F.-A. A. Z. M. Nouri-Goushki, A. Isaakidou, “3d printed submicron patterns orchestrate the response of macrophages,” *Nanoscale*, 2021.
- [264] T. J. Bartosh and J. H. Ylostalo, “Macrophage inflammatory assay,” *Bio-protocol*, vol. 4, no. 14, p. e1180, 2014.
- [265] C.-W. Wei, J.-Y. Cheng, and T.-H. Young, “Elucidating in vitro cell-cell interaction using a microfluidic coculture system,” *Biomedical Microdevices*, vol. 8, no. 1, pp. 65–71, 2006.
- [266] F. Loi, L. A. Córdova, J. Pajarinen, T.-h. Lin, Z. Yao, and S. B. Goodman, “Inflammation, fracture and bone repair,” *Bone*, vol. 86, pp. 119–130, 2016.
- [267] L. A. Córdova, F. Loi, T. Lin, E. Gibon, J. Pajarinen, A. Nabeshima, L. Lu, Z. Yao, and S. B. Goodman, “C cl2, ccl5, and igf-1 participate in the immunomodulation of osteogenesis during m1/m 2 transition in vitro,” *Journal of Biomedical Materials Research Part A*, vol. 105, no. 11, pp. 3069–3076, 2017.
- [268] F. Loi, L. A. Córdova, R. Zhang, J. Pajarinen, T.-h. Lin, S. B. Goodman, and Z. Yao, “The effects of immunomodulation by macrophage subsets on osteogenesis in vitro,” *Stem Cell Research Therapy*, vol. 7, no. 1, p. 15, 2016.
- [269] J. Pajarinen, Y. Tamaki, J. K. Antonios, T.-H. Lin, T. Sato, Z. Yao, M. Takagi, Y. T. Konttinen, and S. B. Goodman, “Modulation of mouse macrophage polarization in vitro using il-4 delivery by osmotic pumps,” *Journal of Biomedical Materials Research Part A*, vol. 103, no. 4, pp. 1339–1345, 2015.

- [270] C. Li, L. Yang, X. Ren, M. Lin, X. Jiang, D. Shen, T. Xu, J. Ren, L. Huang, W. Qing, J. Zheng, and Y. Mu, "Groove structure of porous hydroxyapatite scaffolds (has) modulates immune environment via regulating macrophages and subsequently enhances osteogenesis," *JBIC Journal of Biological Inorganic Chemistry*, vol. 24, no. 5, pp. 733–745, 2019.
- [271] V. Malheiro, Y. Elbs-Glatz, M. Obarzanek-Fojt, K. Maniura-Weber, and A. Bruinink, "Harvesting pre-polarized macrophages using thermo-responsive substrates," *Scientific Reports*, vol. 7, no. 1, p. 42495, 2017.
- [272] K. Igarashi, M. Hirafuji, H. Adachi, H. Shinoda, and H. Mitani, "Role of endogenous pge2 in osteoblastic functions of a clonal osteoblast-like cell, mc3t3-e1," *Prostaglandins, Leukotrienes and Essential Fatty Acids (PLEFA)*, vol. 50, no. 4, pp. 169–172, 1994.
- [273] E.-C. Kim, T.-H. Kim, J.-H. Jung, S. O. Hong, and D.-W. Lee, "Enhanced osteogenic differentiation of mc3t3-e1 on rhbmp-2-immobilized titanium via click reaction," *Carbohydrate Polymers*, vol. 103, pp. 170–178, 2014.
- [274] F. Zhang, L.-f. Ren, H.-s. Lin, M.-n. Yin, Y.-q. Tong, and G.-s. Shi, "The optimal dose of recombinant human osteogenic protein-1 enhances differentiation of mouse osteoblast-like cells: An in vitro study," *Archives of Oral Biology*, vol. 57, no. 5, pp. 460–468, 2012.
- [275] S. Ni, D. Zhai, Z. Huan, T. Zhang, J. Chang, and C. Wu, "Nanosized concave pit/convex dot microarray for immunomodulatory osteogenesis and angiogenesis," *Nanoscale*, vol. 12, no. 31, pp. 16474–16488, 2020.
- [276] P. Neacsu, A. Mazare, P. Schmuki, and A. Cimpean, "Attenuation of the macrophage inflammatory activity by tio nanotubes via inhibition of mapk and nf-b pathways," *International journal of nanomedicine*, vol. 10, pp. 6455–6467, 2015.
- [277] X. Shen, Y. Yu, P. Ma, Z. Luo, Y. Hu, M. Li, Y. He, Y. Zhang, Z. Peng, G. Song, and K. Cai, "Titania nanotubes promote osteogenesis via mediating crosstalk between macrophages and mscs under oxidative stress," *Colloids and Surfaces B: Biointerfaces*, vol. 180, pp. 39–48, 2019.
- [278] E. A. Cavalcanti-Adam, T. Volberg, A. Micoulet, H. Kessler, B. Geiger, and J. P. Spatz, "Cell spreading and focal adhesion dynamics are regulated by spacing of integrin ligands," *Biophysical Journal*, vol. 92, no. 8, pp. 2964–2974, 2007.
- [279] K. Garg, N. A. Pullen, C. A. Oskeritzian, J. J. Ryan, and G. L. Bowlin, "Macrophage functional polarization (m1/m2) in response to varying fiber and pore dimensions of electrospun scaffolds," *Biomaterials*, vol. 34, no. 18, pp. 4439–4451, 2013.
- [280] E. Lamers, X. F. Walboomers, M. Domanski, L. Prodanov, J. Melis, R. Luttge, L. Winnubst, J. M. Anderson, H. J. G. E. Gardeniers, and J. A. Jansen, "In vitro and in vivo evaluation of the inflammatory response to nanoscale grooved substrates," *Nanomedicine: Nanotechnology, Biology and Medicine*, vol. 8, no. 3, pp. 308–317, 2012.
- [281] S. F. B. Mennens, K. van den Dries, and A. Cambi, *Role for Mechanotrans-*

- duction in Macrophage and Dendritic Cell Immunobiology*, pp. 209–242. Cham: Springer International Publishing, 2017.
- [282] S. Wan, X. Fu, Y. Ji, M. Li, X. Shi, and Y. Wang, “Fak- and yap/taz dependent mechanotransduction pathways are required for enhanced immunomodulatory properties of adipose-derived mesenchymal stem cells induced by aligned fibrous scaffolds,” *Biomaterials*, vol. 171, pp. 107–117, 2018.
- [283] G. Girasole, R. Jilka, G. Passeri, S. Boswell, G. Boder, D. Williams, and S. Manolagas, “17 beta-estradiol inhibits interleukin-6 production by bone marrow-derived stromal cells and osteoblasts in vitro: a potential mechanism for the antiosteoporotic effect of estrogens,” *The Journal of clinical investigation*, vol. 89, no. 3, pp. 883–891, 1992.
- [284] T. Kon, T.-J. Cho, T. Aizawa, M. Yamazaki, N. Nooh, D. Graves, L. C. Gerstenfeld, and T. A. Einhorn, “Expression of osteoprotegerin, receptor activator of nf-b ligand (osteoprotegerin ligand) and related proinflammatory cytokines during fracture healing,” *Journal of Bone and Mineral Research*, vol. 16, no. 6, pp. 1004–1014, 2001.
- [285] D. J. Prockop, “Concise review: Two negative feedback loops place mesenchymal stem/stromal cells at the center of early regulators of inflammation,” *STEM CELLS*, vol. 31, no. 10, pp. 2042–2046, 2013.
- [286] M. R. Block, C. Badowski, A. Millon-Fremillon, D. Bouvard, A.-P. Bouin, E. Faurobert, D. Gerber-Scokaert, E. Planus, and C. Albiges-Rizo, “Podosome-type adhesions and focal adhesions, so alike yet so different,” *European journal of cell biology*, vol. 87, no. 8-9, pp. 491–506, 2008.
- [287] V. S. Meli, P. K. Veerasubramanian, H. Atcha, Z. Reitz, T. L. Downing, and W. F. Liu, “Biophysical regulation of macrophages in health and disease,” *Journal of leukocyte biology*, vol. 106, no. 2, pp. 283–299, 2019.
- [288] V. S. Meli, H. Atcha, P. K. Veerasubramanian, R. R. Nagalla, T. U. Luu, E. Y. Chen, C. F. Guerrero-Juarez, K. Yamaga, W. Pandori, and J. Y. Hsieh, “Yap-mediated mechanotransduction tunes the macrophage inflammatory response,” *Science advances*, vol. 6, no. 49, p. eabb8471, 2020.
- [289] J. Li, J. Zhang, X. Wang, N. Kawazoe, and G. Chen, “Gold nanoparticle size and shape influence on osteogenesis of mesenchymal stem cells,” *Nanoscale*, vol. 8, no. 15, pp. 7992–8007, 2016.
- [290] C.-C. Yu and H.-L. Chen, “Nanoimprint technology for patterning functional materials and its applications,” *Microelectronic Engineering*, vol. 132, pp. 98–119, 2015. Micro and Nanofabrication Breakthroughs for Electronics, MEMS and Life Sciences.
- [291] J. L. Williams, J. Iannotti, A. Ham, J. Bleuit, and J. Chen, “Effects of fluid shear stress on bone cells,” *Biorheology*, vol. 31, no. 2, pp. 163–170, 1994.
- [292] C. Wittkowske, G. C. Reilly, D. Lacroix, and C. M. Perrault, “In vitro bone cell models: Impact of fluid shear stress on bone formation,” *Frontiers in Bioengineering and Biotechnology*, vol. 4, no. 87, 2016.

Acknowledgements

I did a Ph.D. for the pleasure of finding things out and proposing new solutions to the current challenges. I have to admit that involving in such a challenging thesis project has changed my viewpoint toward my surroundings from teeny-tiny creatures such as cells towards advanced nanotechnology techniques, for which I am deeply grateful. I hope, in the near future, the results of my thesis can contribute to improving and benefiting of the human lives. Now, I would like to take this space and appreciate my colleagues, friends, and family who assisted me during my four-year journey at TUDelft:

First, I express my most deep and sincere gratitude to my supervisors, **Prof. Amir Zadpoor**, and **dr. Lidy Fratila-Apachitei** for giving me the opportunity to do my Ph.D. at the Department of Biomechanical Engineering, TUDelft. I will not forget your support and trust. Working with you was a great pleasure to me, and I learned a lot from you. You showed me how simple ideas could lead to advanced discoveries. Thanks for all your inspiration, guidance, and motivations.

To my big boss and scientific role model **Amir**: four years ago, I intentionally chose your group to do my Ph.D., since I have been impressed with the achievements and the level of competence of you and your professional group. And now, looking back in time, I am very happy with my decision, as your attitude, leadership and advice helped me to develop, flourish and establish my academic career.

Dear **Lidy**, you are more than just a daily-supervisor. You belong to the group of leaders who motivate their team members upon failures. I have to say that your kind smile and gratitude charged my batteries every single day within my PhD journey. You taught me to learn from mistakes which indeed had a great impact on my life. I will be deeply grateful for the knowledge and the professional skills I have gained from you. A big hug!

I would also like to sincerely thank my **thesis committee** for evaluating my thesis.

Meanwhile, I sincerely thank **Prof. Urs Staufer**, Department of Precision and Microsystem Engineering, TUDelft, for his significant support in nanofabrication part. Your kind advice and comments helped me so much in this period. This project would not advance smoothly without the collaboration of your team, especially **dr. Daniel Fan**, **dr. Angelo Accardo**, and **dr. Luigi Sasso** for the technical assistance with the Nanoscribe equipment and **dr. Murali Ghatkesar** for his support in performing AFM analysis.

Furthermore, I would like to thank **dr. Bram Van der Eerden**, Department of Internal Medicine, Erasmus Medical Center, who provided me an excellent opportunity for performing dynamic cell culture experiment.

Then, I would like to give special thanks to **dr. Pouyan Boukany**, Department of Chemical Engineering, TUDelft, who provided us the facilities for immunofluorescence imaging of our cells and performing AFM experiments in his lab during this period. Thanks for your trust and for offering me a wonderful opportunity to continue my research in your fantastic group.

I would also like to thank my colleagues **dr. Mohammad Mirzaali**, TUDelft for his assistance in computational modeling, **dr. Livia Angeloni**, TU Delft for her support in performing cell mechanics experiment, **dr. Q. Liu**, TU Delft, for her meticulous care in acquiring fluorescence images, and **dr. Cornelis W. Hagen** (Department of Imaging Physics, TU Delft) for the access to the SEM equipment. I enjoyed working with you all.

I would like to sincerely thank **Mr. Sander Leeftang**, **Mr. Rob Lutjebroer**, and **Mrs. Michelle Minneboo** for all the technical supports and training I received from you during the last three years.

I would like to show my gratitude to my colleagues at the Department of Biomechanical Engineering, TUDelft, **Niko** (a committed happy office-mate), **Jiahui** (I enjoyed our conversations about Chinese culture), **dr. Pedro** (I liked the Spanish cookies), **Helda** and **Maryam** (my kind-hearted Iranian office-mates), **Sebastien** and **Delphine** (a great scientist couple), **Yageng**, **Costanza** (it was always fun to have lunch with you), **Eline** (you should get a medal for bravery), **Ingmar** (our tennis player), **Shahram** (a busy Papa), **Teunis** (the first one who taught me to work with 3D printer, thanks), **(Mama)Francoise** (I admire your fascinating social skills), **Kirsten**, **Eric**, **Pier**, **Mauricio** and **Juan** (you added the Latino spirit to the group), **Ebrahim** and **Vahid**, and other staff members: **Jie**: (I wont forget your smile), **Nazli** (a kind and caring person), **Julian**, **Paul**, **Gerwin**, and other floormates for being with me.

I would like to express my particular appreciation to **Mahya**; your valuable help and advice helped me to quickly settle down in the Netherlands. I wish you good luck in your future endeavors.

To **Khashayar**, and **Sara**: I will never forget your help in the first few months of my arrival. I also appreciate your help and commitment in our shared project, **Khashayar**, as what once Lidy said, "*We were the progenitors of CCB lab!*". I wish you lots of success in your new job.

Supervising new students was one of the challenging parts of my journey in which I learned a lot and gained more experience. I'll take this opportunity to say congrats once more to my amazing master students: **Dirk**, **Katerina**, **Bogdan**, **Angeliki** for their outstanding master thesis. I wish you the best of luck with your PhD and in your future career.

To our LATINO's friends **Dictator Tomas**, **Manyu**, **Carlos**, **Carlos (Jesus)**, **Carlos Andres**, **Suad**, **Maolong**, **Mattia**, **Marina**, **Barbara**, **Alejandro**, and **Alfiya**: I have been blessed by our delicious daily lunch, BBQ sessions, weekly cake meetings, amazing LATINO's dishes, weekly basketball meetings, and of course, our friendship over the past years.

To **Nahid**, **Alireza** and their cute baby **Emma**, I never forget our great BBQ and Emma's smiley face, especially on our memorable trip to Zeeland. Thanks for being there with us in the past years and particularly during the pandemic.

I would also like to take the opportunity to raise a toast for 10 years of faithful friendship with my close friends: My gorgeous Engineer **Samin** in Iran, my beautiful business women **Reyhaneh** in the UK, my brilliant professor **Yasaman** in the US, and my lovely dr. **Fatemeh** in Sweden who supported me during my

PhD and help me become the best version of myself. I really needed our phone chats and laughs to start/finish my day.

I would like to thank all my friends in Iran: **Nafiseh, Niloofar, Mohadde-seh, Azar, Godsiyeh, Hadis, Saeedeh, Nastran, Katayoon, Zahra**, and in the Netherlands: **Faezeh, Nasibeh, Amir, Ali, Javad, Azar, Maede** for their kindness and support.

My family is a priceless gift, greater than anything I can imagine. The most important thanks to my lovely **Mom** and **Dad** for their generous support during the past 29 years of my life, for tolerating our two years of physical absence during the Corona pandemic, and much much more. Words are not enough to express my love for you. That was a pity that the pandemic did not allow us to host you on my promotion day. But, I hope that we can celebrate this special moment later together. It is a true blessing to have such smart beautiful funny and caring **siblings**. Although we are miles away, you are too close to my heart to love you. I have incredibly enjoyed watching you grow up and become independent over the years. **Mohadeseh**, my talented artist engineer and manager, I am surprised how quickly you can adapt to all the changes and to develop your skills in different aspects. You are the person who always answers my random calls, no matter what time; thank you for always being there for me. **Mahdi**, my kind, supportive confident, and creative brother, who indeed brings happiness and joy into our lives. I believe your hard work will be paid off very fast and you will reach the top of your field soon. My little sister, **Marry**, you are the most curious one, and I have always been fascinated by your never-ending questions! I am sure there will be a bright future ahead of you. The impact of my siblings on my personal growth is much more than one might think. Thank you all for your support and kindness. I would like to give special thanks to my lovely **mother-in-law** and kind **sisters-in-law**, who always surprised me with your beautiful gifts, warm hospitality and great support.

Last but not least, the biggest special regards go to **Mohammad**, my lovely partner, passionate supporter, and great scientist. It is so hard to explain how blessed I am to spend the rest of my life with such a humble, smart, and kind-hearted man. You have been always there to give me the motivation to keep going. I sincerely appreciate your commitment to work as well as personal life and admire your endless effort. Although we have had our ups and downs, I truly love you, my sweetheart! I do not know how long, but I do know I will be with you till the end.

برای پدر و مادر عزیزم

ایسر کتاب را تقدیم میکنم به مقدس ترین سوخته مادر لغت نامه دلم

مادر مهربانم، که زندگی را بی یون مهر و عطف آن مردانم

و پدرم، که همواره در سایه سار حمایتش، جرئت چشم دوختن به افق های دور را یافته ام

مادر دلسو و پدر صبورم، حکمت قاصر از میان محبت و زحمات بر دریغ شماست؛ فقط میتوانم بنویسم هزاران بار سپاس

از خداوند برایتان آرزوی سلامتی دارم و انشالله دعای خیرتان بر قره را همان ماند

دوستتان دارم

همه

List of Publications

Journal Papers

1. M. Nouri-Goushki, L. Angeloni, K. Modaresifar, M. Minneboo, U. Staufer, P.E. Boukany, M.J. Mirzaali, M. Ghatkesar, L.E. Fratila-Apachitei, A.A. Zadpoor, "3D printed submicron patterns reveal the interrelation between cell adhesion, cell mechanics, and osteogenesis", **ACS Applied Materials and Interfaces**, 2021, 13, 29, 33767–33781, <https://doi.org/10.1021/acsami.1c03687>
2. M. Nouri-Goushki, A. Isaakidou, BIM. Eijkel, M. Minneboo, U. Staufer, L.E. Fratila-Apachitei, A.A. Zadpoor, "3D printed submicron patterns orchestrate the response of macrophages", **Nanoscale**, 2021, 13, 14304-14315, <https://doi.org/10.1039/D1NR01557E>
3. M. Nouri-Goushki, M.J. Mirzaali, D. Fan, M. Minneboo, U. Staufer, L.E. Fratila-Apachitei, A.A. Zadpoor, "3D printing of large areas of highly ordered submicron patterns for modulating cell behavior", **ACS Applied Materials and Interfaces**, 2020, 12, 1, 200–208, <https://doi.org/10.1021/acsami.9b17425>
4. M. Nouri-Goushki, A. Sharma, L. Sasso, S. Zhang, B.C.J. van der Eerden, U. Staufer, L.E. Fratila-Apachitei, A.A. Zadpoor, "Submicron patterns-on-a-chip: Fabrication of a microfluidic device incorporating 3D printed surface ornaments", **ACS Biomaterials Science and Engineering**, 2019, 5, 11, 6127-6136, <https://doi.org/10.1021/acsbiomaterials.9b01155>
5. M. Nouri-Goushki, A. Mousavi, M.J. Abdekhodaie, M. Sadeghi, "Free radical graft polymerization of 2-Hydroxyethylmethacrylate and Acrylic acid on polysulfone membrane surface through circulation of reaction media to improve performance and hemocompatibility properties", **Journal of Membrane Science**, 2018, 564, 15, 762-772, <https://doi.org/10.1016/j.memsci.2018.07.071>.
6. M. Nouri-Goushki, BIM Eijkel, L.E. Fratila-Apachitei, A.A. Zadpoor, "Osteoimmunomodulatory Potential of Submicron Patterns assessed in a Direct Co-culture Model", In revision.
7. L. Angeloni, B. Popa, M. Nouri-Goushki, A.A. Zadpoor, M. Ghatkesar, L.E. Fratila-Apachitei, "Fluidic force microscopy and atomic force microscopy unveil new insights into the interaction of preosteoblasts with submicron patterns", Submitted.
8. A. Dimaraki, P.J. Díaz-Payno, M. Minneboo, M. Nouri-Goushki, M.J. Mirzaali, N. Kops, R. Narcisi, G.J.V.M. van Osch, L.E. Fratila-Apachitei, A.A. Zadpoor "Bioprinting of a zonal-specific cell density scaffold: a biomimetic approach for cartilage tissue engineering", **Applied Sciences**, 2021, 11(17), 7821, <https://doi.org/10.3390/app11177821>

9. M.J. Mirzaali, A. Ghorbani , K. Nakatani , *M. Nouri-Goushki* , N. Tumer , S. Callens , S. Janbaz , A. Accardo , J. Bico , M. Habibi , A.A. Zadpoor "Curvature induced by deflection in thick meta-plates", **Advanced Materials**, 2021, 33, 30, <https://doi.org/10.1002/adma.202008082>
10. L. Angeloni, M. Ganjian, *M. Nouri-Goushki*, M.J. Mirzaali, C.W. Hagen, A.A. Zadpoor, L.E. Fratila-Apachitei, M.K. Ghatkesar, "Mechanical characterization of nanopillars by atomic force microscopy", **Additive Manufacturing**, 2021, 39, 101858, <https://doi.org/10.1016/j.addma.2021.101858>
11. M.J. Mirzaali, M.C. Saldívar, A.H. de la Nava, D. Gunashekar, *M. Nouri-Goushki*, E. Doubrovski, A.A. Zadpoor, "Multi-Material 3D Printing of Functionally Graded Hierarchical Soft–Hard Composites", **Advanced Engineering Materials**, 2020, 22, 7, <https://doi.org/10.1002/adem.201901142>
12. M.J. Mirzaali, A. H. de la Nava, D. Gunashekar, *M. Nouri-Goushki*, R.P.E. Veeger, Q. Grossman, L. Angeloni, M.K. Ghatkesar, L.E. Fratila-Apachitei, D. Ruffoni, E.L. Doubrovski, A.A. Zadpoor, "Mechanics of bioinspired functionally graded soft-hard composites made by multi-material 3D printing", **Composite Structure**, 2020, 237, 111867, <https://doi.org/10.1016/j.compstruct.2020.111867>
13. M.J. Mirzaali, A.H. de la Nava, D. Gunashekar, *M. Nouri-Goushki*, E. Doubrovski, A.A. Zadpoor, "Fracture Behavior of Bio-Inspired Functionally Graded Soft–Hard Composites Made by Multi-Material 3D Printing: The Case of Colinear Cracks", **Journal of Materials**, 2019, 12(17), 2735; <https://doi.org/10.3390/ma12172735>

Conference Presentations

- M. Nouri-Goushki, A. Isaakidou, M. Minneboo, U. Staufer, L.E. Fratila-Apachitei, A.A. Zadpoor, "*Osteogenic and immune responses evoked by additively manufactured nanopatterns*", World Biomaterials Congress (WBC), UK, 2020
- M. Nouri-Goushki, A. Sharma, M. Minneboo, U. Staufer, L.E. Fratila-Apachitei, A.A. Zadpoor, "*Engineering of a 3D cellular microenvironment for bone tissue regeneration*", BioDay congress, Netherlands, 2019, **The winner of the Best Poster Award**
- M. Nouri-Goushki, M. Minneboo, U. Staufer, L.E. Fratila-Apachitei, A.A. Zadpoor, "*Multiscale 3D printed nanopatterned scaffolds*", 30th Conference of the European Society for Biomaterials (ESB), Germany, 2019
- M. Nouri-Goushki, A. Sharma, M. Minneboo, U. Staufer, L.E. Fratila-Apachitei, A.A. Zadpoor, "*3D printed nanopatterned surfaces induced bone regeneration*", 28th Netherlands Society for Biomaterials and Tissue Engineering (NBTE), Netherlands, 2019

Curriculum Vitae

Mahdiyeh Nouri-Goushki was born on August 28, 1992, in Baft, Iran.

Her curiosity about technology in daily life and her excellent score in the Iranian university entrance exam "Konkour" brought her to the top best technical university, "Sharif University of technology", to pursue a BSc in Chemical Engineering. She continued her education with an MSc in Polymer Engineering at Sharif University of technology and obtained her degree in 2016 with a thesis on "chemical surface modification of Polysulfone hemodialysis membranes".

During her Master thesis, she realized her interest in the field of biomaterials and regenerative medicine. To achieve her dream, she moved abroad in 2018 and joined the Biomaterials and Tissue Biomechanics section in the Biomechanical Engineering Department at Delft University of Technology. Mahdiyeh pursued her PhD under the supervision of Prof. Amir A. Zadpoor and dr. Lidy E. Fratila-Apachitei. Her research focused on the development of smart nanopatterned surfaces to manipulate the osteoimmunomodulation properties of the bone biomaterials. Over the course of the PhD program, she attended several (inter)national conferences and contributed as a teaching assistant to several MSc-level courses and side-projects.

Mahdiyeh actively collaborated with multiple research groups to complete her multidisciplinary project. She worked in the Precision and Microsystem Engineering Laboratory of Prof. Urs Stauer (TUDelft) to fabricate the nanopatterned surfaces. Furthermore, She collaborated with Prof. Bram C.J. Van der Eerden (Department of Internal Medicine, Erasmus Medical Center) to develop the dynamic culture models. In addition, she established a collaboration with dr. Pouyan Boukany (Optical Microscopy Laboratory, Department of Chemical Engineering, TUDelft) to acquire confocal imaging data.

In the last year of her PhD journey, she joined dr. Boukany's group as a post-doctoral researcher to broaden her horizons in cancer research.